Magnetospheric energetics in stellar wind–planet interactions

Implications for close–in extrasolar planets

Inaugural-Dissertation

zur

Erlangung des Doktorgrades

der Mathematisch-Naturwissenschaftlichen Fakultät

der Universität zu Köln

vorgelegt von

Filip Elekes

aus Banja Luka

Bonn, 2. Dezember 2024

Die vorliegende Dissertation wurde im Jahre 2024 bei der Mathematisch-Naturwissenschaftlichen Fakultät der Universität zu Köln im Fach Geophysik eingereicht.

Berichterstatter (Gutachter)	Prof. Dr. Joachim Saur
	Prof. Dr. Peter Schilke

Tag der mündlichen Prüfung: 11.02.2025

Abstract

The interaction between exoplanets close to their host stars and the surrounding stellar wind can potentially convert large amounts of electromagnetic energy. The converted powers are believed to exceed the strongest star–planet interactions in the solar system by orders of magnitude. Apart from the strong emissions produced by such interactions, they can have an impact on the evolution of planets, their space environment, atmosphere and interior. Planetary magnetic fields play a crucial role in the amount of energy converted during such interactions. A large number of known exoplanets are in close orbits around their host stars. In addition, many exoplanets have been discovered around sun-like and cool stars that exhibit significant magnetic activity. As magnetic activity increases, so does the possible influence of stars on the space environment of planets through frequent eruptions and flares, known as space weather. The sun's most energetic eruptive events are coronal mass ejections, which can contribute significantly to the erosion of atmospheres, for example. The Earth's magnetic field protects us to some extent, but whether this is a universal property of planetary magnetic fields is currently being debated. All in all, the strength of interactions between planets and their space environment is significantly influenced by the energy content of the stellar wind plasma and that of the stellar eruptive events. A planetary magnetic field increases the size of the planetary obstacle to intercept the plasma. In this work we aim to better understand the energetics of stellar wind-planet interactions and role of planetary magnetic fields in controlling the dissipation of energy contained in coronal mass ejections within the planets. We focus on two exoplanetary systems that are of particular importance for the field of exoplanet science.

In the solar system, most gas planets and terrestrial planets have, or had, a magnetic field. Magnetic fields of exoplanets have not yet been measured conclusively. Long-standing efforts have been made to measure the magnetic fields of exoplanets by means of radio emissions originating from the auroral regions of the exoplanets. Recently, the first promising observation of radio emission from the Hot Jupiter exoplanet τ Boötis b was reported, but to date this measurement has not been confirmed by follow-up observations. With auroral radio emissions from exoplanets the magnetic field strength of the planet can be deduced. In this work we make use of the proposed magnetic field strength of τ Boötis b to constrain its space environment and to dissect the energetics of the systems by means of magnetohydrodynamic simulations. We study the detailed electromagnetic energy fluxes of the interaction that ultimately carry the energy to power the auroral emissions. Due to the uncertainty of stellar wind predictions we also study the role of stellar wind density and magnetic field orientation on the energetics. In our simulations find that Poynting fluxes converted in the magnetosphere of the planet reach up to 10^{18} W. We find that exceptionally high Poynting flux-to-radio efficiencies are needed that exceed those measured at Jupiter by orders of magnitude. Furthermore, the magnetic activity of the host star, τ Boötis A, can cause magnetic polarity reversals

which strongly affect magnetic reconnection between stellar wind and planetary magnetic field. Due to the stars known magnetic cycle we expect periodic increases and decreases in radio power. In a closed magnetosphere the estimated radio flux falls below the observational threshold of the LOFAR telescopes, nearly regardless of the stellar wind density. Despite the high energetics of the interaction, radio fluxes generated in the auroral regions of the planet are, according to our model, too weak to be observable on Earth. These results make it clear that the search for radio emission requires stronger targeted stellar wind-planet interactions and better stellar wind predictions.

The Trappist-1 system of consists of seven terrestrial exoplanets orbiting an active cool star in close distances. In this work we study the space environment of Trappist-1b and e that is exposed to stellar coronal mass ejections (CMEs) by means of time-dependent magnetohydrodynamic simulations. We aim to better understand how planetary magnetic fields influence the intake of energy carried the CMEs. Furthermore, we study the interaction with CMEs dominated by different kinds of energy. We consider purely mechanical CMEs consisting of enhanced density and velocity and magnetically dominated CMEs that posses intrinsic flux ropes. We aim to understand the CME energy dissipation within the planet's interior by calculating inductive heating of the interior due to variations of magnetospheric magnetic fields. In our simulations we find that, for flux rope CMEs, planetary magnetic field only have insignificant effects on the energy dissipated in the interior as the magnetic variability contained in the flux rope translates to the magnetosphere via reconnection. Mechanical CMEs, however, need to convert the mechanical energy to magnetic variability by deforming and perturbing the planetary magnetic field. The magnetospheric dynamo action responsible for the conversion of kinetic energy to magnetic variability, strongly depends on the planetary magnetic field strength. Thus, dissipation rates in the interior scale strongly with the planetary magnetic field. Above a planetary magnetic field near half of Earth's magnetic field strength, the dissipation rates saturate in bot CME models and decrease slowly for stronger magnetic fields. Heating rates for single CME events are in the order of 1-10 TW while Joule heating the a hypothetical ionosphere amounts to several thousands of TW. Atmospheric dissipation rates that high can drive significant atmospheric outflows. In regard to the Poynting fluxes oriented towards the planet we find that the electromagnetic energy converted within the magnetosphere scales with the magnetic field cubed. Thus, planetary magnetic fields amplify the intake of external electromagnetic energy although only a smaller amount is eventually dissipated within the planet or in its atmosphere.

Contents

Statement on Originality

The present dissertation is largely based on a published and not yet published manuscript. I hereby declare that Chapters 1, 2, 3, 5 and 8 are my original work and which I wrote particularly for this thesis, apart from minor exceptions I declare in the following.
Chapter 4 in which I define the goals of this work is partly taken from the introductory sections of the published paper (Elekes & Saur 2023) and from the yet unpublished manuscript. The corresponding parts were rearranged, extended and edited to fit into this work. The description of emission scenarios in section 3.6 is taken from the published paper Elekes & Saur (2023). The last paragraph about atmospheres of the Trappist-1 planets in Sect. 2.2.1.2 is taken from the introduction of the unpublished manuscript.

Chapter 6 is carried over from the published paper, Elekes & Saur (2023), which I wrote and for which I carried out the research. Joachim Saur, the co–author and my supervisor, assisted me with numerous discussions, suggestions and with revising the manuscript multiple times until we considered it publishable. Small editorial changes were done at several places to make the sections from the paper fit into this work. Sections 6.3.1 was partly taken from the appendix of the corresponding paper (Elekes & Saur 2023) and Sect. 6.5.2.4 was extended by two new figures and a discussion on plasma–to gyro frequency ratios, which is all my own work.

Chapter 7 is taken from a yet unpublished manuscript which is currently in preparation and written by me. The first co–author, Joachim Saur, supported me with plenty of discussions, suggestions and revisions of the manuscript. The second co–author, Alexander Grayver, assisted me with discussions, remarks and by providing an implementation of his induction model for planetary interiors (described in Sect. 7.4.2). Changes to the text were made to nearly every section in order to make the manuscript fit into this thesis. Section 7.3, the paragraph about open field line regions in Sect. 7.4.1 is entirely new. The paragraph on the depth dependence of Joule heating in Sect. 7.4.2 is new. Section 7.4.5 as well as parts of 7.5 are partly taken from the appendix of the corresponding manuscript. Sections 7.4.6, 7.6.1 and 7.7.3 are entirely new.

The introduction sections of chapters 6 and 7 are new and written specifically for this thesis. The appendix of the Trappist-1 chapter, Sect. C as well as appendix A, were written specifically for this thesis.
The research for this thesis was conducted by me and all texts were written by me with the exception of individual sentences and phrases the co–authors suggested me during the revisions of the manuscript and paper. The published paper (Elekes & Saur 2023) and the yet unpublished manuscript both correspond directly to the research done and presented in the corresponding chapters 6 and 7 and were written by me.

1. Introduction

We were born too early to fly to other worlds and to explore them up close. We, however, belong to the first generation to discover and to explore these exoplanets for the first time. Within a very short time, since the dawn of exoplanet science when the first extrasolar planet was discovered in the year 1995 (Mayor & Queloz 1995), the number of known exoplanets has increased by vast amounts. And with the number of known exoplanets, we are also realizing more and more how diverse they are.

A large amount of exoplanets reside in close orbits around their stars (Winters et al. 2019; Bochanski et al. 2010). Moreover, many of these stars are found around very active stars (Dressing & Charbonneau 2015; Bonfils et al. 2013). These planets are naturally embedded in a harsh and energetic environment dominated by stellar winds and their magnetic fields (e.g. Dong et al. 2018; Garraffo et al. 2017). These possibly exert a great influence on the planetary space environments, atmospheres and interiors as well as on their evolution (Grayver et al. 2022; Cohen et al. 2014). One of the most important components of magnetic star–planet interactions are planetary magnetic fields. On Earth we are confident to say that the magnetic field protects us from the threat of atmospheric erosion through the solar wind. It is, however, not clear if this is a universal property of planetary magnetic fields (Sakata et al. 2020; Airapetian et al. 2020, 2018; Tilley et al. 2019). Moreover, planetary magnetic fields shape the magnetic interaction between stellar winds and planets. They strongly influence the topology of the interaction and thus also the converted energy channeled towards the planets and stars (e.g. Strugarek et al. 2014, 2015). Magnetic interactions between stellar winds and planets, most notably also violent stellar eruptions that transport large amount of energy towards the planets, have been argued to even influence the interior of planets due to magnetic induction (Grayver et al. 2022; Slavin et al. 2014). Lastly, the strength of star–planet interactions and planetary magnetic fields essentially shape the observable signatures from which we can infer information on the star–planet system.

We aim to provide new insights into the nature of close–in exoplanets by studying the energetics of stellar wind–planet interactions and planetary responses to space weathering in detail. We are specifically interested in understanding the role of planetary magnetic fields in governing the transfer of energy from the stellar wind or stellar eruption towards the planet and ultimately towards their interior. We use magnetohydrodynamic simulations to investigate the plasma environment of magnetized and non-magnetized and the interaction with the surrounding stellar wind. In two distinct projects we focus on different aspects of magnetic stellar–wind planet interactions.

The recently reported tentative measurement of radio emission believed to originate from the magnetosphere of the close–in, gas giant τ Boötis b (Turner et al. 2021),

provides us with the first possible constraint on an exoplanetary magnetic field. We use the inferred magnetic field strength to better characterize the space environment and the local energy fluxes that ultimately provide the energy for the observed radio emission. Due to the uncertainty of stellar wind predictions we systematically vary dominant stellar wind parameters to learn more about the observability of close-in exoplanets in the radio range as a function of stellar winds. Subsequent follow-up observations have not resulted in a confirmation of the first detection (Turner et al. 2024, 2023). We aim to understand possible reasons for non–detections and to improve our search for suitable targets to observe exoplanetary magnetic fields.

Of particular interest for the general public is certainly the search for extraterrestrial life. Since the discovery of numerous terrestrial exoplanets, the view of habitability has become increasingly complex. Here too, magnetic fields certainly play a major role, but what their exact role is in energetically shielding the planet from variable stellar wind conditions and violent stellar eruptions is not yet well understood. Many terrestrial exoplanets, such as the Trappist-1 exoplanets (Gillon et al. 2017), orbit magnetically active cool stars in close orbits. Due to the proximity to the stars the planets are exposed to frequent stellar eruptions, flares and strong, potentially variable, magnetic fields. We aim to better understand the energetic coupling between planets and their space environment in this context by examining the role of planetary fields. We use our magnetohydrodynamic model describe the time–dependent interaction between two rocky Trappist-1 and coronal mass ejections, the most violent type of stellar eruptions. We assess the capability of hypothetical planetary magnetic fields in shielding the planets energetically from the eruptions. We furthermore study the inductive coupling between the planetary interiors and the magnetic variability caused by the interaction with coronal mass ejections. Ultimately, we investigate how planetary magnetic fields govern energy dissipation within the planetary bodies and their upper atmospheres.

In this work we first give an introduction to extrasolar planets, with a focus on planets in close orbits around their star. At the end of section 2 we introduce the primary targets of this study, τ Boötis b and the Trappist-1 system.

In section 3 we provide a comprehensive introduction to star–planet interactions and the basic physical quantities to describe such interactions, where we increasingly focus specifically on stellar wind–planet interactions. After that we introduce the most important aspects of stars, their winds and eruptions, which are most important for this study. We conclude the chapter with a description of the consequences for planets and possible observable signatures.

In section 4 we describe in detail the aim of this study and motivate our approach individually for each project.

In section 5 we provide a detailed description of our general magnetohydrodynamic model, parametrization of physical processes we include to model the exoplanets and numerical specifications of our numerical model.

Sections 6 and 7 contain the project–specific model descriptions, results and their discussions for the τ Boötis b and Trappist-1 project, respectively.

In Sect. 8 we conclude this thesis and summarize our results.

2. Extrasolar planets

With the first definite detection of an extrasolar planet named 51 Pegasi b in the year 1995 by Mayor & Queloz (1995) the new era of exoplanet characterization emerged in which more than 5500 additional exoplanet detections followed in the past decades (exoplanet.eu 2024). The most successful exoplanet detection methods favor the detection of close–in planets. This results in a majority of confirmed exoplanets being in close–orbits around their host stars with orbital periods in the order of days (Wright & Gaudi 2013). Close–in exoplanets are of particular interest for exoplanet research due to the extreme environmental conditions they reside in and due to the promising prospects for possible observations and atmospheric characterizations, made possible by transit or reflected light observations. These planets are also of practical interest, as they are exemplary for interactions that can be found in the solar system, such as Mercury and the Galilean moons of Jupiter, albeit they generally reside in less extreme environments. In this thesis we focus on such close–in planets and how they interact with the extreme stellar environment. Accordingly, in the following sections we introduce the basic characterization of those planets and describe their presumed properties (Sect. 2.1), before introducing the target planets of this work (Sect. 2.2.1) and turning to the subject of star–planet interactions and consequences derived from them (3.1).

2.1. Classification of exoplanets

When examining the catalog of confirmed exoplanets we find a large diversity among all types of exoplanets, their orbital distances from their host stars and the types of host stars themselves. Figure 2.1 shows a diagram of a representative number of confirmed exoplanets. Plotted are planetary masses (in Jupiter masses) as a function of orbital period (in days). Most pronounced is the clustering of detected planets with short orbital periods between 1 and 50 days. These short periods indicate that those planets are close to their host star, with orbital semi–major axes far below one AU. A majority of these planets orbit solar–type stars while terrestrial exoplanets with masses comparable to Earth (with approximately 3×10^3 Jupiter masses) or lighter are most commonly found orbiting low mass and thus cool stars. A second distinct group of exoplanets is formed by gaseous giant planets orbiting sun–like stars (prominently F, G, K and M class stars) at small distances. These gas giants are, due to their proximity to the star, highly irradiated and thus exhibit high surface temperatures. These are named hot Jupiters or warm Neptunes, depending on their mass and orbital distance from the star. These two groups of exoplanets seem to make up a significant fraction of all confirmed exoplanets although one should keep in mind the observational bias caused by our methods to detect exoplanets in the first place. The most successful methods of

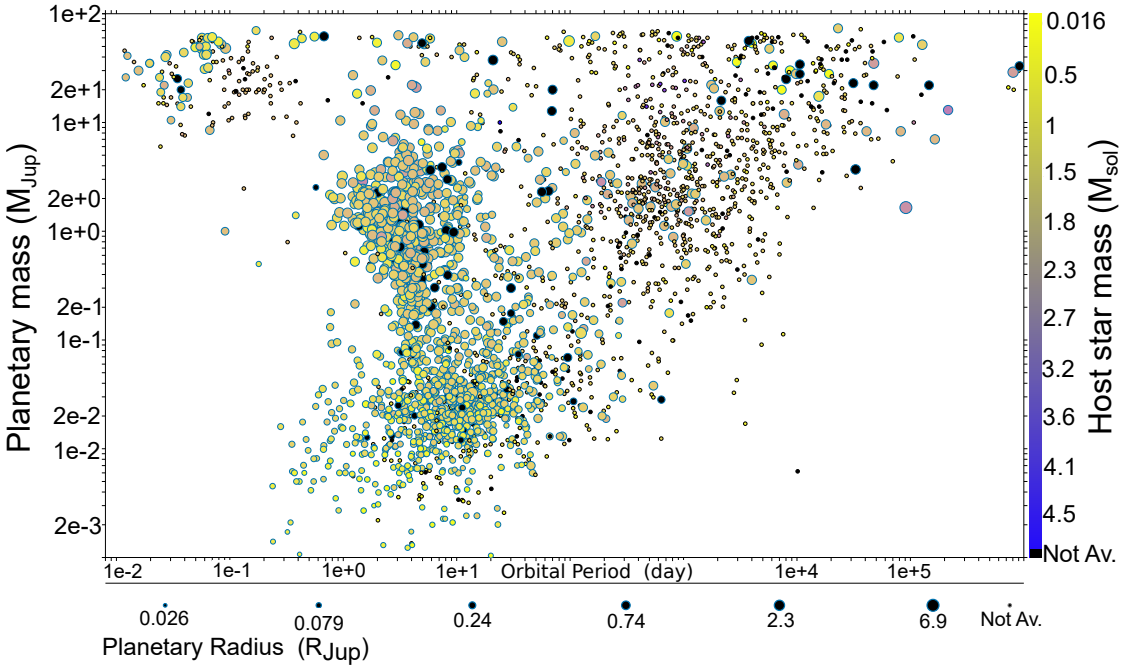

Figure 2.1.: Shown is a planetary mass–orbital period diagram of confirmed exoplanets. The mass of host stars is color–coded (right colorbar in units of solar masses). The size of the dots indicates the planetary radii in Jupiter radius units (legend in the bottom of the figure). The diagram was generated using the plotting tool on exoplanet.eu (2024).

exoplanet detection, namely the transit and radial velocity method, rely heavily on either the planet's effects on observable stellar light curves (by occultation during transits) or on stellar motion caused by the planet's gravitational pull on them (evident in Doppler shifted stellar spectra due to their planet–modulated line–of–sight motion) (Wright & Gaudi 2013). These effects are governed by the planetary mass, size, orbital inclination and proximity to the star. Most terrestrial exoplanets seem to be found around cool and low mass stars (Dressing & Charbonneau 2015; Bonfils et al. 2013). Due to their low mass, planets typically orbit the stars in close orbits, favoring their detection. Low mass M–dwarf stars are the most common stars in the solar neighborhood. It is therefore hardly surprising that we find such a large number of exoplanets around M–dwarfs (Winters et al. 2019; Bochanski et al. 2010).

2.1.1. Hot Jupiter–type exoplanets

Hot Jupiter's are gaseous giant planets in close orbits around their host stars. They are massive and thus exert strong gravitational pull on their host stars. The namesake of this planet type, Jupiter, although orbiting the Sun at about 5 AU, has great influence on the Sun's motion. This applies all the more to Jupiter-like planets close to the stars which leads to strong Doppler shifts of the stellar spectra, so that these planets can be detected relatively well even without planetary transits. To be called a hot Jupiter the

exoplanet typically has a mass similar to Jupiter and orbits the host star below 0.1 AU. Hot Jupiters are of particular interest for exoplanet research due to their possibly strong interactions with stars and stellar winds, leading to promising conditions for observable signatures of these interactions such as auroral emissions (e.g. Zarka 2007). The high temperatures on the daysides of such planets may lead to strong photo–evaporation (Vidal-Madjar et al. 2003a), hydrodynamic escape of their atmospheres (e.g. Dong et al. 2018; Adams 2011) or even accretion towards their host stars (Zhilkin & Bisikalo 2020; Matsakos et al. 2015; Adams 2011). Many Hot Jupiters are expected to reside within a sub–Alfvénic stellar wind (Zhilkin & Bisikalo 2019; Saur et al. 2013), making it possible to also excite emissions on the stars themselves, with prominent targets being AU Mic b (e.g. Klein et al. 2022), τ Boötis b (Turner et al. 2021) or HD 118203 b (e.g. Castro-González et al. 2024). Like all gas giants in the solar system, Hot Jupiters are expected to possess magnetic fields due to the generally convective interior of gaseous planets. On the one hand, magnetic fields would enhance interactions with the star and stellar wind, and on the other hand, the existence of magnetic fields would be expected to result in measurable emissions, making these planets a primary target of observational campaigns targeting extrasolar auroras.

2.1.2. Close–in terrestrial exoplanets

Another group of exoplanets can be summarized as terrestrial, or rocky, exoplanets. These are generally referred to as *Earth–like* regardless of the conditions for life there. We are particularly interested in terrestrial exoplanets close to their star due to their potentially strong coupling with the stellar environment and the favorable conditions for observations. Great motivation also comes from the fact that the understanding of planetary habitability can be tested and researched on such planets. Therefore, they are considered an excellent laboratory to study how atmospheres behave and evolve under extreme environmental conditions, or what role planetary magnetic fields play in the protection of atmospheres, surface and interior from the extreme conditions exerted by the stars. Additionally, most exoplanets are found around cool stars, which are notorious for their magnetic activity and associated harsh space weather conditions. A planetary system consisting of 7 terrestrial exoplanets is the Trappist-1 system (Gillon et al. 2017) which is a primary target in this work. The large number of terrestrial planets in the system makes Trappist-1 an important target for studies of all kinds.

2.2. Properties of exoplanets

Everything we know for certain about planets we have learned from solar system planets. Derived from this knowledge we have certain expectations on what these extrasolar worlds look like and what properties they might have.

Atmospheres From the solar system we know a variety of possible atmospheres planets may have and how they possibly evolve during their lifetime. Atmospheric evolution

highly depends on stellar properties. Due to stellar radiation and stellar winds, atmospheres of close–in planets are affected by escape processes. Thermal escape is controlled by temperatures of upper atmospheres that is dominantly influenced by stellar EUV to X–Ray radiation while non–thermal escape processes include atmosphere–plasma interactions and erosion like sputtering (Gronoff et al. 2020).

Observations of sun–like stars of younger age indicate that stars are more active when they are young. Solar activity certainly affected atmospheric escape in the past due to higher atmospheric energy input to the solar system planets (Lammer et al. 2009). This might result in difficulties for planets around active stars to retain their atmospheres. Most importantly EUV–XUV flux shapes the upper atmosphere temperature profiles and affects particle populations due to photo–chemistry (e.g. Koskinen et al. 2013). Plasma interactions, resulting variations in magnetic fields and induced currents in the conductive plasma may as well deposit large amounts of energy into the upper atmosphere in form of Joule heating (e.g. Vasyliūnas & Song 2005). High temperatures may inflate upper atmospheres and, in return, make them more vulnerable to external forcing and erosion (Gronoff et al. 2020). Atmospheres of non–magnetized exoplanets may be eroded significantly by interaction with the stellar wind in addition to stellar irradiation (Cohen et al. 2015). Surprisingly, weak planetary magnetic fields that get strongly perturbed by stellar winds can erode planetary atmospheres more efficiently than without a magnetic field at all (e.g. for Mars; Sakata et al. 2020).

Characterization of exoplanet atmospheres is mainly done via transit and secondary eclipse observations. Escaping atmospheres can be evident by characteristic absorption lines in stellar spectra, most prominently the Lyman–α absorption line due to neutral hydrogen atoms which led to the first conclusive detection of an escaping atmosphere (HD 209458 b Vidal-Madjar et al. 2003a). More indirectly, dayside temperatures of planets obtained during secondary eclipse measurements can provide hints on the efficiency of redistribution of heat due to atmospheric convection or if atmospheres are even present on the observed planets (e.g. for Trappist-1b and c Greene et al. 2023; Zieba et al. 2023).

Interior The interior of exoplanets is mostly unconstrained due to the lack of in–situ gravity measurements. There are, however, possibilities to get rough estimates on average densities and possible layer structures within the planets by studying planetary rotation, bulk density and transit timing variations (e.g. Agol et al. 2021). Despite characterizing the overall average density of exoplanets, i.e. to associate respective planets either with rocky or gaseous planets, estimates on the interior structure of exoplanets mostly rely on numerous model assumptions (e.g. Dorn et al. 2018).

Magnetic fields There is no confirmed detection of an exoplanetary magnetic field but a considerable list of candidates exists, with the detection by Turner et al. (2021) being the most promising. In the context of signatures of star–planet magnetic interactions (Sect. 3.6) we will go into more detail regarding direct and indirect magnetic field ob-

servations. At this point we nevertheless want to give a short description of what we expect from exoplanetary magnetic fields. The list of target exoplanets for magnetic field characterization is long and is based mostly on the strength of expected dynamo magnetic fields and the strength of predicted star–planet interactions. The most promising method to detect planetary magnetic fields is via radio observations (e.g., Grießmeier 2015; Farrell et al. 1999; Zarka et al. 2001; Zarka 2007). Auroral radio emission is directly related to the planetary magnetic field strength (see Sect. 3.2) and to the power supplied to the electrons that is mostly governed by the strength of the star–planet interaction or, in the case of Jupiter, internal magnetospheric energy fluxes. Planetary magnetic fields are typically estimated via dynamo scaling laws which depend on the unconstrained interior structure and rotation of exoplanets (e.g. Grießmeier et al. 2007b, 2011; Griessmeier 2017) although we do not even know which exoplanets are magnetized. With the use of simple stellar wind estimates and empirically obtained stellar wind–to–radio emission efficiency factors based on solar system observations (e.g. Zarka 2007), the emission characteristics are estimated. In this thesis we will show how misleading such estimates can be in regard to expected radio emission (Elekes & Saur 2023). Even a strongly magnetized planet embedded in a relatively weak stellar wind may produce radio emission way below the observable threshold of current, state of the art radio telescopes (e.g. LOFAR). The topology of the magnetic star–planet interaction also plays a key role (Strugarek et al. 2015), therefore accurate observations of stellar magnetic fields are needed.

Habitability Traditionally, habitability of exoplanets is assessed using planetary equilibrium temperatures based on stellar luminosity and planetary albedo. The equilibrium temperature is the planetary surface temperature in equilibrium between stellar insulation and planetary thermal radiation. An equilibrium temperature at which water exists in liquid state is traditionally considered a prerequisite for habitability (Seager 2013). More sophisticated approaches to assess habitability incorporate radiative–convective, cloud–free climate models and photochemistry that take into account stellar fluxes at certain wavelengths in order to provide additional estimates about water loss and respective greenhouse limits (Kopparapu et al. 2013).
Habitable zones (HZs) around low mass stars lie closer to the stars due to their low luminosity. This ensures habitable temperatures on the planets but at the same time UV and X–Ray fluxes might be considerably stronger. Especially the high luminosity during the early lifetime of low–mass stars might compromise habitability on initially water–rich close–in planets. The reasons are prolonged greenhouse phases, extreme water loss by escape and photo–dissociation on the order of several Earth oceans accompanied by significant abiotic O_2 buildup in the absence of efficient O_2 sinks (Luger & Barnes 2015). While the loss of water is fatal for life, extreme high levels of O_2 may lead to false–positives in the search for life.
The mass of planets is argued to play an important role in determining the width of the HZ by controlling atmospheric densities (Kopparapu et al. 2014). Planetary rotation affects atmospheric radiation balance. Slow rotators generate a weaker Coriolis force

and prolong day times, thus enhancing convection and intensifying the convergent atmospheric flow near the substellar surface. In return, more clouds form that enhance planetary albedo, consequently reducing stellar insulation. Equivalently, slow rotators produce less clouds and reduce planetary albedo (Yang et al. 2014). Other studies showed that tidally locked planets closer to their stars have higher rotation rates that create stronger zonal winds, effectively smearing out substellar clouds across the planet and thus lowering planetary albedo (Kopparapu et al. 2016). This causes the water–vapor greenhouse climatic instability to occur at lower stellar fluxes, thus increasing the probability for planets to lose water by evaporation and escape. The planetary environment is also shaped by the star which strongly affects planetary habitability by altering photo–chemistry and causing atmospheric escape driven by radiation stellar winds and stellar eruptions (Airapetian et al. 2017). Especially the role of magnetic fields in regard to habitability is still an open and controversially discussed question (e.g. Sakata et al. 2020; Airapetian et al. 2020; Tilley et al. 2019; Airapetian et al. 2018).
It is clearly evident that the emerging field of exoplanet research, especially with regard to close–in planets, spawned numerous new questions and discussions on environmental conditions around planets and habitability, where scenarios are thought through that have not been even considered in the solar system.

2.2.1. Target planets of this study

From the pool of over 5000 exoplanets we picked two planetary systems for the research presented in this thesis that are of particular importance: τ Boötis b (Sect. 2.2.1.1) and Trappist-1 (Sect. 2.2.1.2). In context of Trappist-1 we also briefly summarize some properties of Mercury as it is the best observable close–in exoplanet analog exposed to strong space weathering, which helps putting the results of this thesis into context. In the following section we briefly introduce those exoplanets. Later in Sect. 4 we provide a more detailed description and motivation for our study.

2.2.1.1. Tau Boötis b

The detection of the exoplanet τ Boötis b was confirmed in the year 1997 (Butler et al. 1997) and thus it is one of the first exoplanets ever detected. τ Boötis b is a Hot Jupiter type exoplanet with an orbital semi–major axis of 0.046 AU (Butler et al. 1997) (Fig. 2.2). It is a massive gaseous planet with the mass of 5.84 Jupiter masses (Wang & Ford 2011; Brogi et al. 2012; Lockwood et al. 2014) and a radius of approximately 1.01 Jupiter radii (Wang & Ford 2011). The planetary radius is merely a theoretical estimate since τ Boötis b is a non–transiting exoplanet which has been detected via stellar radial velocity measurements (Butler et al. 1997). The orbital inclination with respect to the line of sight is, however, well constrained (about 45 degrees; Lockwood et al. 2014; Brogi et al. 2012) so that the planetary mass is as well. The orbital period of τ Boötis b is approximately 3.3 days (Butler et al. 1997) and the planet is expected to be tidally locked to its host star.
τ Boötis b resides within a binary stellar system. The central host star, τ Boötis A, is

Figure 2.2.: Artists impression of the Hot Jupiter τ Boötis b in its orbit around τ Boötis A. Image credit: ESO/L. Calçada

a solar-like F7 IV-V star (Gray et al. 2001) in a distance of about 15.6 pc from Earth (Stassun et al. 2019). The companion star, GJ 527B, is an M–dwarf star in a distance of about 240 AU from τ Boötis A (Justesen & Albrecht 2019). τ Boötis A is a relatively old star with an age of about 1.3 Gyr (Justesen & Albrecht 2019). Despite its age and spectral type F (i.e. near the upper boundary of partially convective stars), the star is magnetically very active and exhibits a magnetic cycle on the order of one year during which magnetic polarity reversals occur (e.g. Mengel et al. 2016; Fares et al. 2013). The star also shows shorter period activity cycles on the order of 100 days (e.g. Mengel et al. 2016). It is possible that the stellar activity is induced by the massive planet orbiting close to the star due to the star co-rotating with the planet on its orbit (Donati et al. 2008).

τ Boötis b is the exoplanet with the most promising, tentative detection of a planetary magnetic field (Turner et al. 2021) which unfortunately has not yet been confirmed by follow–up detections. The stellar activity and the possible interplay between planetary and stellar magnetic field make the τ Boötis system a unique laboratory to study magnetic star–planet interactions and observational signatures induced by the interaction. The star's properties are observationally comparatively well constrained due to its brightness, proximity to Earth and its size which helps to make relatively confident predictions on the space environment the planet is embedded in.

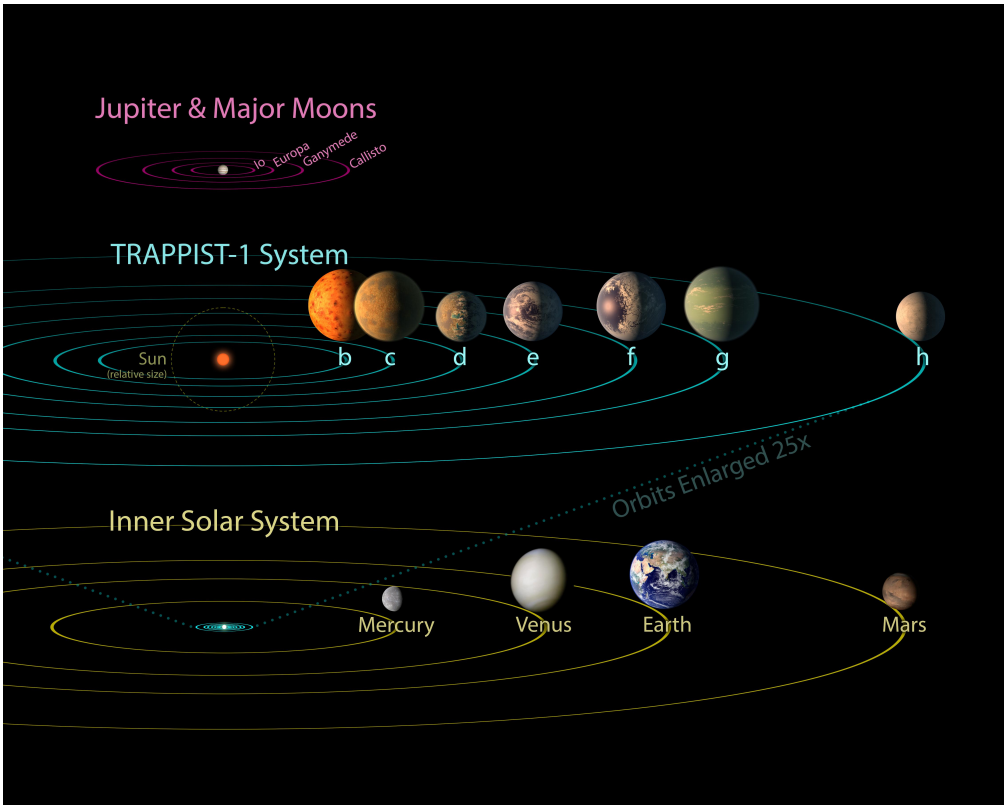

Figure 2.3.: Comparison of the Trappist-1 system to the inner solar system and Jupiter with its Galilean moons. Figure taken from: https://www.jpl.nasa.gov/images/pia21428-trappist-1-comparison-to-solar-system-and-jovian-moons/ (accessed 28.11.2024).

2.2.1.2. Trappist-1 exoplanets

Trappist-1 is a remarkable stellar system where seven terrestrial exoplanets were detected via transit observations so that their sizes are well constrained (Gillon et al. 2017). Three of them, namely Trappist-1d, e and f, are argued to reside within the habitable zone around the central M–dwar star (e.g. Payne & Kaltenegger 2024; Papaloizou et al. 2018; Gillon et al. 2017). The planetary system is extremely compact and would fit well into the orbit of Mercury. In Fig. 2.3 we show the Trappist-1 system next to the inner solar system and the inner Jupiter system. The low distance from Earth of about 12.1 pc and the large number of rocky planets makes the system a popular target for studies on atmospheric characterization, habitability, evolution and on planet formation.
The central star, Trappist-1, is an M8–type red dwarf. The star has a radius of approximately 1.2 Jupiter radii and a mass of about 93 Jupiter masses (Van Grootel et al. 2018) which makes the star a cool star with an effective temperature of about 2500 K. Despite its old age of about 7.6 Gyr (Burgasser & Mamajek 2017), it was confirmed multiple times via flare observations that Trappist-1 is magnetically very active (Howard et al.

2023; Glazier et al. 2020; Paudel et al. 2018; Vida et al. 2017). See Sect. 3.4.1 for a detailed discussion on stellar activity and related phenomena. Additionally, the observed comparatively high X–Ray and EUV luminosity suggest that the star has a hot corona similar to the Sun (Bourrier et al. 2017a; Wheatley et al. 2017). Consequently, the space environment the planets are embedded in could be considerably harsh and threatening to all aspects of habitability like atmospheres, loss of surface water and photo–chemistry. Apart from flares and stellar eruptions, the nominal stellar wind of Trappist-1 that interacts with the planets might be very energetic as well (Garraffo et al. 2017) due to the strong stellar magnetic field of 600 G in average (Reiners & Basri 2010). Furthermore, the Trappist-1 planets are expected to be tidally locked to their host star which results in permanent daysides on all planets and high temperature gradients across the planets (Turbet et al. 2018).

Of particular interest to our study are the planets b and e. The Earth–sized planet Trappist-1b is the planet closest to the star at a distance of 0.01 AU and has an orbital period of 1.5 days (Gillon et al. 2017). As a result of transit observations of the inner planets b and c, Bourrier et al. (2017a) found Lyman–α absorption signatures that hint at extended hydrogen envelopes caused by photo–evaporation. However secondary eclipse measurements of Trappist-1b showed that the dayside temperature of about 500 K is about 100 K hotter than the planetary equilibrium temperature, leading to the conclusion that the planet must be a bare rock without any significant atmosphere (Greene et al. 2023). The presence of a magnetic field is neither proven nor refuted as it is for every exoplanet currently known. The proximity to the star possibly leads to star–planet interaction with high powers involved which makes the planet an interesting target for studies aiming on interaction energetics, associated emissions and consequences for planets and atmospheres (e.g. Dong et al. 2018). Trappist-1e is another interesting planet that possibly resides within the inner edge of the habitable zone (Payne & Kaltenegger 2024) at an orbital distance of 0.028 AU. It is slightly smaller than Earth (about $R \approx 0.9\,R_E$) (Grimm et al. 2018). Whether Trappist-1e possess an atmosphere is currently not known. Considering the stellar system's pre–main sequence history in which the star should have been much more active, de Wit et al. (2018) argued that it is unlikely that all the planet's were able to retain their primordial hydrogen atmospheres. There are no observations that succeeded in characterizing the atmosphere but Trappist-1e is a prominent target for ongoing and upcoming James Webb Space Telescope observations and thus we can expect new data on the planet being published soon.

Mercury: A solar system, close–in terrestrial exoplanet analog?

In the solar system no planet exits within an orbital distance below 0.1 AU with Mercury being closest to the Sun ($\approx$ 0.4 AU). Although Jupiter's moon Io is often considered a useful analog for close–in exoplanets because of the sub–Alfvénic interaction with Jupiter, Io doesn't experience a strong stellar wind or stellar eruptions with associated strong and fast variations of the ambient magnetic field. The Sun is about halfway through her life with the pre–main sequence phase left behind her. Accordingly, due to

the magnetic activity of the sun, the space weather is far calmer than is assumed for cool stars. Nevertheless, the sun is a partially convective star with significant variations in magnetic activity, evident in the 11–year magnetic cycle.

Mercury is a suitable object to contextualize and understand simulated star–planet magnetic interactions, as Mercury is a well-studied planet that has already been measured up close by space probes, namely Mariner 10, MESSENGER and the ongoing BepiColombo mission. In addition, Mercury has a weak intrinsic magnetic field. This allows us to observe interactions between its magnetic field and the solar wind, associated space weathering, effects on Mercury's magnetosphere, surface and even the dynamo inside.

Mercury experiences more direct and strong space weathering interactions (Jia et al. 2015) with violent solar eruptions regularly pushing its magnetopause radius closely towards the surface (Winslow et al. 2017; Slavin et al. 2014). Extreme stellar eruptions were also observed during which Mercury completely lost its dayside magnetopause (Winslow et al. 2020). The strong interactions of Mercury's magnetosphere with its space environment is argued to even affect Mercury's magnetic dynamo by inducing currents in the conductive core (Slavin et al. 2014) which has been studied using sophisticated magnetohydrodynamic models (Massetti et al. 2007; Jia et al. 2015; Anderson et al. 2014). Space weathering effects on Mercury's thin gaseous envelope are evident and it is argued that the interaction with coronal mass ejections and the solar wind are indeed responsible for the existence of the neutral and ionic envelope due to erosion of Mercury's surface through sputtering (Benna et al. 2010; Killen et al. 2007).

3. Star–planet interactions

Planets and their host stars interact with each other in a variety of ways. They interact via force fields such as gravitational fields or magnetic fields. In contrast to this direct interaction, stars and planets can also couple to each other via the interplanetary medium. Interplanetary space is, for almost all stars except some sub–types of white dwarfs, filled with plasma which is emitted by the star, the so-called stellar wind. The stellar wind carries mass, mostly electrons and protons, and is embedded in the interplanetary magnetic field (IMF) generated by the star. Stellar winds flow radially away from the star and carry the stellar magnetic field with it. Planets form obstacles in the stellar wind flow and consequently excite a variety of waves at the interface between flow and planet. These waves carry energy generated by the flow perturbations towards the planet and in some cases towards the star where they may impact their space environment and possibly the objects themselves.

The term star–planet interaction (SPI) encompasses a variety of interactions between stars and planets that are bi–directional (i.e. towards the star and the planet). These interactions can be gravitational, mechanical and electromagnetic in nature. Gravitational interactions do not depend on the medium between the bodies and therefore are always bi–directional. Interplanetary space, however, is not a vacuum and is filled with stellar wind plasma that affects the exchange of electromagnetic energy between the interacting objects. In this case the interaction is governed by plasma dynamics and thus highly depends on the properties of the flowing plasma. Depending on the properties of the stellar wind plasma and the embedded magnetic field the interaction between star and planet may be mono–directional so that the interaction only affects the planet (and the stellar wind past the planet). We call this type of interaction stellar wind–planet interaction to make it clear that in those situations the star does not "feel" the planet. The interaction between a stellar wind and a planet can be described using the theory of magnetohydrodynamics. Moreover, since the stellar wind plasma is usually fully ionized and thus the electric conductivity within can be assumed infinite, the framework of ideal magnetohydrodynamics can be applied. In ideal magnetohydrodynamics the magnetic field is frozen into the plasma and therefore the magnetic field is dictated by the flow and vice versa. This behavior essentially shapes the structure of stellar wind–planet interactions.

In this thesis we focus on electromagnetic star–planet interactions. Therefore, to distinguish those interactions that involve magnetic fields from those involving gravitational interactions, we use the term star–planet magnetic interactions (SPMI).

In this chapter we first introduce the most important concepts of star–planet magnetic and stellar–wind planet interactions, describe the ingredients and properties of such interactions (Sect. 3.1). Then we describe the theory of the associated interaction

energetics (Sect. 3.2) followed by an introduction to stellar winds, modeling approaches and stellar eruptions that form the space weather around planets (Sect. 3.3). Finally, we describe consequences for the interacting objects, observational signatures and what me may learn about the interacting bodies from observations (Sect. 3.5).

3.1. Star–planet magnetic interactions (SPMI) and stellar wind–planet interactions

In this thesis we are particularly interested in SPMI and how properties of the stellar wind and planet affect the energetics of the interaction. The main driver of star–planet magnetic interactions is the relative motion between the stellar wind with an embedded magnetic field and the planet. The stellar wind propagates with velocity $\vec{v}_{sw}$ radially away from the star. The planet orbits the star at a certain distance (for approximately circular orbits denoted by the semi–major axis a) with orbital velocity $\vec{v}_{orb}$. In the rest frame of the planet the stellar wind velocity experienced by the planet is the relative velocity between wind and planet, $\vec{v}_0 = \vec{v}_{sw} - \vec{v}_{orb}$. The most important conditions for SPMI to occur are thus the existence of stellar wind plasma and a relative velocity $|\vec{v}_0| > 0$. In this case the planet acts as obstacle in the stellar wind flow where waves are excited. These waves transfer and exchange energy between the interacting objects. The amount of energy the planet and its space environment receives is essentially dictated by the energy content of the stellar wind, i.e. its kinetic, thermal and magnetic energy density, and the size of the obstacle, i.e. the planetary cross section including a possible atmosphere and magnetosphere.
In the following sections we describe the MHD waves and additional quantities that characterize the plasma flow and SPMI (Sect. 3.1.1). We then define how the stellar wind flow velocity relative to MHD wave velocities defines the type of SPMI (Sect. 3.1.2). The structure of the obstacle in the flow, the planet and its space environment, are the second ingredient for SPMI. In Sect. 3.1.3 we thus shed light on the planetary properties that affect the interaction and discuss magnetic topologies resulting from SPMI.

3.1.1. Magnetohydrodynamic waves and SPMI characteristics

The stellar wind can be described as ideal magnetohydrodynamic fluid and, therefore, the three linear ideal MHD wave modes govern the interaction, namely the slow and fast magnetosonic wave and the Alfvén wave, whereas the magnetosonic waves are a combination of sound and Alfvén waves. Every change in the topology of the stellar wind– planet interaction (i.e. magnetic fields and flow structure) is propagated and communicated via MHD waves.

Alfvén wave

The Alfvén wave is a transversal wave that propagates parallel or anti–parallel to the magnetic field. A perturbation exerted on a magnetic field propagates along the magnetic field. The restoring force on the field that tends to straighten the field is

exerted by the magnetic tension force. The inertia of the ions embedded in the field causes the magnetic field perturbation to oscillate around the unperturbed field and to propagate perpendicular to the perturbation. In the picture of field lines the perturbation propagates along the field lines and the group velocity of the resulting Alfvén wave is

$$\vec{v}_A = \frac{\vec{B}}{\sqrt{\rho\mu_0}} \,, \tag{3.1}$$

where $\vec{B}$ is the magnetic field vector, ρ the mass density of the plasma and μ_0 the magnetic permeability of free space. For later use, we also introduce the Alfvén time $\tau_A = L/|\vec{v}_A|$, which indicates how long an Alfvén wave takes to cover a characteristic distance L. This system-specific time scale must be taken into account in the modeling in order to resolve processes driven by Alfvén waves in a meaningful way.

Sound wave

The hydrodynamic sound wave is a longitudinal and compressional wave. The sound velocity of an ideal gas is

$$c_s = \sqrt{\frac{\gamma p}{\rho}} \,, \tag{3.2}$$

where γ is the adiabatic index and p the thermal pressure. The thermal pressure of an ideal gas is related to the particle number density n and temperature T via

$$p = n k_B T \,. \tag{3.3}$$

Magnetosonic waves

The magnetosonic waves are compressional waves. They are associated with compression and rarefaction of the plasma as well as with oscillations of the embedded magnetic field. They can partly be associated with the propagation of a magnetic pressure gradient pulse and thus the possibly fastest direction of propagation is perpendicular to the ambient magnetic field. The magnetosonic wave velocity,

$$v_{ms}^2 = \frac{1}{2}\left(v_A^2 + c_s^2 \pm \left[\left(v_A^2 + c_s^2\right)^2 - 4 v_A^2 c_s^2 \cos^2\theta\right]^{1/2}\right) \,, \tag{3.4}$$

depends on the Alfvén velocity v_A, sound velocity c_s and on the angle θ between magnetic field and wave vector (Baumjohann & Treumann 1996; Merka et al. 2003). The equation returns two velocities, associated with the slow and fast magnetosonic wave (i.e. slow and fast mode). With the wave vector perpendicular to the magnetic field the fast mode velocity, v_f, is maximal and the slow mode velocity, v_s, is lowest. The fast mode is the fastest MHD wave mode (Eq. 3.4) and therefore determines if a perturbed flow builds up a shock. We discuss this in more detail in Sect. 3.1.2.
Mach numbers show the ratio between flow and wave velocity which defines the structure of SPMI. The most important Mach numbers of a plasma flow with velocity v are those

in regard to the Alfvén wave and fast mode wave, which are defined as

$$M_A = \frac{v}{v_A} \tag{3.5}$$

$$M_f = \frac{v}{v_f} \,. \tag{3.6}$$

Since the fast mode is the fastest wave mode, the Alfvén mach number M_A is always greater or equal to the fast mode Mach number, $M_f \leq M_A$.
Another important quantity that characterizes wether the stellar wind flow is thermally or magnetically dominated is the plasma beta, β, which can be calculated from the ratio between thermal and magnetic pressure,

$$\beta = \frac{n k_B T}{B^2/2\mu_0} \,. \tag{3.7}$$

With $\beta > 1$ the plasma is thermally dominated and consequently the flow shapes the magnetic field. With $\beta < 1$ the magnetic field dominates and therefore dictates or even confines the flow.

3.1.2. Classification of star–planet magnetic interactions

Star–planet magnetic interactions can be classified by the stellar wind Mach numbers and plasma beta β. In the following we define the most important types of SPMI.

Sub–Alfvénic interaction

In a sub–Alfvénic interaction the stellar wind is sub–Alfvénic, $M_A < 1$, and consequently the bulk flow is slower as the Alfvén and fast mode velocity. In a flow that is perturbed by a planetary obstacle, MHD waves are excited at the stellar wind–obstacle interface. All MHD wave modes are able to propagate upstream and, therefore, they perturb the incoming plasma before it intersects the obstacle. Consequently, the plasma decelerates to sub–sonic speeds and no bow shock forms in front of the planet.
Alfvén waves excited by the perturbation of the flow form standing waves that connect the stellar and planetary magnetic field, allowing for significant electromagnetic energy channeling between the two objects, possibly resulting in observable signatures in the stellar and planetary atmosphere (Cuntz et al. 2000; Ip et al. 2004; Saur et al. 2013) (see Sect. 3.6 for a review on emissions).

Super–Alfvénic and super–fast interaction

A super–Alfvénic and super–fast magnetosonic stellar wind is faster than the fastest MHD wave mode and therefore no MHD wave can propagate upstream. Therefore the stellar wind prior to the obstacle remains unperturbed until it reaches the obstacle.
A magnetized planet either with or without an atmosphere interacts with the stellar wind flow. The interaction affects the flow structure by decelerating and deflecting plasma and thus perturbs the plasma. This consequently results in the excitation of MHD waves. Due to their inability to propagate upstream the stellar wind flow is shocked

at the obstacle's boundary. A bow shock is formed in front of the planet. A magnetic field enhances the planet's effective size to intercept the stellar wind flow. Past the bow shock plasma is deflected and slowed down considerably before it intersects the magentopause. The highly turbulent region between shock front and magnetopause is called the magnetosheath.

Interactions with planets without magnetic field and atmosphere

Without a planetary magnetic field and atmosphere the stellar wind plasma is absorbed by the planet where the ions and electrons recombine rapidly to form neutral particles. In this scenario the plasma upstream of the planet is unperturbed due to the lack of perturbations that can propagate the information upstream. At the surface the plasma simply ceases to exist as the particles are now part of the neutral species. This scenario, however, also depends on the electric conductivity of the planet. A weakly conductive planet allows the stellar wind magnetic field to diffuse across the planet at a rate related to the electric conductivity. In a highly conductive planet the magnetic field only diffuses into shallow depths corresponding to the skin depth. Within the planet the magnetic field is subject to diffusion and Ohmic dissipation (Laine et al. 2008) and therefore the magnetic field is not able to diffuse past the planet at the same speed as the ambient stellar wind. Additionally, the conductivity distribution within a planet is typically highly anisotropic, resulting in the stellar wind magnetic field to diffuse at different speeds (Laine & Lin 2011).

Super–Alfvénic and sub–fast interaction

It is possible that the stellar wind is super–Alfvénic and sub–fast. In this scenario no bow shock forms upstream since fast mode waves can perturb the plasma further upstream. Only degenerate Alfvén wings form that rather resemble magnetic lobes in a super–fast interaction. To the authors knowledge this scenario is very rare as it needs very high sound speeds (i.e. high pressures and low densities) paired with relatively weak stellar wind magnetic fields (an example is provided in this thesis (Sect. 6.3.1) or in the the appendix of Elekes & Saur 2023).

3.1.3. Planetary magnetospheres and SPMI topologies

When a planet is magnetized (e.g. possesses an intrinsic magnetic field) SPMI energetics are affected in several ways that affect the magnetospheric intake of stellar wind energy fluxes.

Effective obstacle size. The effective size of the planetary obstacle in the stellar wind flow is enhanced. The energy flux the planet and its magnetosphere receive from the stellar wind is consequently increased. This results in a stronger interaction in the sense of magnetospheric energy budget. In the sub–Alfvénic wind scenario the larger obstacle also enhances the MHD wave energy flux towards the star where the amplitudes of SPMI induced emissions are affected by the obstacle's size (e.g. Strugarek 2016).

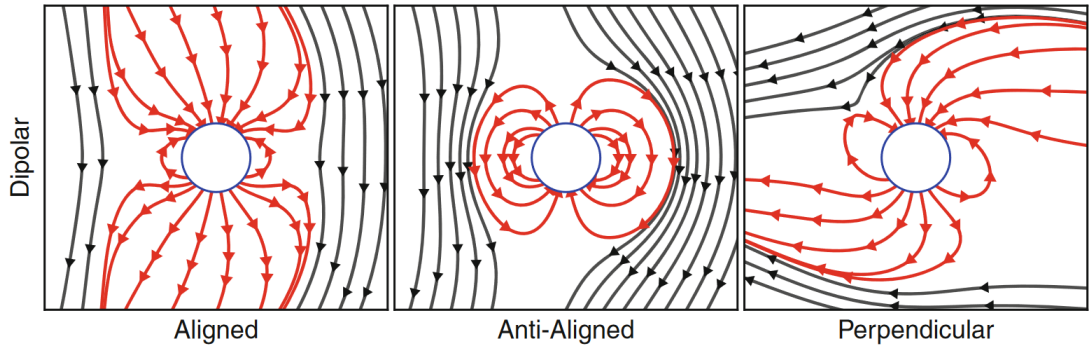

Figure 3.1.: Depicted are three stellar wind–magnetosphere magnetic topologies of SPMI. Depending on the relative orientation between stellar magnetic field B_{sw} and planetary magnetic moment $\vec{M}_p$ the magnetosphere might be open ($B_{sw}|| - \vec{M}_p$), closed ($B_{sw}||\vec{M}_p$) or semi–open ($B_{sw} \perp \vec{M}_p$). Open and semi–open magnetospheres have field lines connected to the stellar wind field while a closed magnetosphere has only magnetic field lines with both foot points on the planet. The image is taken from Strugarek et al. (2015).

Magnetic topology and reconnection. Depending on the orientation between the planetary magnetic moment $\vec{M}_p$ and the local stellar wind magnetic field $\vec{B}_{sw}$ both magnetic fields may reconnect. Reconnection allows stellar wind plasma to be injected into the magnetosphere along magnetic field lines and drive magnetospheric convection (e.g. Dungey cycle Baumjohann & Treumann 1996; Dungey 1961). The polar cusp regions are an important channel for plasma injection whose locations depend on the magnetic topology (Palmroth et al. 2003). When $\vec{B}_{sw}$ is parallel to the negative z–axis, $\vec{B}_{sw} = B_{sw}\hat{e}_z$, reconnection may occur if $\vec{M}_p$ at least has a component $\vec{M}_p \cdot \hat{e}_z > 0$ (Baumjohann & Treumann 1996). Depending on the magnetic topology (i.e. relative orientation of stellar wind and planetary magnetic field) three extreme cases of magnetospheric structure can be identified (see Fig. 3.1):

- When the stellar wind and planetary magnetic field are aligned ($B_{sw}|| - \vec{M}_p$) the magnetosphere is open (left in Fig. 3.1). Planetary field lines are connected with the stellar wind magnetic field and stellar wind plasma may be injected into the magnetosphere along magnetic field lines.
- When the stellar wind and planetary magnetic field are anti–aligned ($B_{sw}||\vec{M}_p$) the magnetosphere is closed (middle in Fig. 3.1). In the ideal case the magnetosphere is a cavity within the stellar wind flow without connection to the ambient magnetic field. Stellar wind plasma may only enter the magnetosphere via diffusive processes.
- When the stellar wind and planetary magnetic field are perpendicular ($B_{sw}||\vec{M}_p$) the magnetosphere is semi–open (right in Fig. 3.1). In this scenario the planetary magnetic field lines are partially connected to the stellar wind field.

In reality, however, reconnection may occur in any of the mentioned field topologies due to the fact that the planetary magnetic field can be locally oriented in any direction

across the magnetosphere boundary (i.e. it never is homogeneous) (e.g. Eastwood et al. 2015; Li et al. 2005; Song & Russell 1992). It was also shown that reconnection under any wind–planet magnetic topology is possible when the stellar wind plasma beta is low ($\beta << 1$) (e.g. at Mercury Dibraccio et al. 2013) which is of particular relevance for close–in exoplanets as they may either orbit the star within its Alfvén radius or due to the passing of a coronal mass ejection that is often accompanied by a magnetic cloud with strong magnetic field strength and low plasma density (see Sect. 3.4.2 for more details on coronal mass ejections). During SPMI the magnetospheric structure consequently affects the energetics of the star–planet system and with it possible emission characteristics as well as magnetospheric or even stellar dynamics (Elekes & Saur 2023; Varela et al. 2018; Strugarek et al. 2015, 2014; Palmroth et al. 2006). At the flanks of the magnetosphere, depending on the magnetic topology, Kelvin–Helmholtz instabilities may occur that affect magnetospheric energetics through reconnection and plasma injection (Nykyri & Otto 2001; Hasegawa et al. 2004). In Sect. 3.5.1 we discuss the consequences of SPMI on the magnetospheric structure in more detail.

Magnetospheric stand–off distance

The amount of the total stellar wind energy flux received by the planetary magnetosphere, P_{ms}, is proportional to the size of the magnetospheric cross–section A_{ms}. The effective radius of the magnetospheric obstacle in the stellar wind flow is the magnetospheric stand–off distance and can be estimated from the sub–stellar wind magnetopause radius R_{mp} measured from the planet's center. The circular cross section therefore is $A_{ms} = \pi R_{mp}^2$. The magnetopause radius can be calculated from an equilibrium between stellar wind pressure and planetary magnetic pressure. We assume the stellar wind to propagate parallel to the x–axis with the planet's center in the origin and thus the sub–stellar wind magnetopause resides on the negative x–axis, $\vec{r}_{mp} = -R_{mp}\hat{e}_x$. The stellar wind pressure is composed of its ram ($\rho_{sw} v_{sw}^2$), thermal (p_{sw}) and magnetic pressure ($B_{sw}^2/2\mu_0$), where B_{sw} is the stellar wind magnetic field, v_{sw} the velocity and p_{sw} the wind's thermal pressure. The pressure balance then reads

$$\rho_{sw} v_{sw}^2 + B_{sw}^2/2\mu_0 + p_{sw} = B_p (R_{mp})^2/2\mu_0 \ , \tag{3.8}$$

where B_p is the planetary magnetic field strength at the magnetopause. The planetary magnetic field might be approximated by a dipole field although it is, in the perturbed state, not a dipole anymore. With the equatorial surface magnetic field B_{eq} the magnetic field at the magnetopause can then be calculated with

$$B_p(R_m p) = B_{eq} \left(\frac{R_{mp}}{R_p} \right)^{-3} \ , \tag{3.9}$$

where R_p is the planet's radius. Plugging Eq. 3.9 into Eq.3.8 and rearranging the equation yields a formula for the magnetopause radius as a function of planetary magnetic field strength and stellar wind total pressure,

$$R_p = R_p B_{eq}^{1/3} \left(2\mu_0\right)^{-1/6} \left[\rho_{sw} v_{sw}^2 + p_{sw} + \frac{B_{sw}}{2\mu_0} \right]^{-1/6} \ . \tag{3.10}$$

Equation 3.10 indeed gives only an estimate due to the planetary dipole approximation. The compression of the magnetosphere (i.e. perturbation of the dipole) is subject to field amplification and thus the magnetopause radius should slightly away from the planet, depending on the stellar wind dynamic pressure (see Sect. 3.5.1 for a more detailed discussion).

3.2. Energetics of SPMI

Stellar wind–planet interactions are associated with energy exchange between the stellar wind and the planet. Stellar wind mechanical and magnetic energy fluxes incident on the magnetosphere convert to magnetospheric mechanical, thermal and magnetic energy to different proportions. Energy might as well be irreversibly dissipated in form of heat or emissions. In SPMI the Poynting flux is the most important quantity to describe the transport of electromagnetic energy. The Poynting flux carries the electromagnetic energy contained in magnetic disturbances associated with Alfvén waves ($\vec{S} \parallel \vec{B}$), fast and slow magnetosonic wave modes as well as the convective mode.

The Poynting vector can be calculated from

$$\vec{S} = \frac{\vec{E} \times \vec{B}}{\mu_0} \,, \tag{3.11}$$

where $\vec{E}$ is the electric field. The evolution of electromagnetic energy is formulated in Poynting's theorem

$$\frac{\partial}{\partial t} w + \nabla \cdot \vec{S} = -\vec{j} \cdot \vec{E} \,, \tag{3.12}$$

where w denotes the electromagnetic energy density, $\vec{S}$ the Poynting vector, $\vec{j}$ the current density and $\vec{E}$ the electric field. The total electromagnetic energy is composed of energy contained in magnetic and electric fields,

$$w = \frac{B^2}{2\mu_0} + \frac{\epsilon_0 E^2}{2} \,, \tag{3.13}$$

where E is the electric field strength. Equation 3.12 states that the temporal change of electromagnetic energy density within a closed volume can either be the consequence of convection, i.e. there is a flux of electromagnetic energy in or out of the system, or of conversion between electromagnetic and thermal energy. The Joule heating term, $\vec{j} \cdot \vec{E}$, not necessarily describes dissipation of energy but merely the conversion between electromagnetic and thermal energy that may be irreversible or reversible.

3.2.1. Stellar wind–magnetosphere coupling

The total energy flux, P_t, available to power the interaction is contained in the stellar wind convected onto the planetary cross section, πR_{eff}^2, with effective stand–off distance R_{eff}. For a non–magnetized planet without atmosphere R_{eff} is simply the planetary radius R_p. An atmosphere increases the planetary stand–off distance. For a magnetized

planet the effective radius is the magnetospheric stand–off distance, R_{mp}, where R_{mp} is the magnetopause radius. The energy budget of the planet and its magnetosphere is governed by the stellar wind–magnetosphere energy transfer function that yields the amount of total stellar wind energy flux that is injected into the magnetosphere. The most general expression for this coupling is $P_{ms} = \epsilon P_t$, where P_{ms} is the total magnetospheric energy flux and ϵ the conversion (or efficiency of conversion) factor. The energetic coupling between solar wind and the terrestrial magnetosphere has been studied intensely in the past decades. A variety of coupling functions have been proposed that relate stellar wind energy input to all kinds of magnetospheric characteristics like Dst (see also 7.4.6) and other indices that are measures of plasma dynamics, auroral powers and magnetic disturbances. The most successful coupling functions incorporate the B_z component of the solar wind (anti–parallel to Earth's magnetic moment) and the reconnection electric field generated by magnetic reconnection between solar wind and the terrestrial magnetosphere (e.g. Newell et al. 2007). This, however, might not be universal since the energy balance between stellar wind and magnetosphere can be dominated by other energetic components, such as the stellar wind dynamic pressure at close–in exoplanets. In this thesis we examine this possibility in detail (Sect. 7).

3.3. Stellar winds

Stars emit steady outflows of plasma that fill interplanetary space and propagate outwards until they terminate at the boundary to the interstellar medium, the termination shock. This type of continuous stellar outflow is called stellar wind and it is argued to be present at nearly all types of stars. Typically stellar winds are composed of a fully ionized hydrogen–helium plasma. Stars lose mass due to continuous stellar winds which affect the rotational evolution of stars, its mass but also the stellar environment including planets. Over a stellar lifetime the star may lose up to 50% of its mass (Lamers & Cassinelli 1999). The radial outflow of mass removes angular momentum from the star and consequently causes the spin–down of stellar rotation which in turn affects the stellar magnetic field as it is tied to the rotation of the star. The stellar environment is thus not constant but varies over the star's lifetime which is consequently reflected in the magnetic activity of the star and which also affects the evolution of planets.
With regard to the existence of star winds we note that exceptions are some white dwarf stars. For surface gravitational accelerations of white dwarfs with $\log g > 7$, stellar winds do not exist (Unglaub 2008). However, observations of ultrahigh excitation absorption lines in the spectra of the hottest white dwarfs revealed that potential stellar winds may be trapped within a circumstellar magnetosphere where the plasma is heated up to temperatures near 10^6 K (Reindl et al. 2019), similar to a stellar corona. Planets around white dwarf planets therefore can interact purely electromagnetically with the star.
Winds of massive stars are dominantly line–driven stellar winds in which stellar plasma is accelerated by plasma absorbing energetic photons which leads to associated momentum transfer. Solar–type cool stars in contrast have thermally driven winds that are accelerated by pressure gradients in the stellar atmosphere.

Stellar winds are embedded within the stellar magnetic field which they carry with them. Altogether, with stellar winds, stellar plasma and their magnetic fields are carried through the heliosphere where they can interact with planets.

3.3.1. Modeling stellar winds

In the following we describe stellar wind modeling approaches that are widely used in extrasolar stellar wind and exoplanet studies and whose limitations and advantages affect the results presented in this thesis. In both projects presented in this thesis, results of stellar wind solutions predicted by different stellar wind models were used as boundary condition for our planetary MHD simulations and therefore knowledge of corresponding model limitations are crucial to assess the quality of our results.
Stellar winds are simulated using MHD models in which the inner boundary (i.e. the base of the stellar corona) shapes the wind solution. Stellar wind models are distinguished by how they treat the inner boundary and consequently how they describe coronal heating. One approach is to simply assume the coronal base temperature. The other approach is to self–consistently simulate the heating. In the following section 3.3.1.1 we describe a thermally driven stellar wind model often used as initial and inner boundary condition (like in the τ Boötis b project, Sect. 6.2.2). Most sophisticated stellar wind models take magnetic surface maps of stars as inner magnetic boundary condition for the magnetic field which we briefly describe in Sect. 3.3.2.

3.3.1.1. Thermally driven stellar wind

The first theoretical description of the solar wind was derived by Parker (1958). His model is a thermally driven wind model and thus only the pressure gradients and gravitational forces influence the stellar wind. The corresponding momentum equation reads

$$\rho\left(\frac{\partial\vec{v}}{\partial t}+\vec{v}\cdot\nabla\vec{v}\right)=-\rho\frac{GM_\star}{r^2}\vec{e}_r-\nabla P\,, \tag{3.14}$$

where $M_\star$ is the stellar mass, G the gravitational constant, r the radial distance from the star's center and $\vec{e}_r$ the radial unit vector. In the solution of Parker (1958) the wind is steady state and radially symmetric. This simplifies Eq. 3.14 to

$$\rho v_r\frac{dv}{dr}=-\rho\frac{GM_\star}{r^2}\vec{e}_r-\frac{dP}{dt}\,, \tag{3.15}$$

where v_r is the radial velocity. The corresponding continuity equation reads

$$\frac{dM_\star}{dt}=4\pi\rho r^2 v_r\,, \tag{3.16}$$

which describes the mass loss rate of the star $\dot{M}_\star = dM_\star/dt$. The equations 3.15 and 3.16 are closed by describing the pressure with the ideal gas law,

$$P=\frac{\rho k_B T}{\mu m_p}=\rho a^2\,, \tag{3.17}$$

where T is the temperature, $\mu = 0.5$ the mean molecular weight and m_p the proton mass assuming a fully ionized hydrogen plasma with 50% protons and 50% electrons. In Eq. 3.17 a is the isothermal sound speed $a = \sqrt{k_b T/\mu m_p}$. The original Parker wind is isothermal, so that $P \propto \rho$. When assuming a polytropic wind, $P \propto \rho^\Gamma$ with polytropic exponent Γ and differentiating the ideal gas law radially, $dP/dr = a^2\, d\rho/dr + \rho a^2/T \cdot dT/dr$, the momentum equation of a thermally driven wind reads

$$\rho v_r \frac{dv}{dr} = -\rho \frac{GM_\star}{r^2} - c_s^2 \left(\frac{\rho}{v_r} \frac{dv_r}{dr} + \frac{2\rho}{r} \right) \tag{3.18}$$

$$\frac{1}{v_r} \frac{dv}{dr} = \left(-\frac{GM_\star}{r^2} + \frac{2c_s^2}{r} \right) \frac{1}{(v_r^2 - c_s^2)}\,, \tag{3.19}$$

where $c_s^2 = \Gamma a^2$ is the polytropic sound speed (for a detailed derivation, see Vidotto 2021; Parker 1958). With $\Gamma = 1$ the equations reduce to the original Parker solution. According to Eq. 3.19 the stellar wind acceleration is independent of the mass density which only controls the mass loss rate Eq. 3.16. Equation 3.19 is continuous at $v_r = c_s$ when the denominator approaches zero simultaneously. By equating the two terms within the brackets on the right hand side one finds an expression for the critical radius at which the stellar wind reaches the sound speed, $r_c = GM_\star/2c_s^2$ which is commonly used as inner boundary for thermally driven wind simulations.
To conclude, in thermally driven winds the free parameters are the base density which controls the mass loss rate and base temperature which controls the stellar wind velocity. For the sake of completeness we mention the stellar wind model derived by Weber & Davis (1967) which incorporates stellar rotation and magnetic fields. This model is thus suitable to describe angular momentum loss of rotating stars.

3.3.2. Stellar magnetic field maps

An important boundary condition to influence coronal heating and the predicted stellar wind is the magnetic field structure in the stellar atmosphere (e.g. Tóth et al. 2005). Therefore magnetic field surface maps serve as inner boundary condition for such stellar wind simulations. These are obtained by the Zeeman–Doppler imaging technique that utilizes spectral line splitting due to local magnetic fields as the result of the Zeeman effect (Semel 1989; Donati & Brown 1997). Therefore more magnetically active stars produce stronger Zeeman signatures (Reiners et al. 2013). By observing the circular polarized stellar spectra over the course of a full stellar rotation cycle the spectra are subject to Doppler shifting that results in red and blue shifted wings of the spectra. The resulting data contains spatial information and thus, by applying inverse modeling techniques, the large scale magnetic field structure at the stellar surface can be reconstructed. Although the method only yields low resolution magnetic field maps it has been shown that smaller scale fields do not affect stellar wind solutions significantly (Jardine et al. 2017). The Zeeman–Doppler imaging method yields non–unique results and merely represents the likely magnetic field structure during the exact moment of the observation. Magnetic fields of stars are not static but may vary in short timescales

depending on the magnetic activity of the star.
Magnetic surface maps of stars have been successfully applied to MHD simulations of stellar winds (e.g. Vidotto et al. 2012; Boro Saikia et al. 2020; Alvarado-Gómez et al. 2016). A drawback of all stellar wind MHD models is, however, the choice of free parameters to describe the initial state of the stellar wind.

3.4. Stellar eruptions and space weather

Apart from stellar winds, stars affect interplanetary space and planets in a variety of different ways. These effects include stellar wind variations, changes in the global stellar magnetic field and eruptive phenomena closely related to stellar activity and magnetism. In regard to planets that experience these temporal variations of their space environment one summarizes these environmental conditions under the term of space weather. In the following we discuss the most important aspects of space weather where we focus on solar–like (spectral classes F, G, K) and cooler stars (spectral class M). We discuss the origin and signatures of stellar activity and stellar flares (Sect. 3.4.1). Subsequently we discuss coronal mass ejections (CMEs) that are the most important and severe manifestations of space weather. We also describe the structure of CMEs and some modeling approaches (Sect. 3.4.2).

3.4.1. Stellar activity of cool stars – Origins and signatures

In this thesis we are particularly interested in the space environment and energetics of exoplanets around solar–like and cool stars. This group of stars exhibits strong activity that is largely responsible for severe environmental conditions near planets in close orbits. M–dwarf stars are the most common type of stars in the solar neighborhood (Winters et al. 2019; Bochanski et al. 2010) hosting a significant amount of potentially habitable exoplanets often residing in proximity to the stars (Dressing & Charbonneau 2015; Bonfils et al. 2013). Consequently, knowledge about stellar environmental conditions around cool stars is crucial in assessing planetary habitability and effects of star–planet interactions in these stellar systems. In the following we describe the main properties of those stars and consequences for their space environment.

Stellar magnetic activity

The term stellar activity comprises several stellar phenomena. Flaring and outburst rates, observable variations in stellar spectra, outflows and occurrence rate of star spots are all indicators for stellar activity. Activity is directly related to the stellar magnetic field and to the stellar rotation rate (Brun & Browning 2017). Apart from influencing interplanetary space strong magnetic activity is argued to also affect stellar global parameters like radius and metallicity (López-Morales 2007). Fast magnetic cycles with related magnetic field polarity reversals are also possible manifestations of stellar activity (e.g. Fares et al. 2009). Solar–like and cool stars of later type generate their magnetic fields through dynamo action powered by turbulent convection and differential

rotation in their interior that is primarily affected by stellar mass, interior stratification and rotation (Brun & Browning 2017; Galloway & Weiss 1981; Parker 1955). The interior of solar–like stars is partially convective, with a convective envelope encasing a radiative region below. Towards lower masses the interior of stars undergoes a transition at $M_\star \leq M_\odot$ (with $M_\odot$ being the solar mass) to a fully convective interior (Chabrier & Baraffe 1997). The transition occurs at stellar spectral classes of M3–M4 (Brun & Browning 2017). Solar–like stars are argued to dominantly generate their magnetic field in the tachocline, a boundary layer between radiative and convective region influenced by strong differential rotation between radiative and convective regions (Charbonneau 2014). Fully convective, low mass M–dwarf stars often have complex magnetic fields deviating from dipolar fields (Kochukhov 2021; Chabrier & Baraffe 1997). Despite the lack of a tachocline average magnetic fields of fully convective stars are typically very strong (up to several kG) (e.g. Reiners et al. 2009) and they show higher activity due to turbulent convective interiors (Reiners 2012). However, evidence exists for the strongest magnetic fields among convective stars to be in a dipolar state (Shulyak et al. 2017). Electron cyclotron maser radio emission observed from cool stars supports the the allegedly strong magnetic fields (Hallinan et al. 2008; Villadsen & Hallinan 2019).

A variety of observational indicators exist that relate magnetic activity to the stellar magnetic field and consequently to stellar rotation. Observations of stellar Ca II H&K lines serve as proxy for stellar activity as emission in these lines is indicative for chromospheric heating due to magnetic field variations (Wilson 1978; Hall 2008). Observations of chromospheric Ca II emission indicate a relation between activity and rotation (Astudillo-Defru et al. 2017). Solar and late–type stars possess coronae composed of hot plasma with temperatures of several 10^6 K which is argued to be heated by magnetic energy release. In their coronae stars emit X–Ray radiation (Vaiana et al. 1981). Coronal X–Ray emission acts as tracer for magnetic activity which has been shown to correlate with the stellar rotation period (Reiners et al. 2014; Pallavicini et al. 1981). This dependence has also been shown for fully convective stars (Wright et al. 2018; Wright & Drake 2016). Coronal Hα is a similar indicator for activity and has also been shown to depend on rotation and magnetic field (Newton et al. 2017). Younger stars typically exhibit stronger X–Ray emission (Telleschi et al. 2007) which is related to the spin down of stars as they age. Consequently, magnetic fields and the activity of stars are stronger in their early lifetime (Irwin et al. 2011). The spin–down itself is caused by removal of angular momentum due to persistent stellar winds (Weber & Davis 1967) and fast rotating lower mass stars supposedly tend to maintain rapid rotation over long periods of time (over several Gyrs) until they spin–down very fast (Newton et al. 2016; Irwin et al. 2011). Old cool stars thus maintain a certain degree of magnetic activity over long time periods.

In summary, observations suggest that cooler stars down to spectral class M show stronger magnetic activity and have stronger magnetic fields compared to solar–like stars (F, G and K) which they maintain for a large fraction of their lifetime.

Stellar flares

Stellar flares are sudden outbursts of electromagnetic energy driven by emerging magnetic flux and reconnection in the stellar atmosphere (Howard et al. 2019; Shibata & Magara 2011; Priest & Forbes 2002). Flare spectra encompass a wide range of wavelengths, from γ and X–Ray radiation across the optical, microwaves and radio band (Priest & Forbes 2002). Magnetically active stars show enhanced flaring activity and the majority of known stars suggest a generally higher flaring activity than the Sun that correlates well with magnetic activity (Karoff et al. 2016), especially for M–dwarf stars (e.g. Seli et al. 2021; Howard et al. 2019; Paudel et al. 2018). Superflares with energies above 10^{32} erg have been reported to occur on other solar–like and cooler stars (Howard et al. 2019; Maehara et al. 2015). Typical solar flares are associated with energies in the range $E_{flare} = 10^{28}$–10^{32} erg (e.g. Aschwanden et al. 2000). Energy released during flares can accelerate particles in the stellar atmosphere to high energies. Exceptionally strong superflare events may even be capable of photo-dissociating the whole ozone layer of an Earth–like planet (Howard et al. 2019). Among about 1800 nearby cool stars roughly 15% stars emit strong flares that could damage potential terrestrial exoplanets (Howard et al. 2019) underlying the expectation that cool stars indeed create potentially hazardous space environments.

One of the most severe consequences of flares are coronal mass ejections whose ejections often coincide with stellar flares. Enhanced flaring rates of cool stars are argued to correlate strongly with enhanced occurrence rates of stellar eruptions (Moschou et al. 2019). In the next section we will discuss coronal mass ejections and their consequences in more detail.

3.4.2. Coronal mass ejections (CMEs)

Coronal mass ejections (CMEs) are among the most energetic stellar eruptive events and can have severe impacts on planets in a variety of ways. CMEs are large clouds of coronal plasma with embedded twisted magnetic flux that are ejected from the stellar corona. Under some conditions they can reach interplanetary space and propagate away from the star while expanding. CMEs are typically composed of several 10^9 tons of coronal plasma that propagate at speeds in the order of several thousand km/s (Forbes 2000).

Flares and CMEs are related phenomena that both are powered by magnetic energy release due to reconnection events in the stellar corona (Compagnino et al. 2017; Amari et al. 2011; Chen 2011; Shibata & Magara 2011; Chen et al. 2006). Not every flare is associated with a CME. However, solar observations indicate that the association rate between flares and CMEs increases for more energetic flares (Aarnio et al. 2011; Yashiro & Gopalswamy 2009) due to their common reconnection–powered origin (Reva et al. 2024; Lin 2004). Solar flares associated with CMEs typically exhibit intense X–Ray emission (Youssef 2012; Moschou et al. 2019) indicative of the highly energetic environment in active regions from which they emerge. Solar CME observations show a well–defined relationship between flare X–Ray energy and CME kinetic energy (velocity and mass). More energetic flares are accordingly associated with faster and more mas-

sive CMEs (Moschou et al. 2019; Drake et al. 2013; Aarnio et al. 2012, 2011; Yashiro & Gopalswamy 2009).
There are currently two methods to estimate kinetic energies and masses of CMEs that can potentially be applied to other stars. One method is based on X–Ray absorption (emission measure) by electrons in a CME emerging from a star following a flare event. The temporal decay of the absorption signature is caused by the propagation and expansion of the CME, thus allowing estimates to be made for mass and density (Moschou et al. 2017). This method is subject to projection effects and therefore prone to misinterpretation of measured velocities. Another method is the observation of flares in the UV where Doppler shifted spectra can be attributed to ejected and falling back coronal material. The Doppler shifts can be used to estimate projected velocities of possible CMEs (Vida et al. 2016, 2019). In the extrasolar context these methods are susceptible to misinterpretations. The X–Ray method, for example, relies on additional CME modeling in order to yield kinematic parameters (e.g. Moschou et al. 2017; Aschwanden 2017; Moschou et al. 2019). In the stellar context, both methods may consequently lead to false–positives and therefore cannot confirm the detection of CMEs. Stellar type II radio bursts are indicative for shocked plasma emerging from the corona and thus such a detection could potentially provide more robust evidence (Mann et al. 2018; Cliver et al. 1999; Bale et al. 1999).
While magnetically active stars are expected to produce more CMEs, at the same time strong stellar magnetic fields are capable of suppressing or completely confining CMEs (Alvarado-Gómez et al. 2018). Observations of CME candidates indeed support the suppression mechanism as these CMEs often exhibit lower velocities compared to solar empirical relations between flare X–Ray energy and CME velocity extrapolated to magnetically active stars (Vida et al. 2016, 2019; Moschou et al. 2019). Figure 3.4.2 shows derived stellar CME mass and velocity as function flare X–Ray energy together with solar CME observations. In Fig. 3.4.2 it is evident that velocities of extrasolar CME candidates fall below the expectation based on solar CMEs.

3.4.3. Structure, propagation and models of interplanetary CMEs

In this section we describe the basic structure of CMEs, their propagation through the heliosphere, physical properties such as magnetic field structure and how they evolve during their propagation. We describe how to estimate stellar CME parameters using empirical flare–CME relations obtained from solar system CME observations. Apart from an overview of CME modeling approaches we only briefly discuss physical flux rope models due to the complexity and depth of this topic. Instead we refer the reader to Sect. 7.2.4 where we describe our specific CME models in detail.

Basic structure

Before eruption, CMEs typically consist of large scale magnetic flux ropes which have both foot points on the star. Flux ropes are characterized by twisted magnetic field lines that spiral around the central magnetic axis. Studies indicate that most CMEs observed near Earth have a flux rope (Song et al. 2020; Jian et al. 2006) and

that flux ropes are always involved in the generation of CMEs (Vourlidas et al. 2013). Flux ropes initially assume their magnetic structure during formation of stellar coronal loops (Amari et al. 2011). One mechanism to generate the helical structure of magnetic field lines is sheering motion of the coronal loop foot points caused by convection in the photosphere (Kilpua et al. 2019). Cutting and merging of magnetic field lines at the bottom of the flux rope caused by magnetic reconnection eventually releases the energy to impulsively eject the flux rope CME and the plasma confined within (Kilpua et al. 2019). The amount of energy released depends on the height above the star (i.e. the local magnetic field strength) and on the tension that has been previously built up.
In interplanetary space flux rope CMEs assume the structure of magnetic clouds (MCs) which are characterized by enhanced magnetic field strength (in contrast to the stellar wind), by a helical magnetic field topology entwining the flux rope axis and low plasma β (e.g. Klein & Burlaga 1982). Across the heliosphere flux ropes typically remain magnetically attached to the star (e.g. Kahler & Reames 1991) so that planets experience a single cylindrical CME structure. Typically interplanetary CMEs are super–fast magnetosonic and therefore form bow shocks in which the stellar wind magnetic field is compressed.

Propagation / evolution

During their propagation through the heliosphere CMEs interact with the stellar wind and, depending on the distance traveled, the CMEs slow down significantly (or accelerate) due to stellar wind drag. Consequently CMEs adapt to the velocity of the stellar wind. This has been observed in the solar system (e.g. Lindsay et al. 1999). CME measurements, however, are obtained from satellites near 1 AU. In the case of close–in exoplanets the distance traveled from the corona to the planets is typically much less than 0.1 AU in the range of very few stellar radii. CMEs also elongate perpendicular to the direction of motion due to interaction with the stellar wind (Riley & Crooker 2004). During their propagation the physical parameters of CMEs evolve as the whole structure expands (Scolini et al. 2021). Staring at a reference distance D_0 that is typically a few stellar radii above the star a physical quantity q evolves with distance traveled D according to

$$q(D) = q_0 \, (D/D_0)^{\alpha} \tag{3.20}$$

where the exponent α specifies the decay rate of the quantity q (e.g. Scolini et al. 2021). From observations and simulations typical exponents were obtained (see Scolini et al. 2021, for a summary): The velocity decays nearly linearly with $\alpha_v \approx 0$ (with rare exceptions up to ≈ -0.3). For the magnetic field magnitude α_B is in the range $\alpha_B \approx -1.3$–-1.95, similar to a Parker solar wind. The CME proton density decays approximately with $\alpha_{n_p} \approx -2.4$. In Fig. 7.2 we show exemplary the evolution of our modeled CME axis magnetic field strength and CME velocity.

CME mass and velocity

Based on solar flare X–Ray and white light coronograph observations of CMEs empirical relations between flare X–Ray energy, CME mass and velocity were obtained

in several studies (e.g. Aarnio et al. 2012; Drake et al. 2013; Kay et al. 2019). We refer the reader to Sect. 7.2.4 where we describe the choice of our CME parameters in detail.

Flux rope magnetic field strength and magnetic helicity

Magnetic helicity is a property of magnetic field structures measuring the twist of magnetic field lines or more precisely it describes how often field lines are interlinked (Blackman 2015). Magnetic helicity has the unit of $\mathrm{T}^2\mathrm{m}^4$. It can be calculated from the magnetic field $\vec{B}$ and corresponding vector potential $\vec{A}$ that is defined as $\nabla \times \vec{A} = \vec{B}$. The magnetic helicity is defined as

$$H_m = \int_V \vec{A} \cdot \vec{B}\, dV \ , \tag{3.21}$$

where V is a volume bounded by a magnetic surface with $\vec{B} \cdot \hat{e}_n = 0$ ($\hat{e}_n$ is the unit vector normal to the surface). In ideal MHD with infinite conductivity, magnetic helicity is a conserved quantity. It has been shown that this also applies in good approximation to plasmas in the solar corona and interplanetary space (Berger 1984). Geometrical properties of CMEs and magnetic helicity can be obtained from solar observations. By applying the conservation of magnetic helicity the magnetic field strength of the near–Sun flux rope can be deduced (Patsourakos & Georgoulis 2017). With the CME parameter decay rates, α (Sect. 3.4.3, Eq. 3.20), one obtains the CME properties at the desired heliocentric distance.

Unfortunately, for stellar CMEs helicity measurements are not available. For this scenario Patsourakos & Georgoulis (2017); Tziotziou et al. (2012) developed an empirical relation from numerous solar active region snapshots associated with CMEs to link free coronal magnetic energy E_m (i.e. the non–potential energy contained in the high–tension coronal loops) to the magnetic helicity of solar active regions (from where CMEs emerge). The derived empirical formula reads

$$\log H_m = 53.4 - 0.0524\,(\log E_{bol})^{0.653} \exp\left(\frac{97.45}{\log E_{bol}}\right) , \tag{3.22}$$

where E_{bol} is the bolometric energy (i.e. integrated radiated energy as function of wavelength) of the flare associated with a CME. Only a fraction of about 10–20% of the flare's free magnetic energy is released during the largest flare evens (e.g. Tziotziou et al. 2012). For simplicity and in order to obtain a reasonable upper limit for the CME magnetic helicity (Eq. 3.22), Patsourakos & Georgoulis (2017) assumed an equipartition between bolometric and free coronal magnetic energy. This also constitutes a convenient assumption for stellar CMEs as bolometric energies are the only accessible quantity.

With an estimate of the extrasolar CME magnetic helicity, the helicity equation (Eq. 3.21) can be solved for the magnetic field to yield an estimate for the CME flux rope magnetic field strength. This step solely depends on the choice of the flux rope model, hence $\vec{B}$, as it determines the topology of the magnetic field. In the next paragraph we give a brief overview of such models.

Interplanetary CME models

Interplanetary CMEs in magnetohydrodynamic simulations can be modeled in two distinct ways. We note that in the following we solely discuss interplanetary CME models that do not necessarily include the corona, injection of free magnetic energy and the initial triggering of the CME eruption.

Pulse models. CMEs can be modeled as magnetized pulses of enhanced plasma parameters (such as density and velocity) superimposed on the background stellar wind following a specific spatial profile (of sinusoidal/Gaussian shape for example). These pulse–like CMEs typically have no own intrinsic magnetic structure but are embedded in the stellar wind field. Many studies using this kind of model can be found in the literature (e.g. Biondo et al. 2021; Hosteaux et al. 2019; Pomoell & Poedts 2018; Riley et al. 2016; Chané et al. 2006; Odstrcil & Pizzo 1999).

Flux rope / magnetic cloud models. CME models may incorporate magnetic flux ropes that may be superimposed on pulse–like or similar background plasma enhancements or reductions (e.g. velocity, pressure, density). Flux rope models typically comprise force–free magnetic field models in which magnetic pressure is balanced by tension on the twisted field lines and magnetic pressure dominates over thermal pressure that is considered negligible. Typically non–linear, uniform twist flux rope models are used to model interplanetary CMEs far above the stellar surface such as the Gold & Hoyle model (Gold & Hoyle 1960). There are many other models that are not of particular interest in scope of this thesis due to our model choices (see Sect. 7.2.4). However, we refer the interested reader to (Patsourakos & Georgoulis 2017) and references therein for a collection of widely used flux rope models.

3.5. Effects of SPMI and space weather on close–in planets

In this section we briefly describe some effects the stellar wind– or CME–planet interaction might have on the planet, its magnetosphere and atmosphere. We focus on effects that are included in our MHD model. We also mention consequences for atmospheres that are not self-consistent in our model, as our results allow inferences for such effects. Emissions generated by SPMI are summarized in Sect. 3.6.

3.5.1. Magnetosphere deformation

The magnetosphere forms a more or less closed cavity in the stellar wind flow. Directly below (planet-ward) the boundary between stellar wind and magnetosphere lies the magnetopause. The thin layer between the magnetopause and stellar wind is permeated by the Chapman–Ferraro current that approximately doubles the magnetic field strength of the unperturbed dipole at the magnetopause due to its induced field (e.g. Ferraro 1952; Beard 1960). The strength of the current depends on the stellar wind ram pressure and the curvature of of the upstream magnetopause surface. In the magnetohydrodynamic picture the amplified magnetic field within the upstream magnetosphere results

from magnetosphere compression and curvature on field lines through applied stresses enforced by the field perturbation. This behavior is described by the MHD induction equation which we will discuss in more detail in the scope of the Trappist-1 project (Sect. 7). Therefore, the equation for the magnetopause radius derived from total stellar wind and magnetospheric magnetic pressure balance (Eq. 3.10) has to be modified in order to account the field amplification. This results in the equilibrium position consequently pushed upstream. This is done by introducing an amplification factor f to the magnetic field, $B = fB_0$. For a planar magnetopause the factor is $f = 2$ and may reach up to $f = 3$ for a circular magnetopause shape (Schield 1969; Beard 1960; Ferraro 1960). In the planar magnetopause case, simple method to estimate the magnetic field amplification is the image dipole method. A second planetary magnetic dipole is placed upstream in a distance that is equal to the magnetopause radius (Schield 1969). Apart from the dynamic pressure of the upstream plasma, stellar wind magnetic field and the inclination of the planetary magnetic axis also affect the magnetic variation in the magnetosphere (Siscoe et al. 1968). Variations within the magnetosphere typically precede the passing of an interplanetary pulse of enhanced pressure due to compressional fast mode waves excited at the upstream magnetopause that propagate the perturbation tailward (Sibeck 1990).

As the magnetic field strength within the magnetosphere can be strongly influenced by the interaction with the stellar wind and variations in the interplanetary plasma this should be well accounted when studying magnetic variations in the vicinity of the planet's surface. Consequences of magnetosphere deformation will be discussed in more detail in the Trappist-1 project chapter where we show that compression might be the most important source of magnetic variability for close–in exoplanets due to high stellar wind and CME dynamic pressures (see Sect. 7.5).

In conjunction with variations in the planetary magnetic field, the magnetosphere responds dynamically to changes in the upstream plasma. A pulse of high kinetic energy plasma can compress the magnetosphere rapidly. Due to the planetary magnetic pressure scaling with $P_B \propto r^{-6}$ a new pressure balance establishes. Due to the inertia of the interplanetary plasma pushing the magnetopause it may overshoot the equilibrium position and consequently the magnetopause position can oscillate around the equilibrium position (Desai et al. 2021; Sibeck 1990).

The solar wind dynamic pressure has been shown to vary strongly in short timescales (on the order of minutes) even in solar quite phases (Siscoe et al. 1968). For more magnetically active stars frequent stellar wind variations and sudden pulses of high dynamic pressure can be expected with possibly more extreme effects on the inner magnetosphere and planet. It is argued that CMEs may dominate stellar winds of magnetically active stars with high flaring activity which in turn could render such stellar environments hostile towards potential exoplanets (Drake et al. 2013). The planet Mercury is a solar system analog for close–in exoplanets in regard to environmental conditions. It has been shown that the compression of Mercury's magnetosphere reveals additional factors causing magnetic field amplification such as an enhancement of the intrinsic magnetic field within Mercury when the magnetosphere is pushed near the surface (Chen et al. 2023).

Ultimately, perturbations of the planet's magnetic environment generate free magnetic energy that is available to do work. The amplitudes of such perturbations depend on the stellar wind energetics and on the planetary magnetic field itself. We investigate within this thesis both, the stellar wind dependence (Sect. 6) and planetary magnetic field dependence (Sect. 7) of stellar wind–planet interactions and associated energetics.

Space weather, geomagnetic storms and aurora

Changes in the upstream plasma in form of simple stellar wind variations or stellar eruptions (i.e. CMEs) perturb the planet's space environment and magnetic field. These perturbations come with generation of free magnetic energy that can drive plasma convection and particle acceleration. Additionally, due to reconnection between stellar wind and the planetary magnetic field, plasma may be injected into the magnetosphere. Consequences can be auroral emissions, closely related geomagnetic storms and interactions with the upper atmosphere that influence the particle population and energetics. Geomagnetic storms are the consequence of planetary magnetic field perturbations and typically manifest in form of magnetic field variability that induces currents within the magnetospheric and ionospheric plasma, the surface or even within the deeper subsurface of rocky planets. The ionospheric responses diamagnetically to magnetic field perturbations and plasma injection due to solar eruptions like coronal mass ejections. The ring current around Earth develops and induces a magnetic field that opposes the terrestrial magnetic field, weakening the surface magnetic field in return. It is subject to debate whether exoplanets also have ring currents and respond similarly to Earth to space weather. Answering this question is one of the main goals of this thesis (see Sect. 4.2 and 7).
Stellar flares from M–dwarf stars and associated stellar eruptions may have a less severe impact on exoplanets as they seem to preferably occur at high latitudes and thus possibly miss the planets (Ilin et al. 2021). The real distribution of stellar magnetic axis inclinations with respect to orbital planes is, however, not known. However, stellar dipole fields may deflect flare–associated eruptions towards the equatorial plane, possibly increasing the rate at which CMEs hit a planet to 30% (Kay et al. 2019, 2016).

Aurora. Energetic electrons resulting from SPMI precipitate onto planetary atmospheres in high magnetic latitudes, generate ionospheric currents and interact with the upper atmosphere by collisions, excitation and ionization. These processes manifest in auroral emissions. Aurora potentially exerts a significant contribution to the upper atmosphere's thermal energy budget and with it to photo–chemical processes. At Earth associated energy fluxes are in the range of several GW (Newell et al. 2010). Jupiter has a much stronger magnetic field and, despite Jupiter's aurora is mostly powered by internal processes (e.g. Eviatar & Barbosa 1984)(see Sect. 6.5.2.1 for a brief exemplary discussion of this mechanism), auroral energy fluxes in the UV are in order of 1 to several tens of TW (Grodent 2015; Gérard et al. 2014). Auroral energy fluxes at Uranus and Neptune are in the order of 1 GW (Grodent 2015) which emphasizes the strong dependence of auroral energy fluxes on the stellar wind energy density. One might expect close–in exoplanets to receive much higher energy input with considerable consequences

for the atmospheric energy budget.

Ionospheric Joule heating

The particle species in the upper atmosphere of a planet is only partially ionized and thus electrical conductivity is finite there due to the introduction of ion–neutral collisions. This circumstance enables ionospheric currents to dissipate energy due to ionospheric Joule heating in the sense of frictional heating due to the relative motion between plasma and neutrals (Vasyliūnas & Song 2005).
Joule heating is described as source or sink of electromagnetic energy in Poynting's theorem (Eq. 3.12), $\vec{j} \cdot \vec{E}$. Within the ionosphere, Joule heating is driven by currents parallel to the convective electric field, $\vec{E} = -\vec{v} \times \vec{B}$, and is governed by the work done by the flow (drag between plasma and neutrals) against the $\vec{j} \times \vec{B}$ force so that both, the drag and $\vec{j} \times \vec{B}$ force are approximately balanced (Vasyliūnas & Song 2005). Thus, the plasma conductivity perpendicular to the magnetic field (and parallel to the electric field), the Pedersen conductivity σ_P, is crucial. In response to the work done by the flow, a dynamical response of the neutral population follows consequently. The inertia of the plasma and thus the flow's work done against the $\vec{j} \times \vec{B}$ force due to collisions with the neutrals is dominated by ions. Therefore, in MHD, we can calculate ionospheric Joule heating Q_J^{ion} with

$$Q_J^{ion} = \vec{j} \cdot \vec{E} = \sigma_P \vec{E}^2 \ . \tag{3.23}$$

Through Joule heating thermal energy is deposited in the upper atmosphere species potentially leading to an increased temperature of several hundred to thousand Kelvins. Joule heating powers on Earth range from several hundred GW to few TW (Lu et al. 1998) possibly causing an increase of the upper atmosphere's mean temperature by about 500 K during magnetic storms (Weimer et al. 2011). This form of energy deposition has been shown to possibly drive atmospheric outflows in form of polar winds (Gombosi & Killeen 1987). Close–in exoplanets are expected to reside in a much more energetic stellar wind environment and Joule heating powers reach up to several hundred TW (Cohen et al. 2014). Rapid motion of planets through varying stellar magnetic fields may result in similar heating rates (Cohen et al. 2024).

Atmospheric erosion

Stellar winds directly interacting with atmospheres in addition to stellar irradiation result in erosion by collisions between energetic stellar wind plasma and the neutral population (Cohen et al. 2015; Tremblin & Chiang 2013). Atmospheric outflow may be be altered or even enhanced when planets are magnetized (Adams 2011; Sakata et al. 2020). Large scale atmospheric outflows may even build up accreting flows towards the star, especially for close–in gaseous planets (Matsakos et al. 2015; Zhilkin & Bisikalo 2019). Stellar eruptions and flares are also capable to significantly erode planetary atmospheres.

Joule heating of planetary interiors

Magnetic variations in the planetary space environment and near the planetary surface can lead to induction in the subsurface, hence inducing currents and secondary magnetic fields. Such electric currents dissipate energy in form of heat. This deposited heat is subject to heat conduction and eventually it contributes to the planetary interior heat flux. In the interior, sources of heat are potentially able to drive dynamic processes. Planetary bodies can experience varying magnetic fields either by their orbital motion through variable magnetic fields (e.g. due to a stellar dipole tilted with respect to the orbital plane) or by plasma interactions in their space environment.
Joule heating of planetary interiors due to the planet's motion through a changing magnetic field has been investigated in the past (Kislyakova & Noack 2020; Kislyakova et al. 2018, 2017). Space weather related magnetic variations and corresponding inductive heating in the interior of planets has also been investigated (e.g. for Trappist-1; Grayver et al. 2022). These studies all showed that varying magnetic fields around close–in exoplanets may pose a significant energy source to potentially drive geodynamic processes.

3.6. Observable signatures of SPMI

Star–planet interactions transfer energy from the stellar wind to the planet and, in the sub–Alfvénic scenario, also back to the star. Some of this energy is emitted in the form of radiation. Such emissions can provide valuable information about the local energetics, properties of the star as well as its wind or the planet including its near space environment. In the next sections we discuss some prominent types of emission and observations that possibly hint at SPI as a source (Sects. 3.6.1 and 3.6.2).
The main driver responsible to power such emissions is the stellar wind that carries energy towards the planet. Depending on the properties of the stellar wind we can differentiate between three possible scenarios for SPMI–related emissions.

Sub–Alfvénic emission scenario

A sub–Alfvénic stellar wind allows all MHD wave modes excited by the stellar wind–planet interaction to travel upstream to eventually reach the star. The energy transported by the MHD waves incident on the stellar surface may modify stellar spectra and excite stellar emissions. It is also possible for sub–Alfvénic star–planet interactions to trigger stellar flares (Cuntz et al. 2000). In the sub–Alfvénic scenario the interaction–generated energy fluxes are bi–directional and therefore emission in the magnetosphere are also possible. Such exoplanetary sub–Alfvénic SPIs were studied in the past with the use of magnetohydrodynamic simulations (e.g., Preusse et al. 2006, 2007; Turnpenney et al. 2018; Zhilkin & Bisikalo 2020; Varela et al. 2018, 2022). Many studies considered both, the stellar and planetary part in their simulations and incorporated self-consistent stellar wind models (e.g., Strugarek et al. 2014, 2019a,b; Cohen et al. 2011; Cohen et al. 2014; Vidotto et al. 2015; Vidotto & Donati 2017).

Super–Alfvénic stellar wind / magnetospheric emission scenario

In a super–Alfvénic stellar wind no MHD wave mode excited at the obstacle of the flow, i.e. the planet, is able to propagate back to the star due to the stellar wind bulk velocity exceeding the fastest MHD wave mode speed, i.e. the fast magnetosonic wave. The interaction generated energy transfer is thus mono–directional and possible emissions can only originate from the planet. The stellar wind–planet interaction perturbs the plasma and magnetic field in the space environment of the planet which generates Poynting fluxes that carry the electromagnetic energy capable of driving planetary emissions. The best candidates for energetic emissions from planets are auroral emissions when the planet is magnetized. From now on we refer to this scenario as the magnetospheric emission scenario. To the authors knowledge, in contrast to sub–Alfvénic SPI, less modeling effort has been put into the study of super-Alfvénic stellar wind–planet interactions and associated emissions (e.g.; Nichols & Milan 2016; Varela et al. 2016, 2018; Turnpenney et al. 2020; Daley-Yates & Stevens 2018; Kavanagh et al. 2020) despite a possibly large number of close-in exoplanets being exposed to super-Alfvénic wind conditions (i.e., orbiting outside the Alfvén surface; Zhilkin & Bisikalo 2019).

Rotation dominated magnetospheric emission scenario

A rotating magnetized planet may power the Poynting fluxes that carry energy to drive emissions internally within its magnetosphere. This scenario depends heavily on plasma sources within the magnetosphere and the presence of radial mass transport. Plasma within the magnetosphere may co–rotate with the rotation of the planetary magnetic axis. Radial mass transport away from the planet causes the co–rotating plasma to slow down its rotational velocity due to conservation of angular momentum. This slow down generates tension on the magnetic field which is frozen into the plasma and resulting Poynting fluxes may carry the energy towards the planet where they can drive auroral emissions. This is, for example, the cause of Jupiter's aurora. The fast rotation, strong magnetic field and plasma sources within the magnetosphere (the Galilean moons and most importantly the Io plasma torus) as well as the relatively weak stellar wind at Jupiter's orbital distance from the Sun result in this rotation–dominated scenario to dominate the emission energetics (Hill 2001).

3.6.1. Radio emissions

Observation of planetary auroral radio emissions are a prominent method to directly probe magnetic fields of planets and stars (e.g., Grießmeier 2015; Farrell et al. 1999; Zarka et al. 2001; Zarka 2007) and radio observations are less susceptible to false positives compared to observations at other wavelengths as the emission frequencies directly relate to the magnetic field strength at the source.
A certain fraction of the energy carried by Poynting fluxes generated by the stellar wind–planet interaction may cause auroral emissions most prominently in the UV via photo–dissociation and excitation of atmospheric particles or strongly beamed auroral radio emission generated by the electron cyclotron maser instability (ECMI) mechanism (Zarka

1998; Treumann 2006) (Fig. 3.2). Interplanetary and interstellar space is optically extremely thin in regard to radio wave transmission due to its long wave length in contrast to short wavelength emission like in the optical or UV bands. The frequency of coherent radio emission produced by the ECMI mechanism is proportional to the local magnetic field strength where the radio waves were emitted. The root source of ECMI radio emissions are electrons gyrating around a magnetic field line and thus the peak frequency of such emissions corresponds mostly to the maximum gyrofrequency, for example near the planetary magnetic poles. Electrons can either be injected by reconnection at the magnetopause which are subsequently accelerated by wave–particle interactions or they may originate entirely from within the magnetosphere (see Sect. 6.5.2.1 for a brief discussion). Radio emission is constrained to emission cones in the polar regions of planets. These cones become narrower as the electrons come closer to the planetary poles due to the enhanced gyro frequency (see Fig. 3.2 for a sketch of this mechanism). This makes radio observations a suitable tool to directly probe magnetic fields in space. Jupiter's magnetic field, for example, was first detected by its auroral emission in the radio band before space probes measured the magnetic field in situ using magnetometers (Franklin & Burke 1958).

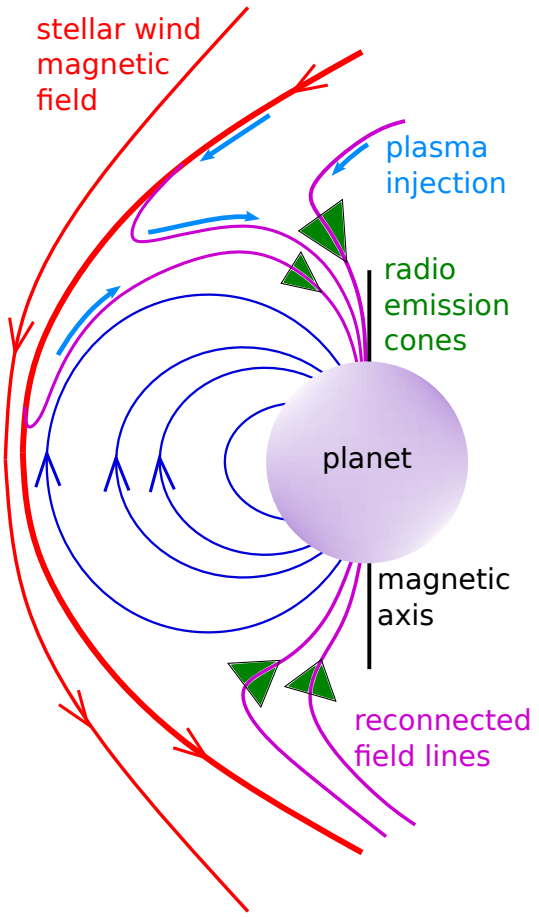

Figure 3.2.: A sketch illustrating planetary auroral radio emission due to stellar wind–planet interactions. Blue lines indicate closed planetary magnetic field lines. Plasma is injected (light blue arrows) through reconnected field lines (magenta). Precipitating electrons gyrate around polar field lines and with increasing field strength towards the planet, the radiation cones (green) become narrower due to enhanced gyro frequency.

Radio observations also allow to derive further constraints on the emission source region. Transmission and refraction of radio waves in plasmas may leave traces in form of signal polarization (Wilson et al. 2009) that may be used to infer properties such as electron densities. Furthermore, it has been theoretically shown that the efficiency of the ECMI mechanism strongly depends on the electron density and electron density in relation to the local magnetic field strength (Weber et al. 2017, 2018). High electron densities enhance the plasma frequency and radio waves below that frequency may be reflected away from the observer or the generation of ECMI radio emission might be

even suppressed.
Temporal variations of the planetary environment can cause radio bursts that, in contrast to expected periodic signal due to star–planet interactions, occur occasionally and irregularly. Such environmental variations are, for example, rooted in temporal changes of the stellar wind properties or pulse like variations due to interplanetary shocks. Observations of Jupiter's auroral radio emission show that compression of the magnetosphere due to enhanced solar wind dynamical pressure creates new radio sources with different emission characteristics that activate nearly simultaneously with the compression (Louis et al. 2023) (or for Saturn; Cecconi et al. 2022).
SPI–induced radio emission may also originate from stars in sub–Alfvénic stellar wind scenarios (Turnpenney et al. 2018; Kavanagh et al. 2021, 2022; Bastian et al. 2022). Radio emission often has the character of fast radio bursts. Such radio emissions from stars have been shown to be caused by several mechanisms, many of them occurring nearly randomly (e.g. due to flaring; Bloot et al. 2024). There are, however, detections of potential SPI–induced radio emissions from stars that point towards a planetary cause due to their seemingly temporal alignment with planetary phases (Trigilio et al. 2023; Pineda & Villadsen 2023; Vedantham et al. 2020). These studies, however, are in desperate need of follow up observations, partly to rule out randomly occurring flares as emission source and to improve on statistical arguments ruling out such non–SPI related sources. Stellar SPI–induced radio emission is after all not suitable to confidently infer planetary properties (apart from orbital periods) since the planets only affect the amplitudes of signals and finding the reason for a given amplitude is a highly non–unique inverse problem as, for example, a non–magnetized planet may also excite Alfvén waves in the stellar wind.

3.6.2. Optical emissions and modification of stellar spectra

Due to the proximity of close–in exoplanets to their host stars interactions can be sub–Alfvénic, so that planets can couple back to the star. It is expected in such sub–Alfvénic interactions that the planet's themselves or the interaction between planet and star can produce observable signatures in the stellar spectrum. One prominent example is the modification and excitation of stellar chromospheric Ca II H & K line emission which is an indicator for intrinsic stellar magnetic activity as well as temporary activity induced by magnetic SPI (e.g. Shkolnik et al. 2003, 2008; Cauley et al. 2019). Other SPI induced emission signatures in super–Alfvénic scenarios comprise asymmetric features in UV stellar light curves and UV absorption signatures caused by transiting planetary bow shocks (Vidotto et al. 2010, 2011; Llama et al. 2011) which are indicative of super–Alfvénic stellar wind–planet interactions. Although not part of magnetic SPI, transiting planets that have photo–evaporating atmospheres can also cause absorption signatures in stellar spectra. A prominent example is the Hot Jupiter HD 209458 b whose extended atmosphere caused Lyman–α absorption lines (Vidal-Madjar et al. 2003a).
Based on absorption signatures and SPI–related chromospheric emissions many studies attempted to infer information on planetary magnetic fields as they influence the amplitude of such signatures, either by enhancing the energy flux towards the star or

by enhancing the magnetosphere size and thus the related absorption signatures. However, all these SPI– and transit–related methods are susceptible to false positives as it is difficult, if not impossible, to find a unique model of the SPI structure including the planetary magnetic field due to numerous model assumptions (e.g., Turner et al. 2021; Kislyakova et al. 2016; Preusse et al. 2006; Lai et al. 2010; Kopp et al. 2011; Miller et al. 2012, 2015; Bisikalo et al. 2013; Alexander et al. 2016; Turner et al. 2016; Gurumath et al. 2018; Route 2019).

The often sparse coverage regarding the orbital phase of exoplanets of observations make it difficult to differentiate stellar emissions due to SPI from randomly occurring intrinsic sources such as flaring. However, observed stellar emissions exist that show approximate modulation near the corresponding planetary orbital period (e.g. Ilin et al. 2024; Ilin & Poppenhaeger 2022; Klein et al. 2022).

Finally, optical observations are also typically limited by extinction caused by stellar and planetary atmospheres as well as the interstellar medium, making optical, down to X–Ray observations difficult if not even impossible.

4. Aims of this thesis

In this section we introduce our motivation for the two projects and provide information on the current state of research regarding the exoplanet τ Boötis b (Sect. 4.1) and the Trappist-1 exoplanets (Sect. 4.2).

4.1. τ Boötis b – A hot Jupiter type exoplanet

The massive hot Jupiter τ Boötis b (Butler et al. 1997) is a very good candidate for remotely observing a powerful interaction of a stellar wind with an exoplanet's magnetosphere for several reasons: At ∼16 pc, the τ Boötis system is relatively close to the Solar System. The planet orbits its host star, τ Boötis A, at a short distance of 0.046 astronomical units (Butler et al. 1997). Additionally, its large mass ($> 5 M_{\mathrm{Jupiter}}$) may cause its exobase to remain close to the planet, possibly leading to a magnetosphere not completely filled with dense plasma and thus allowing for radio emission to be produced efficiently and to escape the planet's vicinity (Weber et al. 2018; Daley-Yates & Stevens 2018).
Recently, tentative measurements of auroral radio emission from the hot Jupiter exoplanet τ Boötis b were obtained with the Low Frequency Array (LOFAR; Turner et al. 2021). These observations might be considered the strongest evidence so far of an intrinsic magnetic field on a planet outside the Solar System if the emission indeed originates from the planet's vicinity. They then also imply that τ Boötis b possesses a magnetosphere that interacts with its surrounding stellar wind. The radio observations by Turner et al. (2021), if confirmed, thus help pave the way for the field of extrasolar space physics. In this work we therefore use properties from the observed radio signals to derive new constraints on the space environment around τ Boötis b.

The tentative radio measurements obtained with LOFAR comprise two signals that probably originate from the vicinity of τ Boötis b (Turner et al. 2021). The circularly polarized signals were detected in the 21-30 MHz and 15-21 MHz frequency bands, respectively. The emission possibly originates from gyrating, energetic electrons precipitating toward the planetary polar regions, emitting radio waves generated through the electron cyclotron maser instability (ECMI), which is expected to be the dominant mechanism for exoplanetary radio emission (Zarka 1998; Treumann 2006). From these signals, the planetary magnetic field strength can be inferred directly since the emission frequency corresponds to the local electron gyro-frequency. The existing observations are consistent with expectations for emitted power from the radio-magnetic Bode's law (Zarka et al. 2001; Zarka 2007; Zarka et al. 2018), for the polarization (e.g., circular polarization; Zarka 1998; Grießmeier et al. 2005), and for the frequency (i.e., slightly above

Earth's ionospheric cutoff; Grießmeier et al. 2007b, 2011; Griessmeier 2017). The measured radio signal, however, needs multisite follow-up observations, preferably at various radio wavelengths, to confirm and to further constrain the magnetic field environment of τ Boötis b (Turner et al. 2021).

Following the first detection, several follow–up observation campaigns were reported but without a new radio detection from τ Boötis b (Turner et al. 2022, 2023, 2024). Many potential causes for non–detections and for a possible false–positive detection exist. The magnetic activity of the star and its respective highly variable magnetic field (e.g. Marsden et al. 2014; Mengel et al. 2016; Jeffers et al. 2018) together with other unknowns such as the stellar wind properties near the planet (see for models of the stellar wind, Nicholson et al. 2016; Vidotto et al. 2012) may cause the interaction energetics to vary at short time scales. Also, the unknown overall magnetic topology of the stellar wind–planet interaction (i.e. how stellar and planetary fields are oriented) and the unconstrained composition of the space environment of τ Boötis b may hinder the detection of SPMI signatures from the planet due to radio wave refraction at the ionosphere, for example (e.g. Weber et al. 2018). In this work we aim to address some of these unknowns and to further restrict the possible non–detection scenarios. We study the influence of stellar wind properties such as density, the interaction's magnetic topology and structure of the hypothetical magnetosphere of τ Boötis b on radio emission. We aim to show that for predictions of exoplanetary radio emission and the search for suitable targets, more detailed knowledge about the prevailing stellar winds is needed, since these, more than the strength of the planetary magnetic field itself, determine the energetics of the interaction and thus the observability of radio emission.

Apart from determining conditions for observable radio emission, when taking the tentative observations of Turner et al. (2021) as true signals, τ Boötis b may be the first exoplanet with a directly observed magnetic field. The planet then provides a unique opportunity to constrain the space environment around this exoplanet and Hot Jupiter exoplanets in general. However, various properties of τ Boötis b itself are unknowns due to it being a non–transiting planet, such as the radius, size, and extent of its atmosphere above the 1 bar level and, as already mentioned, the stellar wind environment. τ Boötis A is a solar-like F7 IV-V star (Gray et al. 2001); its coronal temperature and pressure might therefore be comparable to those of the Sun. The coronal base density, and consequently the stellar wind mass loss rate, is the most uncertain free parameter of previous studies of the stellar wind from τ Boötis A (Vidotto et al. 2012; Nicholson et al. 2016). Recently, new constraints on stellar winds of M dwarf stars were determined via the use of astrospherical absorption signatures induced by the interaction of the stellar wind with the interstellar medium (Wood et al. 2021). The question naturally arises of whether stellar wind–planet interactions might also produce observable signatures capable of providing constrains on stellar wind properties, such as density (i.e., the mass loss rate), pressure (i.e., temperature) or magnetic field structure, which will be addressed in this work.

The generation of radio emission from exoplanets, as well as its properties and dependence on stellar wind and planetary parameters, was studied in the past using numerical

simulations (Nichols & Milan 2016; Varela et al. 2016, 2018; Turnpenney et al. 2020; Daley-Yates & Stevens 2018; Kavanagh et al. 2020). However, little to no emphasis was placed on studying the detailed spatial structure and energetics of the magnetospheric Poynting fluxes that ultimately deliver the available electromagnetic energy capable of driving planetary auroral emissions at various wavelengths.

In order to better understand the space environment around τ Boötis b, we performed magnetohydrodynamic simulations of the near space environment of τ Boötis b and its magnetic field interacting with the surrounding stellar wind plasma using the PLUTO code. The stellar wind model is based on wind simulations (Vidotto et al. 2012; Nicholson et al. 2016) driven by magnetic surface maps derived from magnetic measurements of τ Boötis A (Marsden et al. 2014; Mengel et al. 2016; Jeffers et al. 2018). The magnetic field estimate of the planet's intrinsic field, based on the tentative magnetic field strengths derived by Turner et al. (2021), is used to model the planetary magnetosphere. We specifically aim to better understand the magnetospheric energy fluxes around τ Boötis b and, more generally, hot-Jupiter-type exoplanets that are exposed to similar stellar wind conditions. We also address the question of how stellar wind variability in the time-independent case affects magnetospheric Poynting fluxes and therefore possible radio powers generated by the interaction. The stellar wind–planet interaction may additionally provide information on the stellar wind itself. Confirmed observations of stellar winds are extremely rare, rely on indirect measurement techniques and mostly deliver information on stellar mass loss (e.g. Wood et al. 2021). Understanding the energetics of stellar wind planet interactions and the amplitudes of possible associated planetary emissions as a function of magnetic topology, stellar wind density and pressure can help to additionally constrain stellar winds from the planet's perspective.

4.2. Trappist-1 – Terrestrial exoplanets

One of the striking questions in exoplanet research is whether exoplanets have magnetic fields and, in consequence, what it means for them, their space environment and habitability. In the first project (i.e. Sects. 4.1 and 6) we focused on the role of planetary magnetic fields in shaping the planetary space environment and emissions associated with stellar wind–planet interactions. In this project we aim to further dissect the role of planetary magnetic fields in governing space weather related energy input into the magnetosphere and dissipation. Ultimately we aim to better understand the role of planetary magnetic fields to shape the planetary environment, its interior and atmosphere.
Such questions can be broken down, as in all of physics, to the transfer of energy between interacting entities. We therefore target the detailed interaction energetics, spatially and in time domain, to help understand energy transfers in star–planet systems.

In the Solar system, flares and associated coronal mass ejections (CMEs) are the most energetic eruptive solar events that drastically affect the space weather around the planets. So far there have been no fully conclusive observations of extrasolar CME events,

but it can be assumed that such eruptive events are particularly common around cool stars and that CMEs might be much more extreme than is the case in the Solar system (Moschou et al. 2019). Low mass M–dwarfs are magnetically very active and show strong flaring activity with flare bolometric energies up to 10^{37} erg, thus exceeding Solar extreme events by orders of magnitude (Paudel et al. 2018; Moschou et al. 2019; Seli et al. 2021; Yang et al. 2023). From Sun's observations we know that high flare X–Ray energies typically correspond to strong CMEs (Youssef 2012; Moschou et al. 2019) and cool stars typically have flares bright in X–Ray. M–dwarfs are the most common stars in the universe and many exoplanets have been found in such systems. This raises the question what the space weather is like in such systems and how it affects the planet's space environment, possible atmosphere, and ultimately the interior. Another important factor is the role of planetary magnetic fields in shielding the planets and their atmospheres from space weather and whether intrinsic magnetic fields support or hinder habitability (Airapetian et al. 2018; Tilley et al. 2019; Airapetian et al. 2020). We address the question about the role of intrinsic magnetic fields in regard to electromagnetic shielding by investigating how magnetic fields influence the absorption and dissipation of energy received by external stellar plasma in the space environment as well as the interior of rocky planets.

A promising target of studies aiming at stellar activity, corresponding space weather and its influence on exoplanets is the Trappist-1 system hosting seven terrestrial exoplanets. The planets are of similar size as Earth (Grimm et al. 2018) and are suggested to have a similar interior composition like Solar system rocky planets (Agol et al. 2021). Trappist-1 is a flaring star (Vida et al. 2017; Paudel et al. 2018; Glazier et al. 2020; Howard et al. 2023) with three planets potentially residing within the habitable zone (Gillon et al. 2017; Payne & Kaltenegger 2024). Of particular interest is, if the planets would be magnetized, what effects those magnetic fields may have on the atmosphere, surface and interior in the context of violent space weather conditions imposed by the active host star.

The existence of atmospheres is neither proven nor refuted for the Trappist-1 planets except for Trappist-1b, where a conclusive atmospheric non–detection exists (Greene et al. 2023). Studies suggest that primoridal atmospheres, if they ever existed, would likely not be retained during the long lifetime of Trappist-1 regardless of the composition (Van Looveren et al. 2024). Planetary atmospheres might be subject to strong erosion in several ways. Atmospheric ion escape due to the interaction with the stellar wind could erode the atmosphere completely as demonstrated by Dong et al. (2018). High–energy radiation from the Trappist-1 could deprive most of the planets of their atmospheres (e.g. Bourrier et al. 2017a). Considering atmosphere–interior models, (Krissansen-Totton 2023; Krissansen-Totton et al. 2024) even suggest that for Trappist-1 e and f complete atmospheric erosion is unlikely. Ultimately, without conclusive observational evidence, it remains possible especially for the outer planets to possess atmospheres. Secondary atmospheres can also be produced and replenished, for example via volcanism. Underlying tectonic processes and energy supply for geodynamics can be provided for instance through electromagnetic induction (e.g. Grayver et al. 2022; Kislyakova et al. 2017) and

tidal interactions (e.g. Bolmont et al. 2020). Planets with magma oceans or even lava surfaces that create thick secondary atmospheres are evidently possible, which was confirmed by recent observations (e.g. 55 Cancri e; Hu et al. 2024).
Dynamic processes in the interior of rocky planets do affect surface conditions in other ways. strong interior heat sources and primordial heat may drive geodynamic processes that have been shown to play a key role for the habitability by supporting the carbon cycle due to tectonic subduction (Airapetian et al. 2020; Höning & Spohn 2023), determining the equilibrium state land–ocean fraction (Höning et al. 2019) or by affecting secondary atmosphere compositions through outgassing and volcanism (Tosi et al. 2017; Godolt et al. 2019; Airapetian et al. 2020; Unterborn et al. 2022). In general, star–planet interactions provide many mechanisms for energy exchange between stars, stellar winds and planets. Tidal interactions, for example, can significantly contribute to the energy budget of the planet's interior (e.g. for Io, Tyler et al. 2015; Davies et al. 2024). Modeling studies suggest that Trappist-1 planets might be subject to a strong tidal heating with Trappist-1b exhibiting a heat production rate similar to Io ($\approx$ 100 TW up to 1000 TW in extreme scenarios). Trappist-1c – e may experience a tidally induced heat production rate similar to the Earth (Luger et al. 2017; Barr et al. 2018; Dobos et al. 2019) (a few TW). Bolmont et al. (2020) calculated tidal dissipation of Trappist-1e in the order of 1–10 TW for a multi–layered planet and several hundred TW for a homogeneous planet. High-energy radiation from the star significantly influences the temperature on the surface or photo–chemical processes in the atmosphere, if present (Tilley et al. 2019; García Muñoz 2023) or facilitates an atmospheric escape (Roettenbacher & Kane 2017; Airapetian et al. 2017; Bourrier et al. 2017a). It was also suggested that space weather may impact the interior of exoplanets by Ohmic dissipation due to variable interplanetary magnetic fields (Kislyakova & Noack 2020). Rapidly changing stellar wind conditions due to a fast orbital motion of close–in planets may lead to a significant Ohmic dissipation (i.e. Joule heating) within upper atmospheres, which has also been shown for Trappist-1e (Cohen et al. 2024).

All these possibilities, models and interpretations of measurements rely heavily on our understanding of planetary energy budgets and therefore a detailed understanding of all possible energy sources to the planetary system is crucial. Especially for young cool exoplanet host stars in their pre–main sequence phase stellar wind energy input may provide an important energy supply in addition to high stellar irradiation, planet–planet or planet–disc interactions.

In this project we address the question of whether space weather, more precisely magnetic variability imposed by planet–intersecting CMEs, dissipate energy within close–in rocky exoplanets. We study the energy dissipation as a function of the associated flare energy and planetary magnetic field strength, which provides us with new insights on magnetic field capability to shield the planet energetically from its environment.
With this project we further aim to build upon previous models of planetary interior induction heating induced by stellar CMEs. (Grayver et al. 2022) used a Trappist-1 flare frequency distribution to estimate the occurrence rate of CMEs intersecting the planets. The geomagnetic response of the terrestrial magnetic field environment was

scaled to CME events associated with flare energies from the observed flare frequency distribution (Paudel et al. 2018). The study showed that CME–induced Ohmic dissipation in planetary interiors represents a permanent heating mechanism that influences interior heat budgets. Grayver et al. (2022) considered Earth–like magnetized and non–magnetized planets and also found that planetary magnetic fields amplify the interior heating significantly.

In our model we extend the modeling of CME–induced interior heating of Grayver et al. (2022) by considering the full plasma interaction between interplanetary CMEs and planets, taking into account a parameter range to describe intrinsic magnetic fields, and better understand the role of planetary magnetic fields in such star–planet magnetic interactions. We implement a magnetohydrodynamic model of the planet, its magnetic field and the interacting CME with intrinsic magnetic flux rope structure. We study the CME–planet magnetic interaction as a function of CME energy and CME type by assessing the electromagnetic energy transfer towards the planetary surface, surface magnetic variability and the resulting Ohmic dissipation in the planet's interior. We also consider a thin O_2 dominated atmosphere for Trappist-1e, and assess the energy dissipated within the ionosphere. We assess the energy transfer from the CME towards the planet's surface in high resolution, spatially and temporal, to better understand the conversion of CME kinetic to magnetospheric electromagnetic energy as well as how CME magnetic energy is transferred towards the planetary surface. In order to study energy conversion, we model a non–magnetic pulse like CME with enhanced kinetic energy and also a magnetic cloud like CME with intrinsic magnetic flux rope.

5. Simulation of stellar wind–planet interactions

Modeling of space plasmas can be done using the kinetic or magnetohydrodynamic (MHD) approach. While kinetic theory is applicable to all regimes of space plasma, from dilute near vacuum space to dense plasma regions like stellar atmospheres or planetary ionospheres. The kinetic approach is numerically very costly as it involves the motion of a large number of single particles. Considering multiple scales, from single particles to extended space plasmas up to astropyhsical scales, makes this approach computationally very demanding. For most applications in space physics and astrophysics the fluid framework, precisely the MHD approach, is more suitable as it describes macroscopic properties of plasma flow, such as plasma density ρ, thermal pressure p, bulk velocity $\vec{v}$ and magnetic flux $\vec{B}$. In this way larger plasma systems may be described with less computational effort. However, fluid simulations of plasma are based on solving non–linear systems of coupled partial differential equations and are as well demanding.
In this thesis we study plasma in the space environment of close–in exoplanets using magnetohydrodynamics. In this chapter we describe our basic MHD model, introduce all relevant MHD equations (Sect. 5.1) and added source terms. We describe our coordinate system in Sect. 5.1.1. In the subsequent sections we introduce our approach to model the space environment of close–in exoplanets by describing all additional source terms in detail that were added to the set of ideal MHD equations (Sect. 5.2). Parameterizations of the physical models used to describe the effect of atmospheres, plasma production and loss on the ion species are introduced in the subsequent sections 5.2.1–5.2.3.

5.1. Magnetohydrodynamic (MHD) model

The description of a plasma using MHD involves four evolution equations for the four plasma variables, density ρ, pressure p, velocity $\vec{v}$ and magnetic flux density $\vec{B}$. The

equations are as follows

$$\frac{\partial \rho}{\partial t} + \nabla \cdot [\rho \vec{v}] = P m_n - L m_i \tag{5.1}$$

$$\frac{\partial \rho \vec{v}}{\partial t} + \nabla \cdot \left[\rho \vec{v}\vec{v} + p - \vec{B}\vec{B} + \frac{1}{2}B^2 \right] = -(L m_i + \nu_n \rho)\vec{v} \tag{5.2}$$

$$\begin{aligned} \frac{\partial E_t}{\partial t} + \nabla \cdot \left[(E_t + p_t)\vec{v} - \vec{B}(\vec{v} \cdot \vec{B}) \right] = & -\frac{1}{2}(L m_i + \nu_n \rho) v^2 \\ & - \frac{3}{2}(L m_i + \nu_n \rho)\frac{p}{\rho} \\ & + \frac{3}{2}(P m_n + \nu_n \rho)\frac{k_B T_n}{m_n} \end{aligned} \tag{5.3}$$

$$\frac{\partial \vec{B}}{\partial t} - \nabla \times \left[\vec{v} \times \vec{B} \right] = 0 \, . \tag{5.4}$$

The continuity equation Eq. 5.1 describes conservation of mass. The source terms on the right–hand side account for plasma production, P, and loss, L, in terms of photo–ionization and dissociative recombination and will be described in Sect. 5.2.2 and 5.2.3. The mass of ions and neutrals are denoted by m_i and m_n, respectively. The Equation 5.2 describes the evolution of momentum density and resembles the Newtonian equation of motion of a plasma element governed by pressure gradients and magnetic fields. We do not include viscous effects in our MHD model. Plasma motion is affected by ion–neutral collisions, ionization and recombination processes which can be found on the right–hand side. The parametrization of collision processes will be introduced in Sect. 5.2.1 where we describe our neutral atmosphere model. The evolution of total energy density, E_t, is described by the energy equation 5.3. The total energy density, $E_t = \rho e + \rho v^2/2 + B^2/2\mu_0$, is the sum of internal energy density e, kinetic (2nd term) and magnetic (3rd term) energy density. The several source terms on the right–hand side account for ionization, recombination, collisions and charge exchange between colliding particles. Lastly, the induction equation 5.4 describes the evolution of the magnetic field that is governed by the plasma bulk motion. In Eq. 5.4, $-\vec{v} \times \vec{B}$ is the convective electric field in the ideal MHD limit where electrical conductivity is infinite. We use ideal MHD and thus neglect electric resistivity of the plasma by setting the magnetic diffusivity on the right–hand side equal to zero. This in principle locks us out of the possibility of magnetic diffusion that is needed for magnetic reconnection since in ideal MHD the magnetic field is strictly frozen into the plasma according to the frozen–in flux theorem (Baumjohann & Treumann 1996). However, we note that magnetic diffusion and thus reconnection is indeed present in our simulations due to the numerical grid introducing numerical diffusion because of the grid cell sizes of several tens to hundreds of kilometers. A discussion on the effect of physical plasma resistivity on our results can be found in Sect. 5.3 where we show the differences between resistive and non–resistive models. The set of MHD equations 5.1–5.4 is closed by an adiabatic equation of state, $p = \rho e(\gamma - 1)$, with the ratio of specific heats of $\gamma = 5/3$.

5.1.1. Coordinate system

For our simulations we choose a spherical coordinate system centered around the planet's center that naturally fits to the geometry of the planetary systems we want to study. In addition the spherical coordinate system in which the governing MHD equations are formulated, we use a Cartesian grid with the origin in the planet's center for presentation of results. The coordinates (r, θ, ϕ) are depicted in Fig. 5.1 where r is the radial distance from the origin. The co–latitude θ is measured from the positive z–axis towards the negative z–axis. The longitude ϕ is measured from the positive y–axis counter–clockwise. In our model the orbital plane of the planet is aligned with the x–y plane. The relative velocity of the stellar wind in the planet's rest frame, $\vec{v}_0 = \vec{v}_{sw} - \vec{v}_{orb}$, where $\vec{v}_{sw}$ is the bulk velocity of the stellar wind and $\vec{v}_{orb}$ is the orbital velocity vector of the planet, is parallel to the x–axis. We note that the direction $-\vec{v}_0$ is not necessarily aligned with the star–planet line but is usually inclined by several degrees due to the planet's orbital motion. The z–axis is perpendicular to the x–y plane and orbital plane. The y–axis points in no specific direction and completes the right–handed Cartesian coordinate system.

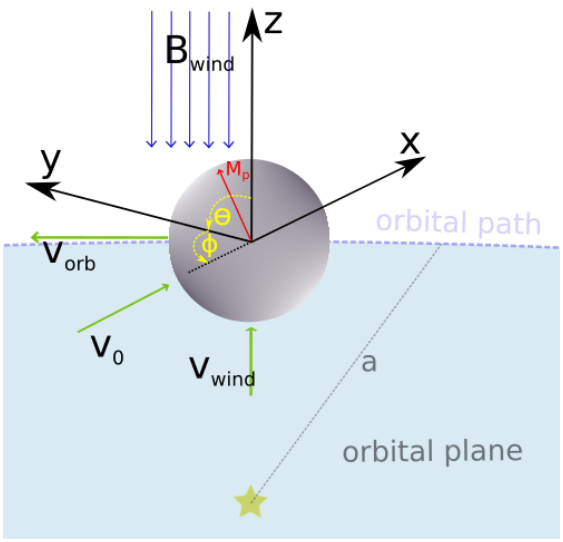

Figure 5.1.: The coordinate systems used for both projects. The MHD equations 5.1–5.4 are solved in spherical coordinates. The Cartesian grid is used for simulation input, data processing and presentation of results. Displayed are the spherical angular coordinates, co–latitude θ and longitude ϕ. The orbital distance of the planet from the host star is a. The planetary magnetic moment $\vec{M}_p$ is displayed with an arbitrary inclination with respect to the z–axis.

5.2. Physical models and their parametrization

To adopt the general MHD model from Sect. 5.1 to the planetary systems we study, we include additional source terms to the MHD equations in order to parameterize physical processes that occur in the space environment of planets. In the following sections we introduce the upper atmosphere model (Sect. 5.2.1) and describe how we account for plasma production (Sect. 5.2.2) and loss processes (Sect. 5.2.3) due to presence of a neutral species. Since photo–ionization depends on stellar irradiation, the planet's shadow imposes a strong asymmetry on this process. In Sect. 5.2.4 we describe our planetary shadow model.

5.2.1. Atmosphere model

A planetary atmosphere alters the space plasma surrounding the planet in several ways. Collisions between ions and neutral particles modify the momentum of the ions. During collisions kinetic energy is transferred from ions to the neutral species. Additionally, collisional excitation, ionization or charge exchange may occur following particle–particle collisions. In our model we only consider momentum transfer, photo–ionization and charge exchange. We assume photo–ionization to be the dominating ionization process in the space environment of close–in exoplanets and therefore we neglect electron impact ionization.
We consider the atmosphere to be spherically symmetric and purely dependent on the radial distance r from the planet's center. Thus we apply a barometric law that scales the neutral particle density with height according to

$$n_n(r) = n_{n,0} \exp\left(\frac{R_p - r}{H}\right) , \tag{5.5}$$

where R_p is the planet radius, H is the atmospheric scale height specific to the neutral species we consider and $n_{n,0}$ is the neutral particle density at the base of the atmosphere. A realistic scale height, depending on the neutral species and temperature, often lies below 100 km, which is less than our finest grid resolution in radial dimension, thus making a realistic scale height impossible to model within our framework. We assume the scale height to be at least larger than the 3 innermost grid cells for our atmosphere model to be sufficiently resolved. The atmosphere following the height profile of Eq. 5.5 is not simulated in our model and thus not altered by the interaction with the plasma. It remains constant during the whole simulation and merely acts as source term for energy and mass of the ion species.
Ion–neutral collisions are added to the MHD equations via a collision frequency ν_n,

$$\nu_n(r) = n_n(r)\, \sigma_n\, \bar{v} \tag{5.6}$$

where σ_n is the collisional cross section of the neutral particle or particle assembly and $\bar{v}$ is the characteristic velocity in the space environment of the planet. The cross section depends on the geometry of the neutral particle or particle assembly. However, following the argumentation of Johnstone et al. (2018) we assume a constant cross section of 2×10^{-19} m^2 for all considered neutrals as in the relevant energy regime and for the sizes of the neutrals considered in this thesis, e.g. molecular hydrogen for τ Boötis b and oxygen for Trappist-1e, the cross sections vary very little and small differences in σ_n do not significantly change the effect of bulk ion–neutral collisions. Corresponding source terms including deceleration and energy loss due to collisions are added to the right hand side of the MHD momentum equation 5.2 and in the first term of the right hand side in Eq. 5.3 in terms of change in kinetic energy density. When an ion collides with a neutral particle, the neutral may transfer an electron to the ion. In this case the ion is lost and a new ion is generated whose energy corresponds to the pre–collision neutral energy in addition to the transferred momentum after the collision. We model this process by adding a sink in internal energy (second term on the right hand side

including the collision frequency ν_n) and a source of internal energy dependent on the initial internal energy density of the neutral population (third term on the right hand side including the collision frequency ν_n) to the energy equation Eq. 5.3, where p is the thermal pressure, k_B is the Boltzmann constant, T_n is the neutral temperature and m_n the mass of a neutral particle. The first of the terms describes internal energy density loss due to loss of ions and the second term describes the gain of internal energy from the previously neutral particles that has been ionized during the collision.

5.2.2. Plasma production model - Photo–ionization

Neutral particles in the atmosphere are subject to stellar irradiation and can be ionized in the process by UV – XUV or XRay radiation. We add this plasma source to our MHD equations by supplying a photo–ionization rate. In the MHD equations 5.1 and 5.3 we add source terms for plasma production, P,

$$P(r) = \nu_{ion} n_n(r) \ , \tag{5.7}$$

where we assume the photo–ionization cross section to be constant and thus apply a constant ionization frequency, ν_{ion}. The production of plasma therefore only depends on the neutral particle density which itself is a function of radial distance from the planet center. Since observations of large scale atmospheric escape driven by photo–ionization exists that hint at its dominant role among the ionization process for close–in exoplanets (Koskinen et al. 2013; Vidal-Madjar et al. 2003a), we neglect impact ionization and assume its frequency being at least an order of magnitude lower compared to photo–ionization. In Eqs. 5.1 and 5.3 we multiply P with the mass of the produced ion species that is approximately the mass of the neutral particles, m_n. In the energy equation 5.3 the generated ions supply the plasma species with the internal energy density of the neutral species.

5.2.3. Plasma loss model - Recombination

Naturally ionized particles recombine occasionally with free electrons to form neutral particles. We account for this process by plasma loss terms, L, in the MHD equations 5.1 – 5.3. The loss term is defined as

$$L(\vec{r}, t) = \alpha n(\vec{r}, t)(n(\vec{r}, t) - n_{sw}) \ , \tag{5.8}$$

where α is the recombination rate in units of $\mathrm{cm}^3\ \mathrm{s}^{-1}$. Recombination only occurs if the local plasma density at a given time, $n(\vec{r}, t)$, is above the background plasma density of the stellar wind n_{sw}. For $n(\vec{r}, t) \leq n_{sw}$ recombination is deactivated locally since ions in the stellar wind recombine slower with electrons compared to the magnetosphere due to higher electron temperatures in the stellar wind. We assume the electron temperature within the relevant regions near the atmosphere to be constant and thus L depends only on the plasma density $n(\vec{r}, t)$. We multiply L with the mass of the simulated ions, m_i, and add the loss term to the continuity equation 5.1 as mass sink, to the momentum equation 5.2 as sink in momentum density and to the energy equation 5.3 as sink in internal and kinetic energy density.

5.2.4. Planetary shadow model

A neutral atmosphere is subject to anisotropic energy supply due to the planet casting a shadow cone on the anti–stellar hemisphere. The lack of stellar photons within the shadow region affects the ionization rate. Photo–ionization no longer takes place and electron–impact ionization dominates eventually leading to a decreased plasma density in the night side. A planetary shadow usually exhibits the two distinct zones of half shadow (penumbra) and core shadow (umbra) introduced by the geometry of the star–planet system, where both shadow regions form a cone. For close–in exoplanets the difference between these two regions is significantly more distinct compared to planets in larger orbital distances like in the Solar system, where the umbra fills the whole shadow cone due to the near point–like (and thus effectively smaller) light source of the distant star compared to the planet's size. Figure 5.2 displays a sketch of the geometry used for shadow calculations. For our calculations we treat the star as spherical disc instead of an extended spherical body. For any grid cell (e.g. blue cell in the sketch) we take the position vector $\vec{r}$ and calculate the projection of $\vec{r}$ on the unit vector pointing from the planet to the star, $\hat{r}_{ps}$, which gives us

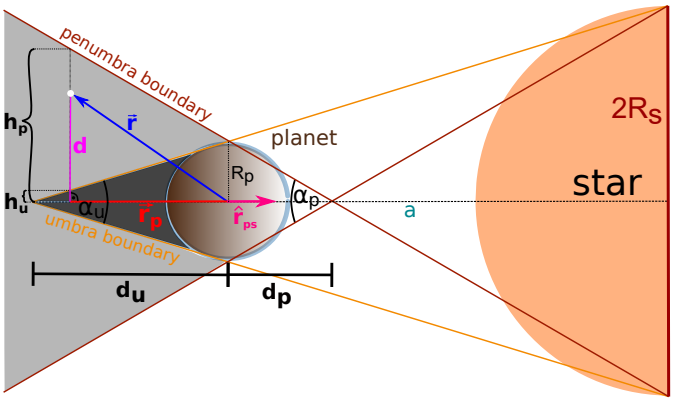

Figure 5.2.: Geometry used in the calculation of the planetary shadow (Sect. 5.2.4).

$$r_p = |(\vec{r} \cdot \hat{r}_{ps})\hat{r}_{ps}| \,, \tag{5.9}$$

which measures the cell's distance from the planet along the planet–star line. A negative sign denotes that the cell is on the night side. The distance of the cell from the star–planet line is $\vec{d} = |\vec{r} - \vec{r}'|$. From geometrical considerations (Fig. 5.2) we find the distance of the planet's center from the umbral (d_u) and penumbral cone end point (d_p) to be

$$d_u = \frac{a\, R_p}{R_s - R_p} \tag{5.10}$$

$$d_p = \frac{a\, R_p}{R_s + R_p} \,, \tag{5.11}$$

where R_p is the planetary radius, R_s the stellar radius and a the planet–star distance. The respective cone angles are

$$\alpha_u = \arcsin\left(\frac{R_p}{d_u}\right) \tag{5.12}$$

$$\alpha_p = \arcsin\left(\frac{R_p}{d_p}\right) \,. \tag{5.13}$$

The height of the umbra and penumbra cone boundaries at the respective position $\vec{r}$ can then be calculated via

$$h_u = d_u - r_p \tan \alpha_u \tag{5.14}$$

$$h_p = d_p + r_p \tan \alpha_p \, . \tag{5.15}$$

For each grid cell with position $\vec{r}$ we first test if $r_p < 0$ (Eq. 5.9) and then we compare r_p to the umbra and penumbra cone radius h_u and h_p (Eq. 5.14). If $r_p \leq h_u$ the respective position $\vec{r}$ lies in the full shadow. If $r_p > h_u$ and $r_p \leq h_p$ then $\vec{r}$ lies within the half shadow.

5.2.5. Planetary magnetic field model

Planetary dynamo magnetic fields play an important role for the structure and energetics of stellar wind–planet interactions and therefore an accurate dynamo magnetic field model is needed. Here we introduce the inner boundary condition that defines the magnetic field above the planetary surface. Planetary surfaces usually act as electric insulators and thus suppress currents that are galvanically injected into the planetary body. Physically this means that the magnetic field boundary condition needs to ensure that no radial electric current penetrates the planetary surface by incorporating the curl of the magnetic field at the surface. The boundary condition that fulfills this requirement is implemented using the insulating boundary method by Duling et al. (2014). The dynamo magnetic field is defined using the multipole expansion of the internal magnetic field. We only consider dipolar fields, thus the three first Gauss coefficients g_1^0, g_1^1 and h_1^1 must be specified. Given the equatorial magnetic flux density of the planet in question, B_p, and the magnetic moment tilt, θ_B, with respect to the z–axis (Fig. 5.1), we can calculate the Gauss coefficients using the following formulas:

$$g_1^1 = B_{eq} \frac{\tan(\theta_B)}{\sqrt{1 + \tan^2(\theta_B)}} \frac{1}{\sqrt{1 + \tan^2(360° - \lambda_{np})}} \tag{5.16}$$

$$h_1^1 = \tan(360° - \lambda_{np}) \, g_1^1 \tag{5.17}$$

$$g_1^0 = \frac{\sqrt{(g_1^1)^2 + (h_1^1)^2}}{\tan(\theta_B)} \, . \tag{5.18}$$

A derivation of the coefficient formulas can be found in the appendix A.1.

5.3. Plasma resistivity and magnetic diffusion

Ideal MHD does not allow for magnetic reconnection. However, this process essentially shapes the magnetic environment and plasma dynamics around planets and thus needs to be taken into account. It has been shown that numerical resistivity, in contrast to physical electric resistivity, is able to cause magnetic diffusion and thus magnetic reconnection that mimics physical resistivity sufficiently (Varela et al. 2018). This effect is introduced by finite grid cell sizes and thus by small but significant jumps of physical

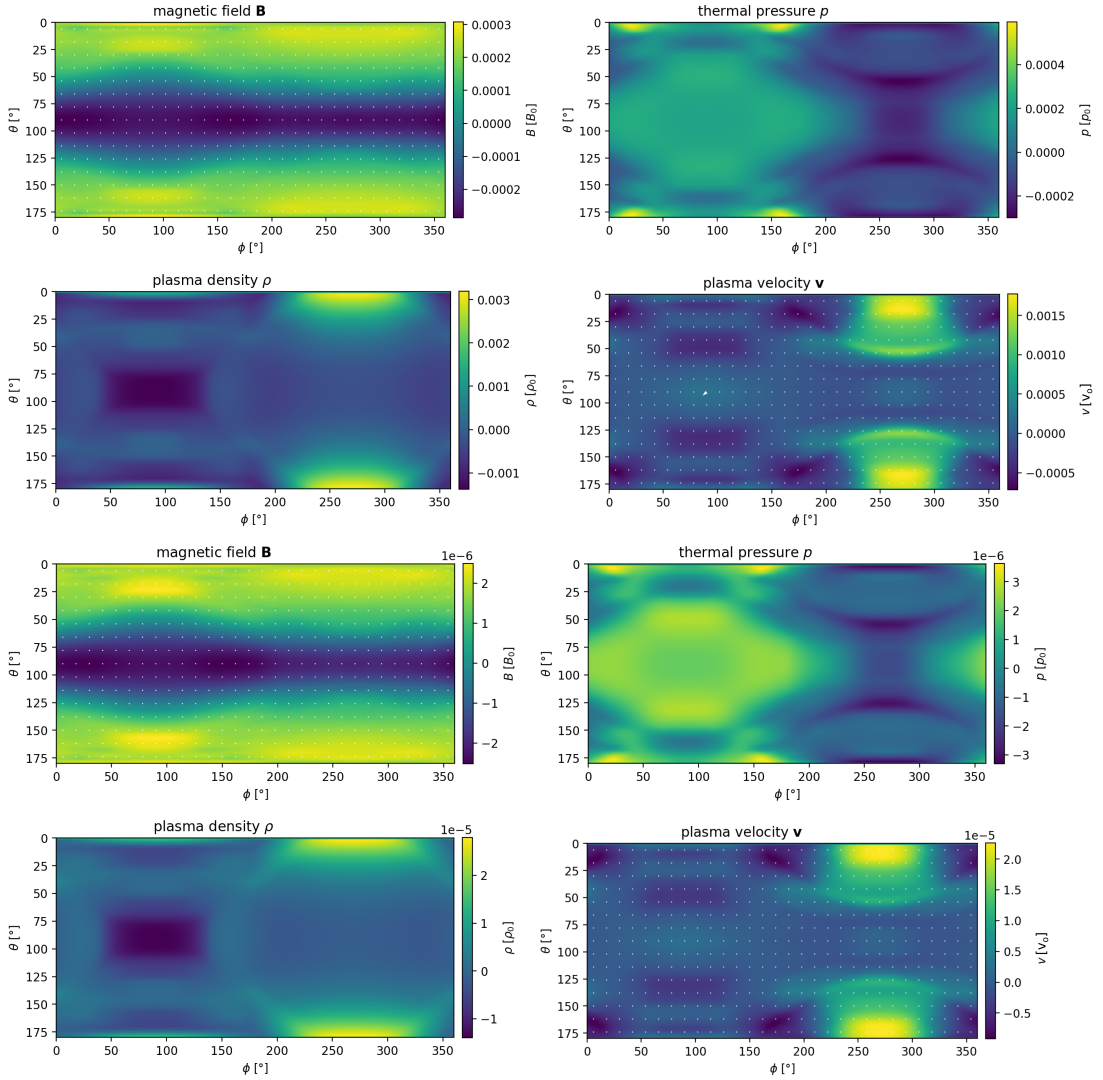

Figure 5.3.: Deviations of simulated plasma parameters (magnetic field $\vec{B}$, pressure p, density ρ and velocity $\vec{v}$) between resistive and non–resistive MHD simulations. The parameters are plotted across the planetary surface within the planetary ionosphere, with co–latitude θ and longitude ϕ. The deviations between plasma variables in resistive and non–resistive simulations are shown in arbitrary units. The upper panel shows $\Sigma_P = 1$ S, lower panel $\Sigma_P = 100$ S results.

quantities across grid borders. The coarser the grid resolution the greater the effect of numerical resistivity.
In this section we discuss the effect of electric resistivity on simulation results. This discussion is based on our τ Boötis b model which will be described in Sect. 6.2. This model involves the strongest magnetic field considered in all simulations of this thesis. The resistive induction equation (Eq. 5.4) reads

$$\frac{\partial \vec{B}}{\partial t} - \nabla \times \left[\vec{v} \times \vec{B}\right] - \frac{\eta}{\mu_0} \Delta \vec{B} = 0 \,, \tag{5.19}$$

where η is the resistivity tensor. We assume isotropic resistivity and therefore all the diagonal elements of η are equal and all off–diagonal elements are zero. Plasma conductivity is introduced by ion–neutral collisions and therefore we scale the resistivity according to a barometric law with atmospheric scale height H so that it correlates with the neutral particle density,

$$\eta(r) = \eta_0 \exp\left(\frac{R_p - r}{H}\right) \,, \tag{5.20}$$

where η_0 is the surface magnetic diffusivity, $R_p = 72875$ km the planetary radius, r the radial distance from the planet center and $H = 4373$ km the scale height (see Sect. 6.2 for details on the τ Boötis b model). We assume a height integrated Pedersen conductivity, Σ_P of 1 as well as 100 S which encompasses the range of conductivities near the Galilean moons (conductivities near close–in exoplanets are unfortunately not available). Together with the scale height we can calculate the surface magnetic diffusivity with (Duling et al. 2014)

$$\eta_0 = H \mu_0^{-1} \Sigma_P^{-1} \,, \tag{5.21}$$

where μ_0 is the vacuum permeability. The associated surface diffusivity is therefore $\eta_0 \approx 3.5 \times 10^{10}$ and 3.5×10^{12} $m^2 s^{-1}$ for $\Sigma_P = 1$ and 100 S, respectively.
Fig. 5.3 shows the relative deviations of simulated plasma variables with physical resistivity (i.e. $\vec{B}_{res}$, $\vec{v}_{res}$, ρ_{res}, p_{res}) from those without (i.e. $\vec{B}_0$, $\vec{v}_0$, ρ_0, p_0). The results show the steady state plasma variables on the surface of a sphere with radius $2\,R_p$ relative to the planet's center. The x and y–axes indicate co–latitude θ and longitude Φ, respectively, with the upstream hemisphere being at $\Phi < 180°$. The units are arbitrary since the absolute deviations are the same in each unit system. The upper block corresponds to $\Sigma_P = 1$ S and the lower block to $\Sigma_P = 100$ S. We observe maximum deviations of 10^{-4}–10^{-3} in the low conductivity case with $\Sigma_P = 1$ S. In the higher conductivity case ($\Sigma_P = 100$ S) which more closely resembles an ideal MHD scenario the deviations are reduced to 10^{-6}–10^{-5} by one order of magnitude. We conclude that in the $\Sigma_P = 1$ S scenario which is adapted to our problem (see Sect. 6.2 for a detailed model description) the deviations are insignificant (in the order of 10^{-3}). Therefore, electric resistivity does not significantly affect our results in the regime we are interested to study (i.e. ionosphere and magnetosphere of the planet).

5.4. Boundary conditions

Solving the MHD equations is a boundary value problem and thus boundary conditions are needed to be specified. The spherical simulation domain used in this work has an inner and outer boundary. Figure 5.4 shows a sketch of the simulation domain in the $\theta = \pi/2$ plane. The inner boundary lies at a radius of 1 R_p (green circle) and thus defines the surface of the planet we aim to study. The outer boundary has a radius of R_{max} (purple circle). We divide the outer boundary and simulation domain in an inflow ($\Phi < \pi$, light blue) and outflow regime ($\Phi \geq \pi$, light red). Our outflow boundary conditions ensure the gradients of the plasma variables in the direction normal to the boundary surface to be zero within the boundary ghost cells, $q(\vec{r}, t)/\delta\vec{n} = 0$ (i.e. Neumann boundary conditions), where q represents each of the plasma variables and $\vec{n}$ the unit vector normal to the boundary. At the inflow boundary the desired plasma variables are set either to constant (e.g. Sect 6.2) or time–dependent values (e.g. Sect. 7.2). The inner boundary is implemented as outflow boundary for plasma velocity, mass density and pressure, while for the magnetic field the insulating boundary method of Duling et al. (2014) is used. The surface layers of planets and moons with rocky or icy surfaces usually show low electric conductivity (Clark 1980) compared to the extremely conductive plasma in the near space environment (Neubauer 1998). Within the non–conducting surface layer the magnetic field is a potential field and $\nabla \times \vec{B} = 0$. The boundary condition prevents magnetospheric currents parallel to the magnetic field to close within the surface by prohibiting galvanic injection of radial currents into the surface (i.e. $\vec{j}_r = 0$).

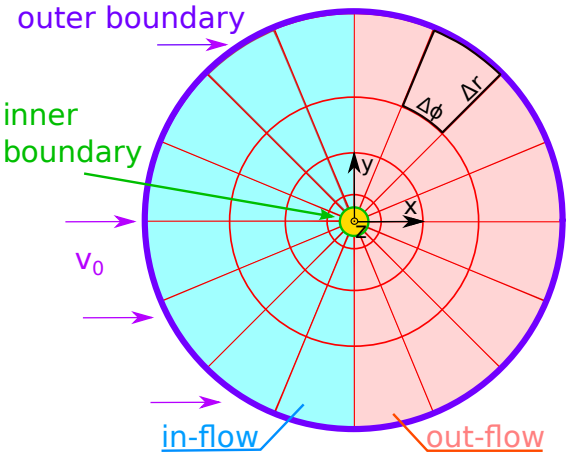

Figure 5.4.: Sketch illustrating the simulation grid and boundaries from a top view (onto the x–y plane). Blue cells indicate the inflow red the outflow boundary. The Cartesian grid is also shown with the origin at the planet's center. The yellow circle is the planet itself and is not part of the simulation domain. The planet surface (green circle) is the inner boundary defined in Sect. 5.4.

5.5. Initial conditions

As a first step in each simulations the computational and boundary grid cells of the simulation domain are filled with initial values for the plasma variables. We initialize all cells with the corresponding stationary background stellar wind parameters. Especially when considering an atmosphere model that introduces collisions between ions and neutrals

the collision terms of the MHD equations (Eqs. 5.2 and 5.2) may reach unreasonable magnitudes which introduce artifacts, unrealistic accelerations and negative pressures. To avoid this we reduce the initial plasma velocity near the planet from $R = 6R_p$ to $3R_p$ linearly to zero and below $3R_p$ the velocity is set to zero. This avoids plasma with stellar wind velocities to interact with the neutral atmosphere.

5.6. Simulation

We use the open-source code PLUTO (v. 4.4) (Mignone et al. 2007) in spherical coordinates to solve the set of single-fluid, ideal, non-resistive and non-viscous MHD simulations, Eqs. 5.1 – 5.4. The numerical specifications used in the respective project are described in the associated model section (Sects. 6.2 and 7.2).

6. The space environment of Tau Boötis b

6.1. Introduction

In this section we present and discuss our results of the τ Boötis b project. In order to pursue our goals as described in Sect. 4.1 we developed an MHD model in which we incorporated the planetary atmosphere, plasma production and loss processes as well as a magnetic field model for τ Boötis b based on the magnetic field strength proposed by (Turner et al. 2021). We conducted steady stat simulations of the planetary space environment with a constant stellar wind provided by (Nicholson et al. 2016). After an discussion on the magnetospheric structure τ Boötis b in context of the stellar wind interaction (Sect. 6.3–6.3.1) we assess magnetospheric energetics as a function of magnetic topology and stellar wind dynamic and thermal pressure (Sects. 6.5,6.5.1). We study the transfer from stellar wind to auroral Poynting fluxes (Sect. 6.4) which we use to estimate potential radio emission and put the results into the observational context provided by (Turner et al. 2021) (Sect. 6.5.2).

6.2. MHD model

We use the ideal MHD model presented in 5.1. We use the complete equations 5.1–5.4 with the source terms described in Sect. 5.2.1. We adapted our general model to τ Boötis b by incorporating observed and inferred properties of the planet. In the following we introduce the detailed model parameters to describe the space environment of τ Boötis b. In Sect. 6.2.1 we describe the planet model including the neutral atmosphere. The stellar wind model is described in 6.2.2. Numerical specifications of our simulation grid, used numerical algorithms and the solution process are described in 6.2.3.

6.2.1. Planet model

For the τ Boötis b simulations we utilize the radially symmetric neutral atmosphere model with photo–ionization and recombination which were introduced in Sects. 5.2.1–5.2.3.
We assume a scale height of $H = 4373$ km so that it encompasses three radial grid cells and consequently the neutral atmosphere is sufficiently resolved within the numerical grid (see Sect. 6.2.3 for details on the grid). We assume an atmosphere consisting of molecular hydrogen as it is, followed by helium, the most abundant constituent of the Jovian atmosphere (Atreya et al. 2003). The collisional cross-section is assumed to be $\sigma_{in} = 2 \times 10^{-19}\,\mathrm{m}^2$ for H^+ – H_2 collisions with momentum transfer for low–eV relative

Table 6.1.: Physical simulation parameters for the τ Boötis b simulations.

	Symbol	Value	Source
τ Boötis b			
Planet radius	R_p	72875 km	[1]
Orbital period	P_{orb}	3.31d	[1,2]
Semi-major axis	a	0.046 AU	[2]
Atm. surface density	$n_{n,0}$	$8{\times}10^{12}$ m^{-3}	–
Atm. scale height	H	$0.06\,R_p$	–
Magn. flux density (eq)	B_p	455μT	[3]
Basic Stellar wind model			
Therm. pressure	p_{sw}	2.5×10^{-5} Pa	[4]
Ion density	n_{sw}	1.4×10^{12} m^{-3}	[4]
Velocity	v_{sw}	224.5 km s^{-1}	[4]
Relative velocity	v_0	270.98 km s^{-1}	–
Magnetic flux density	B_{sw}	2.715 μT	[4]
Alfvén Mach number	M_A	5.36	
Fast mode Mach number	M_f	1.9	
Plasma beta	β	8.31	

[1] Wang & Ford (2011)
[2] Butler et al. (1997)
[3] Turner et al. (2021)
[4] Nicholson et al. (2016)

velocities between the colliding particles (Tabata & Shirai 2000) (we note that the stellar wind we apply to our simulations is purely composed of hydrogen ions, see Sect. 6.2.2). In our simulations the collision frequency is $\nu_{in} \approx 0.5$ s^{-1}, so that $\nu_{in} = \bar{v}\sigma_{in}n(r)$, where $\bar{v} \approx v_0$ denotes a typical velocity in the system and $n_n(r)$ is the atmosphere number density as function of radial distance from the center, where $n_{n,0} = 8 \times 10^{12}$ m^{-3} is the surface number density. Based on test studies, we found that for $n_{n,0} \approx 8 \times 10^{12}$ m^{-3} the ion-neutral collisions nearly completely bring the incoming plasma flow to a halt in the atmosphere. This results in plasma pile up in form of a shell around the planet. Increasing the density would thus not produce a larger interaction.
We do not include the shadow produced by the planet to modify ionization rates, but the radially symmetric ionization partially mimics some night side ionization through electron impact ionization due to expected high electron temperatures for close–in exoplanets around an F–type star (Koskinen et al. 2010). For the photo-ionization frequency of hydrogen exposed to a solar-like UV radiation environment at a distance of approximately 0.046 AU from the star we take the value from Kislyakova et al. (2014), $\nu_{ion} = 6 \times 10^{-5}$ s^{-1}.
Given an electron temperature of about $T_e \approx 7500$ K for a Hot Jupiter exoplanet's ionosphere with semi-major axis of 0.046 AU around a Sun-like star derived by Koskinen

et al. (2010) and using the formula of Storey & Hummer (1995),

$$\alpha = 4 \times 10^{-12} \left(\frac{300\mathrm{K}}{T_e} \right)^{0.64} \mathrm{cm}^3\,\mathrm{s}^{-1}\ , \tag{6.1}$$

we find the hydrogen ion recombination rate, α, to be 5.1×10^{-19} m^3 s^{-1}.
Recent tentative auroral radio measurements from τ Boötis b give a first observational constraint on its magnetic field strength. Turner et al. (2021) found the polar surface magnetic flux density B_p to lie between 7.5 and 10.7 G for two right-handed circularly polarized signals. We assume a dipole field and adopt the average value of both Stokes V$^+$ signals (Turner et al. 2021), B_p = 9.1 G, for our simulations. Furthermore we study the effect of dipole orientation on the stellar wind – planet interaction through simulating an open (0° tilt), semi-open (90° tilt) and closed MS (180° tilt), where the tilt is measured with respect to the negative z axis. The various tilts are realized by rotating the stellar background magnetic field accordingly so that the planetary dipole axis is always parallel to the z-axis. Given the strong magnetic variability of τ Boötis A (e.g. several magnetic polarity reversals were observed as well as a chromospheric activity cycle in terms of S–indices of roughly 240 days Donati et al. 2008; Fares et al. 2009, 2013; Mengel et al. 2016; Mittag et al. 2017; Jeffers et al. 2018) we are also able to study the effect of the host star's magnetic field topology on the stellar wind–planet interaction and associated magnetospheric energy fluxes.
The magnetic field is implemented using the insulating–boundary method by Duling et al. (2014) (Sect. 5.2.5). We assume the insulating boundary to be the planet's neutral atmosphere below its ionosphere.

6.2.2. Stellar wind model

MHD simulations of the stellar wind of τ Boötis A were performed by Nicholson et al. (2016) based on a previous model by Vidotto et al. (2012). The magnetic field of τ Boötis A was studied excessively during several epochs and magnetic surface maps as well as several magnetic polarity reversals were observed (Donati et al. 2008; Fares et al. 2009, 2013). Eight magnetic surface maps obtained between 2009 and 2015 were used as boundary condition for the MHD simulations performed by Nicholson et al. (2016). For the simulations they assumed a polytropic index of $\gamma = 1.1$ similar to the solar wind (Van Doorsselaere et al. 2011). The stellar coronal base temperature, which is not well constrained by observations, is set to 2×10^6 K as typical value for the solar coronae (Nicholson et al. 2016; Vidotto et al. 2012; Van Doorsselaere et al. 2011). The coronal base density remains an educated guess based on a comparison of emission measure (EM) values obtained from X-Ray spectra of τ Boötis A (Vidotto et al. 2012; Maggio et al. 2011). Due to the uncertainty of the base density estimate, different stellar wind densities will be investigated separately within this thesis in the scope of magnetospheric Poynting fluxes and possible radio powers (see Sects. 6.4 and 6.5.2).
For each epoch Nicholson et al. (2016) extracted the stellar wind parameters (mass density, pressure, velocity and magnetic flux density) at the position of τ Boötis b since its orbital phase and distance to the star were known. We assume the stellar wind to

be composed of hydrogen ions. The simulated stellar wind velocities are in the stellar frame of reference. We transform the velocities into the planet's frame of reference by calculating the relative velocity $\vec{v}_0$ between the stellar wind and planet using the planetary orbital velocity, v_{orb},

$$v_0 = \sqrt{v_{sw}^2 + 4\pi^2 \times a^2/P_{orb}^2}\,, \tag{6.2}$$

where v_{sw} is the stellar wind velocity in the stellar frame of reference, a is the semi–major axis of the orbit of τ Boötis b and P_{orb} is its orbital period. We averaged the stellar wind parameters over all eight epochs studied by Nicholson et al. (2016). The stellar wind and planetary parameters used in our basic model can be found in Table 6.1.
The stellar wind is applied through constant in–flow boundary conditions at the upstream hemisphere ($\Phi = 0$ to $180°$) (see Sect. 5.4). The magnetic field is assumed to be perpendicular to the relative velocity v_0 of the wind (i.e. parallel to the negative z axis). The relative velocity v_0 is parallel to the x–axis.

6.2.3. Numerical grid and simulation setup

We use a spherical coordinate system as described in Sect. 5.1.1. The corresponding numerical grid consists of 256 non–equidistant radial, 64 and 128 equally spaced angular grid cells in θ and ϕ dimension, respectively. The radial grid is divided into three regions. From 1 to 1.2 planetary radii the grid contains 10 uniform cells. After that from 1.2 to 12 R_p the next 150 cells increase in size with a factor of ≈ 1.01 per cell. The last 96 cells from 12 R_p towards the outer boundary at 70 R_p increase gradually with a factor of ≈ 1.02. The highest radial grid resolution directly above the inner boundary is $\Delta r = 0.02\,R_p \approx 1457$ km. The angular grid resolution is approximately 2.8° which corresponds to a maximum resolution above the inner boundary of about 3577 km.
The conservative form of Eqs. 5.1 – 5.4 are integrated using a approximate hll-Riemann solver (Harten, Lax, Van Leer) with the diffusive *minmod* limiter function. The $\nabla \cdot \vec{B} = 0$ condition was ensured by the mixed hyperbolic–parabolic divergence cleaning technique (Dedner et al. 2002; Mignone et al. 2010).
We ran all simulations for approximately 3.6 h physical time until a quasi-steady-state is reached in the vicinity of the planet ($r < 30$). Small fluctuations cannot be avoided, although larger-scale structure and dynamics within the MS remain already almost constant after approximately 2 hours physical time

6.3. Magnetospheric structure of τ Boötis b

In this section we give an overview of the interaction for the three magnetic configurations of our basic τ Boötis b model (i.e. open, closed and semi–open magnetosphere).

The simulated plasma velocities and pressures according to the basic model (Table 6.1) are displayed in Fig. 6.1 for the open ($\theta_B = 0°$), semi-open MS ($\theta_B = 90°$) and closed MS ($\theta_B = 180°$) case. The magnetic field tilt θ_B is the angle between the external field

(parallel to the z axis) and the planet's magnetic moment. We note that, due to the symmetries chosen in our model studies, the stellar wind and intrinsic magnetic field are not inclined with respect to the z-axis, therefore we also show projected field lines (black solid lines) in the xz-plane. Color contours denote plasma pressure in μPa (right colorbar). Arrows represent velocity components, their magnitudes are color coded (left color bar). The length of arrows indicate the magnitudes of the shown components. Spatial dimensions are given in units of planetary radii.
The intrinsic magnetic field and its corresponding MS poses an obstacle to the stellar wind flow coming from negative x – direction. The flow outside the MS is super-Alfvénic ($M_A = 5.36$) and super-fast magnetosonic ($M_f = 1.6$) (see Table 6.1), where $M_f = v_0/(v_A^2 + c_s^2)^{1/2}$, with the sound speed $c_s = \sqrt{\gamma p_{sw}/\rho_{sw}}$, polytropic index $\gamma = 1.1$ (Nicholson et al. 2016) and Alfvén velocity $v_A = B_{sw}/\sqrt{\mu_0 \rho_{sw}}$. The super-fast interaction enforces a bow shock to be formed roughly $5R_p$ in front of the planet followed by a fairly thick magnetosheath. Since no wave is able to propagate upstream, the stellar wind plasma is unperturbed until the bow shock. The structure of the MS strongly depends on the internal field orientation as visible in Fig. 6.1 with an increase of overall MS size towards higher magnetic axis tilts. For the open and semi-open MS (Fig. 6.1 top and middle plot respectively) two magnetic lobes form, separated by a thin plasma sheet, where open magnetic field lines connect to the stellar wind field several planetary radii downstream (not shown in the plots). The day side magnetopause, defined by the location of the last closed field line, lies between 3 and 3.5 R_p, while the night side magnetopause is located at roughly 5 R_p for the open and semi-open MS respectively. The downstream side magnetopause is very narrow in the z – direction as expected due to the magnetic field lines convected downstream together with the stellar wind flow and due to the magnetic stresses stretching the magnetic field. The closed MS case (Fig. 6.1, bottom plot) has a night side magnetopause lying several planetary radii ($\sim 17R_p$) downstream (not shown in the plots). While the day side magnetopause is controlled by the stellar wind thermal and magnetic pressure balanced with those exerted by the planet's surroundings, the night side MS is influenced by reconnection (i.e. the merging of planetary with stellar wind field lines). Magnetic reconnection is most efficient for a magnetic moment parallel to the ambient field (here the z-axis), therefore the fraction of open planetary field lines connected to the star decreases significantly with an intrinsic field moment being directed anti-parallel to the stellar field. As the stellar wind plasma primarily penetrates the MS along magnetic field lines, the amount of plasma and thermal pressure decreases as well with increasing magnetic axis tilt.
We note that, as visible in Fig. 6.1 (bottom), the magnetosphere is completely closed. This is due to the perfect anti–parallel alignment of the planetary and stellar wind magnetic field.
Within the MS the flow velocity is strongly reduced and has weak upstream components in the negative x direction due to magnetic tension exerted on planetary field lines. Magnetic reconnection takes place at the upstream and downstream side where velocities, both within and outside the MS, are strongly enhanced due to acceleration through released magnetic energy. Velocities are slightly larger at the flanks of the MS compared to the upstream side and exceed the initial stellar wind velocity at the downstream side

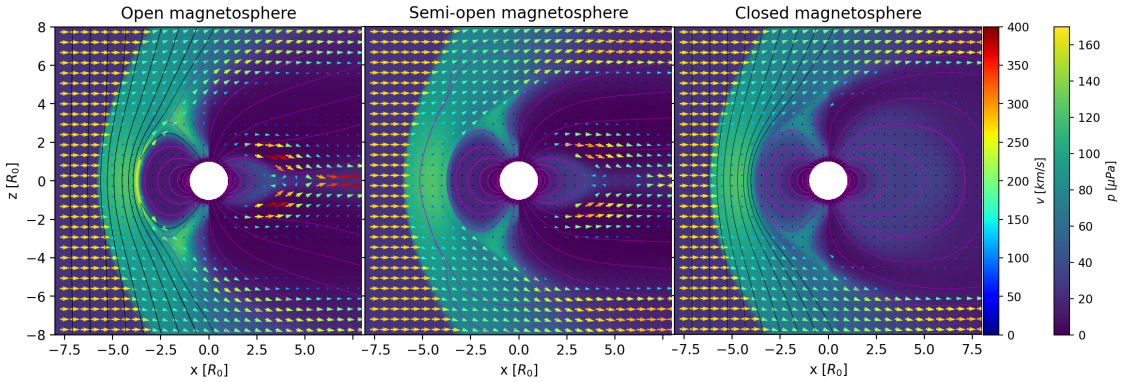

Figure 6.1.: Velocity fields (colored arrows, left colorbars) and plasma pressure (color contours, right colorbars) in the xz-plane for the open MS ($\theta_B = 0°$, top), semi-open ($\theta_B = 90°$, middle) and closed ($\theta_B = 180°$, bottom) MS case. Projected stellar wind magnetic field lines are indicated as black solid lines within the xz-plane parallel to the ambient magnetic field. Closed and open magnetospheric field lines are colored in magenta.

where stellar wind as well as planetary field lines merge together again and accelerate the plasma.

Thermal pressures are strongly enhanced within the magnetosheath, where stellar wind plasma is decelerated abruptly and compressed, so that kinetic energy is converted into heat. Plasma may penetrate the MS along open magnetic field lines in the polar cusps where pressure is enhanced as well. The cusps act as channels for plasma transport into the MS. There is a trend towards lower pressures in the cusps for increasing magnetic axis tilt. This is directly connected to the amount of stellar wind plasma advected towards the planet as the amount of injected plasma is related to the ability of magnetic field lines to merge with the ambient field. This becomes increasingly difficult for planetary magnetic moments having components anti-parallel to the ambient field, therefore the area fraction of open magnetic field lines and thus the size of the plasma injection channel is maximal for a completely open MS. Here pressures up to 160 μPa can be reached while the closed MS case shows pressures up to roughly 90 μPa.

6.3.1. Magnetospheric structure in extreme stellar wind scenarios

In order to illustrate the effect of stellar wind density and pressure on the magnetospheric structure, we show xz–plane slices (Figs. 6.2) similar to Fig. 6.1 for the extreme cases (0.05 ρ_{sw} and 100 ρ_{sw}) of our parameter study (see Sects. 6.4.3 and 6.5.1). The plots show plasma velocity and thermal pressure in the near space environment of τ Boötis b. We briefly note that, due to the use of spherical coordinates to numerically describe the space environment around τ Boötis b, mathematical singularities along the pole axis are present. For exceptionally small upstream plasma densities, this can lead to numerical artifacts (i.e. jumps for the scalar variables along the pole axis in the PLUTO code). This is visible in Figure 6.2 (left). In the vector fields and thus the Poynting fluxes this discontinuity is negligible. This effect occurring at the extremely low upstream

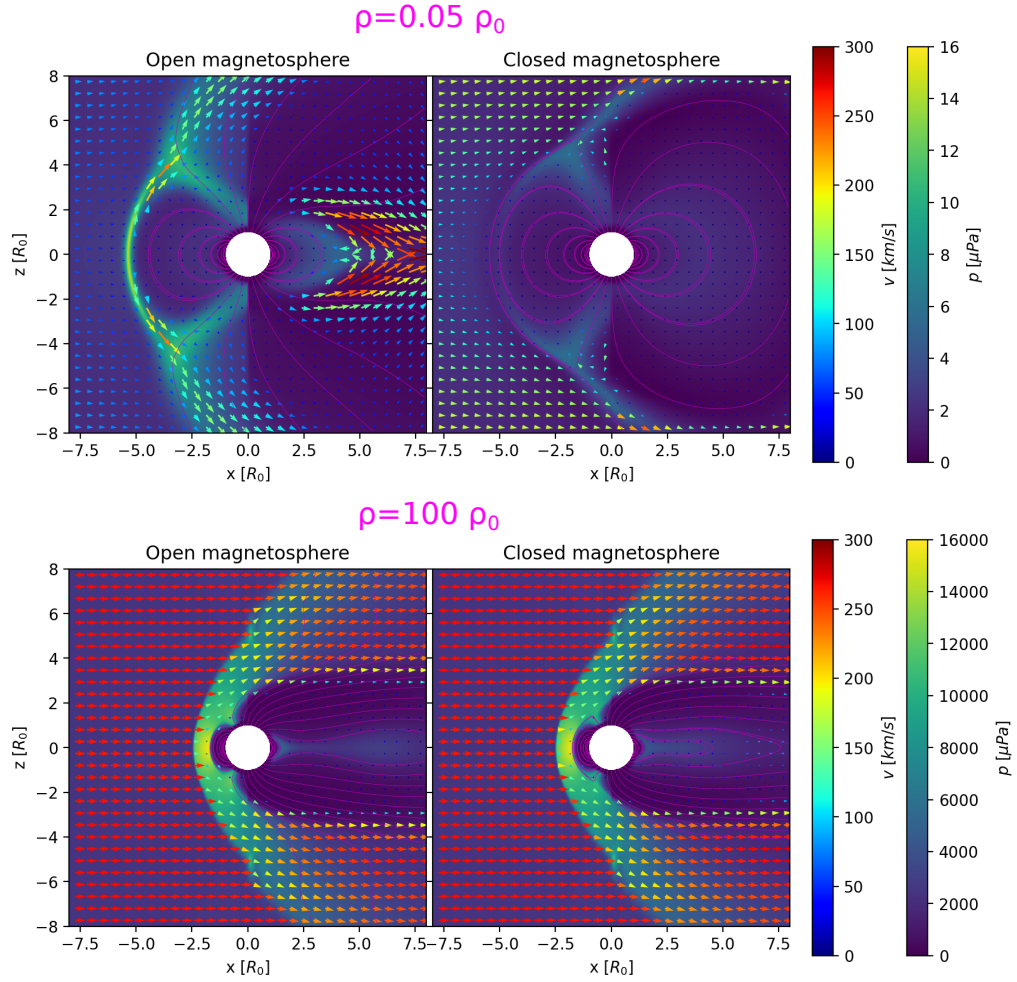

Figure 6.2.: Same caption as in Fig. 6.1 but for the extreme simulations with $\rho = 0.05\rho_0$ (top) and $\rho = 100\rho_0$ (bottom). Left panels show open, right panels closed magnetosphere scenarios.

conditions thus does not have an effect on the conclusions of this work.
The effect of stellar wind pressure and density on the size of the magnetosphere is clearly visible. The day side magnetopause location is ~ 5 R_p for the lowest density case (0.05 ρ_{sw}, left panels) and ~ 1.2 R_p for the highest density case (100 ρ_{sw}, right panels). Also visible is the sub–fast magnetosonic nature of the interaction in the lowest density case, where no bow shock forms upstream and thus incident plasma flow is perturbed prior to intersecting with the magnetosphere. However, the stellar wind is super–Alfvénic and therefore degenerate Alvén wing–like magnetic lobes form.

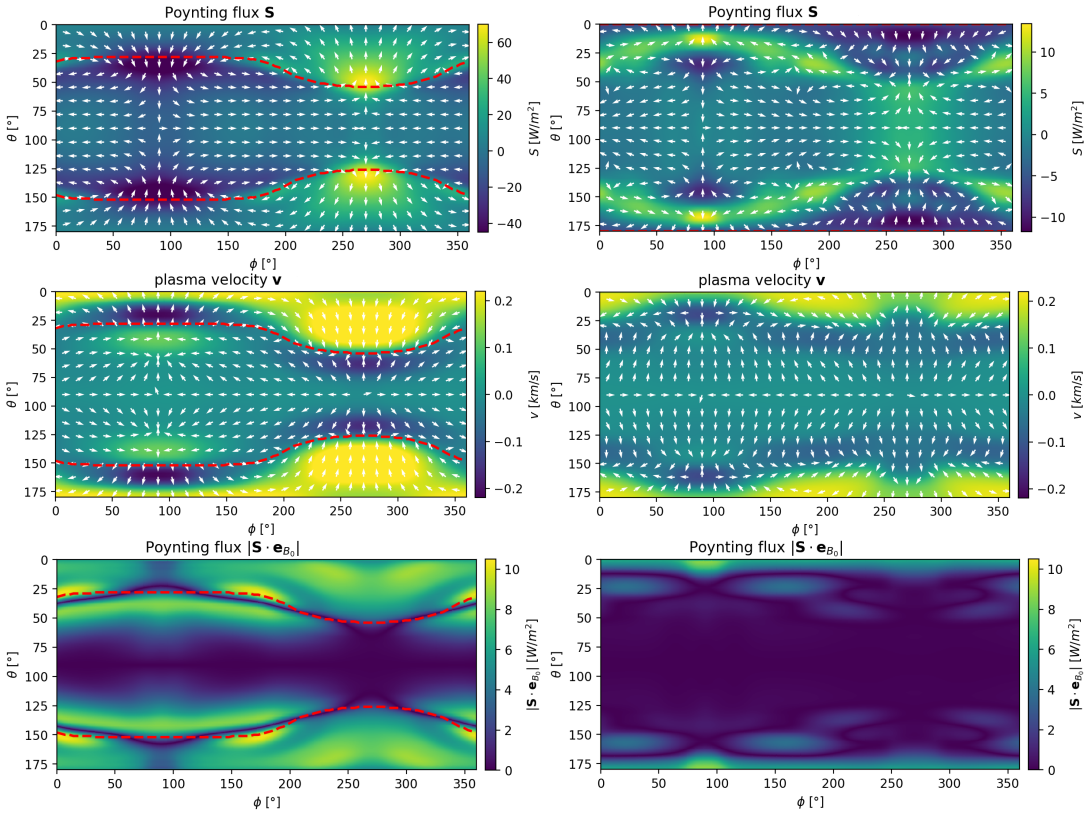

Figure 6.3.: Mercator projections of the Poynting flux (upper row), plasma velocity (middle row) and absolute values of Poynting flux components parallel to the unperturbed planetary field plus small background field from stellar wind (bottom row). The results are shown at an altitude of one planetary radius above the surface. The left column displays maps for the open MS case ($\theta_B = 0°$), the right column for the closed MS case ($\theta_B = 180°$). Arrows indicate normalized angular components, color contours denote radial components. Red dashed lines indicate the location of the OCFB.

6.4. Energetics of the interaction

We are interested in understanding the electromagnetic coupling of the stellar wind with the magnetosphere of the exoplanet, its atmosphere and ionosphere. The energy fluxes associated with these electromagnetic coupling processes provide the energetics for the auroral emission from the exoplanet's magnetosphere at radio and other wavelengths. Therefore we study the Poynting flux to calculate the maximum available electromagnetic energy fluxes.

6.4.1. Structure of magnetospheric Poynting fluxes

We first describe the spatial structure of the Poynting fluxes and plasma velocities within the MS as displayed in the top and middle row of Fig. 6.3 respectively. The plots show

Mercator projections of the angular vector components over a spherical shell with radius $2R_p$. The angle θ denotes the co-latitude, and ϕ the longitude. Arrows indicate the orientation of vectorial quantities and color contours their magnitudes. Positive values indicate radial components pointing away from the planet. Red dashed lines represent the open – closed planetary field line boundaries (OCFB). Magnetic field lines with both foot points on the planetary surface are closed field lines. Each field line having only one foot point on the planet is an open field line. The OCFB separates areas with open from areas with closed field lines. Thus, the OCFB also represents the magnetopause at that specific radial location. The open and closed MS cases are shown left and right, respectively.

The Poynting vector $\vec{S}$ can be rewritten in the ideal MHD case using the convective electrical field (e.g. Saur et al. 2013)

$$\vec{S} = \frac{\vec{E} \times \vec{B}}{\mu_0} = \frac{-\vec{v} \times \vec{B} \times \vec{B}}{\mu_0} = \frac{B^2}{\mu_0} \vec{v}_\perp \, , \tag{6.3}$$

which is bodily carried by the plasma flow perpendicular to magnetic field lines, denoted by the perpendicular velocity $\vec{v}_\perp$. The Poynting flux describes the transport of magnetic enthalpy, which is a factor of two larger than the magnetic energy density $B^2/2\mu_0$ (e.g. Saur et al. 2013). In the remainder of this work we mostly present Poynting fluxes, but need to consider the factor of two when we compare magnetic energy densities with thermal (i.e. internal energy) or kinetic energy densities based on their flows.

For both, the open and closed MS case, flow velocities are strongly reduced at the upstream (ϕ = 0–180 degrees) and downstream (ϕ = 180 – 360 degrees) side down to speeds below 10 km s^{-1}. This occurs due to interaction with the intrinsic magnetic field and momentum transfer with the neutral atmosphere. The OCFB is located at roughly $\theta \approx 30°$ and 150° in the open MS case. Due to the perfectly anti–parallel configuration of the stellar wind and planetary magnetic field no open planetary field lines exist in the closed MS model. This has also been observed in sub-Alfvénic simulations using this field topology (Ip et al. 2004; Strugarek et al. 2015).

Open Magnetosphere model (Fig. 6.3 left): The very narrow vertical extend of the downstream closed field line region of the open MS is caused by magnetic tension due to the magnetized stellar wind. Highest velocities are found within the open field line region mainly at the downstream side where plasma is accelerated downstream through magnetic tension on open lines.

Strong Poynting fluxes occur where plasma velocities have strong components perpendicular to the magnetic field. They are found within the open field line region mainly at the downstream side with outward directed Poynting fluxes. Comparatively strong Poynting fluxes, but directed toward the planet, are located on the upstream side near the magnetopause. Within the closed field line region and especially near the equator Poynting fluxes mostly vanish.

Closed Magnetosphere model (Fig. 6.3 right): In the closed MS model highest velocities can be found near the planetary poles confined to an area below 25 degrees

co–latitude and similar in the south. This high velocities are caused by tension on high latitude closed field lines that are strongly stretched towards the downstream side by the stellar wind and reach up to 17 planetary radii.
Poynting fluxes oriented away from the planet are confined to narrow bands encircling the high latitude polar regions between 40 and 80 degrees co–latitude and similar in the south. At the upstream side Poynting fluxes vanish near the equatorial regions due to plasma flow being mainly aligned with planetary field lines. Inward oriented Poynting fluxes occur near the polar axis slightly shifted towards the downstream side.

We now study the Poynting fluxes parallel to the unperturbed background magnetic field because in the solar system magnetospheres they are considered the root energy fluxes from which a small fraction can be converted into auroral radio emission. Poynting fluxes provide the energy from which wave–particle interaction can draw energy to accelerate electrons (e.g. for Jupiter Hill 2001; Saur et al. 2021). The resulting energetic electrons then can be subject to the electron maser instability (Treumann 2006; Zarka 2007). The interaction of the stellar wind with τ Boötis b's magnetic field perturbs the magnetic and electric field, which causes the Poynting fluxes. To quantitatively assess the associated Poynting flux, we therefore use the unperturbed magnetic background field $\vec{B}_0 = \vec{B}_{p,0} + \vec{B}_{sw}$ (i.e. the initial dipole and stellar wind field) to calculate the Poynting flux on this field, $\vec{S} \cdot \vec{e}_{B_0}$. The unit vector $\vec{e}_{B_0}$ points in the direction of unperturbed magnetic field lines. These projections give insight on where electromagnetic energy is transported either through propagating magnetic disturbances (i.e. Alfvén waves) or convection. The bottom row of Fig. 6.3 shows $|\vec{S} \cdot \vec{e}_{B_0}|$ for the open MS (left) and closed MS (right). We note that only absolute values are shown in the plots in order to clearly identify zero or near-zero power densities.
Strongest energy transport along unperturbed field lines occurs over narrow bands encircling the polar open field line regions at the flanks of the planet where velocities are nearly perpendicular to the magnetic field as seen in Fig. 6.3. Moreover, the spatial structure of Poynting fluxes along B_0 is strictly symmetric with respect to the equator (at $\theta = 90°$). A significant amount of energy is transported parallel to the unperturbed field within the polar open field line regions in the open MS case. Parallel energy fluxes reach values up to 10 Wm^{-2} at the flanks of the planet just outside the closed field line regions. Poynting fluxes up to 9 Wm^{-2} are found at the downstream side, above the OCFB. For both, open and closed MS model, strongest convected energy can be found extensively in high latitude regions due to high velocities perpendicular to the magnetic field. Here the planetary field lines are most mobile in a sense that they are bent over towards the downstream side by the stellar wind. For the closed MS parallel Poynting fluxes up to roughly 9 Wm^{-2} can be found directly at the planetary poles slightly shifted towards the upstream side. At lower latitudes parallel Poynting fluxes up to 6 Wm^{-2} are confined to narrow bands at the flanks of the planet. Auroral emission is expected to be strong where Poynting fluxes are large, hence near the OCFB (e.g. mostly confined to the $L = 3$–3.5 shell at the upstream side) and in the polar regions for both MS models. They vanish completely along the equator. Generally said Poynting fluxes are

Table 6.2.: Integrated magnetospheric Poynting fluxes for different magnetic field topologies

Model	Dipole tilt	P_a [W][a]	$P_a \vert\vert \vec{B}_0$ [W][b]
Open MS	0°	3.46e+18	8.73e+17
Semi-open MS	90°	1.77e+18	4.88e+17
Closed MS	180°	6.91e+17	1.09e+17

Integrated Poynting fluxes over a sphere with radius $r = 2R_p$.

[a] Magnetospheric Poynting flux (Eq. 6.5)

[b] Auroral Poynting flux parallel to $\vec{B}_0$ (Eq. 6.6)

significantly weaker and confined to the small polar regions for the closed magnetosphere model compared to the open MS case. In the open MS model strong parallel Poynting fluxes cover the whole open field line area with their maximum at the flanks of the planet in contrast to the closed MS where the regions of strongest parallel Poynting fluxes are partitioned into smaller areas around the planetary poles.

6.4.2. Energetics of the stellar wind–planet interaction

To estimate the total available Poynting flux, which serves as the root energy flux, we assume for simplicity that the radio emission is generated in a shell 1 R_p above the surface of the exoplanet. This particular choice is inspired by the fact that radio emission around Jupiter and other solar system planets arises from altitudes about $1R_p$ (or larger) above the planet's surface (e.g. Zarka 1998; Hess & Zarka 2011) where strong electron acceleration takes place (e.g. for Jupiter Mauk et al. 2020). Poynting fluxes within the magnetosphere of τ Boötis b only vary little as function of distance from the planet (see appendix B.1, Fig. B.1 for a discussion on the choice of r).
Available electromagnetic power for possible conversion into electron acceleration and radio emission is given by the divergence of the Poynting flux in this shell with Volume V,

$$P_a = \int_V \nabla \cdot \vec{S} dV = \int_{A_{shell}} \vec{S} \cdot \hat{\vec{n}} \, dA_{shell} \ , \tag{6.4}$$

where A_{shell} is the surface area of the shell and $\hat{\vec{n}}$ the surface normal vector. To investigate the maximal Poynting flux which can be dissipated in the shell we assume that the Poynting flux entering the shell from above or below is dissipated within the shell. For mathematical simplicity we further let the thickness of the shell grow infinitesimally small such that

$$P_a = \int_{A_{sphere}} |\vec{S}_r| \, dA_{sphere} \ , \tag{6.5}$$

with A_{sphere} the area of the sphere located at 2 R_P from the center. In physical terms it means that the possible dissipation in the shell can be supplied with energy fluxes from below the shell (i.e. coming from the planet's ionosphere) or from above the shell (i.e. coming from the magnetosphere or stellar wind). Ultimately, the energy flux is coming

from the stellar wind, but the energy flux can be reflected or converted in the ionosphere and can be redirected away from the planet again. This integrated Poynting flux serves as a proxy for maximum available electromagnetic energy dissipated within an auroral acceleration region.
Alternatively, we integrate the components of the Poynting flux parallel to the unperturbed magnetic field, $\vec{B}_0 = \vec{B} - \delta\vec{B}$, where $\delta\vec{B}$ denotes the magnetic field perturbation generated by the interaction. These Poynting fluxes take into account the energy flux of which a fraction can directly contribute to particle acceleration and powering the ECMI driven emission,

$$P_{a,||} = \int_A |\vec{S} \cdot \vec{e}_{B_0}| \, dA \, , \tag{6.6}$$

where $\vec{e}_{B_0}$ is the unit vector pointing in direction of $\vec{B}_0$. We refer to this Poynting flux component as the auroral Poynting flux. As opposed to Eq. 6.5, $P_{a,||}$ (Eq. 6.6) serves as a more realistic estimator for calculating auroral energy dissipation since Eq. 6.5 includes significant contribution of convected energy which is likely not converted into particle acceleration. Table 6.2 summarizes integrated Poynting fluxes according to Eq. 6.5 (third column) for all three intrinsic magnetic field orientations. The 4th column shows integrated Poynting fluxes along the unperturbed field (Eq. 6.6). Integrated Poynting fluxes range from 3.5×10^{18} down to 6.9×10^{17} W for the open towards the closed MS model. Poynting fluxes along the unperturbed field (Eq. 6.6) amount to $\sim 9 \times 10^{17}$ and 10^{17} W for the open and closed MS respectively. The effect of magnetic topology on convected energy within the magnetosphere is therefore significant as the powers differ by almost one order of magnitude. Magnetic stress due to the stellar wind interaction can work on the magnetospheres less strongly if the magnetosphere is closed, thus giving rise to weaker flows and therefore weaker convected Poynting fluxes. The trend is similar for Poynting fluxes along $\vec{B}_0$, $P_{a,||}$, but here the powers are reduced by almost an order of magnitude below the integrated total Poynting fluxes P_a.

6.4.3. Influence of stellar wind variability on magnetospheric energetics

For modeling the space environment of τ Boötis b, the properties of its surrounding stellar wind carry very large uncertainties, in particular the stellar wind density. In Nicholson et al. (2016) and Vidotto et al. (2012), the coronal base density was estimated by choosing the electron density so that it can reproduce electron measure (EM) observations of τ Boötis A. The energy fluxes within the MS are powered by and limited by the maximum incident power of the stellar wind flow transferring onto the magnetospheric obstacle. Zarka (2007) found that the observed radio power of solar system planets is nearly a constant fraction of the incident kinetic and magnetic energy convected through the obstacle's cross section, πR_{mp}^2, where R_{mp} is the magnetospheric stand-off distance of the magnetized planet. This energy is utilized in perturbing the topology of the planets magnetic field which in turn results in currents induced by changes in magnetic flux. Therefore the incident power controls the energetics within the MS. The magnetic Poynting flux, P_B, and the kinetic energy flux, P_{kin}, convected through the obstacle's

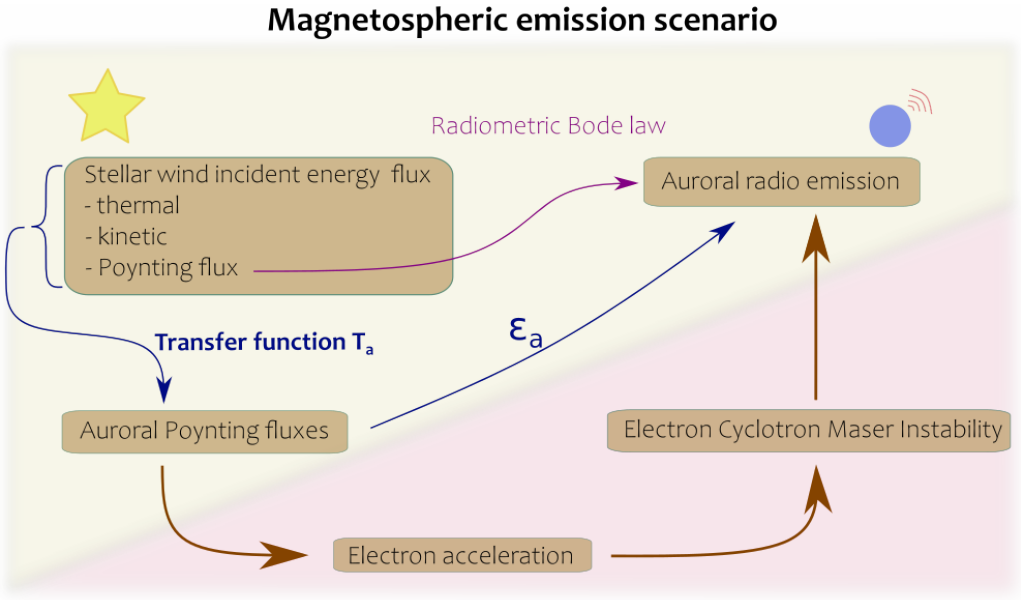

Figure 6.4.: Schematic illustrating the several steps from incident stellar wind energy flux towards auroral radio emission. The transfer function T_a (see Sect. **??**) describes the conversion from incident stellar energy to auroral Poynting fluxes. The conversion efficiency from auroral Poynting fluxes (Eq. 6.6) to radio emission, ϵ_a, implicitly includes the efficiency of electron acceleration and the ECMI mechanism. The steps within the pink shaded area are not included in our model. Brown arrows indicate physical processes, blue arrows denote model parameters quantifying energy conversion and the magenta arrow the radiometric scaling law.

cross section can be calculated as follows

$$P_{kin} = \frac{1}{2}\rho_0 v_0^2 \cdot \pi R_{mp}^2 v_0 \tag{6.7}$$

$$P_B = \frac{B_{sw}^2}{\mu_0} \cdot \pi R_{mp}^2 v_0 \ . \tag{6.8}$$

Additionally, the thermal energy flux should be considered as well as it cannot be neglected for close-in orbits where stellar wind temperature, T, pressure and density are high,

$$P_{therm} = \frac{3}{2} n_{sw} k_B T \cdot \pi R_{mp}^2 v_0 \ , \tag{6.9}$$

with n_{sw} being the stellar wind particle density and v_0 denoting the incident stellar wind velocity.
The magnetopause distance R_{mp} can be obtained from an equilibrium between stellar wind and planetary ram ($p_{ram} = \rho_{sw} v_0^2$), magnetic ($p_B = B^2/2\mu_0$) and thermal pressure. Both, the magnetospheric thermal and ram pressures are considered negligible, thus $p_{ram,sw} + p_{B,sw} + p_{therm,sw} = p_{B,pl}$, where the subscript sw stands for stellar wind and pl for planet. The magnetopause distance (or magnetospheric stand-off distance) can then

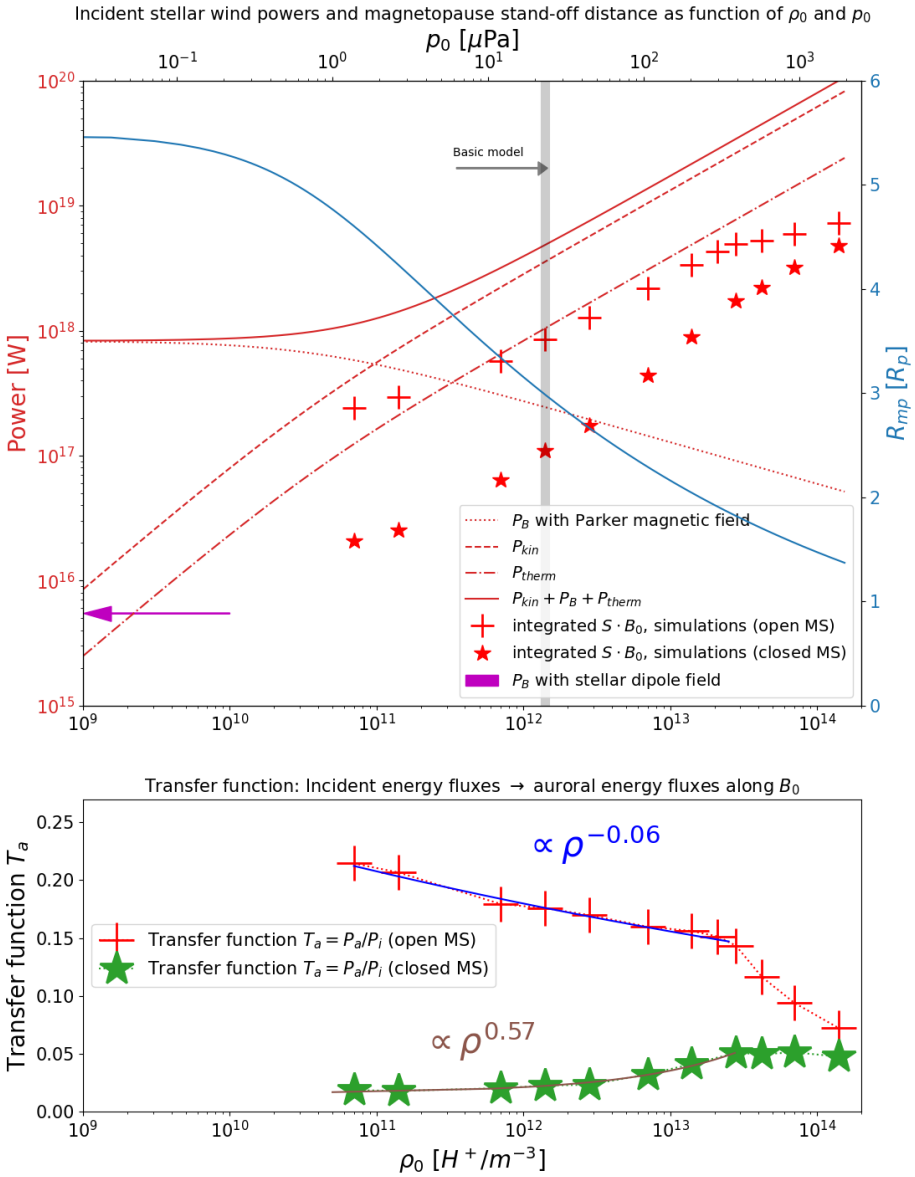

Figure 6.5.: Top: Analytically calculated incident kinetic (red dashed line), Poynting (red dotted line) and thermal (red dashed–dotted line) energy fluxes convected through the magnetospheric cross section πR_{mp}^2 as function of stellar wind density at the position of τ Boötis b. The pressure varies accordingly through $p_0 \propto \rho_0$ (see Table 6.1 for the basic stellar wind model). The powers are calculated using Eqs. 6.7 - 6.9 and 6.11. The red solid line represents the sum of the three energy components. The Magnetosphere stand-off distance R_{mp} (blue solid line) is calculated with the same set of ρ_0 and p_0 using Eq. 6.10. The stand-off distance is displayed on the right y-axis, given in planetary radii R_p. The magenta arrow indicates the convected power in the limiting case where the plasma density in the astrosphere approaches zero and the planet is only exposed to the stellar dipole field (see Sect. 6.5.1.1). Red crosses show Poynting fluxes along the unperturbed magnetic field over a spherical shell with radius $2R_p$ for the closed MS (Eq. 6.6). Red stars indicate simulated Poynting fluxes for the closed MS.
Bottom: Transfer function $T_a = P_a/P_i$ as a function of ρ_0 and p_0 (i.e. the conversion from incident energy to auroral Poynting fluxes). The scaling behavior according to power laws of T_a is indicated by exponents above the data.

be calculated from (see Sect. 3.1.3 for a more detailed derivation)

$$R_{mp} = R_p B_p^{1/3} \left[2\mu_0 \left(\frac{1}{2} \rho_{sw} v_0^2 + p_{sw} \right) + B_{sw}^2 \right]^{-1/6} . \tag{6.10}$$

All parameters can be found in Table 6.1. The parameter v_0 refers to the relative velocity between the stellar wind and planet and B_p to the planetary surface magnetic field at the equator.
A certain fraction of the total incident power,

$$P_i = P_{kin} + P_B + P_{therm} , \tag{6.11}$$

intersecting with the magnetopause can eventually be converted for the generation of radio emission within the magnetosphere. The fraction of total incident energy, ϵ, that may result in radio emission is expected to range from 10^{-5} to $\sim 3 \times 10^{-3}$ (i.e. $P_{radio} = \epsilon P_i$) in the radiometric Bode law (see Fig. 6.4) (Zarka 2007). We point out that various efficiencies for converting incident energy flux into electromagnetic radiation are discussed in the literature. For example, the efficiency of conversion from magnetospheric, auroral Poynting fluxes to radio emission, which accounts for the efficiency of electron acceleration through wave-particle interaction and the efficiency of the electron-cyclotron maser, should be separated from the generic efficiency factor obtained from the radiometric Bode law (Zarka 2007) (see Fig. 6.4). For Jupiter's radio emission the efficiency for conversion from magnetospheric, auroral Ponyting fluxes to radio emission is roughly 0.3 – $3{\times}10^{-4}$ (Saur et al. 2021). We denote this efficiency by ϵ_a (Fig. 6.4).
As the stellar wind density is the most uncertain parameter we performed simulations with densities ranging from $0.05 \cdot \rho_0$ to $100 \cdot \rho_0$ (see Table 6.1 for the basic model). In Sect. 6.3.1 wo demonstrated how stellar wind variability affects the structure of the magnetosphere for the two extreme cases $0.05 \cdot \rho_0$ and $100 \cdot \rho_0$ (Fig. 6.2). We do not solve a self consistent stellar wind model but instead follow the solar wind solution of Parker (1958) where the solution of the solar wind velocity $v(r)$ is independent of the coronal base density $n_{c,0}$ (see Sect. 3.3.1.1). In this solution, stellar mass and base temperature control $v(r)$ and $T(r)$, where r is the distance from the sun. For simplicity of the parameter study of this subsection, we choose an isothermal approach and change the density together with the pressure p_0 (and therefore T) according to $p_0 \propto \rho_0$ (see equation 6.9). We therefore keep the temperature constant and consequently the velocity does not change according to Parker (1958). Given the average stellar mass loss rate of τ Boötis A of $\dot{M} \approx 2.3 \times 10^{-12}\, M_\star$ yr^{-1} estimated by Nicholson et al. (2016) (see also our basic model, Table 6.1) the parameter range of stellar wind densities considered in this parameter study translates to mass loss rates between $1.15 \times 10^{-13}\, M_\star$ yr^{-1} and $2.3 \times 10^{-10}\, M_\star$ yr^{-1} since $\dot{M} \propto \rho_0$.
We integrate the Poynting flux along the unperturbed field over a spherical shell with radius $2R_p$ (e.g. Eq. 6.6) in order to obtain an understanding of how much incident energy flux is eventually converted to auroral Poynting fluxes. Resulting powers are shown as red crosses and stars (open and closed MS respectively) in Fig. 6.5 as a function of ρ_0 (and p_0). The simulated convected energy fluxes follow the trend of incident energy flux

estimates (red solid line in Fig. 6.5) but are reduced to fractions of the total incident energy flux, P_i, between 15 and 20 % for the open MS and between 1 and 5 % for the closed MS. Changes to the stellar wind density ρ_0 (and in the same manner p_0) affect the incident power inflicted on πR_{mp}^2 but also influence the magnetospheric cross section in an opposite manner, as it can be seen in Fig. 6.5 (blue solid line). The magnetospheric stand-off distance scales according to $R_{mp} \propto (\rho_{sw} v_0^2 + p_{sw})^{-1/6}$ and the incident energy flux with $P_i \propto \rho_{sw} + p_{sw}$, therefore the incident energy flux increase dominates over the effect of a shrinking MS due to increasing thermal and kinetic pressure. This is also validated by our simulation results (Fig. 6.5), implying a approximately linear scaling of auroral Poynting fluxes with ρ_0 and p_0 at least in the regime between 3×10^{11} and $3 \times 10^{13} H^+$ m^{-3}. Below the point where stellar wind magnetic energy dominates over thermal and kinetic energy near $10^{11} H^+$ m^{-3}, auroral Poynting fluxes seem to saturate near 2–3 $\times 10^{17}$ W (open MS) and near 1–2$\times 10^{16}$ W (closed MS). Above $3 \times 10^{13} H^+$ m^{-3} the increase of auroral Poynting fluxes with ρ_0 (and p_0) deviates further from the course of incident flux, implying a saturation towards 10^{19} W (open MS). This, however, has to be validated further through future simulations.

6.5. Discussion

6.5.1. The effect of stellar wind variability on magnetospheric energetics

In this section we discuss the conversion of incident to dissipated power within the magnetosphere as a function of stellar wind density and pressure. We also discuss the limiting case of an absent stellar wind.

We separate the considered stellar wind density and pressure range introduced in Sect. 6.4.3, Fig. 6.5 in two regimes:
Regime 1 ranges from a vanishing stellar wind up to a density at roughly $10^{11} H^+$ m^{-3} where kinetic and thermal energy fluxes fall below the persistent magnetic energy flux which dominates the flow (compare red curves in Fig. 6.5). Above roughly $10^{11} H^+$ m^{-3} the flow is super-Alfvénic ($M_A \approx 2$) and super-fast ($M_f \approx 1$). The interaction is super-Alfvénic for the whole parameter space used in our simulations and sub-fast only for the lowest simulated density ($\rho_{sw} = 7 \times 10^{10}$ H^+ m^{-3}, $M_A \approx 1.2$). The incident energy nearly stagnates below $\rho_0 = 10^{10}$ H^+ m^{-3} (red dotted line). Below this point the incident energy flux asymptotically approaches its minimum at 8×10^{17} W as we assume that only the plasma density decrease but the incident magnetic field is kept constant. In this regime it can be expected that the stellar wind magnetic field solution transitions from the Parker solution (e.g. $B \propto r^{-2}$) to a pure stellar multipole (here dipole) solution (e.g. $B_{sw} = B_{star} \propto r^{-3}$) with decreasing stellar wind density. Eventually, when the stellar wind density hypothetically approaches zero, only the dipolar stellar magnetic field interacts with the planetary magnetic field. This limiting case will be separately discussed in Sect. 6.5.1.1.
Regime 2 ranges from roughly $10^{11} H^+$ m^{-3} up to arbitrarily high stellar wind densities. Here kinetic and thermal energy fluxes dominate the flow. We will now focus on this

regime. Considering the total energy flux convected through the magnetospheric cross section πR_{mp}^2, P_{total} (red solid line in Fig. 6.5), we observe a nearly constant efficiency of conversion from incident stellar wind energy towards magnetospheric Poynting fluxes at auroral altitudes (we assumed $r \approx 2R_p$) with increasing density and pressure. We calculate the transfer function T_a as the conversion ratio from total incident energy flux P_i to the simulated auroral Poynting fluxes parallel to the unperturbed field (Eq. 6.6), P_a (red crosses and stars in Fig. 6.5), within the MS, such that $T_a = P_a/P_i$ (see Fig. 6.4 for a schematic illustrating the role of T_a). The transfer function also contains information on the magnetic topology and thus the efficiency of reconnection. The transfer function is displayed in the lower panel of Fig. 6.5. For the open MS, auroral Poynting fluxes decrease as a function of ρ_0 and p_0 according to an approximately constant ratio up to $\sim 3 \times 10^{13} H^+$ m^{-3}. For higher densities and pressures, the transfer function scales with an exponent of ~ -0.4, indicating a decrease of efficiency for conversion from incident to auroral energy fluxes. As the MS is increasingly compressed due to stronger ram and thermal pressures, the magnetopause eventually crosses the spherical shell with $r = 2R_p$ after a critical density of $\sim 3 \times 10^{13} H^+$ m^{-3} and pressure of 3×10^{-4} Pa.
For the closed MS, T_a behaves differently. The transfer function instead increases slightly from 7×10^{10} to $\sim 3 \times 10^{13} H^+$ m^{-3} following a power law with exponent ~ 0.6. The opposite behavior compared to the open MS transfer function might be a consequence of a geometry where less reconnection occurs. The stronger ram and thermal pressure exert stronger tension on planetary field lines which in turn release stronger energy fluxes during reconnection.

6.5.1.1. Beyond the MHD limit

The more the stellar wind density decreases, the emptier the heliosphere of τ Boötis A becomes. In analogy with the solar wind, the stellar wind density upstream of the magnetosphere of τ Boötis b may change by orders of magnitude. The solar wind density is observed to vary by more than two orders of magnitude (see e.g. Chané et al. 2012) such that Earth's bow shock can disappear and the Earth develops Alfvén wings. In the hypothetical limit when the density approaches zero, τ Boötis b will still be exposed to the stellar magnetic field $B_\tau(r)$ (which then decreases according to $B_\tau(r) \propto r^{-3}$ instead of $B_{sw} \propto r^{-2}$) and will propagate through it. Therefore the incoming Poynting flux of the star does not, in contrast to kinetic and thermal energy flux, vanish and is maintained by the relative motion between the stellar and planetary magnetic field. In case of an empty heliosphere, the interaction around τ Boötis b is not magnetohydrodynamic any more, but turns electromagnetic. Then the movement of τ Boötis b within the external magnetic field of the star is a unipolar or homopolar interaction (i.e. a moving conductive object with external field similar to a current generator in classical electromagnetism). In the case of a stellar magnetic field rotating at the same speed as the planet orbits around its host star (i.e. in case of total orbital and spin synchronization), non-existent changes in magnetic flux lead to a system where no work can be done by the magnetic fields. Therefore no currents are induced and the magnetosphere remains energetically silent. Although it is expected that close-in exoplanets are in nearly tidally

locked rotation, Murray & Dermott (2000) suggest in their textbook that completely synchronous rotation might not be possible if the planet has no permanent magnetic quadrupole moment and its eccentricity is not zero, which is the case for τ Boötis b (Wang & Ford 2011). Taking the rotation period of τ Boötis A, $P_\tau = 3.1 \pm 0.1$ d (Brown et al. 2021; Mengel et al. 2016), and the sidereal rotation period of τ Boötis b, $P_{orb} = 3.31$ d (Butler et al. 1997; Wang & Ford 2011), we can calculate the relative velocity between the stellar and planetary magnetic field $v_0 = 2\pi a \times (1/P_\tau - 1/P_{orb}) \approx 10.4$ km s^{-1}, where $a = 0.046$ AU is the semi-major axis of τ Boötis b. We use an average surface magnetic flux density of τ Boötis A obtained by Marsden et al. (2014); Mengel et al. (2016); Jeffers et al. (2018), $B_{\tau,0} = 2.4$ G, and calculate the flux density at 0.046 AU using the dipole formula, $B_\tau(r = a) = B_{\tau,0} \cdot (a/R_\tau)^{-3} \approx 0.73$ G, where $R_\tau = 1.43 R_\odot$ is the stellar radius (Bonfanti et al. 2016). The magnetospheric stand-off distance in this case is defined purely by the balance of stellar and planetary magnetic pressure, i.e.

$$R_{mp} = R_p \cdot (B_\tau(a)/B_p)^{-1/6} \approx 8.6\ R_p\ . \tag{6.12}$$

Now we can calculate the stellar magnetic power convected on the MS using

$$P_B = B_\tau(a)^2/\mu_0 \cdot v_0 \pi R_{mp}^2 \approx 8 \times 10^{15}\ \text{W}\ . \tag{6.13}$$

This value is included in Fig. 6.5 as magenta arrow. We can conclude the following:
(**a**) The maximum possible magnetospheric stand-off distance is reached in complete absence of a stellar wind and if the stellar and planetary magnetic fields are anti-parallel. If the stellar and planetary fields are parallel (i.e. open MS) the planetary field lines are all connected to the stellar field and no magnetopause can be determined. In the closed MS case the magnetopause lies at roughly 8.6 planetary radii in the upstream direction.
(**b**) Even if there is no stellar wind, the magnetic interaction between the stellar and planetary magnetic field still has the potential to drive an interaction with an available power limit of roughly 8×10^{15} W due to the relative motion of τ Boötis b in the stellar magnetic field. Radio emission would still be possible although very weak; corresponding radio fluxes at Earth's position would be far below today's telescope sensitivity limit. Considering Poynting flux–to–radio power efficiencies between 10^{-4} and 10^{-2}, radio powers can reach values between 10^{11} and 10^{14} W. These emitted powers exceed the strongest radio sources within the solar system by several orders of magnitude, with Jupiter's aurora being the strongest radio emitter ($P_{radio} \approx 10^{10} - 10^{11}$ W Zarka 2007), although Jupiter's emission is, in contrast to close-in exoplanets, powered by internal, rotationally driven mechanisms. The transition from a magnetosphere interaction with a stellar wind field (according to the Parker solution Parker 1958) to an interaction with a pure dipolar stellar magnetic field goes with an energetic transition followed by a decrease of maximum emitted radio power. This might pose a possible opportunity for constraining stellar wind densities in the future. Solving a self consistent stellar wind model and comparing auroral Poynting fluxes for different stellar wind base densities could reveal the critical density range where the transition from a stellar magnetic field dominated electrodynamic interaction to a stellar wind dominated magnethydrodynamic

interaction takes place. Comparing the magnetospheric Poynting fluxes and corresponding radio powers with possible future observations could reveal if the stellar wind density lies below or above the critical density.

6.5.2. Radio emission

In this section we study how magnetic topology of the interaction as well as stellar wind variability affects auroral radio emission output (Sect. 6.5.2.3). We also discuss the possibility of a sub–Alfvénic emission scenario (Sect. 6.5.2.2) as well as a rotation driven magnetosphere of τ Boötis b in Sect. 6.5.2.1, followed by a discussion on possible source regions and radio frequencies of auroral emission in Sect. 6.5.2.4.

6.5.2.1. Rotation–dominated magnetosphere

One of the possible generators for auroral emissions is radial mass transport within the MS as it is the case for Jupiter (e.g., Hill 2001; Zarka et al. 2018, 2021). Plasma is moving radially outward due to centrifugal forces within an exoplanet's MS. For small distances from the planet (or stellar host) the plasma corotates with the host. After a certain distance $\hat{L}$ in units of planetary radii, $\hat{L} \times R_p$, the corotation breaks down due to conservation of angular momentum (i.e., the plasma orbits its host with a smaller angular velocity than those from the rotation of the host). The relative velocity exerts magnetic stresses on the frozen-in field lines, the tension accelerates plasma along the field lines back to the host. The distance of corotation breakdown can be estimated using the colatitude of the region, where auroral emission occurs, θ_a, following Hill (2001), $\sin(\theta_a) = \hat{L}^{-1/2}$. Saur et al. (2021) derived a so-called auroral power potential for magnetized rotation-dominated hosts,

$$S_{pot} = B_{host}^2 \Omega_{host}^2 R_{host}^2 \ , \tag{6.14}$$

where the subscript *host* refers in our case to the planet τ Boötis b. The hosts magnetic flux density is denoted by B_{host}, $\Omega_{host} \approx 2\pi/P_{orb} = 2.2 \times 10^{-5}$ rad s^{-1} is its angular velocity and $R_{host} = R_p$ the planet's radius. We note that the discussion in this subsection is only based on theoretical considerations since we neglected planetary rotation in our MHD model. Following Saur et al. (2021) we can calculate the energy flux due to mass transport, P_{mag}, by using

$$P_{mag} = S_{pot} \left(\pi \frac{R_p^2}{\hat{L}^2} \right) \Sigma_p \ , \tag{6.15}$$

where Σ_p denotes the Pedersen conductance. We assume a value of 1 S and 10 S that are of the same order of magnitude as observed conductances near Jupiter (e.g., Hill 2001; Strobel & Atreya 1983; Hinson et al. 1998). For a hot Jupiter exoplanet the ionospheric Pedersen conductivity might be larger due to the larger ionization (Koskinen et al. 2010). However, the height of the resulting ionospheric layer and thus the mobility of the electrons and ions within the atmosphere also play an important role for the values of

its conductivity. To our knowledge no dedicated study for the conductance of τ Boötis b is available. We also note that in Eq. 6.14 the distance of corotation breakdown $\hat{L}$ is proportional to $\Sigma^{1/4}$ (Hill 2001). Thus, the P_{mag} in Eq. 6.15 depends effectively weaker on Σ_p (i.e., P_{mag} is proportional to $\Sigma_p^{1/2}$). In our simulations we integrate the ion component of the Pedersen conductivity along the z-axis at the poles from the surface ($r = R_p$) to $r = 1.1\ R_p$ where the plasma density peaks and find the height integrated Pedersen conductance to be on the order of 10 S. We find, with aurora occurring at field lines with L-parameter smaller than ~ 4 that have to lie within the MS (e.g., $\hat{L} \approx 3.5$), the auroral power potential to be $S_{pot} \approx 0.5$ W m^{-2} S^{-1} and the magnetic power to lie between $P_{mag} \approx 10^{14}\ W$ and $10^{15}\ W$. The auroral power potential of Jupiter, for comparison, is roughly 600 W m^{-2} S^{-1}. The resulting energy flux between the MS and ionosphere lies near the Jovian value (3.1×10^{14} W Saur et al. 2021). This result is several orders of magnitude below the power of magnetospheric Poynting fluxes powered by the stellar wind–planet interaction in our model (e.g., 10^{17} – 10^{18} W, Table. 6.2). Therefore, we can safely assume that the MS of τ Boötis b is not rotationally dominated, which is in agreement with the expected slow rotation nearly synchronized with its orbit around the star.

6.5.2.2. Sub–Alfvénic emission scenario

Although there is no sub-Alfvénic interaction within the parameter space we considered, the possibility of such an interaction and its consequences on possible radio emission should not be neglected. By choosing a stellar wind density of $\rho_{sw} = 0.03\ \rho_0$ we find an Alfvénic Mach number of $M_A \approx 0.9$. In this case Alfvén waves may propagate back to the star through Alfvén wings connecting the planetary magnetic field with the star. The electromagnetic energy channeled through this flux tube can be calculated using the model from Saur et al. (2013),

$$P_S = 2\pi R_{mp}^2 \frac{(\bar{\alpha} B_{sw} \cos\theta)^2}{\mu_0} M_A v_0 \ , \tag{6.16}$$

where $\theta = 0°$ is the angle that describes the deviation of the flow from being perpendicular to the stellar wind magnetic field, $R_{mp} \approx 5R_p$ the magnetospheric stand–of distance and $\bar{\alpha}$ the interaction strength. Due to the planet presumably possessing an ionosphere, which favors a strong plasma interaction, we chose $\bar{\alpha} \approx 1$. Using v_0 and B_{sw} from our basic model (Table 6.1), the energy flux channeled through Alfvén wings parallel to magnetic field lines amounts to $P_S = 1.2 \times 10^{18}$ W. This energy flux may contribute to electron acceleration and consequently to ECMI-driven radio emission in the space environment near the star. Taking the same range of Poynting flux to radio efficiencies (10^{-4}–10^{-2}), the expected radio power ranges from roughly 10^{14} to 10^{16} W, which partially overlaps with the range of radio power deduced by Turner et al. (2021). The emission frequency would, however, be much lower compared to the signals observed by Turner et al. (2021) due to the low magnetic field strength of τ Boötis A (Turner et al. 2021). Additionally, Turner et al. (2021) state that stellar emission would be less

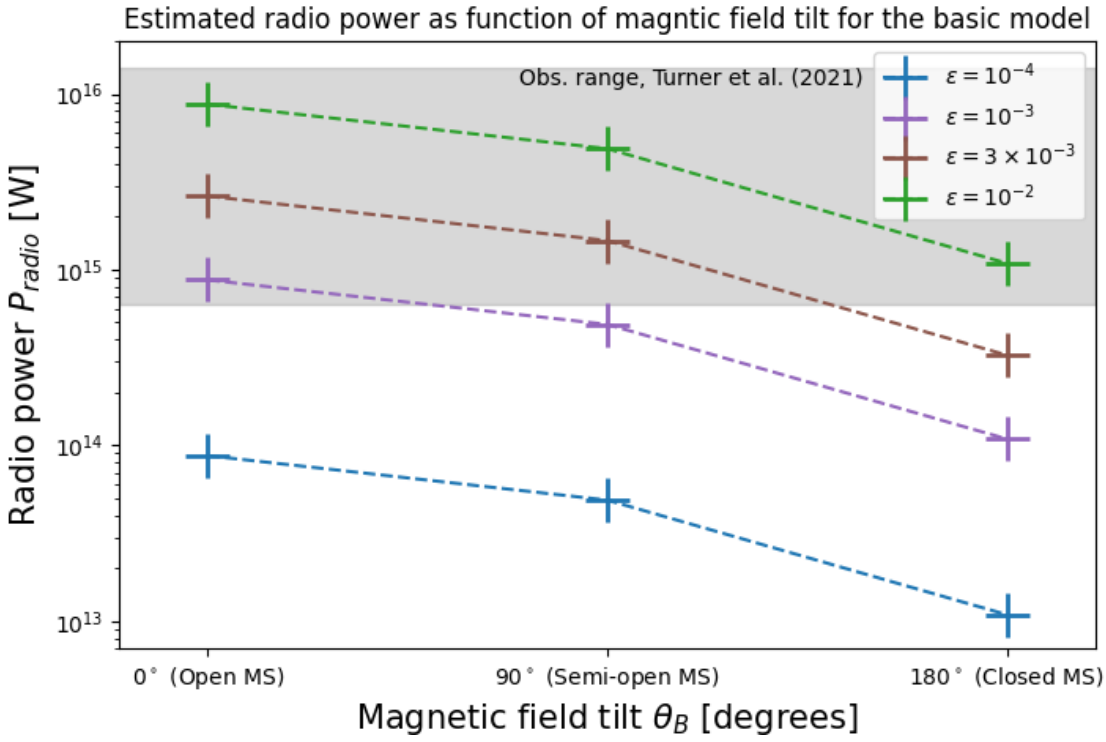

Figure 6.6.: Expected radio powers as a function of planetary magnetic axis tilt using auroral-to-radio power conversion efficiencies between 10^{-4} and 10^{-2}. The auroral Poynting fluxes, $\vec{S} \cdot \vec{B}_0$, are integrated over a spherical shell with radius $2R_p$. The gray shaded area represents the observational limits given by Turner et al. (2021).

strongly circularly polarized compared to planetary emission. Nevertheless the root energy flux able to possibly drive radio emission near the stellar atmosphere from such a sub–Alfvénic interaction exceeds the auroral Poynting fluxes in the magnetospheric emission scenario by roughly half an order of magnitude. Consequently this scenario might provide energetically a possible explanation for the observed radio emission if the interaction is indeed sub–Alfvénic. This scenario requires the stellar wind density to be reduced by at least a factor of ~ 30 compared to our basic model. This, however, could well be within the realm of possible densities given the observed density variations of the solar wind even tough the intervals of variability are short (Chané et al. 2012).

6.5.2.3. Magnetospheric emission scenario

Figure 6.6 shows radio powers as a function of magnetic axis tilt. Radio powers are obtained by multiplying integrated auroral Poynting fluxes (i.e., Eq. 6.6), which serve as a proxy for the maximum available electromagnetic energy that is transported along magnetic field lines, by efficiency factors for converting magnetospheric Poynting fluxes to radio power, ϵ, ranging from 10^{-4} to 10^{-2}. This range covers proposed (Zarka 2007) and observed efficiency factors (e.g., $\epsilon \approx 10^{-4}$ for Jupiter Saur et al. 2021). The modeled

magnetic field tilt can also be interpreted as stellar magnetic field orientation within this work, allowing us to study the effect of varying stellar magnetic field polarity on magnetospheric Poynting fluxes and limits for associated radio emission. Radio powers within the limits inferred from observations by Turner et al. (2021) lie within the gray shaded area. It is visible that efficiency factors in the range of $\epsilon \approx (0.3-1) \times 10^{-2}$ deliver radio powers most consistent with observations if the MS is open or at least semi open given the basic model (Table 6.1). This indicates that the efficiency of auroral Poynting fluxes driving electron acceleration and the electron cyclotron maser emission may be higher in the MS of τ Boötis b than in the Jovian MS (Saur et al. 2021). Electric fields generated by reconnection between stellar wind and planetary magnetic field lines are expected to contribute significantly to powering electron acceleration and therefore the ECMI (Jardine & Collier Cameron 2008). In our studies we find reconnection to indirectly play an important role (Fig. 6.6) because auroral Poynting fluxes and consequently radio powers drop by nearly an order of magnitude from an open to a closed MS. This is due to magnetic stress exerted by the stellar wind interaction being less strong for closed MSs. The polarity of τ Boötis A's magnetic field switches every approximate 360 days (Fares et al. 2013). Shorter cycles in magnetic activity levels (by means of S-indices) were also observed (Mengel et al. 2016). A difference of half an order of magnitude to almost an order of magnitude can therefore be caused by a polarity reversal of τ Boötis A's magnetic field. This results in radio emission whose observability is expected to fluctuated periodically in a nearly 1-year cycle. We note that the stellar wind magnetic field strength was kept constant in our parameter study, although in reality the field strength may vary strongly and influence produced radio emission significantly (See et al. 2015). The emitted radio flux observed at Earth's position can be calculated with (Grießmeier et al. 2005, 2007b)

$$\Phi = \frac{P_{radio}}{\Omega \, \delta\nu \, d^2} \, , \tag{6.17}$$

where Ω is the solid angle of the beam and $\delta\nu$ the emission bandwidth that is approximately equal to the maximum gyro frequency (Grießmeier et al. 2007b), $\nu_{g,e} \approx 24$ MHz. We assume a solid angle of $\Omega = 1.6$ sr, similar to Jupiter's decametric radio emission (Zarka et al. 2004). The distance to the τ Boötis system is 15.6 pc. We calculate the radio flux for both, the open and closed MS model, as a function of ρ_0 and p_0 with radio efficiencies $\epsilon_a = 10^{-4}$–10^{-2}. The results are displayed in Fig. 6.7. Solid and dashed colored lines represent radio fluxes originating from open and closed MSs, respectively. The gray shaded area again denotes the range of observed radio fluxes form Turner et al. (2021). Horizontal gray lines indicate theoretical sensitivity limits of the LOFAR telescopes for 20 MHz. As stated by Turner et al. (2019), the realistic sensitivity might be slightly lower for circularly polarized (Stokes V) signals. We therefore include the expected sensitivity calculated by Turner et al. (2019) as yellow line. The results in Fig. 6.7 indicate that radio efficiencies between $\sim 3 \times 10^{-3}$ and $\sim 10^{-2}$ are most consistent with the tentative observations (Turner et al. 2021). The efficiency accounts for several steps from conversion of auroral Poynting fluxes to radio emission (e.g., wave-particle interaction, electron acceleration and ECMI), and therefore an efficiency on the order of 1–10% might be unrealistic. The efficiency for Jupiter's auroral emission is roughly

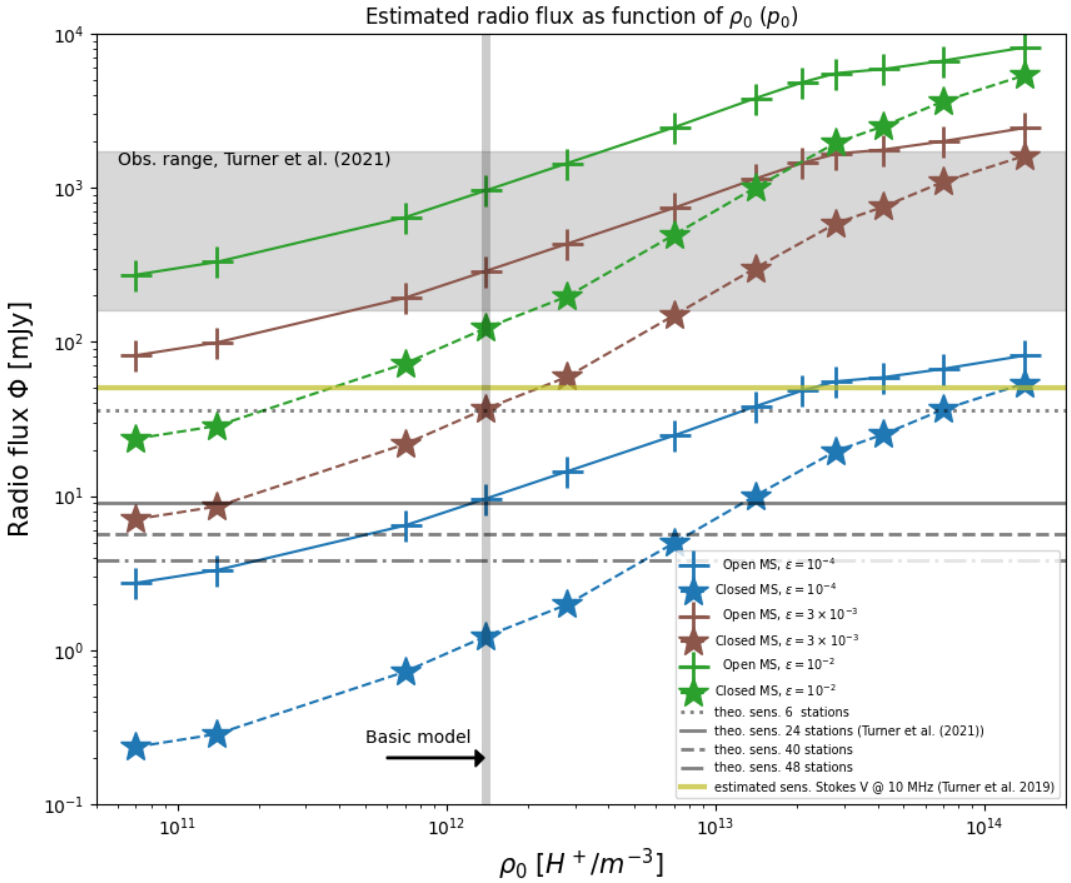

Figure 6.7.: Radio flux (Eq. 6.17) as a function of stellar wind density and pressure for different efficiency factors. Colored solid and dashed lines represent fluxes for the open and closed MS models. Observational limits (Turner et al. 2021) are indicated by the gray shaded area. Horizontal gray lines display theoretical sensitivity limits of the LOFAR telescope. The real sensitivity for Stokes V signals obtained from Turner et al. (2019) is plotted as a yellow line. The vertical gray line marks the basic model (Table 6.1).

$\epsilon_a = 0.3$–3×10^{-4} (Saur et al. 2021), and therefore $\epsilon_a = 10^{-2}$ might be too high. Moreover, high plasma densities within the MS injected by the dense stellar wind and due to strong irradiation, which results in high ionization rates and inflated atmospheres (e.g., for ν And b, see Erkaev et al. 2022), may further decrease the ECMI efficiency or even prevent it (Weber et al. 2017, 2018; Daley-Yates & Stevens 2018). Assuming the radio efficiency to lie near 10^{-3}, the radio flux from a closed MS falls below the detection threshold (yellow line). Therefore, in the case of a polarity reversal of τ Boötis A's magnetic field (i.e., from aligned with the planetary field to anti-aligned), the radio signal would not be observable anymore in the case of radio efficiency equal or below $\sim 3 \times 10^{-3}$. In the case of $\epsilon_a \approx 10^{-4}$ all radio fluxes for the basic model fall below the sensitivity limit. The observability increases, however, if stellar wind density and pressure rises, rendering $\epsilon_a = 10^{-3}$–10^{-2} to possible efficiencies to observe emission from open

and closed MSs. Additionally, the ECMI efficiency (Treumann 2006; Weber et al. 2017) as well as efficiency of electron acceleration through wave-particle interaction decreases dramatically with increasing plasma density (Saur et al. 2018), making the higher density and pressure regime a less likely scenario to explain the tentative observations. As the pressure rises, the magnetopause is getting closer to the planet, reducing the space of magnetospheric diluted plasma regions between the magnetopause and atmosphere where radio emission might occur. We therefore conclude that the basic model (vertical gray line) and slightly different configurations represent the most likely scenarios if the emission is indeed generated by stellar wind-driven auroral Poynting fluxes. In this case radio emission is only observable, if the stellar wind and planetary magnetic fields are aligned (i.e., the MS is open). Given the high efficiencies ($\epsilon > 10^{-3}$) needed by our model in order to generate radio emission that is consistent with the tentative observations, the magnetospheric emission scenario might not be energetic enough to explain the observations.

6.5.2.4. Properties, observability and source regions of auroral radio emission

Auroral radio emission is mainly characterized by signal strength and frequency. The peak frequency is defined by the local electron gyrofrequency,

$$\nu_{g,e} = \frac{|e|B}{2\pi m_e} \,, \tag{6.18}$$

where e is the electron charge, m_e its mass and B the local magnetic flux density (Farrell et al. 1999; Grießmeier et al. 2007a,b). We already discussed possible radio powers from τ Boötis b in Sect. 6.5.2.3, now we focus on possible signal frequencies. Turner et al. (2021) observed signals within the 21 – 30 MHz range. The magnetic flux density inferred from the maximal signal frequency by the authors is almost certainly underestimated since ECMI-driven auroral radio emission typically arises from altitudes above the polar regions of the planet's atmosphere (Zarka 1998; Hess & Zarka 2011) due to three reasons: (**a**) High ionospheric electron densities cause the electron plasma frequency, $\nu_{p,e}$, to exceed the local gyro frequency, $\nu_{g,e}$, thus prohibiting the transmission of emitted waves (see discussion below); (**b**) radio wave amplification through the ECMI mechanism works most efficiently in regions where $\nu_{g,e} >> \nu_{p,e}$ (Treumann 2006; Weber et al. 2017) and (**c**) the electrons are usually accelerated in regions where the plasma density along a field line is the smallest (or B/ρ is maximum) (e.g., Saur et al. 2018). There wave particle interaction to accelerate electrons is maximum efficient. The electron plasma frequency is given by

$$\nu_{p,e} = \sqrt{\frac{n_e e^2}{\epsilon_0 m_e}} \frac{1}{2\pi} \,, \tag{6.19}$$

where $n_e = n_i$ is the particle density in a quasi-neutral plasma and ϵ_0 the vacuum permittivity. The source regions of Jupiter's radio emission lie several planetary radii above the surface (e.g., Zarka 1998) where strongest electron acceleration is expected (e.g., Mauk et al. 2017). The maximum gyro frequency in our model (directly above

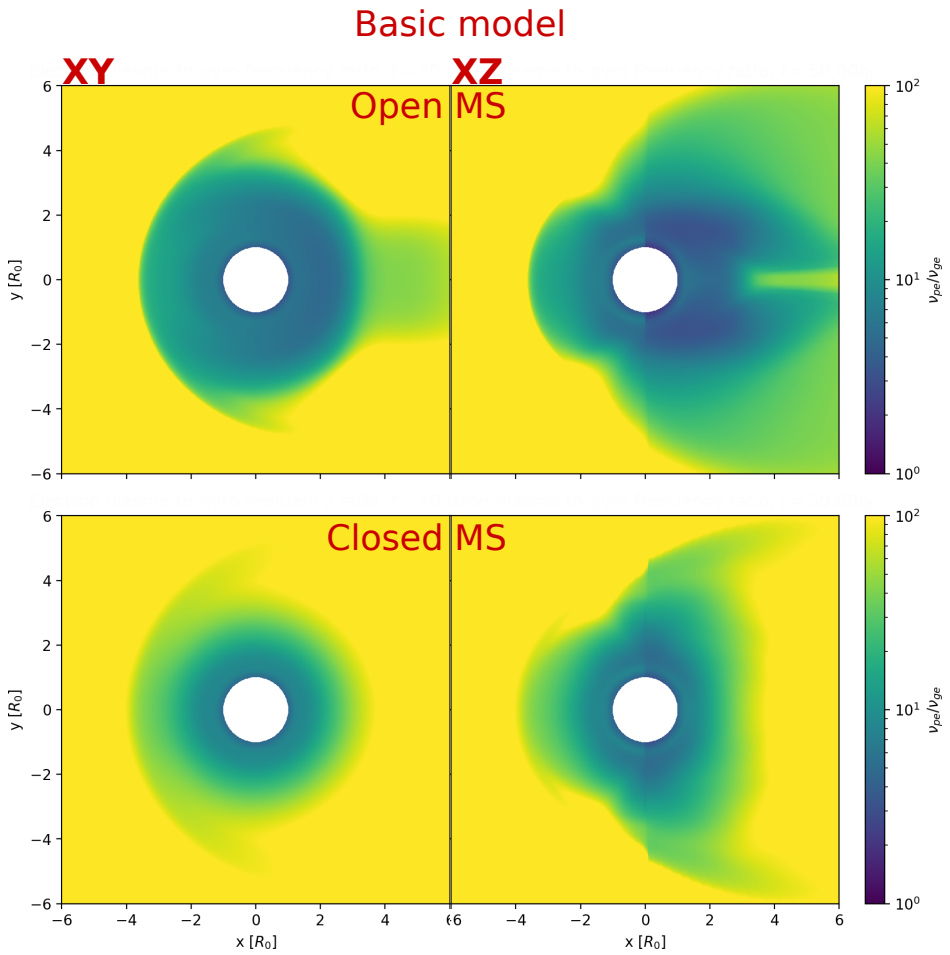

Figure 6.8.: Shown are ratios between electron plasma (Eq. 6.19) and gyro frequency (6.18) in the basic model (Sect. 6.2). Left and right panels show cuts through the xy– and xz–plane, respectively. Upper panels correspond to the open MS, bottom panels to the closed MS scenario. Results for the lowest density stellar wind model are shown in 6.9.

the magnetic poles) is $\sim$ 24 MHz. Auroral emission, however, typically arises from near the OCFB. In our simulations we indeed see that strongest Poynting fluxes are confined to narrow bands encircling the OCFB (or magnetopause) near L=3 and L=3.5 shell field lines (Fig. 6.3). Since source regions of ECMI induced emission typically lie at higher altitudes the magnetic flux density and thus emission frequency is even further reduced. The conditions (**a**–**c**) for efficient ECMI-driven radio emission might particularly be fulfilled for regions with low plasma density at the night side of the planet where the shadow exerted by the planet prevents photo–ionization. Since τ Boötis b is likely in tidally locked rotation around its host star, the night side might exhibit relatively low temperatures, favoring a recombination of electrons and hydrogen ions as well as further electron capture processes. In the shadow zone (i.e., permanent night side of the

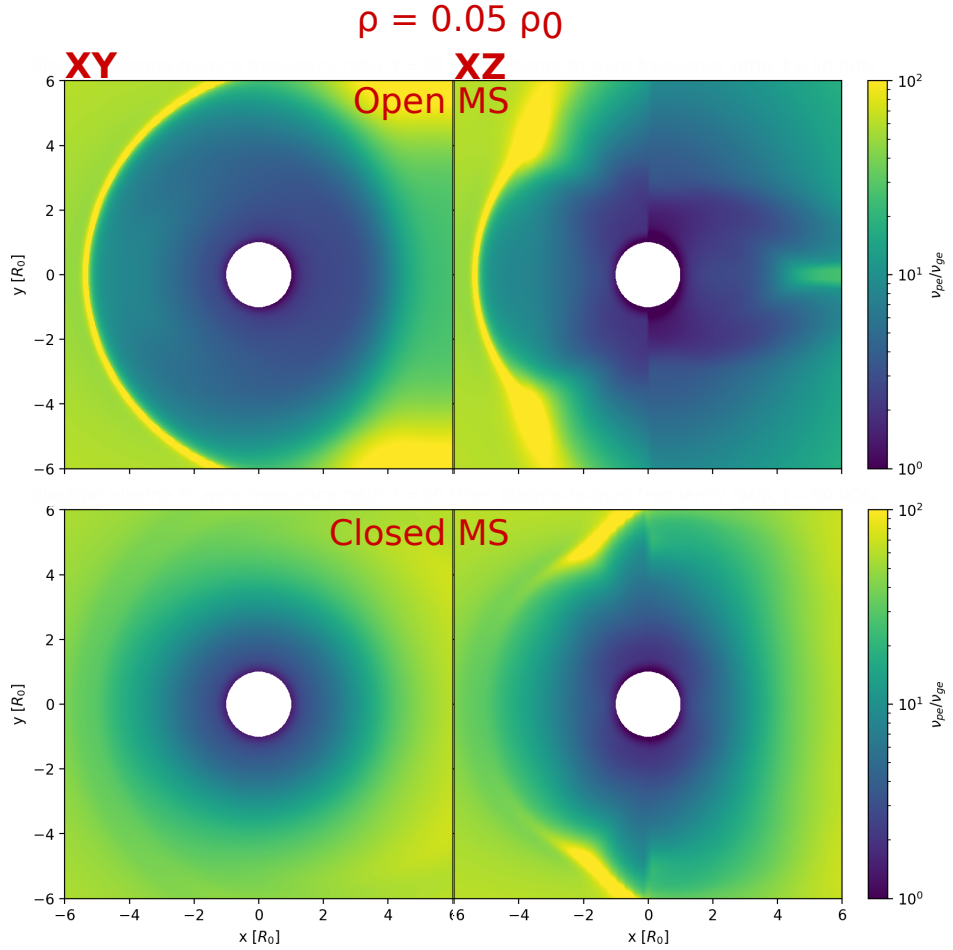

Figure 6.9.: Same caption as in Fig. 6.8 but for the lowest density stellar wind model ($\rho = 0.05\,\rho_0$).

planet), ECMI induced emission might be more likely and might as well occur in lower altitudes, where the magnetic field is stronger (and thus emission frequency is higher).

To assess the possible source regions of radio emission from the magnetosphere of τ Boötis b we need to compare the electron plasma with the electron gyro frequency (condition **a**). The refractive index of a plasma is defined by (Wilson et al. 2009)

$$n = \sqrt{1 - \frac{\nu_{pe}^2}{\nu^2}}\,, \tag{6.20}$$

with the respective electromagnetic wave frequency of interest, ν. For radio waves generated by the ECMI mechanism with a frequency defined by the local gyro frequency, we can replace ν with Eq. 6.18. Therefore, when the gyro frequency is smaller than the plasma frequency the refractive index n becomes imaginary due to the negative square

root. In this case the radio waves are reflected completely and thus can not pass the local plasma environment. In Figs. 6.8 and 6.9 we show the ratio ν_{pe}/ν_{ge} in the basic model (6.8) and lowest density stellar wind scenario (6.9). In our simulations we find that only with the lowest stellar wind density considered a small shell directly above the planet exists (up to $\approx 1.1 R_p$). Only radio waves emitted in this region have a gyro frequency above the local plasma frequency and may escape the planet's vicinity. As the plasma frequency decreases with distance from the planet, it is ensured that the respective gyro frequency remains greater that the plasma freuquency anywhere within the magnetosphere. In all models with higher stellar wind density radio emission could not escape and additionally, since $\nu_{ge} \approx \nu_{pe}$, the ECMI mechanism would not function at considerably high efficiency (Treumann 2006; Weber et al. 2017). We note again that, when including a planetary shadow in our model the nightside electron densities may be considerably lower thus favoring the escape of radio emission at the night side. But in summary, according to our model, radio emission could not escape the planet's vicinity unless the stellar wind density is reduced by almost two orders of magnitude relative to the basic model proposed by (Nicholson et al. 2016).

6.6. Summary

In this study we modeled the magnetosphere of the Hot Jupiter exoplanet τ Boötis b and its interaction with the stellar wind. In order to study magnetospheric energetics by means of Poynting fluxes we performed MHD simulations of the near space environment of τ Boötis b with the stellar wind being injected into the simulation domain. The magnetic field of τ Boötis b is constrained by tentative observations of auroral radio emission Turner et al. (2021). The stellar wind model is based on simulations where observed magnetic surface maps of τ Boötis A were utilized Nicholson et al. (2016); Vidotto et al. (2012). We investigated magnetospheric energetics, available electromagnetic power and limits of possible radio emission originating from above the planet's polar regions. The effect of stellar wind variability in terms of density, pressure and magnetic field orientation on magnetospheric energetics was additionally investigated.

We find that the stellar wind-magnetosphere interaction is super-fast and super-Alfvénic for the whole range of stellar wind densities and pressures considered in this study (from $7 \times 10^{10}\, H^+\, m^{-3}$ and 1.3×10^{-5} Pa to arbitrarily high stellar wind densities and pressures). Maximum available electromagnetic energy convected within the magnetosphere amounts to $3.5{\times}10^{18}$ W, $1.8{\times}10^{18}$ W and $7{\times}10^{17}$ W for an open, semi-open and closed magnetosphere configuration. Auroral Poynting fluxes at altitudes of $1 R_p$ above the planet reach powers of $8.7{\times}10^{17}$ W down to $1.1{\times}10^{17}$ W for the open and closed magnetosphere, indicating a strong decrease of stellar wind energy converted to magnetospheric Poynting fluxes as a function of magnetic field tilt (either stellar or planetary).

We present Poynting flux maps of the planet's near space environment. Strongest

fluxes are confined to a narrow band encircling the open-closed field line boundary (i.e. the magnetopause) that is displaced towards the planet's downstream side due to the magnetic stresses exerted by the stellar wind and its high plasma β. Electromagnetic energy transported along field line perturbations are as well confined to a band near the magnetopause and the polar open-field line regions.

Considering the stellar wind density as free parameter, we choose values between 0.05 and 100 times the basic density, $\rho_{sw} = 1.4 \times 10^{12}\ H^{+}m^{-3}$ (Table 6.1), and change the stellar wind pressure in the same manner in order to keep the wind isothermal. Comparing the incident total energy flux convected through the magnetospheric cross section, we find that the transfer function T_a (i.e. the amount of stellar wind incident energy flux converted to magnetospheric Poynting fluxes parallel to unperturbed field lines) amounts to a fraction of roughly 20 % for the open and 2% for the closed MS. We find that $T_a \propto \rho_0^{-0.06}$ and $T_a \propto \rho_0^{0.57}$ for the open and closed MS respectively in the density range $7{\times}10^{11}$ – $2{\times}10^{13}$ $\mathrm{H}^{+}\,m^{-3}$. Increasing stellar wind ram and thermal pressure and thus incident energy flux causes a shrinking of the magnetosphere. The reduced capability of the MS for receiving stellar wind energy is outperformed by the increasing pressure and density. The scaling of T_a and thus energy output of the magnetosphere nearly stagnates from that point on where the magnetopause turns so small that the planetary atmosphere starts to interact with pre-bow shock and magnetosheath flow.

We considered several efficiencies for conversion of auroral Poynting fluxes to radio emission and compared the results with observations together with theoretical limits based on the tentative observations by Turner et al. (2021). We find that generation of radio emission near τ Boötis b is either more efficient ($\epsilon_a \approx 1$–5×10^{-3}) compared to Jupiter ($\approx 10^{-4}$) Saur et al. (2021) or the radio emission can not originate from τ Boötis b according to our model. Furthermore, we assessed the the possibility of radio emission to escape the planet's vicinity and we found that, according to our model, radio emission could only escape the magnetosphere when the stellar wind density is reduced by a factor of 20 compared to the basic model (Nicholson et al. 2016).

Furthermore we find a strong dependence of radio emission observability on magnetosphere topology. In case of a polarity reversal of τ Boötis A's magnetic field from an aligned to anti-aligned (with respect to the planetary field) configuration, the estimated radio power falls below the observational limit. We therefore expect an on–off nature of detectable radio emission in phase with τ Boötis A's magnetic cycle.

7. Space weather around the Trappist-1 planets

7.1. Introduction

In this chapter we present our modeling approach and results of the Trappist-1 project, introduced in Sect. 4.2. We pursue our project goals described in Sect. 4.2 by applying a time–dependent MHD model of CME–planet interactions. Our CME models incorporate pulse–like interplanetary shock waves and trailing high velocity and density plasma as well as CMEs with intrinsic magnetic flux rope. Magnetic variability generated by the CME–planet interactions is used as a basis for an interior Joule heating model. By modeling purely mechanical and mixed mechanical–magnetic CMEs we are able to assess the planets and its magnetosphere's energy intake and conversion towards magnetic variability at the planet's surface. We aim to better understand the time–dependent energetics in the space environment of close–in terrestrial exoplanets that are exposed to strong space weathering and assess in detail the role of planetary magnetic fields in shielding the planets energetically from their environment. We aim to pave the way for a clearer understanding of close–in exoplanet energetics and how they differ considerably from interactions we know from the solar system.

In Sect. 7.2 we introduce our MHD model including the magnetic field (Sect. 7.2.1) and atmosphere model (7.2.2) followed by a detailed description of our CME models (Sect. 7.2.4 and subsequent sections). We present results for single CME events, magnetospheric structure and resulting heating of the interior in Sect. 7.4, followed by a discussion on the interaction energetics in Sect. 7.5. In Sect. 7.6 we discuss the effect of CME–associated flare energy on interior heating and the corresponding scaling of heating with energy and planetary magnetic field. Lastly we discuss possible long–term and observational effects of CME–planet interactions in Sect. 7.7.

7.2. MHD model

In order to model the space environment of the Trappist-1 exoplanets and their interaction with the time–variable stellar environment we make use of the MHD model presented in Sect. 5. We adopted the model to the Trappist-1 planets (Sect. 7.2.1–7.2.3) and implemented coronal mass ejection models described in Sect. 7.2.4.

Table 7.1.: Physical simulation parameters. Details of the stellar wind, planet and atmosphere model are discussed in Sects. 7.2.1, 7.2.2 and 7.2.3. Parameters are given in Cartesian coordinates where the x–axis is parallel to the the star–planet line. The z–axis is parallel to the orbital plane and planetary magnetic moment. The y–axis completes the right–handed coordinate system.

	Symbol	**Tr-1 b**	**Tr-1 e**	Ref.
Planet				
Planet radius	R_p	6926.9 km	5855.2 km	1,2
Orbital period	P_{orb}	1.51 d	6.09 d	1
Semi-major axis	a	0.011 au	0.028 au	1
Stellar wind				
Therm. pressure	p_{sw}	1.83E−6 Pa	1.01E−7 Pa	3
Ion density	n_{sw}	6.59E+10 m^{-3}	5.79E+9 m^{-3}	3
Velocity	$\vec{v}_{sw}$	$(-470, 80, -1)$ km s^{-1}	$(-604, 50, 3)$ km s^{-1}	3
Magnetic flux density	B_{sw}	$(381, 81, -147)$ nT	$(-149, 13, -42)$ nT	3
Atmosphere				
Surface density	$n_{O_2,0}$	-	8e12 m^{-3}	
Scale height	H	-	0.06 R_p	
H^+–O_2 cross sect.	σ_c	-	2e19 m^2	
H^+–O_2 coll. freq.	ν_c	-	≈ 1 s^{-1}	
Photo–ion. freq.	ν_{ph}	-	6.43e-5 s^{-1}	
Recombination rate	α_r	-	5e-14 m^3 s^{-1}	

[1] Gillon et al. (2017)
[2] Turbet et al. (2020)
[3] Dong et al. (2018)

7.2.1. Planet and magnetic field model

We chose the Trappist-1b and e planets as targets for our study. At Trappist-1b the CME-planet interaction is most energetic due to the proximity to the star and Trappist-1e is of particular interest for atmosphere and habitability studies and is the target of numerous ongoing and future JWST campaigns. We take the inner boundary of the simulation domain as the planetary surface which acts as outflow boundary for all plasma variables (see Sect. 5.4) and as special boundary condition for the dynamo magnetic field described in Sect. 5.2.5. We used the planetary radii of Trappist-1b and e as well as their semi–major axes from the literature (Gillon et al. 2017; Turbet et al. 2020). The planetary parameters are listed in Table 7.1.
Although only tentative observations of exoplanetary magnetic fields exist (Turner et al. 2021), three of four terrestrial planets in our Solar system have or had intrinsic magnetic fields (e.g. Mars Mittelholz et al. 2020). Therefore, our study also includes an investigation of the roles of exoplanetary magnetic fields on the CME–planet interaction and CME energy dissipation within the planets. We assume purely dipolar planetary magnetic fields with magnetic moments parallel to the planetary rotation axis, and per-

pendicular to the orbital plane. To reduce the computing time, Equatorial strengths between $B_p = 0$ G and $B_p = 0.21$ G are used (for reference, Earth's equatorial magnetic field strength is $\approx 0.4 - 0.5$ G). In order to put our range of magnetic fields into perspective of what to expect for Tr-1b and e, we estimate the planetary magnetic moments using a dynamo scaling law suited for tidally locked planets (Stevenson et al. 1983; Samara et al. 2021),

$$M = 3.45 \times 10^5 \mathtt{A} \cdot \mathtt{s} \cdot \mathtt{kg}^{-0.5} \rho_c^{1/2} \omega^{1/2} R_c^3 \sigma^{-1/2} \,, \tag{7.1}$$

where ρ_c is the core mass density, R_c the core radius, ω the planet rotation period and σ the core's electric conductivity. We assume the core density to be equal to the planet's mean density ,$R_c = 0.48\ R_p$ (Grayver et al. 2022; Agol et al. 2021) for both planets and $\sigma = 10^6\,\mathrm{Sm}^{-1}$ (Grayver et al. 2022). The rotation period is set to the planet's orbital period since we assume tidal locking (Table 7.1). For Trappist-1b and e the resulting equatorial magnetic flux densities are $B_p^b = 0.24$ G and $B_p^e = 0.12$ G, respectively. The expected magnetic field of Trappist-1e lies well within our parameter range while the magnetic field of Trappist-1b lies above our maximum value due to its faster rotation. However, we point out that recent dynamo scaling laws propose a weak scaling of magnetic field strength with rotation and indicate the importance of buoyant heat flux within the dynamo region (Christensen et al. 2009). The anatomy of planetary interiors highly depends on several factors including the formation history of planets which is currently unknown.
The planetary magnetic fields are implemented using the insulating–boundary method by Duling et al. (2014) which ensures that magnetospheric currents do not close within the planetary surface (see also Sect. 5.2.5).

7.2.2. Atmosphere model

In our basic model we assume the planets to not possess any atmospheres. This assumption is most likely true for Trappist-1b, corroborated by newest JWST secondary eclipse observations (Greene et al. 2023). The existence of an atmosphere on Trappist-1e is neither proven nor refuted.

Therefore we also study the effect of thin atmospheres on magnetic variability and CME energy dissipation within and around Trappist-1e. For this purpose we implement a radially symmetric upper atmosphere composed of molecular oxygen O_2 (see Sect. 5.2.1 for the model description). This assumption is based on the study of Bourrier et al. (2017a) who have estimated XUV induced atmospheric loss of H and O_2 due to photo–dissociation of H_2O (Krissansen-Totton & Fortney 2022). The proposed low density of Trappist-1e may indeed indicate a substantial amount of H_2O present within its mantle and crust (Barr et al. 2018). We assume an O_2 atmosphere due to the mass loss rates of this species being a factor of five greater than for hydrogen and due to its larger collisional cross section. We include a plasma production as well as loss by the photo–ionization and dissociative recombination as described in Sect. 5.2.1.
Given the mass loss rate proposed by Bourrier et al. (2017a), $\dot{M}_{O_2} = 5.7 \times 10^7$ g/s, the

volume of the atmosphere of Trappist-1e, V, and the mass of O_2 molecules, we can solve the following integral,

$$\dot{M}_{O_2} = m_{O_2}\,\nu_{ion}\int_V\int_z n_{O_2}(r)\,d\mathrm{V}\ , \tag{7.2}$$

to calculate the corresponding photo–ionization rate, ν_{ion}. The O_2 number density of the neutral atmosphere, $n_{O_2}(r)$, is given by our model (Eq. 5.5). We integrate equation 7.2 from the surface at R_p to a height z, hence

$$\dot{M}_{O_2} = m_{O_2}\,n_{O_2,0}\,\nu_{ion}\int_{R_p}^{R_p+z}\int_0^{\pi}\int_0^{2\pi} r^2\sin\theta\exp\left(\frac{R_p-r}{H}\right)drd\theta d\phi \tag{7.3}$$

$$\dot{M}_{O_2} = m_{O_2}\,n_{O_2,0}\,\nu_{ion}\,2\pi\left[He^{-\frac{z}{H}}\,C - HR_p^2 - 2R_pH^2 - 2H^3\right]\ , \tag{7.4}$$

with

$$C = R_p^2 + 2R_pz + 2R_pH + z^2 + 2zH + 2H^2\ , \tag{7.5}$$

where H is the atmosphere scale height and z an arbitrary height (due to the decay of $n_n(z)\to 0$ for $z\to\infty$ the value can be chosen arbitrarily high). In the appendix C.1 a detailed derivation of Eq. 7.4 is provided.
We assumed a neutral surface density of $n_{O_2,0} = 8\times10^6\,O_2\,\mathrm{cm}^{-3}$ that corresponds to an atmospheric pressure of about 1 nbar. With this particle density a shell with an increased plasma density is created above the planetary surface and incoming plasma is nearly brought to a halt. Larger surface densities would thus not enhance the strength of the interaction. With a scale height of $H = 0.06\,R_p$ the atmosphere is sufficiently resolved in our grid without making the grid resolution too high which we tested in several simulations with varying scale height.

With the surface neutral density and scale height given we can calculate the photo–ionization rate using Eq. 7.4. Hence we apply a photo–ionization rate of $\beta_{ph} = 6.43\times10^{-5}\,s^{-1}$ that results in the O_2 mass loss rate estimated by Bourrier et al. (2017a). The plasma production model via photo–ionization is given by Eq. 5.7. To model the H^+–O_2 collisions we assume a collisional cross section of $\sigma_c = 2\times10^{-19}$ m^2 (e.g. Johnstone et al. 2018; Duling et al. 2014). The collision frequency ν_n in on the order of $\nu_n\approx 1\,s^{-1}$ (see Eq. 5.6).

Photo–ionization is affected by the planet's shadow. In the full shadow (i.e. umbra) ionization is set to a minimum value of $0.1\cdot\beta_{ph}$ to mimic electron impact ionization in the night side. From the umbra terminator towards the half shadow (i.e. penumbra) terminator β_{ph} increases linearly towards the basic value. The sub–stellar point is approximately equal to the upstream side at co–latitude 90° and longitude 90° (i.e. near the -x axis) (see Fig. 5.1). A full description of the shadow model is provided in Sect. 5.2.4. We note that the neutral species is not simulated and not altered by the interaction, it only affects the production, loss and deceleration of plasma. Dissociative recombination of O_2 ions with free electrons is also included (see Sect. 5.2.3 for a description). Recombination is switched off when the plasma density falls below the background stellar wind density. The recombination rate of O_2 is assumed to be

$\alpha_r = 5 \times 10^{-14}$ m^3 s^{-1} for an ionospheric electron temperature of $T_e = 2500$ K and is calculated using the following formula (Christensen et al. 2012; Walls & Dunn 1974)

$$\alpha_r = 1.6 \times 10^{-7} \left(\frac{300}{T_e} \right)^{0.55} . \tag{7.6}$$

We note that in the range 1500 – 3000 K the variation of the rate coefficient is minor, thus, the value is applicable as a first approximation although the electron temperature near Trappist-1e is not known.
For simulations without an atmosphere the production and loss terms, P and L, as well as the collision frequency ν_n in the MHD equations (Eqs. 5.1–5.4) are set to zero.
All atmospheric and planetary model parameters are listed in Table 7.1.

7.2.3. Stellar wind model

We apply time-independent stellar wind boundary conditions to the in–flow boundary at the upstream hemisphere ($\Phi = 0$ to 180°). Stellar wind plasma parameters were taken from Dong et al. (2018) and are summarized in Table 7.1. For all simulations we chose the maximum total pressure stellar wind parameters from Dong et al. (2018) as the planets are exposed to this wind regime for most of the time according to the model. In contrast to the τ Boötis b project (see Sect. 6) we make use of the complete 3D stellar wind solution and incorporate all magnetic field and velocity vector components. In reality, planets that reside within a super–Alfvénic stellar wind typically experience an inclined stellar wind magnetic field with strong radial components (nearly parallel to the x–axis) due to the typically high plasma β stellar wind flow. The orbital motion of the planets is not included in the relative velocity $\vec{v}_0$, hence all velocity components in Table 7.1 are $\neq 0$. The stellar wind plasma consists purely of hydrogen ions.
As magnetic boundary condition for the stellar wind model of (Dong et al. 2018) a solar magnetic field map under solar minimum condition was used. Trappist-1 is an active M–dwarf star and its nature should be excepted to deviate from the Sun, a G–type star, but the X–Ray luminosity of Trappist-1 is observed to be similar to that of the quit Sun (Bourrier et al. 2017b) which indicates similar magnetic activity. However, we note that we do not aim to develop a realistic model of the Trappist-1 system but rather focus on studying space weather related magnetic variations around close–in terrestrial exoplanets and on improving our understanding on the role of planetary magnetic fields in such interactions.

7.2.4. Coronal mass ejection model

Motivated by solar system CME observations we model two distinct types of CME that can be experienced by a planet. Not all CMEs observed near the Earth show signatures of magnetic flux ropes but it is expected that all CMEs indeed do possess flux ropes, the space probes observing them possibly just miss them entirely (Song et al. 2020; Jian et al. 2006). Without magnetic flux rope one might get the impression that the CME is solely a pulse of high plasma velocity and density, for example. Figure 7.1 gives an

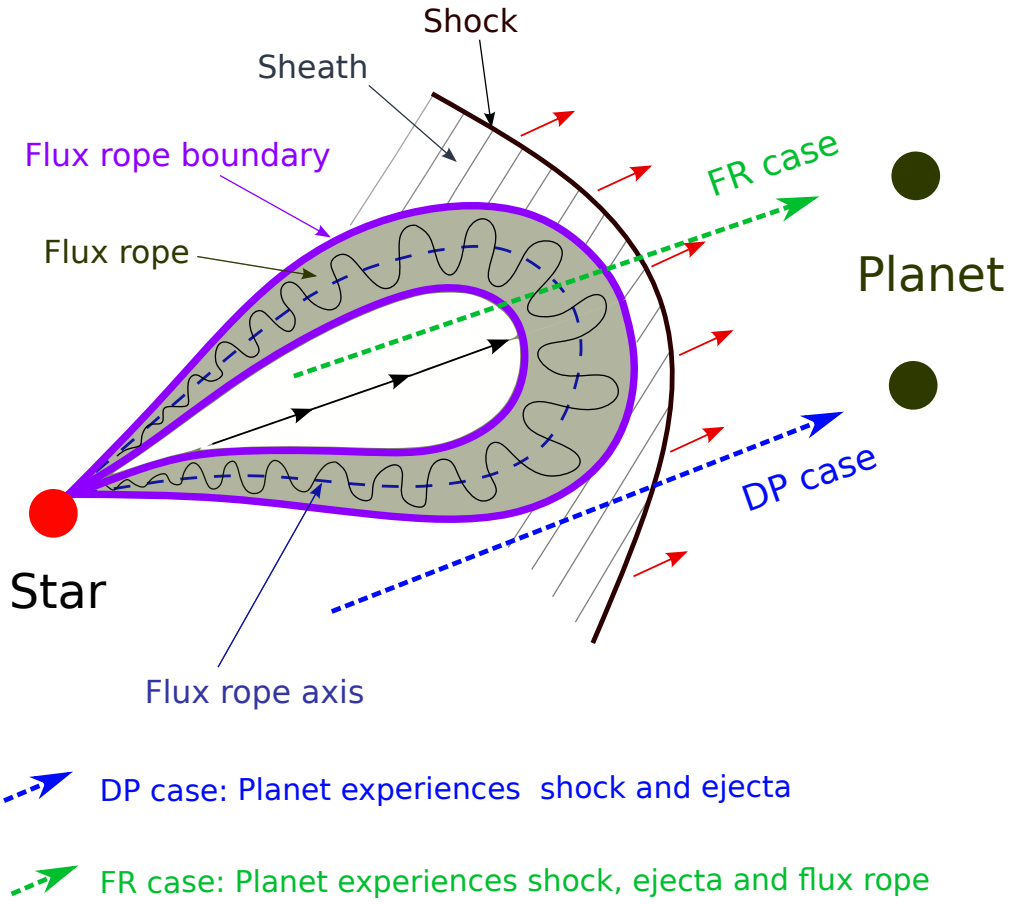

Figure 7.1.: A sketch indicating the motivation behind the DP and FR CME models in this work. In our FR CME simulations the planet experiences the CME shock, sheath and flux rope. In DP CME simulations only the CME shock and sheath hit the planet.

impression of the CME overall structure and that planets may experience different features of the same object. Moreover, short time–scale stellar wind variations from active stars are expected to occur and in the solar system the solar wind density, for example, may nearly instantaneously vary by orders of magnitude (e.g. Chané et al. 2012; Siscoe et al. 1968). With the DP model we also aim to capture these types of stellar events.
In the following sections the two CME models used in our study are described. The density pulse CME model (DP) and flux rope CME model (FR) are described in Sect. 7.2.4.1 and Sect. 7.2.4.2 respectively. In the subsequent sections we describe the initialization and injection of CMEs in our MHD simulations (Sect. 7.2.4.3).

As basic properties of the CMEs we first need their velocities and masses since they are directly connected to the associated flare energy via empirical scaling laws obtained from the Sun (e.g. Sect. 3.4.2).
We constrain the CME total energy density by assuming an associated flare bolometric

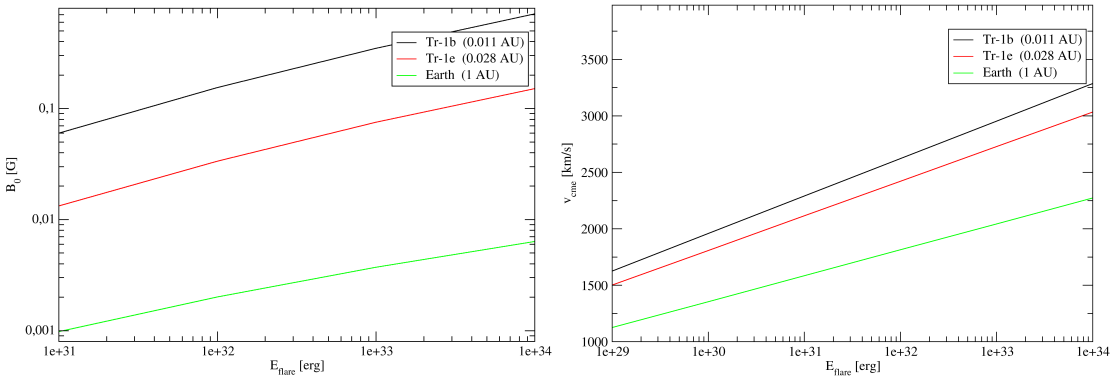

Figure 7.2.: We show the CME axis magnetic field B_0 (left) and CME velocity v_{CME} (right) as function of associated flare energy E_{flare} based on the empirical scaling relations Eqs. 7.7–7.8 and 7.14 for the planets Tr-1b (black), Tr-1e (red) and Earth (green). We propagated the CMEs from the reference distance $D_0 = 10\,R_\star$ to the orbital position of the respective planets by scaling down the CME velocity and magnetic field strength (see Eq. 7.9 and subsequent text).

energy of $E_{bol} = 10^{31}$ erg for the basic model and by using appropriate scaling laws for CME parameters obtained from solar system based flare–CME association studies (Aarnio et al. 2012; Patsourakos & Georgoulis 2017; Kay et al. 2019). According to the flare frequency distribution of Trappist-1 (Howard et al. 2023) flares with bolometric energies of 10^{31} erg occur roughly once per day. For our basic model we use this energy to estimate the CME mass using the scaling law of Aarnio et al. (2012)

$$M_{CME} = 2.7 \times \left(\frac{E_{bol}}{100}\right)^{0.63} \mathrm{g}\,, \tag{7.7}$$

where E_{bol} (erg) is divided by 100 to give the approximate X–Ray energy contained in the bolometric energy following Günther et al. (2020). The estimated mass is then used to calculate the CME velocity according to the scaling law (Kay et al. 2019)

$$v_{CME} = 660 \log M_{CME} - 9475\,\mathrm{km/s}\,. \tag{7.8}$$

Density pulse CMEs are solely characterized by enhanced stellar wind density and velocity, whereas FR CMEs include an intrinsic twisted magnetic structure together with a bulk stellar wind velocity enhancement. The choice of these two models is based on the fact that, depending on which part of a CME the planet intersects, it may experience the CME shock and ejecta or the shock together with the flux rope. In Fig. 7.1 we illustrate this idea. We note that in this work we refer to sheath and ejecta as a similar structure. The sheath denotes the part of the CME that lies between the shock and flux rope. With ejecta we refer to the CME part that follows the shock but with no flux rope behind. In this work we use the terms synonymously. Observational evidence from the Solar system suggests that all interplanetary CMEs should have a flux rope structure, but depending on the location of space probes in the solar wind, they may miss the flux rope structure completely (Song et al. 2020).

However, the major motivation behind our choice of a density pulse CME as well as a flux rope CME is to divide the external forcing the planets are exposed to into a purely mechanical (DP) and combined mechanical and magnetic (FR) perturbation. With these distinctive models we are able to study the conversion of different forms of energy from the CME towards magnetic variability at the planetary surface. We can then dissect the role of planetary magnetic fields to channel energy towards the planet and wether they act as catalyst or inhibitor for interaction generated energy fluxes.

The CME parameters described above correspond to a CME shortly after ejection from the stellar corona. We propagate the CMEs to the planetary orbits by using CME evolution parameters summarized in (Scolini et al. 2021). In general, CME parameters as a function of distance from a reference distance D_0 follow the scaling law of the form

$$q(D) = q_0 \, (D/D_0)^{\alpha} \, , \tag{7.9}$$

where q is either velocity v, density ρ or magnetic field B and D is the distance from D_0. We assume D_0 to be at $D_0 = 10\,R_{star}$. From there we propagate the velocity according to $v \propto D^{0.05}$ and the magnetic field according to $B \propto D^{-1.6}$ (Scolini et al. 2021) to the corresponding planetary orbit (the semi–major axes are listed in Table 7.1). Figure 7.2 shows the evolution of CME velocity and magnetic field across the heliosphere at Trappist-1b, e and Earth to illustrate the significant drop of CME kinetic and magnetic energy with distance traveled. Figure 7.2 elucidates that, for example, a CME with associated flare energy of 10^{34} erg incident on the Earth has a comparable velocity and a much lower magnetic field strength than a CME with $E_{flare} = 10^{32}$ erg at Trappist-1b. This shows how significantly the proximity to the star intensifies the space weather for close–in planets, even if there were statistically weaker flares and associated CMEs.
The DP CME density is calculated in such a way that the magnetic and kinetic energy density of the FR CME (with only the velocity and magnetic field enhanced) are equal to the kinetic energy density of the DP CME. For the FR CME the density is set to the background stellar wind density. This way both CMEs have the same total energy density. This leads to the CME density not following the density decay observed in the solar system.

Lastly, due to computational cost of time–dependent high resolution simulations we constrain the CME event duration to one hour. The external and internal timescales, i.e. background plasma convection time across the planet and Alfvén time within the magnetosphere, allow the magnetosphere to respond properly to the changes in the upstream plasma conditions.

7.2.4.1. Density pulse CME model

We model the density pulse CME by enhancing the background stellar wind plasma parameters according to a Gaussian profile constrained by the CME front, x_{front}, and rear, x_{rear}, position along the x–axis. The length between these two positions is defined by the maximum CME velocity (7.8) and an event duration of one hour. The DP model

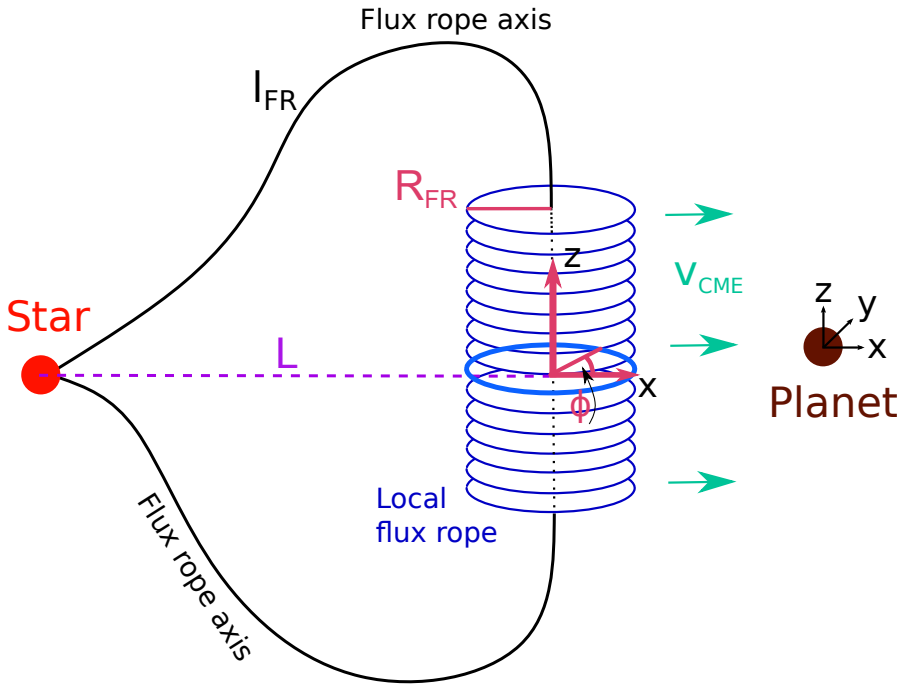

Figure 7.3.: Schematic illustrating the basic geometrical properties of the flux rope CME model discussed in the FR model section 7.2.4.2. Also indicated are the planet–centered Cartesian coordinate system in which all boundary conditions are specified and the flux rope–centered cylindrical coordinate system in which the flux rope model is formulated (Eq. 7.11).

profile follows

$$q(x) = q_0 + q_{max} \cdot \exp\left(-\frac{1}{2}\frac{(x - x_c)^2}{\hat{D}^2}\right) , \tag{7.10}$$

where q is either the plasma density ρ or the velocity v. The quantity q_0 is the steady state stellar wind value and q_{max} is the maximum enhancement of the given quantity. $\hat{D}$ is the characteristic decay parameter defining the shape of the Gaussian curve. The value of $\hat{D}$ is determined by finding a CME profile that completely fills the space between CME rear and front position (see a summary of the CME shape parameters Table 7.2). x_c is simply the midpoint between rear and front. Pulses of enhanced stellar wind parameters with the enhancements spatially following a sinusoidal or similar profile in CME simulations have been applied in numerous studies (e.g. Biondo et al. 2021; Hosteaux et al. 2019; Pomoell & Poedts 2018; Riley et al. 2016; Chané et al. 2006; Odstrcil & Pizzo 1999).

7.2.4.2. Flux rope CME model

We use the non–linear, force–free uniform twist Gold & Hoyle flux rope CME model (Gold & Hoyle 1960) to describe the interplanetary magnetic flux rope. The magnetic

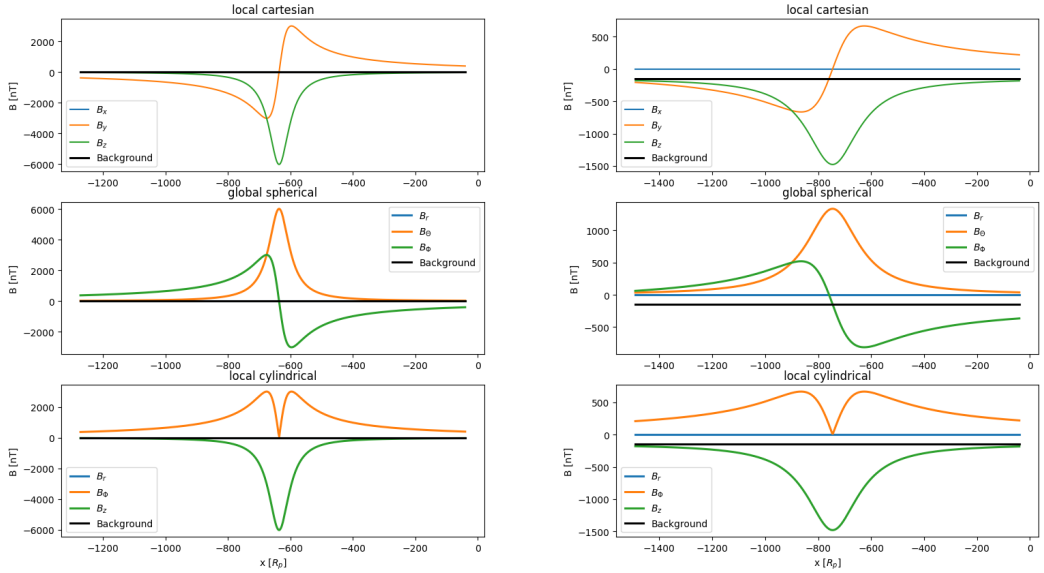

Figure 7.4.: Shown are magnetic field profiles of the flux rope before the CME is released to propagate towards the planet (positive x) for Trappist-1b (left) and e (right). The flux rope model (Eq. 7.11) is given in cylindrical coordinates centered around the FR axis (bottom panel). The magnetic field components are then converted to the global spherical coordinate system (middle panel) and then to the Cartesian coordinate system in which all boundary conditions are specified (see 5.1.1). Also shown is the magnitude of the background stellar wind magnetic field (black line).

field components in flux rope–centered cylindrical coordinates are

$$B_r = 0 \tag{7.11}$$

$$B_\phi = \frac{Tr}{1+T^2r^2}B_0 \tag{7.12}$$

$$B_z = \frac{1}{1+T^2r^2}B_0\ , \tag{7.13}$$

where T is the twist parameter, r the distance from the flux rope axis and B_0 the maximum magnetic flux density along the axis. The twist parameter, $T = 2\pi n/l$, depends on the axis length l and on the number of turns n along the axis (Wang et al. 2016). The axial length ranges from $2L$ (i.e. the axis is parallel to CME nose–star line) to $\pi \cdot L$ (i.e. flux rope axis connects via a full circle with the star), where L is the heliocentric distance of the CME nose from the star. See Fig. 7.3 for a sketch of all important geometrical CME parameters. At 1 AU l is approximately 2.6 AU (Démoulin et al. 2016). We assume $l = 2.6\,L$ in our simulations. The number of turns $n = 10$ together with $l = 2.6\,L$ is chosen so that a clear helical magnetic field structure can be seen on the cross-sectional width of the CMEs modeled here. The number of turns is

the same for CMEs at Trappist-1b and e due to the conservation of magnetic helicity. We obtain the axial magnetic flux density B_0 by estimating the flux rope's magnetic helicity using a scaling law (Patsourakos & Georgoulis 2017; Tziotziou et al. 2012),

$$\log H_m = 53.4 - 0.0524\,(\log E_{bol})^{0.653} \exp\left(\frac{97.45}{\log E_{bol}}\right) . \tag{7.14}$$

From the estimated magnetic helicity H_m we calculate the axial magnetic flux density B_0 using the solution of the magnetic helicity integral for the Gold & Hoyle flux rope. The solution is given by the following equation (Dasso et al. 2006),

$$\frac{H_m}{L} = \frac{\pi B_0^2}{2T^3}\left[\ln\left(1+T^2R^2\right)\right]^2 , \tag{7.15}$$

where R is the radius of the flux rope. We choose R in such a way that the CME event experienced by the planet has a duration of 1 hour, therefore R is determined by the CME velocity (Eq. 7.8) and the event duration of one hour. The axial FR magnetic field and the most important CME shape parameters are summarized in Table 7.2.
In Fig. 7.4 we show the initial magnetic field components of the flux rope according to $E_{flare} = 10^{31}$ erg at Trappist-1b and e before the CME is released. Most of the profile is initialized outside the simulation domain. The inflow simulation boundary lies approximately at $x = -400_p$. The figure shows the FR magnetic field components in cylindrical (centered around FR, Eq. 7.11), spherical (centered around planet) and Cartesian coordinates.

7.2.4.3. Simulation procedure and CME injection

We inject the interplanetary CMEs through time–dependent boundary conditions exerted on the inflow boundary at the upstream hemisphere ($\Phi = 0$ to $180°$). First we run the simulation with constant stellar wind boundary conditions until a quasi–steady state is reached. Except for minor oscillations near the flanks of the planetary magnetospheres steady state is reached after about 2 minutes. Then we initialize the CME by superimposing its plasma parameters onto the background stellar wind and upstream boundary conditions. This superposition is confined to x–positions between $-40\ R_p$ and $-420\ R_p$ at the upstream boundary. The CME then propagates towards the planet as the simulation progresses. The rest of the CME is injected through boundary conditions whose fixed parameters follow the CME front position that starts at $-40\ R_p$ with the local CME velocity directed parallel to the x–axis. The CME rear, x_{rear}, is defined by the CME duration (1 hour) and maximum velocity. Boundary conditions at boundary cells with $x < x_{rear}$ (behind the rear of the CME) are set to the steady state stellar wind parameters. When the rear of the CME reaches the planet, i.e. $x_{rear} >= 0$, the CME is switched off. With this setup the CME propagates as a structure with length $|x_{rear}| + |x_{front}|$ along the x–axis across the simulation domain while its lateral extend along y and z reach beyond the simulation boundary. The CME plasma flow is super–fast magnetosonic, therefore a shock front builds up as the CME propagates towards the planet. This results in CME durations slightly shorter than 1 hour due to a plasma

Table 7.2.: Physical (top) and shape parameters (bottom) of the CME models.

Trappist-1e	**DP**			**FR**		
E_{flare}	B_{cme} [G]	v_{cme} [km/s]	ρ_{cme} $[H^+m^{-3}]$	B_{cme}	v_{cme}	ρ_{cme}
10^{29} erg	-	1501.4	3.47e6	1.28e-3	1501.4	-
10^{30} erg	-	1807.98	2.99e7	4.53e-3	1807.98	-
10^{31} erg	-	2114.56	1.88e8	1.33e-2	2114.56	-
10^{32} erg	-	2421.13	9.19e8	3.37e-2	2421.13	-
10^{33} erg	-	2727.71	3.61e9	7.51e-2	2727.71	-
CME Shape						
E_{flare}	$\hat{D}$ $[R_p]$	R_{cme} $[R_p]$		T $[m^{-1}]$		
10^{29} erg	210	932.1		1.43e-11		
10^{30} erg	250	1111.6		1.43e-11		
10^{31} erg	310	1300.1		1.43e-11		
10^{32} erg	340	1488.6		1.43e-11		
10^{33} erg	380	1577.1		1.43e-11		

Trappist-1b	**DP**			**FR**		
E_{flare}	B_{cme} [G]	v_{cme} [km/s]	ρ_{cme} $[H^+m^{-3}]$	B_{cme}	v_{cme}	ρ_{cme}
10^{31} erg	-	2290.23	3.29e9	6.02e-2	2290.23	-
CME Shape						
E_{flare}	$\hat{D}$ $[R_p]$	R_{cme} $[R_p]$		T $[m^{-1}]$		
10^{31} erg	270	1191.8		3.64e-11		

compression. Our models produce CME shocks and profiles similar to previous modeling studies (Hosteaux et al. 2019; Chané et al. 2006) as well as combined observational and theoretical studies (Desai et al. 2020; Scolini et al. 2021).

7.2.5. Numerical model

We use the numerical setup already described in Sect. 5.6. Du to the extreme physical conditions in our time–dependent simulations due to CMEs with high velocity we needed to more aggressively enforce the $\nabla \cdot \vec{B} = 0$ condition. Thus tn the Trappist-1 model the $\nabla \cdot \vec{B} = 0$ condition was ensured by the extended mixed hyperbolic–parabolic divergence cleaning technique (Dedner et al. 2002; Mignone et al. 2010).
The spherical grid consists of 380 non–equidistant radial, 96 angular non–equidistant and 72 equally spaced angular grid cells in ϕ and θ dimension respectively. The radial grid is divided into three regions. From 1 to 1.2 planetary radii (R_p) the grid contains 10 uniform cells. After that from 1.2 to 12 R_p the next 150 cells increase in size with a factor of ≈ 1.01 per cell. The last 96 cells from 12 R_p towards the outer boundary

at 420 R_p increase gradually with a factor of ≈ 1.02. We reduce the angular resolution in ϕ dimension gradually from the highest resolution near the planetary equator to the poles with a factor of 1.02 in order to lower the time step constraint on grid cells near the polar axis. We chose a simulation regime that large to avoid any interaction of the altered planetary environment and interplanetary CME magnetic structure with the outer boundary.

7.3. Modeled CME structure

In this section we give an overview of the modeled CMEs and take a look at the physical parameter profiles experienced by the planet. We furthermore describe the shape of the CMEs and subdivide their overall structure into two regimes that are of significance for the subsequent sections.
In Fig. 7.5 we show time series of the CME plasma parameters obtained immediately before the planetary bow shock. In all profiles we can distinguish several parts of the CME: The CME shock reaches the planetary bow shock at about 30 min physical time after the start of the simulation. The shock is evident by a sharp increase in velocity, density and pressure. In the sheath region after the shock, the magnetic field either follows the FR CME profile (upper plots of the right panels) without steep increase of there is no significant magnetic field enhancement at all (DP scenario, upper plots of the left panels). Within the CME sheath the enhanced plasma variables decay slightly. After the sheath at about 43 ($E_{flare} = 10^{31}$ erg) to 63 min ($E_{flare} = 10^{33}$ erg) physical time, the CME peak follows. The peak is characterized by a sharp increase in velocity (up to the maximum CME velocity shown in Table 7.2). Plasma density and pressure are decreased significantly which can be attributed to plasma rarefaction behind the leading fast moving CME front. The peak is more defined by its front rather than its duration. From this point all plasma parameters decay. We refer to this region as the CME tail. We note that we did not simulate the whole decay phase as well as the associated magnetosphere recovery phase due to time reasons. However, the geoeffectiveness of the CME and thus the interaction strength with the magnetosphere is concentrated on the shock, sheath and parts of the CME peak which we will show at a later convenience. Without simulating the full recovery phase we nevertheless capture all important aspects of the interaction energetics, which is the aim of this study.

In our CME models the flux ropes are embedded in the CME sheath region between shock and peak. In Fig. 7.6 we show a top view (xy–plane) of the FR CME approaching and propagating past the planet. There the distinct CME regimes, sheath, flux rope, and peak (lowest magnetic field strength) are visible. During the CME peak the velocity is highest, plasma density and thermal pressure are lowest due to rarefaction behind the fast moving CME peak. In the solar system the low density region coincides with the flux rope, which is typical for magnetic clouds. However, we note that, in the solar system, only in about one third of all CMEs the magnetic cloud, flux rope and CME sheath coincide with each other spatially and there are deviations from the classical structure (Kilpua et al. 2013).

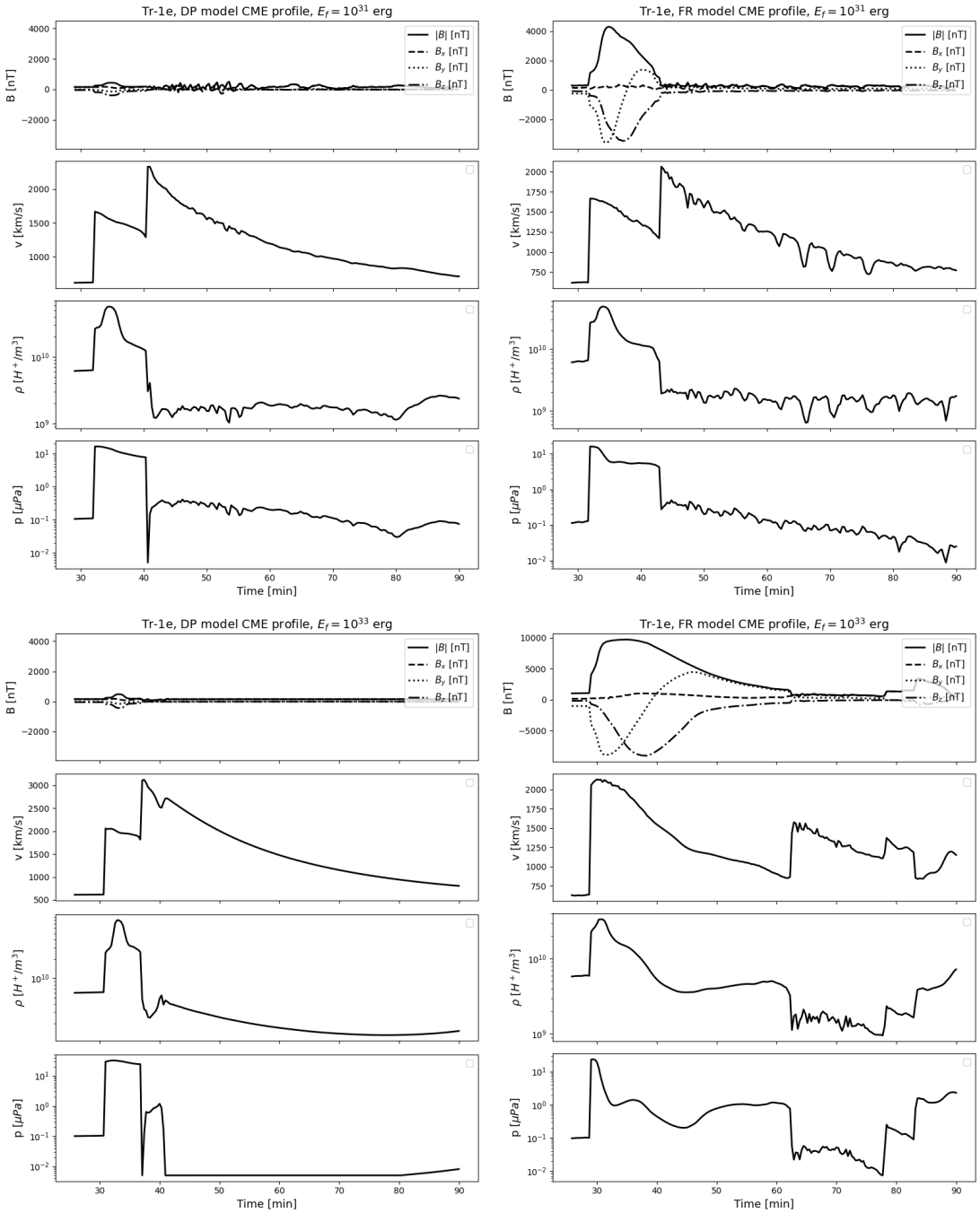

Figure 7.5.: Time series of the unperturbed CME plasma parameters obtained just before bow shock for density pulse CMES (DP, left) and flux rope CMEs (FR, right). The top panels show profiles according to the basic CME model with associated flare energy $E_{flare} = 10^{31}$ erg. The bottom panels show the respective profiles with $E_{flare} = 10^{33}$ erg. Time is given in minutes (x–axis). Of the 4 sub–panels, the upper ones show Cartesian magnetic field components, below them the velocity magnitude, then the mass density and at the bottom the thermal pressure.

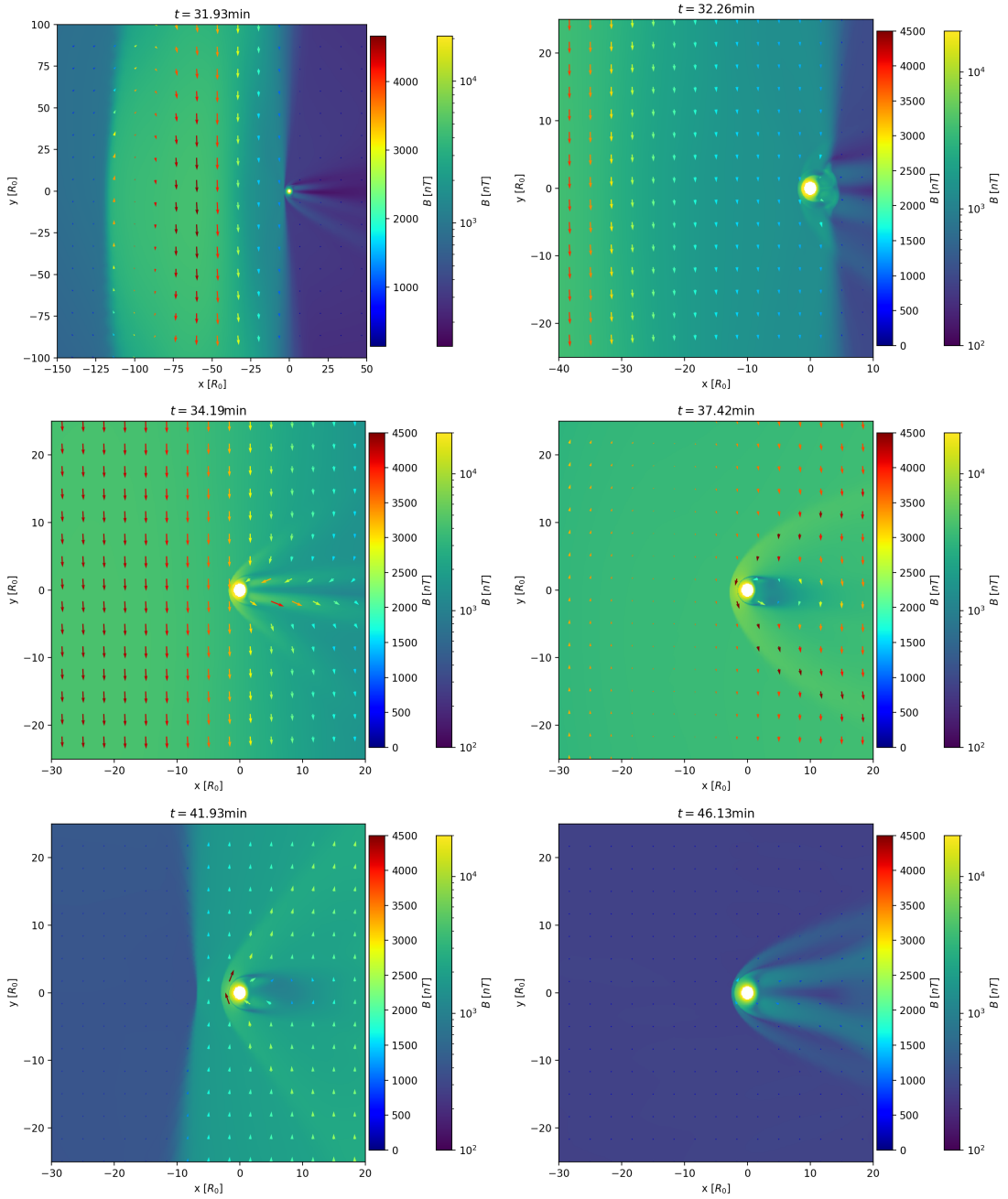

Figure 7.6.: Top view (x–y plane) onto the space environment around Trappist-1e. The CME approaches from the left and propagates in right direction. Arrows depict magnetic field vectors with colors indicating their magnitude (left colorbar). Color contours show the magnetic field magnitude continuously.

7.4. Structure of the interaction and interior Joule heating

In this section we show our simulation results. First we discuss the magnetospheric structure during the CME event in Sect. 7.4.1 followed by the investigation of magnetic variability at the planet surface and resulting interior heating in Sect. 7.4.2.

7.4.1. Structure of the space environment

Here we describe the magnetospheric structure during the CME event as well as the planet's plasma environment for the non–magnetized planet scenario. Cross sections through the xz–plane for DP and FR model runs are displayed in Figs. 7.7 and 7.8 respectively. Planetary magnetic fields weaker than $B_p = 0.05$ G do not withstand the CME's forcing and the magnetopause is compressed to the planet's surface. From $B_p = 0.05$ G to $B_p = 0.21$ G (approximately terrestrial magnetic field) the magnetosphere before the CME has larger sizes from about $R_{mp} = 1.4\ R_p$ ($B_p = 0.05$) to nearly $R_{mp} = 2.6\ R_p$ ($B_p = 0.21$). The difference in magnetopause locations due to different B_p gets significantly smaller during the CME main phase (32 to 43 min). For DP and FR CMEs the minimum magnetosphere positions range from just above $1\,R_p$ ($B_p = 0.05$) to approximately $1.3\,R_p$ ($B_p = 0.21$). There are no significant differences in the magnetosphere compression between DP and FR CMEs due to the high kinetic energy flux contained in both CME models. The kinetic energy scales with the velocity squared v^2 and thus the enhanced velocity adds most energy to the CME. A major difference, however, is the magnetic field structure of the FR CME, where a strong axial component (i.e. parallel to the z–axis) is added to the CME. The stellar wind magnetic field is nearly radial (i.e. parallel to the flow). The CME front compresses the stellar wind field and tends to align it with the shock front, which can be seen in Fig. 7.7. This gives the otherwise radial stellar wind field a dominant z-component (i.e. roughly parallel to the planet's magnetic moment), which facilitates reconnection between stellar wind and planetary magnetic field lines. In Fig. 7.7 it is visible how the ambient magnetic field is rotated towards an aligned configuration (i.e. towards -z). Flux rope CMEs have a purely axial magnetic field in the center with magnetic field components becoming toroidal (i.e. within the x–y plane) towards the FR boundary. In Fig. 7.8 the stronger axial field component of the FR CME compared to DP CMEs is visible and towards the CME center the z–component increases. This enhances the reconnection efficiency between ambient and planetary magnetic field. As field lines merge at the upstream side and reconnect at the downstream side after the field is convected across the planet by the plasma flow, high tension on downstream field lines stores magnetic energy and, by releasing it during the reconnection, accelerates plasma towards the planet and away from it. This can be seen in Figs. 7.7 and 7.8 indicated by high velocities in the planet's plasma shadow at roughly $x > 2\ R_p$ where stream lines diverge. This is best visible for strong magnetic fields like in the $B_p = 0.21$ G case as those store more magnetic energy when the field is strongly perturbed.

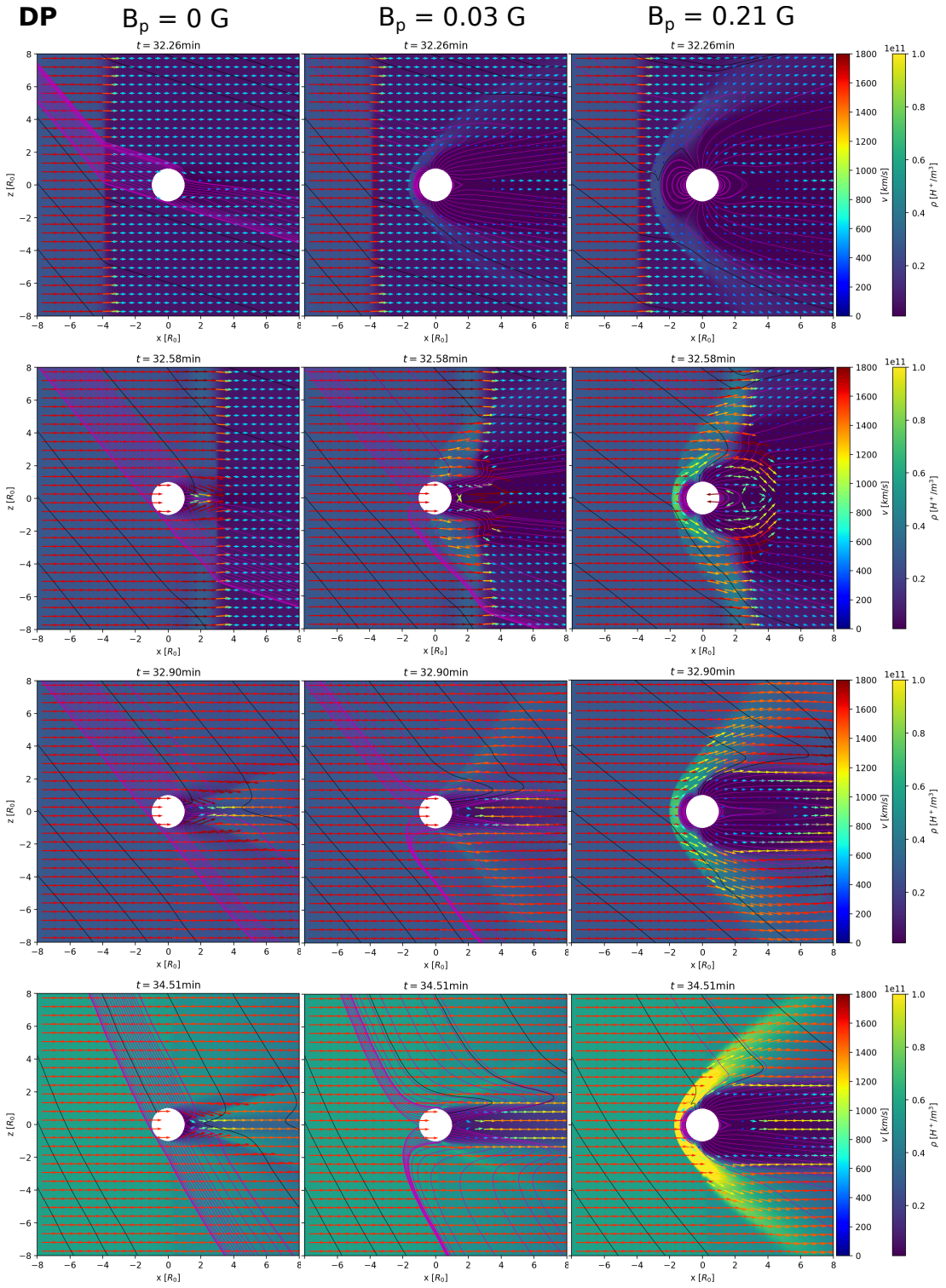

Figure 7.7.: Density pulse (DP). XZ-plane cross sections centered at Trappist-1e. Positions are given in R_p. Arrows depict velocity vectors and their magnitudes (left color bar). Contours show plasma density (right color bar). Black and magenta lines depict IMF and planetary field lines, respectively. All field lines are projections due to the asymmetry of the system. We show results before the CME (top), during the shock (upper middle), the sheath (lower middle) and during CME peak (bottom). Intrinsic magnetic fields are depicted above.

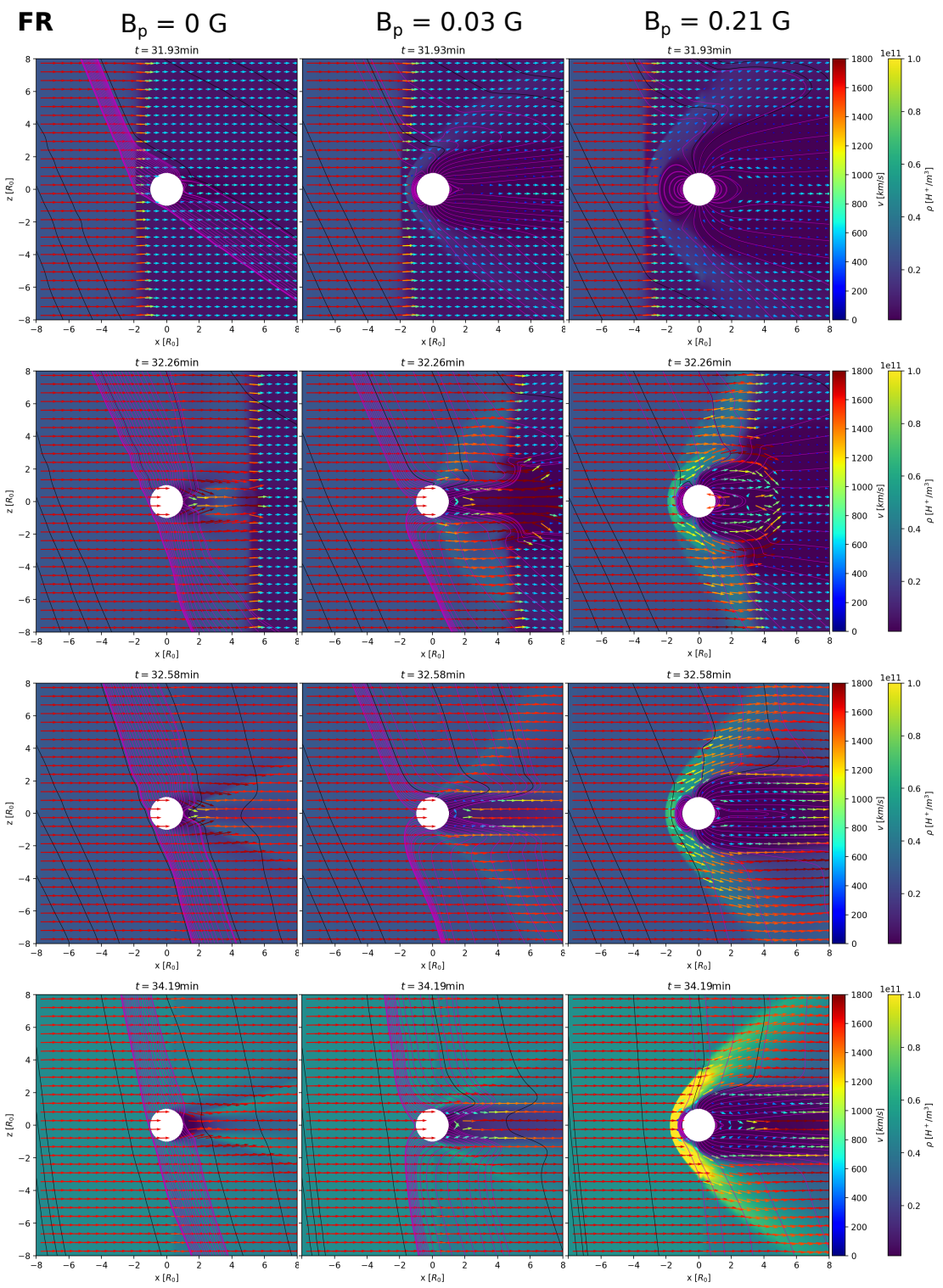

Figure 7.8.: Flux Rope (FR). Same caption as in 7.7. Because of a slightly enhanced CME size due to the FR magnetic pressure the CME shock crossing occurs approximately 30 s later compared to the DP case.

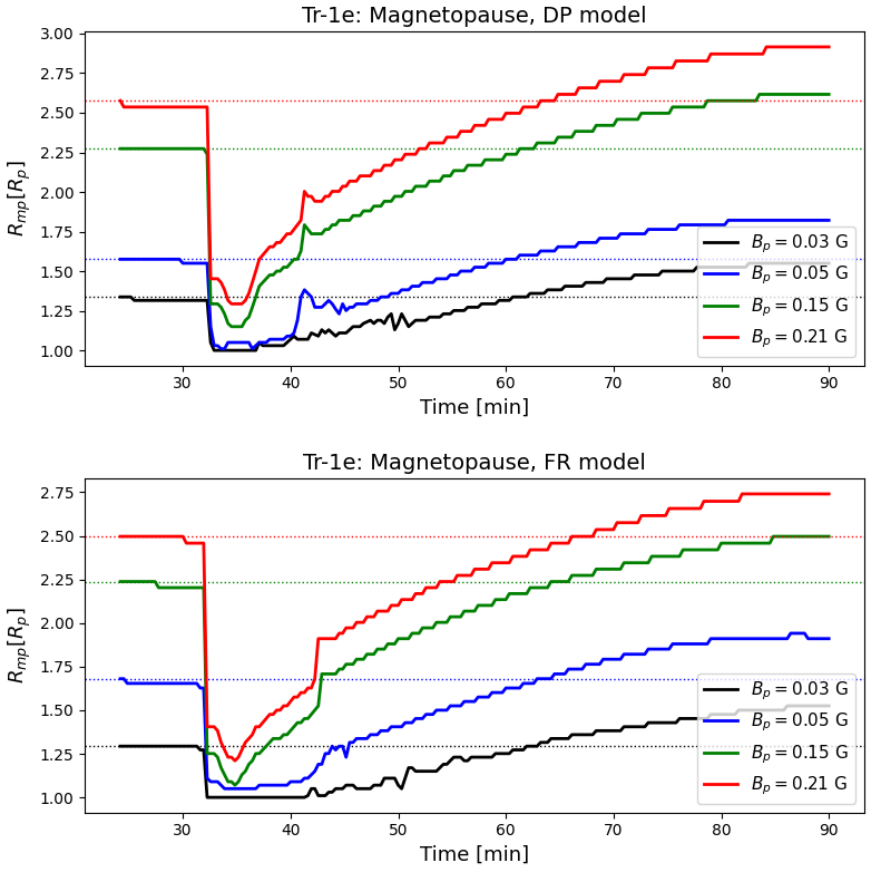

Figure 7.9.: Displayed are the upstream magnetopause locations (in planetary radii R_p) of Trappist-1e for a planetary field with surface strength B_p = 0.03, 0.05, 0.15 and 0.21 G as a function of time. The upper and bottom panels display DP and FR model runs, respectively.

Magnetopause during the CME

We track the upstream magnetopause position during the CME event to better examine the mechanical and magnetic forcing of the CME on the planetary magnetosphere. First we extract magnetic field profiles along the x–axis for each step. In our simulations, the magnetic field of the CME that piles up within the CME shock is mostly anti–parallel to the z–axis. From the magnetic field profiles we extracted the position of the magnetopause by determining the position of the reversal of the magnetic field and jump in its magnitude. This method was verified for all simulation results and yields sufficiently precise results. Magnetopause location time series for DP and FR model runs are displayed in top and bottom panels of Fig. 7.9, respectively. We note that the small jumps in Fig. 7.9 are due to the grid resolution. For all planetary magnetic field strengths considered the CMEs compress the magnetopause to R_{mp} = 1–1.3 R_p. For magnetic fields below $B_p = 0.05$ G the magnetopause is pushed to the planetary surface by the CME (also visible in Figs. 7.7 and 7.8). A similar situation with strong CMEs

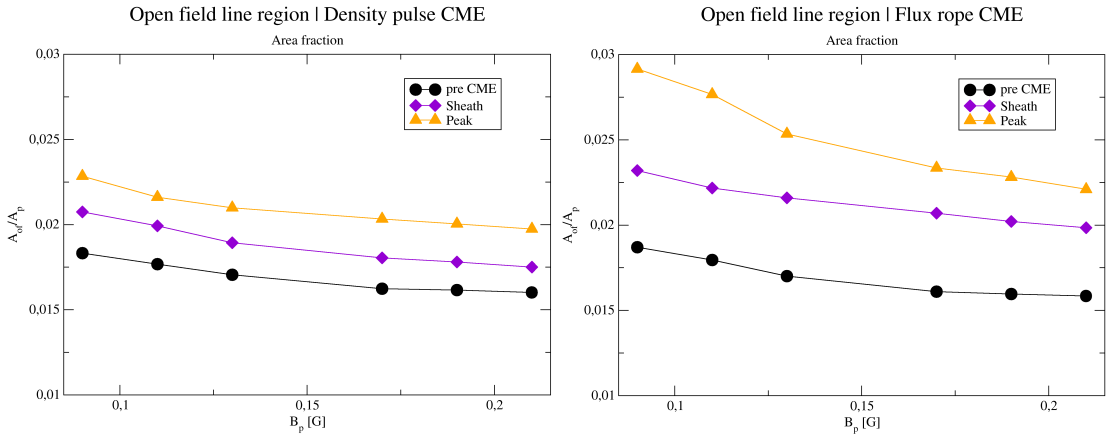

Figure 7.10.: Fraction of open field line area A_{of} relative to the planetary surface area A_p before the CME (black), during CME sheath passing (violet) and during CME peak (yellow) as function of planetary magnetic field B_p in G. DP and FR CME results are shown in the left and right panels, respectively.

and weak planetary magnetic fields were observed at Mercury (e.g.; Winslow et al. 2020). Even in the nearly Earth–like magnetic field case the magnetopause location drops from approximately 2.5 R_p to about 1.25 R_p. The CME sheath region (i.e. the region between the shock and the CME peak) exerts the strongest ram pressure on the magnetosphere. It starts after the shock crossing at 32 minutes and lasts for about 10 minutes. It is visible in Fig. 7.9 that the CME's sheath region is slightly extended laterally in FR CME models. This is due to the additional magnetic pressure within the CME that tends to expand the CME structure during its propagation towards the planet. In all simulations the magnetosphere undergoes a structural change that remains as long as the CME decays. After the CME main phase a new temporary equilibrium between magnetospheric and stellar wind pressure is reached. The dayside magnetosphere size after the CME main phase compared to the steady state size is enhanced by about 0.3 R_p in all simulations and the magnetosphere inflates slightly. During the CME decay phase a tail of diluted low plasma density follows the CME and accordingly decreases the CME kinetic energy while the velocity and magnetic flux density are mostly restored to their steady state values. We neglect the lengthy recovery phase after the CME due to the long simulation run times and because we are interested in relatively fast magnetic variability during the CME main phase that is fully captured within our simulations. We do not expect strong inductive response of the planet due to the slow varying magnetic fields during the recovery phase.

Open field line regions and polar cusps When planetary magnetic field reconnect with the stellar wind (or FR) magnetic field external plasma can be injected into the magnetosphere as plasma can move freely along the open magnetic field lines. We denote the area segment of the spherical planetary surface through which only open field lines pass the open field line area. This area is separated from the closed field line area (the closed

magnetosphere) by the open–closed field line boundary. The size of the open field line area is related to the efficiency of reconnection and the amount of stellar wind (or CME) energy flux injected into the magnetosphere (Baumjohann & Treumann 2012). Reconnection is most efficient when the planetary and stellar wind (or FR) magnetic fields are anti–parallel (discussed in Sect. 3.1.3). The size of the open field line area is also influenced by the dynamic pressure exerted on the magnetosphere (e.g. like on Mercury; Trávníček et al. 2007; Massetti et al. 2007). Ultimately, the efficiency of reconnection also controls magnetospheric convection and with it the induction within the magnetospheric plasma that is responsible for magnetic variability (e.g. induction equation 5.4). We will discuss the induction efficiency in detail in Sect. 7.6.1.
To study the effect of planetary magnetic field strength and CME type (DP or FR) on the reconnection efficiency and plasma injection into the magnetosphere we calculate the open field line area (A_{of}) fraction with respect to the total planetary surface area (A_p). Figure 7.10 shows the fraction A_{of}/A_p as function of planetary magnetic field for three different stages during the CME event (pre CME, sheath passing and during peak).

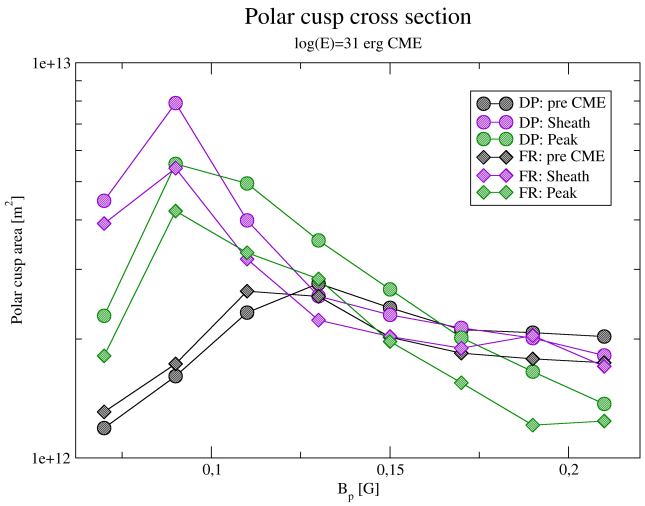

Figure 7.11.: Estimated cross sectional area (m^2) of the polar cusps (north and south) on a reference spherical surface with radius 1.03 R_p as function of planetary magnetic field B_p (G). Black, violet and green denote the moments before the CME, during the sheath passing and during the CME peak, respectively. Circles depict DP and diamonds FR model results.

Just before the CME intersects the planet, the area fraction is nearly equal for DP and FR CMEs and declines very slowly from about 18% (B_p = 0.09 G) to 16% (B_p = 0.21 G). We note that weaker magnetic field could not be considered due to inconsistent results of this method thar arise from the magnetosphere being pushed towards or nearly towards the planetary surface. From 0.09 G the magnetosphere is relatively stable and allows the clear identification of the open field line regions. As soon as the CME shock intersects the planet the area fractions in DP and FR simulations deviate from each other. In DP CME results we observe a slight increase of area faction from before the CME to the sheath passing and again towards the CME peak. The area fraction is highest during the peak with $A_{of}/A_p \approx 23\%$ ($B_p = 0.09$ G). Towards stronger magnetic fields the area fraction decreases to about 20%. In FR CME results A_{of}/A_p increases significantly to its maximum value near the CME peak with $A_{of}/A_p \approx 29\%$. The decline of open field line area with increasing magnetic field strength is slightly more dramatic in this scenario.

At $B_p = 0.21$ G the A_{of}/A_p is approximately 22 %.

These result underline the importance of an anti–aligned external magnetic field with respect to the planetary field as reconnection efficiency is significantly enhanced by adding a magnetic flux rope to the CME. The FR axis and thus its maximum magnetic field component B_z is anti–parallel to the planetary magnetic axis and therefore reconnection occurs more frequently in contrast to the steady state situation before the CME where the major magnetic field component of the stellar wind B_x is perpendicular to the planetary field. It is intriguing, however, that the size of the open field line regions seems to decrease with increasing planetary magnetic field strength. We attribute this to the enhanced magnetic tension on the planetary field lines that counteracts the drag exerted by the CME (or stellar wind) plasma. The weaker the magnetic field the more mobile are the planetary field lines and thus the open field line areas are accordingly extended more to the rear when the field is weak.

In addition to the open field line area we also characterized the cross sectional area of the polar cusps. The polar cusps are part of the open field line area in the upstream hemisphere and are characterized by enhanced plasma density. Magnetic energy is injected through all open field lines and most significant plasma injection occurs within the polar cusps (Baumjohann & Treumann 2012). We not that the field lines at the cusps are not static and therefore this plasma channel should not be seen as static either. The magnetic field lines are convected downstream by the stellar wind (or CME) flow and eventually reconnect again in the magnetotail. Nevertheless, the size of the polar cusps is decisive in determining the amount of stellar wind (or CME) plasma capture during the reconnection process.

We identify the polar cusps by measuring the surface area of a spherical shell with radius $1.03R_p$ around the planet in which the plasma density is at least 80% of the maximum plasma density within this spherical shell. With this threshold we were able to consistently identify the cusp area.

The cross sectional areas of the combined northern and southern polar cusps are shown in Fig. 7.11. Interestingly, in contrast to the open field line area fraction the polar cusp area is consistently larger during DP CME events with peak values (in both DP and FR scenarios) within the CME sheath. In DP as well as FR CMEs the sheath is characterized by enhanced plasma density due to shocked plasma and the faster CME peak region compressing and pushing the plasma in front of it. In DP CMEs, however, the density is larger due to the additional, initial density enhancement in the pulse model (Sect. 7.2.4.1). The more plasma is compressed due to stagnation at the magnetopause, the more mass flux can be expected to enter the magnetosphere via reconnected field lines. The high density in the magnetosheath and polar cusps is associated with enhanced thermal pressure. The thermal pressure gradient within the polar cusps tends to expand the cusps which in return leads to an enhanced cross sectional area. This expansion of the cusps is counteracted by the $\vec{j} \times \vec{B}$–force which balances the pressure gradient and thus we observe a significant decrease of cusp area with increasing magnetic field strength. From its maximum at $B_p = 0.09$ G the area decreases by a factor of 3 to 4

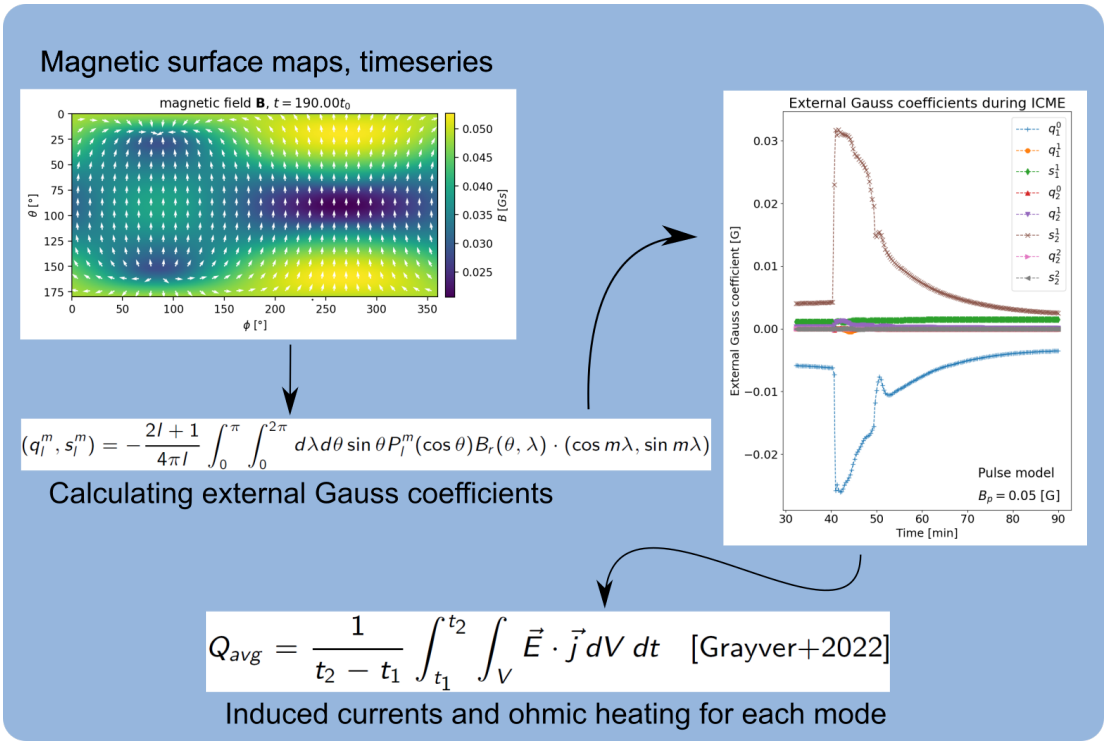

Figure 7.12.: A schematic of the post–processing pipeline to calculate CME induced Joule heating in the interior of a planet.

towards $B_p = 0.21$ G.

In summary we observe a general decrease of open field line area and polar cusps cross section with an increase of planetary magnetic field strength. From this direct CME energy injection into the magnetosphere point of view a stronger magnetic field thus tends to decrease the CME energy intake.

7.4.2. Surface magnetic variability and interior Joule heating

In this section we study CME energy dissipation within the interior of the exoplanet due to Ohmic dissipation averaged over a single CME event. CME-induced changes in magnetic flux at the planet's surface generate electric currents in the planet's interior by virtue of electromagnetic induction. We study the effect of CME induced interior heating for different planetary magnetic fields ranging from $B_p = 0$ G to 0.21 G. The CME–associated flare energy of our basic model is $E = 10^{31}$ erg (see Sect. 7.2.4). We later also discuss the scaling of the produced heat energy with flare energy in Sect. 7.6. To calculate the internal heating, we extract vectorial magnetic field maps directly above the planet's surface during the CME event and decompose the external field (e.g. the magnetic field without the constant dynamo magnetic field) for each step up to the quadrupolar order ($l = 2$) using spherical harmonics multipole expansion. This decomposition is valid for potential fields within the non–conducting upper subsurface but

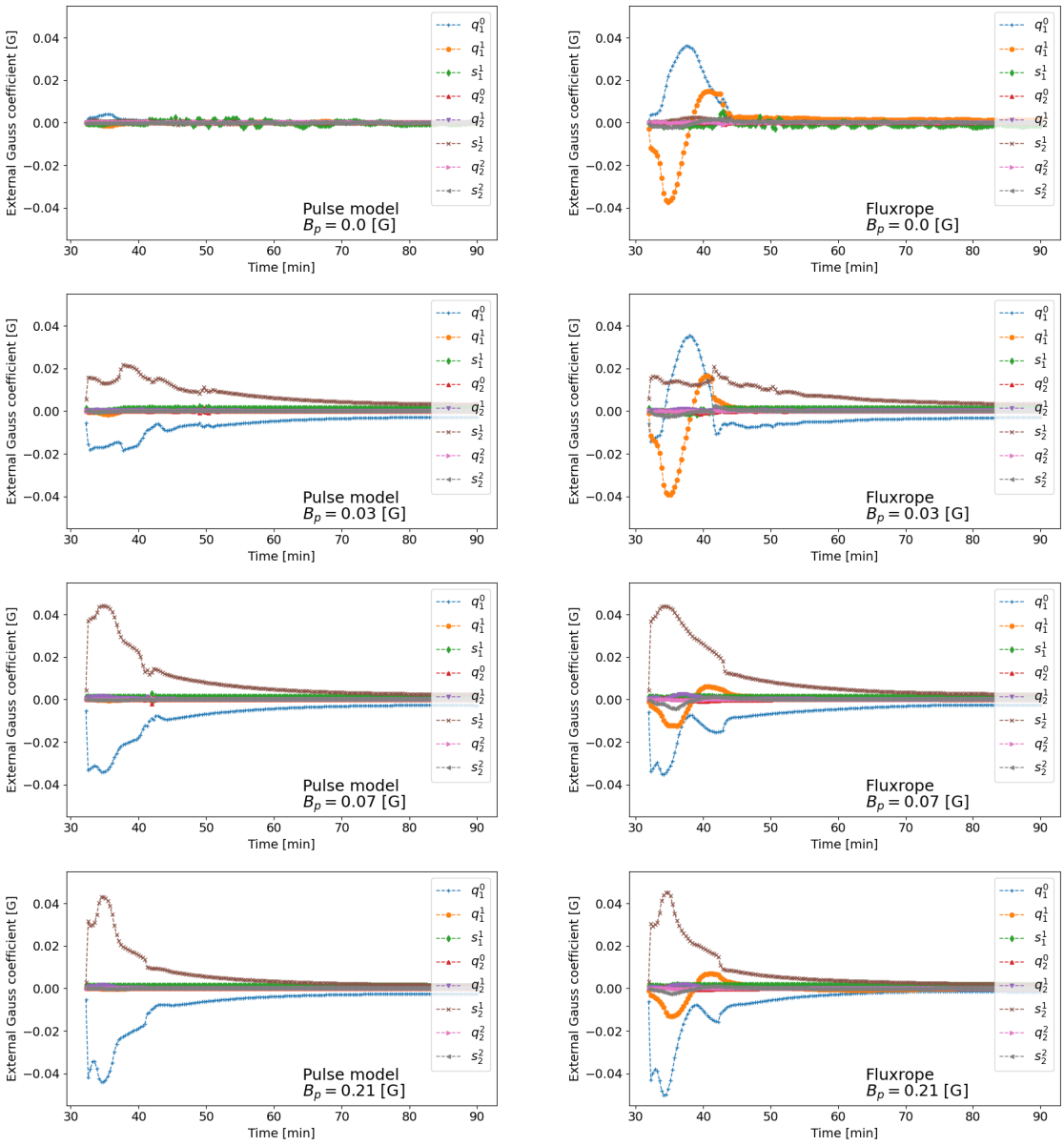

Figure 7.13.: Shown is the evolution of the external Gauss coefficient (Eq. 7.16) during one CME as function of time (minutes) for planetary magnetic field strength $B_p = 0$ (top), 0.03 (upper middle), 0.07 (lower middle) and 0.21 G (bottom). The left column shows DP, right column FR model results. Displayed are all considered external Gauss coefficients up to quadrupolar degree ($l = 2$).

we only have access to magnetic field components above the surface. We note that the subsurface is indeed conductive but compared to the plasma conductivity in the magnetosphere it can be considered non–conductive. We, however, tested potential field approximation directly above the surface and as a result the magnetic field at the surface can be approximated as potential field. The coefficients of the multipole expansion of the field give us information about which magnetic field mode (e.g. dipolar or quadrupolar) that is generated by the interaction is dominating the magnetic field variations at the surface of the planet. We calculate the external Gauss coefficients,

$$\begin{pmatrix} q_l^m \\ s_l^m \end{pmatrix} = n(l) \int_0^{\pi} \int_0^{2\pi} d\lambda d\theta \sin\theta P_l^m(\cos\theta) B_r(\theta,\lambda) \begin{pmatrix} \cos m\lambda \\ \sin m\lambda \end{pmatrix} , \tag{7.16}$$

where $n(l) = -\frac{2l+1}{4\pi l}$ is the Schmidt semi-normalization factor, P_l^m are the associated Legendre polynomials of order l and degree m. The radial magnetic field components B_r as function of co–latitude θ and longitude λ are extracted from the simulations. We note that this process is done in post–processing and thus, induction in the interior does not couple back to the space environment. The calculations and steps done to obtain the interior Joule heating rates are summarized in Fig. 7.12.
External Gauss coefficient time series are shown in Fig. 7.13 for Trappist-1e with magnetic fields of $B_p = 0$, 0.03, 0.07 and 0.21 G. For simplicity we omit Trappist-1b in this discussion due to the similarity of dynamical behavior of the magnetic fields (i.e. the physical behavior is the same but differs only in magnitude).

Flux ropes have spatially inhomogeneous magnetic fields and when convected on the planet it causes time-variable fields near the surface. Density pulse CMEs on the contrary have approximately constant magnetic fields but carry significantly more mechanical energy than flux rope CMEs due to plasma density enhancement. This incident mechanical energy, i.e. kinetic energy, compresses the planetary upstream magnetic field which is the main source of magnetic flux variability observed in the DP model results.

In DP CME simulations magnetic variability is dominated by the q_1^0 (vertical dipole mode) and s_2^1 (equatorial quadrupolar mode) coefficients. The decrease of q_1^0 corresponds to an increase in north–south magnetic flux density due to magnetosphere compression. The increase of s_2^1 is associated with equatorial magnetic field components with minima at the flanks, sub– and anti–sub stellar point. As we increase the planetary magnetic field strength these coefficients enhance accordingly until reaching the maximum near 0.04 G for $B_p \geq 0.07$ G. In the $B_p = 0$ G case there is only a slight increase of the q_1^0 coefficient that is due to stellar magnetic field line draping around the planet. There are small fluctuations in the s_1^1 component most pronounced in the $B_p = 0$ G case relating to flow instabilities at the flanks of the planet. Variability in q_1^0 and s_1^1 scales with B_p due to the enhanced inductive response of the plasma in the planet's space environment (Eq.5.4).

In FR CME simulations with a non–magnetized planet the dominant Gauss coefficients are q_1^0 and q_1^1. The increase and decay of q_1^0 around 40 minutes directly correlates with

the magnetic flux density profile along the FR with its maximum north–south component at the FR axis. Similarly the change of the twisted FR horizontal field components (within the xy–plane) is reflected in the sinusoidal variation of equatorial q_1^1 coefficient. The helical shape of the FR magnetic field is directly experienced by the planet. With increasing B_p the magnetic topology variations from FR simulations increasingly resemble those from DP simulations. The equatorial field component of the FR in the xy–plane (q_1^1) translated to the planet decreases in strength as the compression of the magnetosphere gains in effectiveness (q_1^0, s_2^1). Therefore, with strong planetary magnetic fields the twisted magnetic field structure of FR CMEs is increasingly shielded off by the planet's field. With strong magnetic fields, however, the magnetic variations associated with magnetosphere compression due to the CME dynamic pressure get dominant.

The time series of the external Gauss coefficients are used as input for the interior induction heating model of Grayver et al. (2022) where electromagnetic induction and resulting Ohmic heating is calculated for each Gauss coefficient separately. Induced currents within the planetary subsurface give rise to energy dissipation through Joule heating. For the whole CME duration we calculate the Joule heating rate within the whole planetary volume V, Q_J, for all modes according to (Grayver et al. 2022)

$$Q_J = \frac{1}{T} \int_{t_0}^{t_1} \int_V \vec{E} \cdot \vec{j} \, dV \, dt \, , \tag{7.17}$$

where V is the volume of the planetary body, $\vec{E}$ and $\vec{j}$ are the electrical field and current density within the planet induced by magnetic variations at the surface. The integration is performed from start t_0 to end t_1 of the CME event and the result is divided by the CME duration T to yield the average heating rate. With Eq. 7.17 we obtain the heating rate during an one–hour CME event. Physically, magnetic variations $\dot{B}$ induce eddy electric fields in the subsurface that drive electric currents which dissipate energy when electric conductivity is finite. We refer the reader to Grayver et al. (2022) for a detailed description of the induction heating model. We use a simple homogeneous interior model with the constant electrical conductivity of $\sigma = 0.01$ S/m which corresponds to the typical conductivity in the Earth's asthenosphere and lower lithosphere (Naif et al. 2021). This choice is motivated by the proposed interior composition of the Trappist-1 planets similar to that of Earth (Agol et al. 2021). The likely enhanced electrical conductivity at larger depths does not have a strong effect on our assumption of $\sigma = 0.01$ S/m because of the skin effect attenuating currents towards the center of the body. See Fig. 7.19 where we displayed volumetric heating rates for each multipole mode as function of depth. Accordingly most heating occurs in the uppermost layers of the planets in depths up to a few 100 km. From the surface up to a depths of about 300 km volumetric heating rates decrease by approximately 10 orders of magnitude (see Fig. 7.19).

The dissipation rates Q_J in the interior of the Trappist 1b and e for one CME are shown in Fig. 7.14. In the $B_p = 0$ G scenario we calculate a heating rate averaged within one hour of approximately 0.01 TW (Tr-1e) and 0.1 TW (Tr-1b) in the DP

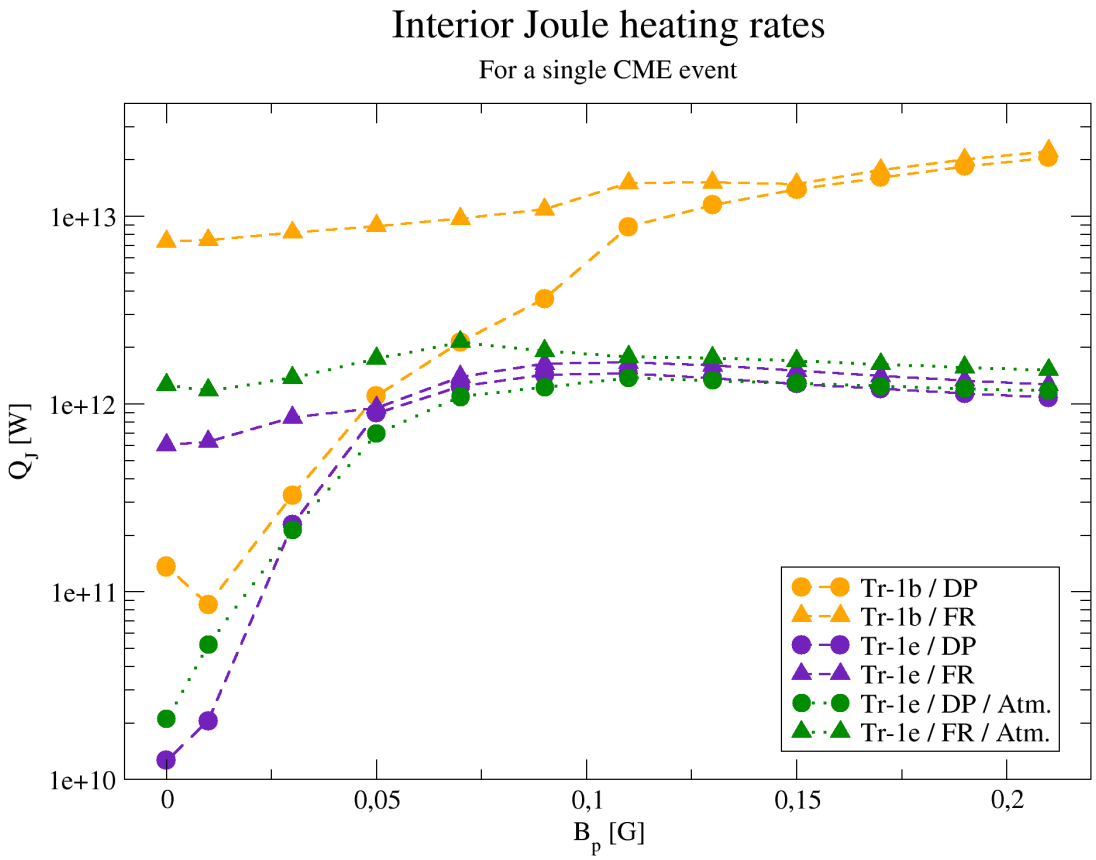

Figure 7.14.: Joule heating averaged within one hour CME events in the interior of the planets, Q_J (Eq. 7.17), given in Watts as a function of planetary magnetic field strength B_p. Triangles denote FR, circles DP CME cases. Yellow data points correspond to Trappist-1e, purple to Trappist-1e. Green data points denote the results with an atmosphere around Trappist-1e.

case. CMEs expand during their propagation through the heliosphere and therefore the energy density decreases accordingly. Because of that Trappist-1b experiences stronger CMEs, resulting in higher Q_J as magnetic perturbations scale with incident energy. With increasing B_p, Q_J scales for DP CMEs following a weak power law. Heating increases up to 1–2 TW at $B_p = 0.09$ G for Trappist-1e. The maximum heating lies outside our parameter space for Trappist-1b but the saturation towards $B_p = 0.21$ G suggests the maximum to be near the terrestrial magnetic field strength with Joule heating rates near 20 TW. In comparison with the Gauss coefficients time series (Fig. 7.13) the scaling of Q_J with with B_p correlates well with the measured magnetic variability. For DP CMEs the free magnetic energy is contained within the magnetic field that is mechanically perturbed by the CME. For FR CMEs there is only a small increase in dissipated power towards the same maxima as in the DP case. Starting at $B_p = 0$ G, Joule heating amounts to approximately 0.6 TW (Tr-1e) and 8 TW (Tr-1b), afterwards it increases with B_p up to 2 TW (Tr-1e) and 20 TW (Tr-1b). Above $B_p = 0.05$ G (Tr-1e) and ≈ 0.15

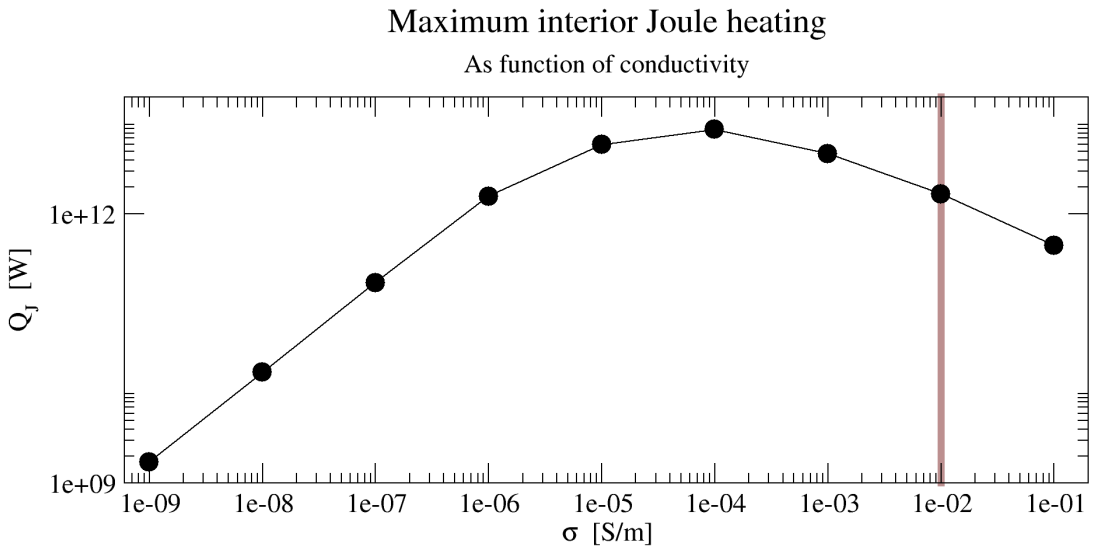

Figure 7.15.: Heating rates at $B_p = 0.11$ G for Trappist-1e as a function of the electric conductivity σ in S/m. The brown vertical line indicates the homogeneous model conductivity adopted in this study.

G (Tr-1b) Joule heating induced by FR CMEs scales exactly like in the corresponding DP CME case. At this point the magnetic energy of the planetary field overcomes the magnetic energy of the CMEs and thus external magnetic variations are increasingly shielded by the planetary magnetic field's tension.

For magnetic fields $B_p \geq 0.11$ G interior Joule heating decreases slowly with increasing B_p, here visible only in the Tr-1e case. The stiffness of a magnetic field increases with increasing field strength due to enhanced tension. This results in magnetic perturbations not growing further when increasing the magnetic field strength.

Interior heating rates for the Trappist-1e with an atmosphere are similar to those without an atmosphere. However, for weak magnetic fields $B_p < 0.1$ G heating rates are slightly enhanced in the FR CME case. An atmosphere weakens the plasma flow near the planet. Therefore mechanically generated perturbations are damped accordingly that results in slightly lower inductive response in the planetary interior. The increase in heating rates in the FR case ($B_p < 0.1$ G) comes from enhanced tension on the reconnected field lines since the dynamic response of magnetospheric plasma to external forcing is counteracted by the atmosphere that acts as energy sink.

We present total heating rates within the planetary volume during one CME event. Locally, volumetric heating rates are much higher due to the exponential attenuation of Q_J with depth, so that the Joule heating rates presented here are effectively constrained to a small fraction of the planet's volume due to the skin effect.

To visualize the effect of the interior electric conductivity on Ohmic dissipation, we additionally calculated heating rates with conductivities between 10^{-9} to $\sigma = 0.1$ S/m

(Fig. 7.14). The shape of the curve $Q_J(B_p)$ (Fig. 7.14) remains unaltered when varying the conductivity but values are shifted non–linearly towards other maxima. As the maximum heating rate in the Tr-1e model is achieved at the $B_p = 0.11$ G we only show the maximum heating rates as a function of the electrical conductivity in Fig. 7.15. The conductivity influences the skin depth according to $\delta \propto \sigma^{-1/2}$ and energy dissipation scales with $Q_J \propto \sigma$. Therefore, as σ decreases, the penetration depth of induced electric currents increases. At the same time the rate of energy dissipation decreases due to weaker currents, leading to the maximum in Q_J. In our case the maximum, $Q_J = 7$ TW, is reached with $\approx \sigma = 10^{-4}$ S/m (Fig. 7.15). Therefore, a lithosphere conductivity comparable to that of Earth already produces maximum heating rates in our model. More insulating as well as more conducting lithospheres lead to a lower Ohmic dissipation.

In a more realistic scenario, the conductivity would vary with depth owing to variations in temperature and composition. Such multi–layered interior models may produce heating rates that are substantially different from a homogeneous case, as was shown by (Grayver et al. 2022) for the case of CME-induced heating or the planetary motion through time–variable magnetic fields (Kislyakova et al. 2017).

Lastly we note that we also examined the effect of CME duration on heating rates. For durations $T >> 1$ h heating rates approach a lower limit approximately a factor of two smaller than those presented here for $T = 1$ h. The effect of CME duration on interior heating is thus, according to our model, insignificant. In Sect. 7.4.5 we discuss this result in detail.

7.4.3. Ionospheric Joule heating

In addition to interior Joule heating energy is also dissipated in the ionosphere through ionospheric Joule heating. Due to the presence of a neutral species that introduces collisions between plasma and neutral particles, the non–vanishing electric conductivity of the plasma gives rise to energy dissipation due to electric currents. Ionospheric Joule heating can be calculated using the electric field $\vec{E} = -\vec{v}\times\vec{B}$ and the plasma conductivity perpendicular to the magnetic field, i.e. the Pedersen conductivity $sigma_P$. We calculate the ion term of the Pedersen conductivity for each grid cell which is a function of the ion–neutral collision frequency ν_c, ion gyro frequency ω_g, electron number density $n_e = n_i$ (due to quasi-neutrality)(Baumjohann & Treumann 2012),

$$\sigma_P = \frac{n_e e^2}{m_i} \frac{\nu_c}{\nu_c^2 + \omega_g^2} \,, \tag{7.18}$$

where e is the elementary charge, m_e the electron mass and m_i the ion mass. The collision frequency is defined like in Eq. 5.6 and the ion gyro frequency can be calculated with $\omega_g = eB/2\pi m_i$. Ionospheric Joule heating per grid cell can then be calculated with $q_{J,ion} = \sigma_P E^2$. We integrate this expression over the whole magnetosphere volume V to get the total ionospheric Joule heating rate and integrate the resulting heating rates over the CME event duration. By dividing the result by the CME duration T we get

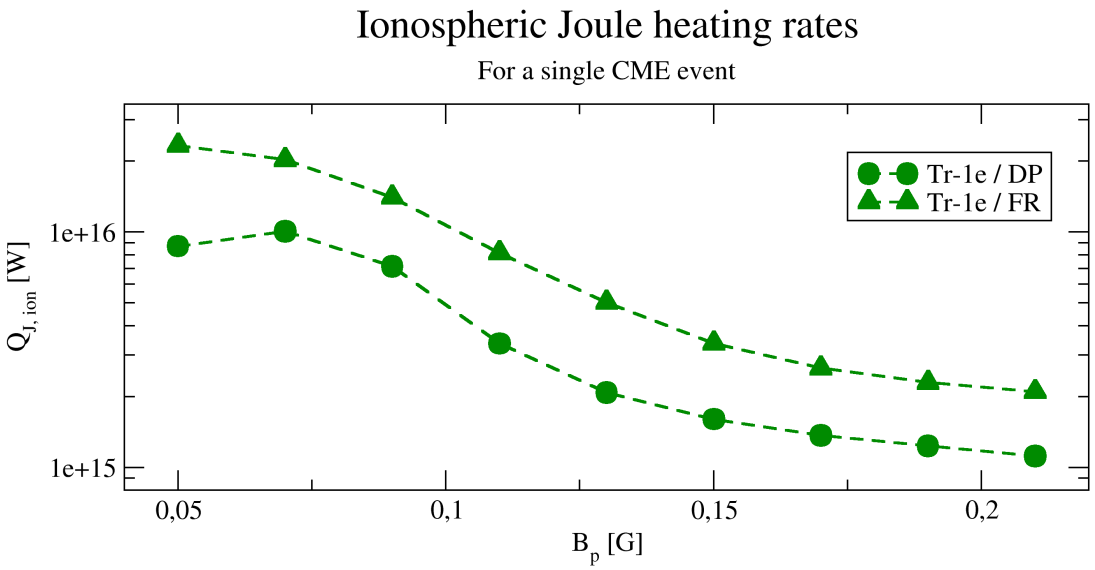

Figure 7.16.: Ionospheric Joule heating rates (Eq. 7.19) averaged within 1 hour CME events for Trappist-1e as a function of planetary magnetic field B_p. Density pulse (DP) and flux rope (FR) model results are denoted by circles and triangles, respectively.

the average ionospheric Joule heating rate for one CME event,

$$Q_{J,ion} = \frac{1}{T} \int_{t_0}^{t_1} \int_V \sigma_P(\vec{r},t) E(\vec{r},t)^2 \, dV \, dt \, , \tag{7.19}$$

where t_0 and t_1 are the start and end time of the CME event. We integrate Eq. 7.19 from the surface at $1\,R_p$ to $1.5\,R_p$ to avoid including the shock and unshocked CME plasma. We only consider magnetic fields ≥ 0.05 G due to the magnetopause being pushed to the planetary surface for weaker fields. Resulting heating rates are shown in Fig. 7.16. For DP model runs we obtain heating rates from 2×10^4 TW ($B_p = 0.05$ G) down to $1 - 2 \times 10^3$ TW ($B_p = 0.21$ G) while heating rates in the FR case are approximately a factor of 2 higher. Contrary to interior Joule heating, ionospheric Joule heating rates decrease with increasing magnetic field strength. Compression of the magnetosphere increases the plasma density within it and thus also the ion–neutral collision frequency. With stronger magnetic fields the magnetosphere is larger in volume. Together with enhanced tension on the field lines plasma compression is less effective when increasing the magnetic field strength, which also reduces the amount of dissipated energy due to ionospheric Joule heating.

In contrast to the interior Joule heating, the effect of Joule heating on ionospheric plasma is nearly instantaneous and about 4 orders of magnitude stronger. Therefore CME induced ionospheric Joule heating directly heats up the space plasma which may lead to comparably severe effects on the upper atmosphere like atmospheric inflation and higher escape rates.

7.4.4. Localization of interior heating heating

Induction driven interior Joule heating is proportional to the temporal change of magnetic flux, i.e. $Q \propto dB/dt$. The plasma interaction between planet and space environment is fundamentally asymmetric since the orientation of the magnetic field and the ambient plasma velocity field are key variables that deform and align the magnetosphere with the flow and ambient magnetic field. In Fig. 7.17 we show maps of time–averaged $|dB/dt|$ over the surface of the Trappist-1e with planetary magnetic fields of $B_p = 0.0$, $B_p = 0.05$, $B_p = 0.15$ and $B_p = 0.21$ G. The trends we describe in the following are also observed in Trappist-1b simulations. We therefore omit these results for simplicity.
The non–magnetized planets show the weakest magnetic variability.

In the DP CME case the maxima lie near the equator, mostly in the wake of the planet. There magnetic field curvature and thus tension is highest so that strongest magnetic variations can be expected there. In the FR CME case dB/dt is more homogeneously distributed.

In the non–magnetized planet case, most magnetic variability due to DP CMEs occurs at the downstream side ($\phi > 180°$). In the wake of the planet plasma stagnates and densities are low ($\phi \approx 270°$ in Fig. 7.17). As a consequence of the magnetic field being frozen into the plasma the field exhibits strong curvature in the wake due to the field at the flanks of the planet being convected downstream with the CME flow. Magnetic field curvature is proportional to magnetic tension and the field strength, thus strongest dB/dt is observed in the tail near the equator during the crossing of the CME. Upstream dB/dt is governed by magnetic field line draping which consequently also leads to enhanced magnetic flux.

For FR CMEs the maps show a more homogeneous picture. Contrary to the DP model, dB/dt nearly vanishes at the sub-stellar point ($\phi \approx 90°$). For magnetized planets the distribution of highest dB/dt changes significantly. In DP and FR model runs, as the magnetic field becomes stronger, the regions with high dB/dt tend to focus on the upstream polar cusp regions where magnetic field lines are mostly radial (i.e. perpendicular to the surface). In DP model cases magnetic variability is generated mostly upstream by mechanically induced field perturbations that travel along magnetic field lines (see Sect. 7.5 for a more detailed discussion). The lack of dB/dt near the equator hints at lower significance of fast mode magnetic perturbation near the equatorial surface regions. Therefore strongest dB/dt is found where closed field lines intersect the planet between $\theta = 15°$ and $60°$. Reconnection and stresses on open field lines in the tail region also generate magnetic perturbations that travel along the downstream field lines towards the planet. The low dB/dt band at the downstream equator is caused by the magnetic field being parallel to the surface so that the field and thus the perturbations do not intersect the planet.

In FR model runs average dB/dt is more inhomogeneously distributed over the planetary surface apart from the two strong maxima near the polar cusps at open magnetic field lines. The twisted magnetic field of the FR with a strong north–south component reconnects with the planetary field at the upstream side and imposes its intrinsic curvature on the it, which governs dB/dt in the high–latitude open magnetic field regions.

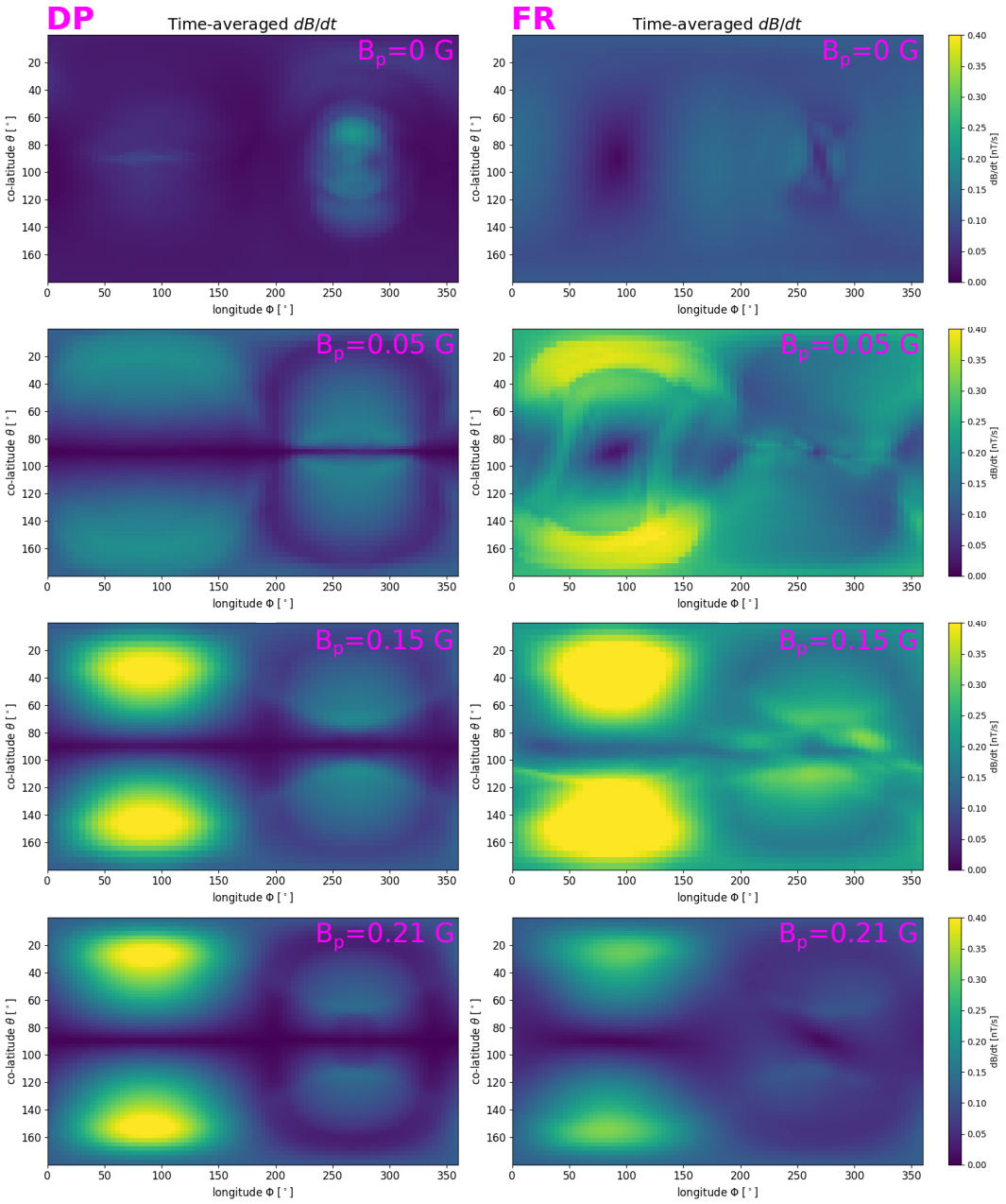

Figure 7.17.: Maps of time–averaged magnetic variability, dB/dt, in nT/s obtained directly above the planetary surface. Co–latitude and longitude are shown on the Y and X axes, respectively. Upstream direction is at longitude below 180 degrees. The left column shows density pulse (DP), the right column flux rope (FR) model results. We show maps for $B_p = 0$ (top), 0.05 (upper middle), 0.15 G (lower middle) and 0.21 G (bottom).

This is best visible for $B_p = 0.05$ G in Fig. 7.17. The FR field intersecting the planet may be oriented in all directions due to its twisted nature and therefore relatively small average dB/dt can be found everywhere over the surface. With stronger B_p the inductive response of the space plasma due to the flow and field perturbations generated by the CME enhances. We observe in Fig. 7.17 (FR, $B_p \geq 0.15$ G) that dB/dt peaks near the polar cusps like in the DP case. This indicates the takeover of magnetic variability generated by magnetospheric compression towards stronger B_p, which we also observed in Fig. 7.13. Notably, for strongest magnetic fields considered ($B_p = 0.21$ G) time–averaged dB/dt decrease in magnitude. We attribute this to enhanced magnetic tension on the planetary field that damps field perturbations. For induction heating in general the field amplitude as well as frequency of variation are important and the interplay of both are not directly visible in the maps. The Gauss coefficient time series (Fig. 7.13) hint at an extended timescale of the geomagnetic response to the CME impact when B_p is lower (i.e. the magnetic variability due to the CME sheath crossing shortens with increasing B_p). Together with the slightly lower perturbation amplitude this explains a lower average dB/dt in Fig. 7.17.

Depth dependence of Joule heating

Most heating occurs in the uppermost layers of the planets. In Fig. 7.19 we show heating rate depth profiles within Trappist-1e to visualize the very fast exponential decay of heating with increasing depth. In general, the most important modes of the external field are the g_1^0 (dipolar) and s_2^1 (quadrupolar) modes. The simplest mode of the external field, namely the zero-th order dipole mode g_1^0, can explain nearly half of the total heating rates. Apart from the weakly magnetized DP case ($B_p = 0.05$ G), however, s_2^1 is slightly more important. Heating rates due to all multipole modes decay similarly with depth, whereby heating due to g_1^0 and s_2^1 decrease by 8 orders of magnitude within the depth of 300 km from the surface. In the FR scenario more complex multipole mode play a significant role in heating (e.g. q_1^1, q_1^2), that play a lesser important role in the DP scenario. In the $B_p = 0.05$ G scenario the depth profiles look similar (DP and FR) with them deviating from each other as the magnetic field strength increases.

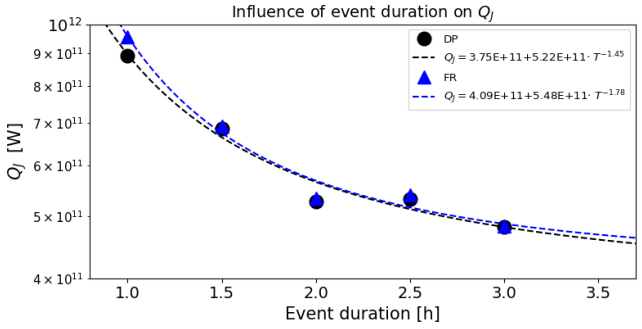

Figure 7.18.: Interior heating rates for Trappist-1e with $B_p = 0.05$ G as function of CME event duration (hours) in the DP (circles) and FR (triangles) cases. Dashed lines show fitted curves (Eq.).

Overall our results suggest that the degree of local focusing of the heating correlates strongly with the planetary magnetic field strength. Stronger magnetic fields favor

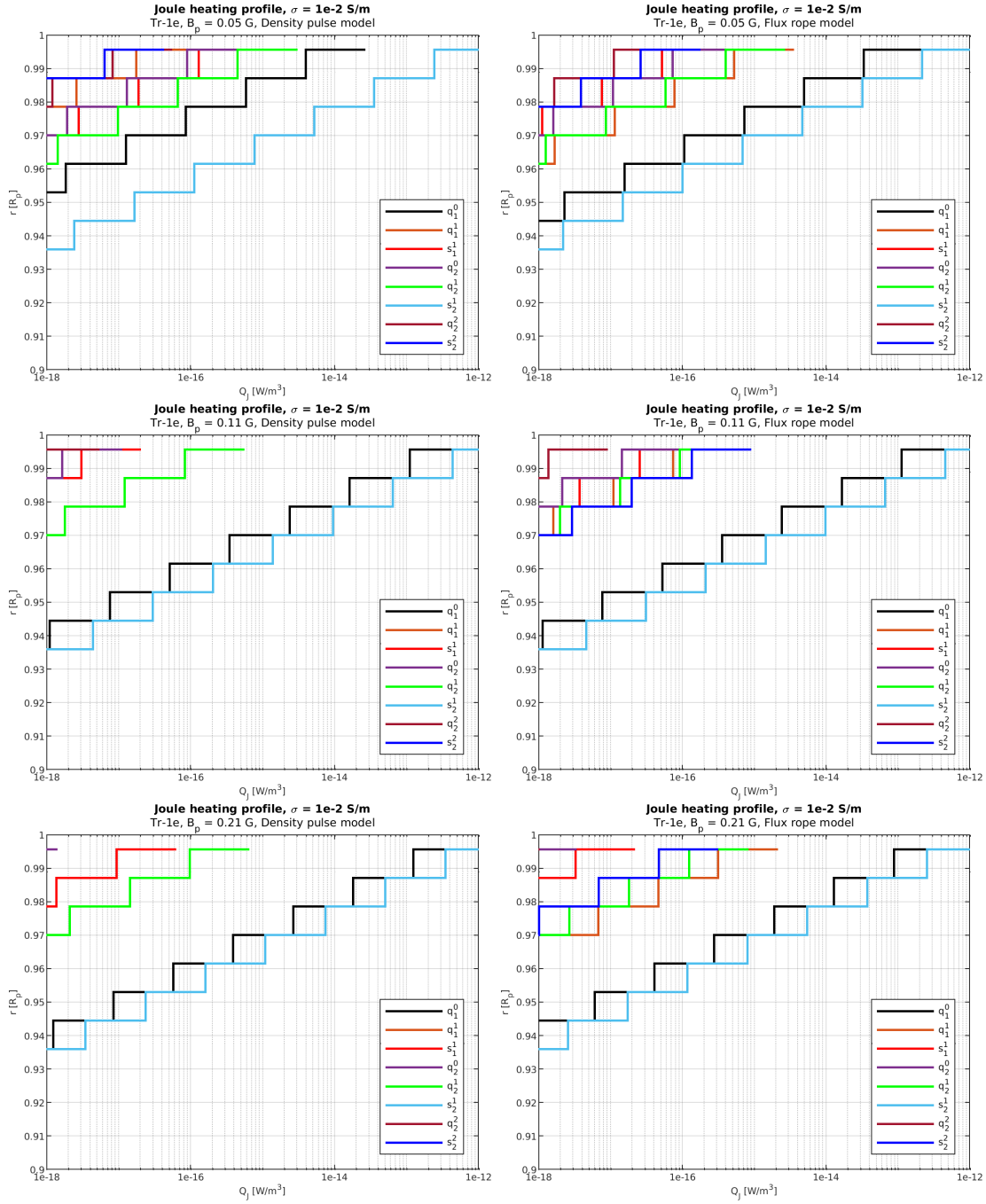

Figure 7.19.: Volumetric heating rates in the interior of Trappist-1e averaged over spherical shells with respective constant conductivity ($\sigma = 10^{-2}$ S/m). The heating rates are averaged over 1–hour CME events. Heating rates for each considered multipole mode (colored lines) are shown for the DP (left) and FR (right) scenario. We show results with $B_p = 0.05$ G (top), $B_p = 0.11$ G (middle) and $B_p = 0.21$ G (bottom).

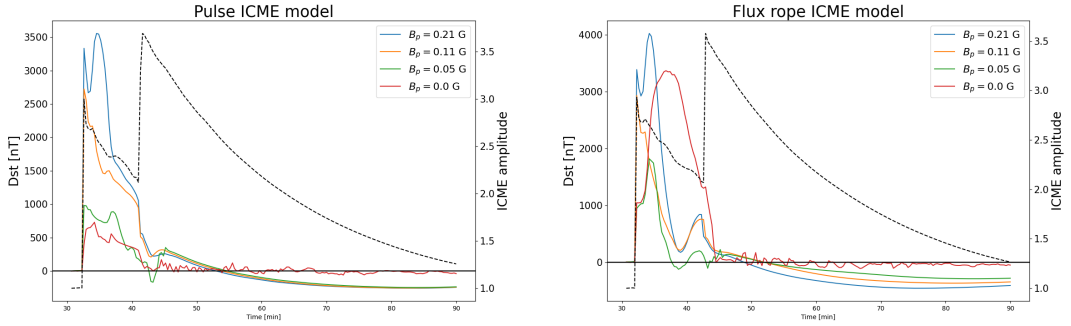

Figure 7.20.: Dst index (in nT) obtained from averaging the horizontal magnetic field perturbations (B minus the pre–CME steady state magnetic field) along the equator as a function of time (min). The colored lines denote different planetary magnetic field scenarios and the black dashed line represents the CME velocity profile (normalized to stellar wind velocity) experienced by the planet at the respective time. Left corresponds to the DP, right to the FR scenario.

CME–induced interior heating to peak on the upstream hemisphere at high latitudes.

7.4.5. Effect of event duration on interior heating rates

In the solar system CME events typically last for several hours up to several days with a majority lasting for at least 12 hours. In our model we chose one hour event durations and this naturally raised the question of whether the duration has a major effect on the time-averaged interior heating rates. We tested the dependence of Q_J on event duration by running our model for $B_p = 0.05$ G with event duration of 1 h, 1.5 h, 2 h, 2.5 h and 3 h. We extended the CME peak (DP model) in form of a plateau with maximum amplitude from the CME center towards the front in such a way so that the front of the curve (i.e. the nose of the Gaussian) has the same shape as in our basic model. With this setup the shape of the shock and sheath region of the CME remain the same so that the geometry, which is largely responsible for the magnetic variations near the planet, remains unchanged. The tail of the CME is, however, stretched out accordingly. We only consider CMEs with associated flare energy of 10^{31} erg. We find in our results that the heating rates for a single event decrease towards longer event durations (Fig. 7.18). This is caused by the extended decay of the CME parameters in the tail which results in weaker and slower magnetospheric topology change and in lower average dB/dt since the heating rates are averaged over longer periods. The extended peak has no great influence on magnetic variations as the forcing remains predominantly the same during the peak plateau. For inductive coupling of the space environment to the planet's interior the planet must experience variations in the magnetic field which should not occur during the extended peak if the CME magnetic variability would directly translate to dB/dt in the subsurface. However, the magnetosphere shows smaller oscillations during this phase which are caused by compression and repulsive expansion of the dayside magnetosphere and thus the constant peak still leads to significant magnetic variability near the planet.

We fit a power law function to the data and normalize the function with the heating rate for the 1 h event, $Q_{J,1h}$. The fitted scaling function reads

$$\gamma(t) = \frac{Q_{J,\infty} + a\, t^c}{Q_{J,1h}} \,, \tag{7.20}$$

where $Q_{J,\infty}$ is the limit value for infinite durations t_∞. The constant a and the exponent c are fit parameters. The derived parameters are displayed in the legend of Fig. 7.18. For CME durations $t > 4$ h the scaling factor approaches $\gamma = 0.44$ for both DP and FR model runs. This result is presumably not universal but an effect of our model choice. Nevertheless we arrive at the conclusion that, with our model, the CME duration does not affect the time–averaged heating rates considerably.

7.4.6. Magnetic disturbance, Dst and effect of the ring current

On Earth the magnetic variability generated by space weather is, among others, measured using the Dst index (Disturbance storm time index) (e.g. Iyemori 1990). Roughly speaking, the Dst index corresponds to the averaged disturbance of the horizontal terrestrial magnetic field components along the magnetic equator compared to the Earth's magnetic field during a solar quit phase (i.e. without nominal space weather apart from an approximately steady state solar wind). The Dst index is usually given in nT and, since the diamagnetic response of the ionospheric ring current to a magnetospheric perturbation opposes the terrestrial magnetic field and thus weakens it near the equator (Ganushkina et al. 2017). At Earth the strong magnetic field and CMEs with lower total energy density as compared to our CMEs in the Trappist-1 system allows the terrestrial magnetosphere to efficiently resist compression due to the CME dynamic pressure. During CME events the dominant magnetic variability at Earth's surface is induced by the ring current magnetic field. The Dst is typically in the order of a few -100 nT at most. Analytical relations between ring current energy density and magnetic variability at the planetary surface exist (e.g. Sckopke 1966; Dessler & Parker 1959). We do not know if all or only few planets have rung currents. Especially in cases were the external forcing due to stellar winds and eruptions is strong compared to the planetary magnetic field and its ionosphere, it is not clear wether a ring current can develop. Mercury is the best example for such conditions in the solar system as the interaction of its weak magnetic field and dynamo with space weather might be dominated by magnetospheric compression and induction like possibly in the Trappist-1 system (Glassmeier et al. 2007). Theoretical studies, however, showed that a partial ring current may indeed develop in Mercury's ionosphere, adding to the complexity of the respective magnetospheric dynamics (Trávníček et al. 2007).

The ring current is not included in our model but with the use of the DPS–relation (Sckopke 1966; Dessler & Parker 1959) we may estimate the effect of the ring current by evaluating the kinetic energy of ions in a ring around the planet. The DPS–relation has been proven to estimate the Dst*–index (Dst index but without magnetic field contributions from other sources than the ring current) within 20–30 % accuracy when

only considering ring current ions as energy input (Liemohn 2003). The relation reads

$$\frac{\Delta B(r=0)}{B_p} = -\frac{2E_{rc}}{3E_B}\,, \tag{7.21}$$

where $B(r=0)$ is the magnetic field perturbation at the center of the planet, B_p the equatorial magnetic field strength, E_{rc} the kinetic energy of ring current ions and E_B the magnetic energy of the unperturbed dipole field outside the planet. We integrate the kinetic energy along a torus–like volume around the planet (from $\Phi = 0$ to 2π latitude) with inner radius $R_{min} = 1.01\,R_p$ and outer radius $R_{max} = R_{mp}$ where R_{mp} is the magnetopause radius. The volume is enclosed between co–latitude $\theta = \pi/4$ and $3\pi/4$. We thus calculate $\Delta B(r=0)$ (Eq. 7.21) for each time step with

$$E_{rc}(\vec{r},t) = \int_{R_{min}}^{R_{mp(t)}} \int_{\pi/4}^{3\pi/4} \int_{0}^{2\pi} r^2 \sin\theta \left[0.5\rho(\vec{r},t)v(\vec{r},t)^2\right] \mathrm{d}r\mathrm{d}\theta\mathrm{d}\phi \tag{7.22}$$

and $E_B = (4/3)\pi R_p^3 B_p^2/2\mu_0$ (Dessler & Parker 1959). We find the Dst indices in DP as well as FR scenarios with $B_p \geq 0.07$ G to be consistently on the order of -100 nT with a slight increase in Dst for stronger magnetic fields B_p. The increase results mainly from our integration limit of R_{mp} that controls the volume of ions included in the calculation. In the cases with $B_p < 0.07$ G the integration volume was too small in order to yield consistent results ($R_{mp} \to R_p$).

Assuming the DPS relation (Eq. 7.21) to give at least estimates accurate on the order of one magnitude we can confidently say that the effect of a ring current might be insignificant at close–in exoplanets that experience CMEs with higher energy density compared to Earth. In Fig. 7.20 we show the Dst index directly obtained from our simulations without the addition of ring current contributions. The magnetic variability in our simulations is, as discussed in Sects. 7.4.2–7.5. According to our model the weakest Dst index of about 500 nT (DP) caused solely by magnetosphere compression is much higher than the estimated ring current induced Dst index. In the FR scenario the Dst indices are generally higher with the maximum value around 1800 nT in the weakest magnetic field case ($B_p = 0.05$ G). We note that our Dst indices are positive due to the lack of diamagnetic ring current contribution and because of the magnetic field amplification by compression. Maximum Dst indices range up to 4000 nT which exceed extreme Dst indices on Earth by one order of magnitude. Therefore, we conclude that for close–in exoplanets magnetic field compression and amplification dominates magnetic variability instead of ring currents and diamagnetic effects within the magnetosphere.

7.5. Energetics during CME–magnetosphere interactions

In this section we aim to better understand the electromagnetic energy fluxes around the planets and how they relate to CME–induced interior heating. We first discuss the energetics of the CME–magnetosphere interaction in Sect. 7.5. We begin with discussing the time variability of near–surface Poynting fluxes during the CME event and assess the

energy transfer from CME to the magnetosphere (Sect. 7.5.2). In Sect. 7.5.3 we consider time averaged Poynting fluxes, compare them to interior Joule heating and study the scaling of input power near the surface as function of planetary magnetic field strength. In Sect. 7.6 we briefly discuss the scaling of interior heating with CME–associated flare energy. Afterwards we point out possible observable long term effects of continuous CME–induced planetary heating in Sect. 7.7.

7.5.1. Dominant regimes of magnetospheric energy fluxes

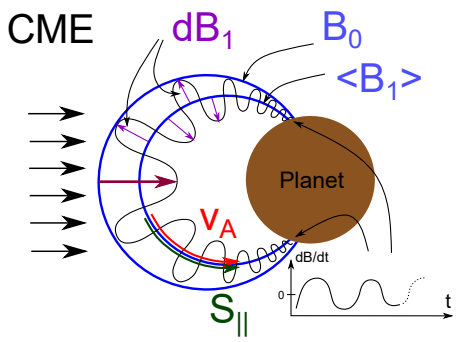

Figure 7.21.: This sketch illustrates the generation of magnetic field aligned Poynting fluxes associated with Alfvén waves. Surface magnetic variability is dominantly generated by closed magnetic field perturbation due to magnetospheric compression if the ram pressure of the CME exceeds its magnetic pressure. We do not show fast mode waves due to the negligible effect on surface dB/dt found with our model.

Magnetic variability is mostly caused by electromagnetic energy being propagated by Poynting fluxes. In our model studies these Poynting fluxes are generated by the CME–planet or CME–magnetosphere plasma interaction and ultimately deliver the electromagnetic energy to the planet's surface where it is, to some extend, dissipated by Joule heating. We distinguish between two regimes where electromagnetic energy transfer takes place that contributes to magnetic variability above the planet's surface. **A)** The closed field line region (i.e. the magnetosphere) is defined by all planetary magnetic field lines that intersect the planet's surface twice. Here magnetic energy is propagated mostly along field lines. **B)** The open field line region is defined by highly mobile magnetic field lines that originate in the planet and connect to the stellar magnetic field. Stellar wind / CME energy and mass are injected into the magnetosphere across the open magnetic field. Magnetic energy transport in this regime is dominated by convection.

In the following we describe the two regimes before we study the contributions of those to the surface Poynting flux and magnetic variability during the CME event.

A) Closed field line regime Figure 7.21 shows a schematic illustrating how magnetic variability is transported within closed field lines. In a steady state magnetosphere that is in equilibrium with its surroundings (e.g. before the CME), the planetary magnetic field is shaped like dipole perturbed by the (here steady state) stellar wind, $\vec{B}_0$. This perturbed dipole is compressed on the upstream side and elongated on the downstream side (e.g. top panels of Figs. 7.7 and 7.8). A CME or any variation in the interplanetary medium perturbs the steady state field (dark violet arrow). If persistent in its forcing, the total CME incident force and the $\vec{j} \times \vec{B}$

force within the magnetosphere reach a new equilibrium state where the initial dipole is further perturbed. This dipole field, which is perturbed by the stationary stellar wind and additionally by the CME, is denoted by $\vec{B}_1$. When the CME decays, $\vec{B}_1$ steadily approaches $\vec{B}_0$ again. At some point during the initial forcing the magnetic pressure within the magnetosphere overcomes the CME forcing at the magnetopause. With this repulsive force, the magnetic field lines of the planet tend to oscillate about the mean perturbed magnetic field $\langle\vec{B}_1\rangle$. The magnetic field variability is the residual magnetic field $\delta\vec{B}_1$ that is perpendicular to the mean field $\langle B_1\rangle$. This perturbation corresponds to the generation of free magnetic energy (i.e. work done against $\vec{j}\times\vec{B}$). From now on we omit the subscript 1 for simplicity. With $\vec{B}$ we now mean the perturbed mean field. Magnetic perturbation is propagated by Alfvén waves with velocity v_A towards the planet. These Alfvén waves carry electromagnetic energy that is associated with inward Poynting flux $\vec{S}_{||}$ parallel to $\langle\vec{B}\rangle$, generated by the residual magnetic and associated electric field,

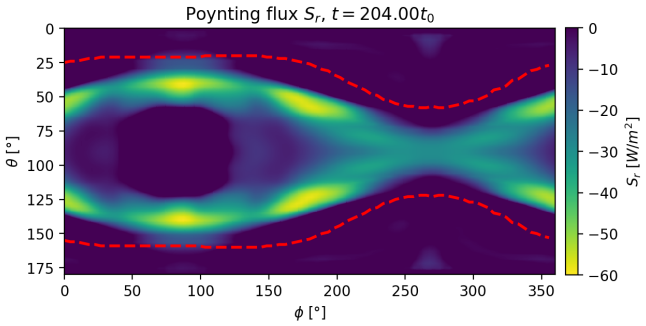

Figure 7.22.: The open-closed field line boundary (red lines) plotted on top an inward Poynting flux, S_{in}, map for Trappist-1e, $B_p = 0.21$ G, DP model. As an example, the map is shown during the CME sheath crossing, but the boundary remains almost constant over the entire simulation period, for DP as well as FR simulations.

$$\vec{S}_{||} = S_{in} = \frac{\delta\vec{E}\times\delta\vec{B}}{\mu_0} = \frac{\delta B^2}{\mu_0}\vec{v_A}\ , \tag{7.23}$$

where the velocity $\vec{v}_A$ is the Alfvén velocity (Park et al. 2017; Keiling 2009). The planetary surface experiences the temporal change of $\langle B\rangle$, namely $d\langle B\rangle/dt$. The maximum dB/dt can be expected where $\langle B\rangle$ is perpendicular to the surface of the planet, $\langle B\rangle \approx B_r$ (i.e. the field lines are purely radial), so that $S_{in} \approx S_r$.
We note that this mechanism for generating magnetospheric Poynting fluxes also works in reverse, for example when the magnetosphere expands due to decreasing stellar wind pressure.

In Fig. 7.22 we show a map of S_{in} directly above the surface of Tr-1e. Only Poynting fluxes towards the planet are shown. The red line denotes the open–closed field line boundary (OCFB). For latitudes below the OCFB the field lines are closed. The OCFB shown here is similar in all magnetic field as well as CME models and it changes only minimally during the CME event. Figure 7.22 shows that almost all Poynting fluxes S_{in} lie within the closed field line region indicating that the electromagnetic energy parallel to the magnetic field is generated almost exclusively within the closed magnetosphere due to magnetosphere compression. In the polar regions as well as near the OCFB, a large part of the electromagnetic energy is transported via convection as the plasma flow

at the poles and flanks of the planet is mostly perpendicular to the planetary magnetic field. The field lines near the OCFB are most mobile in a sense that they are convected downstream by the external plasma flow. Given the magnetic variability maps in Fig. 7.17 we expect the magnetic variability to be mostly transported along magnetic field lines and the distribution of S_{in} within the OCFB supports this. We also show S_{in} maps for $B_p = 0.05$, $B_p = 0.15$ and $B_p = 0.21$ models during the CME main and decay phase in Fig. 7.23 to illustrate the general dominance of S_{in} in regions where most magnetic variability (i.e. dB/dt, Fig. 7.17) is found independent of the CME model. Furthermore the Poynting flux distribution near the CME peak (middle column) correlates best with the magnetic variability maps, indicating that most heating might be generated during the CME main phase and not during the shock crossing.

We note that magnetic perturbations are also carried by fast mode waves dominantly perpendicular to the magnetic field. However, in the magnetic variability maps (Fig.7.17) we find no significant average magnetic perturbations near the equator and therefore conclude that fast mode wave perturbations are negligible in our model.

Due to the above considerations we focus our analysis in the following sections on the electromagnetic energy that is delivered inward by radial Poynting flux components, S_r. To get a measure of how much interaction–generated electromagnetic energy intersects the planetary surface, we formulate the integrated Poynting flux as integral over radial Poynting fluxes directed towards the planet,

$$S_{in}^{-} = \int_{A_{planet}} S_r^{-} \, dA \, , \tag{7.24}$$

where A_{planet} is the surface area of the planet and S_r^{-} are the radial components of the Poynting flux directed towards the planet. Due to the spherical coordinate system these vector components are negative, therefore we omit the sign and express the inward components with the minus superscript.

B) Open field line regime Planetary magnetic field lines that reconnect with the ambient magnetic field act as open channels for stellar wind or CME energy and mass transfer towards the planet. Field lines reconnect at the upstream hemisphere and are then convected downstream together with the ambient plasma flow. This convection shapes the magnetic field and exerts stresses on the field lines. This magnetic variability is most dominant in the planet's geographical polar regions. Poynting fluxes generated by convection are mostly not parallel to the field lines. Therefore, when assessing dB/dt and inward Poynting fluxes S_{in}, we naturally miss the portion of Poynting fluxes that is dominated by convection. We, however, showed that the dominant regime of electromagnetic energy transfer and generation occurs within the closed field line region (see Fig. 7.23).

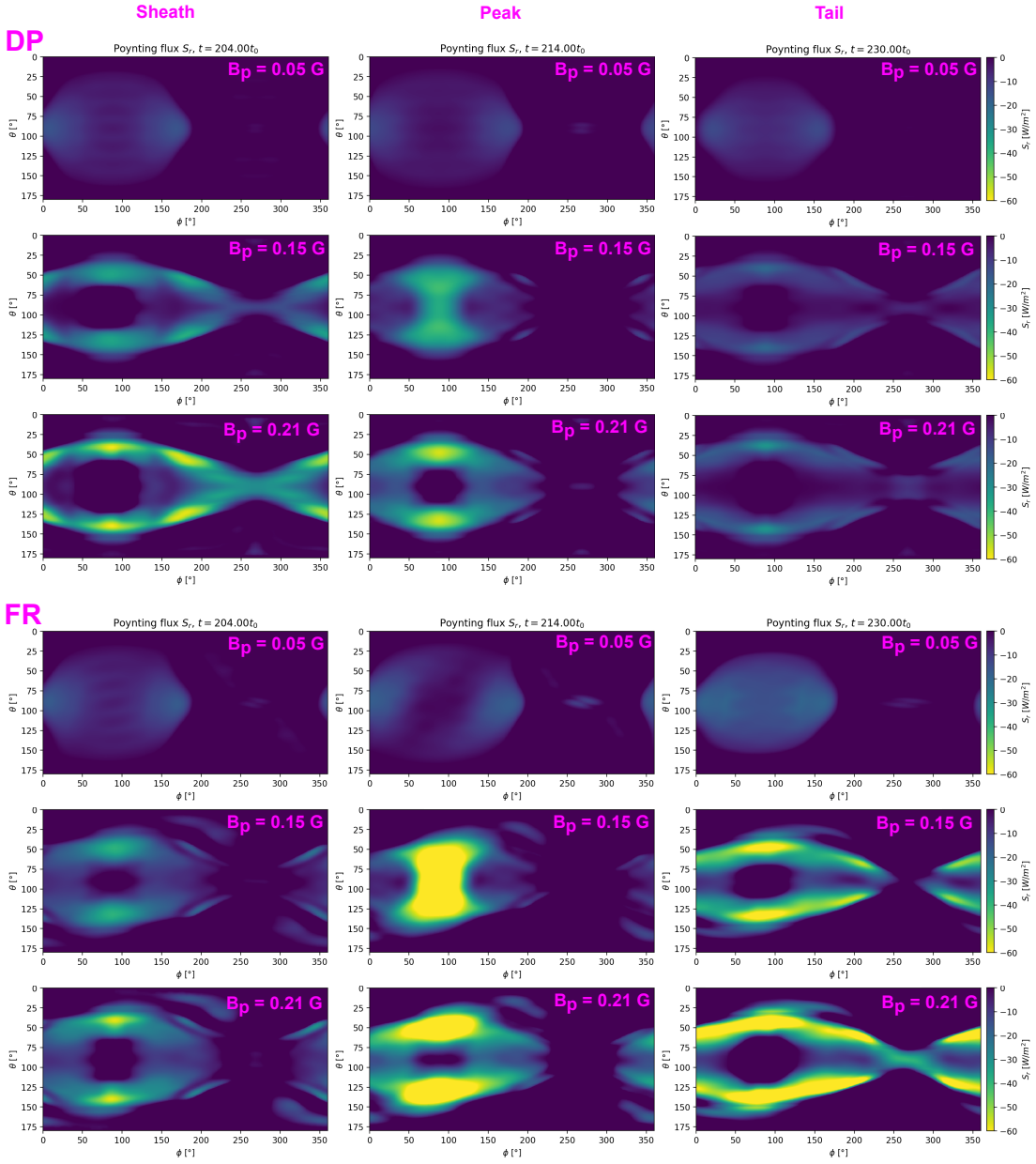

Figure 7.23.: Maps of radial Poynting flux components, S_r, directly above the surface of Trappist-1e. Negative values correspond to the direction towards the planet. The upper and lower block correspond to the DP and FR case. Maps during the CME sheath (left), peak (middle) and tail (right) are shown which illustrate the major structure of Poynting fluxes. The distributions of S_r during the tail as shown remain approximately constant with the magnitude of S_r decreasing steadily.

Poynting flux maps

In Fig. 7.23 we present spatial trends and the evolution of the inward radial component of the Poynting flux, S_{in}^{-}, above the planet's surface. In Sect. 7.5 we discussed the importance of the Poynting flux S_{in}^{-} as a quantity that illustrates magnetic perturbations associated with Alfvén waves that are propagated towards the planet surface. Here we want to show that this argumentation is justified by comparing S_{in}^{-} with dB/dt measured at the surface. Figure 7.23 shows S_{in}^{-} during CME sheath (left), peak (middle) and tail crossing (right) for Trappist-1e. The upper block shows DP the lower FR simulations. We show $B_p = 0.05$ G (top), 0.15 G (middle) and 0.21 G (bottom) cases. The plots show clearly that inward Poynting fluxes are focused mostly around the dayside closed field line region (see the exemplary open–closed field line boundary in Fig. 7.22) with a strong focus on a band near the OCFB. There is, however, a thin band near the OCFB, towards the poles, that is likely dominated by convection driven Poynting fluxes that are not represented by radial Poynting fluxes as the convection dominated Poynting fluxes are dominantly perpendicular to magnetic field lines. This picture becomes increasingly pronounced the stronger B_p becomes. Due to the spatial agreement of S_{in}^{-} with averaged dB/dt (Fig. 7.17) we propose the inner–magnetospheric generation of Poynting fluxes due to magnetospheric compression to be the main driver of interior Joule heating. In Fig. 7.23 is also evident that the best spatial agreement between average dB/dt (Fig. 7.17) and S_{in}^{-} occurs during the CME peak and tail. This indicates that the fast magnetic topology changes during the shock and sheath do not contribute significantly to the magnetic variability. Most heating, thus, is presumably generated during the CME peak and during the decay of the CME peak.

In the following sections we use S_{in}^{-} exclusively to study temporal evolution of interaction generated magnetic variability as function of CME model and time in detail and eventually how planetary magnetic fields affect the transfer of magnetic energy towards the planet surface.

7.5.2. Magnetospheric Poynting fluxes during the CME

The upper panels of Figs. 7.24 and 7.25 show integrated Poynting fluxes as defined in Eq. 7.24 for Trappist-1e and magnetic fields of $B_p = 0.03$, 0.05, 0.09, 0.11 and 0.21 G during the CME event.

The CME shock hits the magnetosphere at about 32 minutes and is followed by a sheath region where plasma density, pressure and magnetic flux density is strongly enhanced. The sheath crossing ends at approximately 42 minutes with DP CMEs and slightly delayed (1-2 minutes) with FR CMEs. Inward Poynting fluxes rapidly increase by 1 to 2 orders of magnitude with the shock hitting the magnetosphere. For planetary magnetic fields from $B_p = 0.05$ G and stronger S_{in}^{-} reach powers of 10^{15-16} W. S_{in}^{-} increase with increasing B_p, the differences, however, become small for $B_p > 0.05$ G. We note that above $B_p = 0.05$ G the magnetospheres always have magnetopause radii greater that R_p and thus complex magnetosheath dynamics do not contribute directly

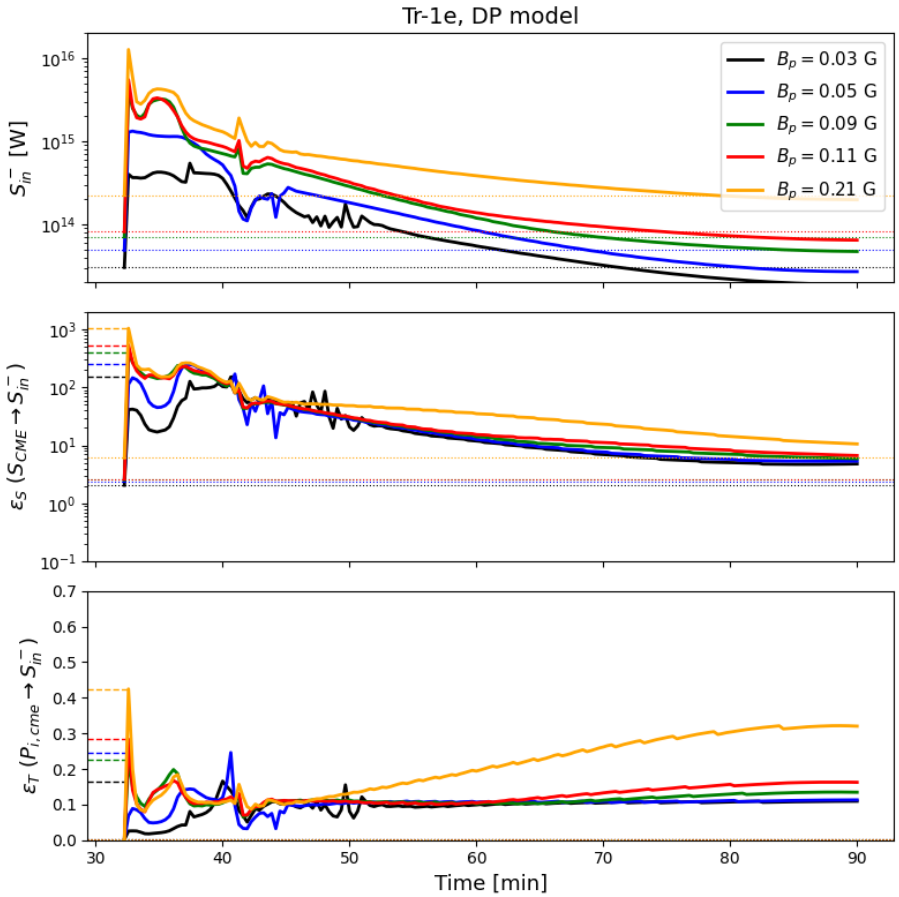

Figure 7.24.: Shown are the time series of S_{in}^- in W (top), ϵ_S (middle) and ϵ_T (bottom) for Trappist-1e DP simulations as function of time during the CME event (see Fig. 7.25 for the FR scenario). Horizontal dashed and dotted lines indicate maximum and initial values. The transfer functions ϵ_S and ϵ_T are defined in Eqs. 7.28 and 7.29.

to the calculated Poynting fluxes. In DP and FR simulations we observe an oscillatory evolution of S_{in}^- during the first 4 minutes. During this time the CME–induced compression and strong magnetic pressure of the compressed planetary magnetic field counteract each other periodically. In both models the total CME energy flux decays following the exponential decrease of the initial CME profile that is stretched and therefore diluted along the flow direction due to the fast CME front. The magnetopause radius increases due to the decreasing CME ram pressure of the diluted CME tail plasma (Fig. 7.9). The stronger B_p is, the slower is the decay of S_{in}^- due to the larger area to intercept CME energy.

For all models strongest Poynting fluxes are generated during the CME sheath and peak crossing with S_{in}^- amounting to 10^{15-16} W. The convected Poynting flux clearly scales with B_p with weaker scaling for $B_p \geq 0.09$ G. From the beginning of the CME

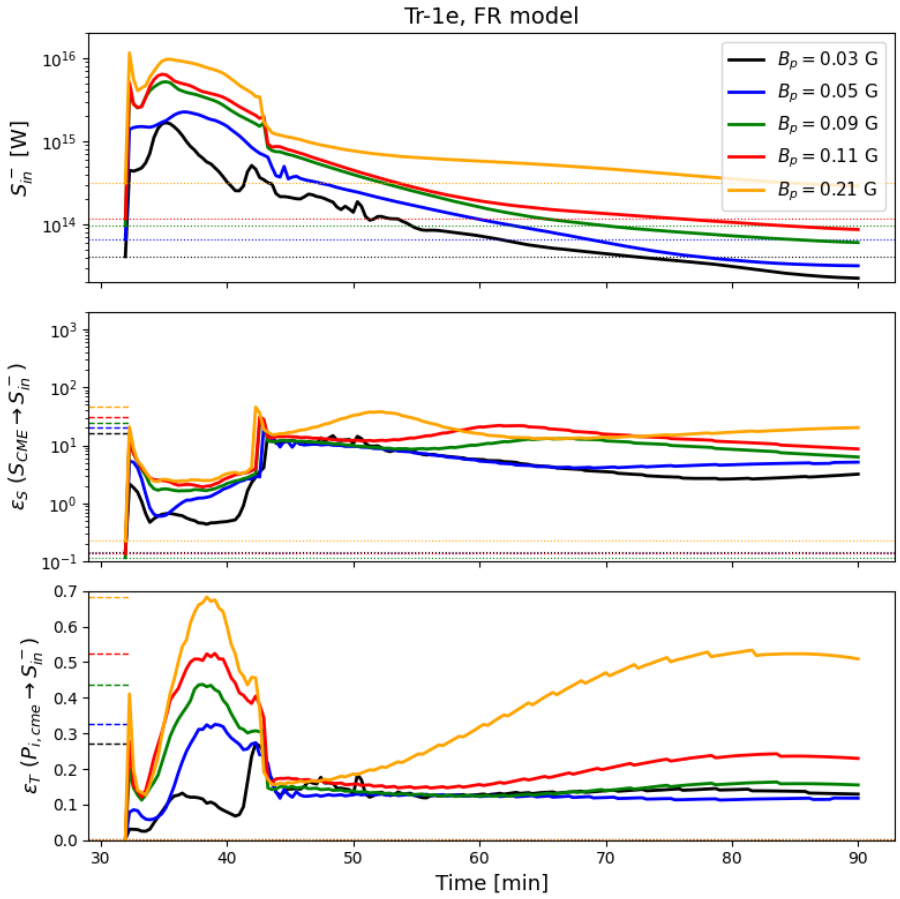

Figure 7.25.: Same caption as in 7.24 but for the FR CME scenario.

event up to the decay phase (50–90 minutes) S_{in}^- drop by approximately one order of magnitude. Nevertheless, the magnetosphere is subject to magnetic topology changes even after the CME peak and it is exposed to enhanced Poynting fluxes for a larger time span compared to the CME sheath and peak crossing.

Transfer of energy fluxes

We now study the transfer of CME energy incident on the magnetosphere towards the planet's surface. We calculate the CME kinetic energy flux, P_{kin}, thermal energy flux, P_{th} and Poynting flux, S_{CME}, with plasma parameters obtained from our simulations

incident on the magnetospheric cross section πR_{mp}^2,

$$P_{kin} = \frac{1}{2}\rho v^3 \pi R_{mp}^2 \tag{7.25}$$

$$P_{th} = \frac{3}{2} n k_B T \pi R_{mp}^2 v \tag{7.26}$$

$$P_B = \frac{B^2}{\mu_0} \pi R_{mp}^2 v_\perp \, , \tag{7.27}$$

where v denotes the CME plasma velocity, $v_\perp$ the velocity perpendicular to the magnetic field, n the plasma number density, T the temperature and B the magnetic flux density. All these parameters are obtained directly in front of the magnetosphere where the CME plasma is not yet perturbed due to the super–fast magnetosonic flow.
We compare the incident CME Poynting flux with S_{in}^- by calculating the Poynting flux ratio

$$\epsilon_S = S_{in}^- / P_B \, . \tag{7.28}$$

We note that ϵ_S is not an efficiency factor (that must be ≤ 1) but a fraction that allows us to get an idea of the amount of S_{in}^- that is generated within the magnetosphere due to magnetic field perturbation (case A, if i.e. $\epsilon_S > 1$). When $\epsilon_S \approx 1$ or < 1 we may expect that Poynting flux is dominantly injected through reconnection and convection (case B).
Additionally, following Elekes & Saur (2023), we calculate the transfer function between total incident energy flux (Eqs. 7.25–7.27) and S_{in}^-,

$$\epsilon_T = \frac{S_{in}^-}{P_{kin} + P_{th} + P_B} \, . \tag{7.29}$$

The transfer function measures the conversion efficiency of incident energy to magnetospheric inward Poynting fluxes. As ϵ_T relates the total available energy to magnetospheric Poynting fluxes it must be smaller than unity. Together, both quantities may be used to assess the interaction strength and to identify energy transfer that occurs due to mechanical interaction (case A) or via reconnection and convection (case B).

In the middle and bottom panels of Figs. 7.24 and 7.25 we show the time series of ϵ_S and ϵ_T, respectively.

In DP model runs, S_{in}^- exceeds the incident Poynting flux by several orders of magnitude. During the CME shock crossing ϵ_S increases for all B_p by two orders of magnitude up to 10^3. These high ϵ_S to indicate a high amount of S_{in}^- generated by closed field line perturbations (case A) within the magnetosphere. The transfer function ϵ_T reaches a maximum value of 0.4 during the shock crossing in the $B_p = 0.21$ G case and about 0.2–0.3 for $B_p \approx 0.05$ G. Afterwards ϵ_T is rather low, near 0.1 and 0.2, indicating a low efficiency of CME energy injection due to reconnection (case B). We thus identify case A to be the dominant mechanism for DP CMEs which is supported by most dB/dt

occurring near the polar cusps (Fig. 7.17, left).

In FR model runs we observe a different behavior of the energy transfer. ϵ_S is significantly lower, between 1 and 60, while ϵ_T is generally higher, between 0.1 and 0.7. This is due to the strong intrinsic magnetic variability and thus Poynting flux already contained within the FR that dominates the total energy flux. Smaller ϵ_S during the FR passing indicate that less magnetic energy is released due to a mechanical interaction. This becomes more clear when focusing on the CME sheath and peak passing, where, nearly for all B_p, ϵ_S falls to values between 0.5 and 3 while ϵ_S is smaller for weaker B_p which is supported by the Q_J scaling with weak B_p in Sect. 7.4.2. This is indicative for dominant Poynting flux and thus magnetic variability transfer along open field lines due to reconnection. Magnetic curvature and thus tension is translated to planetary field lines and with it magnetic perturbations are transferred to the planet. This transfer of magnetic variability is the root cause for the persistent heating efficiency seen in Fig. 7.14. If no or a weaker planetary magnetic field is present the dynamo mechanism (Eq. 5.4) that converts motional energy into magnetic energy (i.e. dB/dt) is weaker. For stronger $B_p \geq 0.05$ G magnetic energy released due to compressional perturbation increases, raising ϵ_S to 2–3.

After the CME peak at about 43 minutes, ϵ_S in FR model runs is about 10 to 40. ϵ_T increases slowly from ≈ 0.2 until the peak value is reached near 80 minutes. The maximum value correlates strongly with with B_p. For $B_p = 0.21$ G it reaches its maximum at 0.5, for $B_p = 0.11$ G roughly 0.2 and for weaker fields ϵ_T remains constant. A similar but much weaker behavior can also be seen in DP model runs where ϵ_S drops fairly constant during the CME tail crossing towards values near 10 and ϵ_T increases slowly up to 0.3 maximum. We interpret the drop in ϵ_S and increase of ϵ_T as an increase in reconnection driven Poynting flux input. For $B_p \leq 0.09$ G ϵ_T remains fairly constant for both models. In the CME tail region, density and velocity drop to minimum values and in the same time, R_{mp} rises (Fig. 7.9). This regime is dominated by CME magnetic field as well as magnetosphere topology changes. The CME magnetic topology is in both models strongly affected by the velocity gradient over the CME tail. This velocity gradient causes stresses in the tail magnetic field and decreases the magnetic pressure within. The FR twisted magnetic field structure slowly breaks down to approach the steady state magnetic field configuration. With increasing magnetosphere size due to the diluted CME tail plasma and the magnetosphere's large cross sectional area to capture CME energy flux we expect the magnetosphere to react more sensitive to changes in the ambient plasma. In the upper panel of Figs. 7.24 and 7.25, for both models S_{in}^{-} also shows much weaker decay after the CME peak for stronger magnetic fields supporting this interpretation. With R_{mp} reaching its maximum ϵ_T also saturates.

In summary we found evidence for a strongly enhanced CME Poynting flux–to–magnetospheric Poynting flux transfer if the CME possesses a flux rope. Mechanically dominated CMEs convert only a small fraction, $\epsilon_T \leq 0.2$ (0.4 peak during shock crossing), of the total energy flux to inward Poynting fluxes above the planet surface. Flux

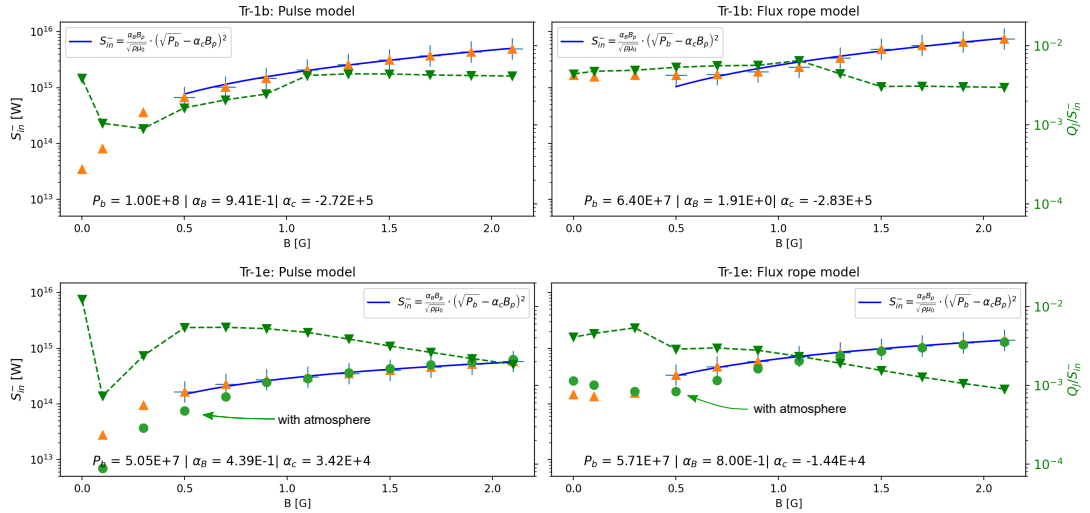

Figure 7.26.: Displayed are time–averaged S_{in}^- in W as function of planetary magnetic field flux density B_p in G. DP results are left, FR results are right. The top row shows Trappist-1b and the bottom row Trappist-1e. Orange triangles denote time–averaged S_{in}^-. Green downward triangles denote the corresponding Ohmic heating to S_{in}^- ratio (right y–axis). The blue solid line is the fit of Eq. 7.34 to the Poynting flux data. Derived fit parameters are shown above the x–axis.

rope CMEs convert the Poynting flux much more efficient to S_{in}^- through reconnection. With the total energy flux dominated by magnetic energy, the fraction of transferred total energy scales very strongly with B_p and reaches up to 0.7.

7.5.3. Scaling behavior of magnetospheric Poynting fluxes and the role of planetary magnetic field strength

As a single–value measure of total inward Poynting flux during the whole CME event, we average S_{in}^- over the CME duration and display it as a function of B_p (Fig. 7.26). We show the average Poynting flux for Trappist-1b (upper panels) and Trappist-1e (bottom panels). Left we show DP and on the right FR model results. Contrary to the heating rates in Fig. 7.14 the averaged Poynting fluxes do not have a maximum within our parameter range. In the Trappist-1b case S_{in}^- increase from about 10^{13} W to 5×10^{15} W (DP) with the magnetic field B_p while in the FR case the Poynting fluxes exhibit a lower limit of 5×10^{15} W. For Trappist-1e the Poynting fluxes are significantly reduced by approximately an order of magnitude while the behavior of S_{in}^- as function of B_p is similar to Trappist-1b. As the external forcing (i.e. the CME) is kept constant this scaling of Poynting fluxes with the intrinsic magnetic field illustrates that stronger fields are capable of absorbing and converting more electromagnetic energy, so that the electromagnetic shielding capability of intrinsic magnetic fields is reduced when they become stronger.

We are interested in understanding the role of B_p on the scaling of S_{in}^- and thus how planetary magnetic fields affect the Poynting flux above the planet's surface.

We argue that the dayside compression of the magnetosphere is the main driver of magnetic variability near the planet for the majority of our parameter range as stated in Sect. 7.5. The Poynting flux generated in this interaction is driven by the perturbation magnetic field δB (case A, see 7.5). The good spatial alignment of S_{in}^- with the majority of dB/dt (Figs. 7.17 and 7.23) supports the interpretation of the Poynting fluxes being associated with Alfvén waves. To get an expression of δB we consider the pre–CME pressure balance between stellar wind and magnetosphere,

$$P_{sw} = \frac{B_p^2(R_{mp})}{2\mu_0} + P_{ms} \ , \tag{7.30}$$

where P_{sw} is the total stellar wind pressure (magnetic, thermal and kinetic) and P_{ms} is the thermal and kinetic pressures of the magnetosphere. Equation 7.30 is valid at the upstream magnetopause, near the stagnation point of the CME plasma. $B_p(R_{mp})$ is the intrinsic magnetic field strength at the magnetopause. During the CME this balance is perturbed by an increase of the incident pressure. The average total pressure during the CME is then $P_{tot} = P_{sw} + \Delta P$. In the new pressure equilibrium the magnetopause is shifted towards the planet where $B_p(r)$ is stronger, $B = B_p(R_{mp}) + \delta B$. This additional δB is produced by the CME forcing and drives the Poynting fluxes that travel along the closed field lines towards the planet. The pressure balance during the CME is then

$$(P_{sw} + \Delta P) = \frac{(B_p(R_{mp}) + \delta B)^2}{2\mu_0} + P_{ms} \ , \tag{7.31}$$

where we assumed the insignificant magnetospheric thermal and ram pressure to remain constant. From Eq. 7.31 we can find an expression for the perturbation magnetic field,

$$\delta B = \sqrt{2\mu_0 \left(P_{tot} - P_{ms}\right)} - B_p(R_{mp}) \ . \tag{7.32}$$

Plugging Eq. 7.32 into the Poynting flux equation (Eq. 7.23) we find

$$S_{in} = \frac{B}{\sqrt{\mu_0 \rho}} \left[\sqrt{2\mu_0 \left(P_{tot} - P_{ms}\right)} - B_p(R_{mp})\right]^2 \mu_0^{-1} \ , \tag{7.33}$$

with the Alfvén velocity $v_A = B/\sqrt{\mu_0 \rho}$. The quantities B and ρ are the magnetic flux and plasma density along the closed field lines. To simplify this expression in order to use B_p as input parameter, we add scaling factors to the magnetic field variables that account for deviations of B at a certain position from the equatorial B_p value, i.e. $\alpha_B B_p$ and $\alpha_c B_p$. The parameters α_c and α_B account for any change of B due to compression of the magnetosphere and for other magnetic contributions to the pressure balance (e.g. magnetic tension or geometric effects as the origin of local δB may be located anywhere at the magnetopause where the CME and planetary contributions in the pressure balance may be different compared to the sub–solar magnetopause where Eq. 7.31 holds). The factor α_B additionally accounts for the deviation of B from B_p

that represents the equatorial magnetic field strength and the error introduced by the assumed constant mass density ρ in the denominator (see below). Since Eq. 7.33 is only valid at the magnetopause near the CME plasma stagnation point, the factors α_B and α_c also accounts for errors introduced by this approximation because the stellar and planetary components of the pressure balance (Eq. 7.31) vary along the magnetopause. To further condense the equation we combine the pressure terms to a single variable, $P_b = P_{tot} - P_{ms}$. The expression for S_{in} now reads

$$S_{in} = \frac{\alpha_B B_p}{\sqrt{\mu_0 \rho}} \left[\sqrt{2\mu_0 P_b} - \alpha_c B_p \right]^2 \mu_0^{-1} \,, \tag{7.34}$$

In our simulations we find the plasma mass density ρ to be approximately $m_i \times 10^{10}$ m^{-3} for Trappist-1b and $\approx m_i 10^9$ m^{-3} for Trappist-1e, with the ion mass $m_i = m_{H^+}$. We keep the corresponding density value in Eq. 7.34 fixed to reduce the number of fit parameters. This however introduces additional errors that might influence the remaining fit parameters, α_B, P_b and α_c.

We fit Eq. 7.34 to the time–averaged S_{in}^- as a function of B_p (Fig. 7.26). We only fit Eq. 7.34 to data with $B_p \geq 0.05$ G because of the magnetospheres being compressed to the surface for weaker fields. Our argumentation for the model does not account for magnetosheath and shock contributions to the Poynting fluxes. In Fig. 7.26 we display the results of the fit as blue curve. The derived fit parameters, α_B, P_b and α_c are shown in the bottom of the plots. Equation 7.34 fits the average S_{in}^- very well. The results in 7.26 suggest that inward Poynting fluxes above the planet's surface scale only with B_p given the fixed incident energy flux and the ion density in the planet's upstream magnetosphere. Effectively S_{in}^- scales with B_p^3 indicating that stronger intrinsic magnetic fields enhance the magnetosphere's intake of external electromagnetic energy. This scaling supports the power law scaling of interior Joule heating due to DP CMEs for $B_p < 0.09$ G (Fig. 7.14).

Due to our model assumptions (i.e. purely compression generated Alfvén waves and no fast mode waves) and the assumed constant mass density render the fit parameters on their own not very useful to interpret. Instead we use the derived α_c, P_b and the input B_p to calculate the characteristic δB from Eq. 7.32. For all data points as well as CME models we find $\delta B \approx 40$ nT for Trappist-1b and $\delta B \approx 30$ nT for Trappist-1e. This typical perturbation is responsible for the radial Poynting fluxes at the planet's surface averaged over the CME event. As the CME energy density is higher at Trappist-1b we also expected δB to be higher. This value corresponds to typical magnetic perturbation at the source region (about 1 R_p away from the planet's surface) from where the perturbation is propagated towards the planet via Alfvén waves.

In Fig. 7.26 we also display the ratio of Q_J to S_{in}^- as green, dashed line to assess how the radial Poynting fluxes translate to interior heating as they supply the planetary surface with the majority of magnetic variations. The Poynting flux–to–interior heating efficiency for magnetic fields above 0.05 G is largest for Trappist-1b, approximately 2–3×10^{-3}, and slightly reduced for Trappist-1e with approximately 10^{-3}. Therefore, according to our model the efficiency is roughly doubled for Trappist-1b compared to

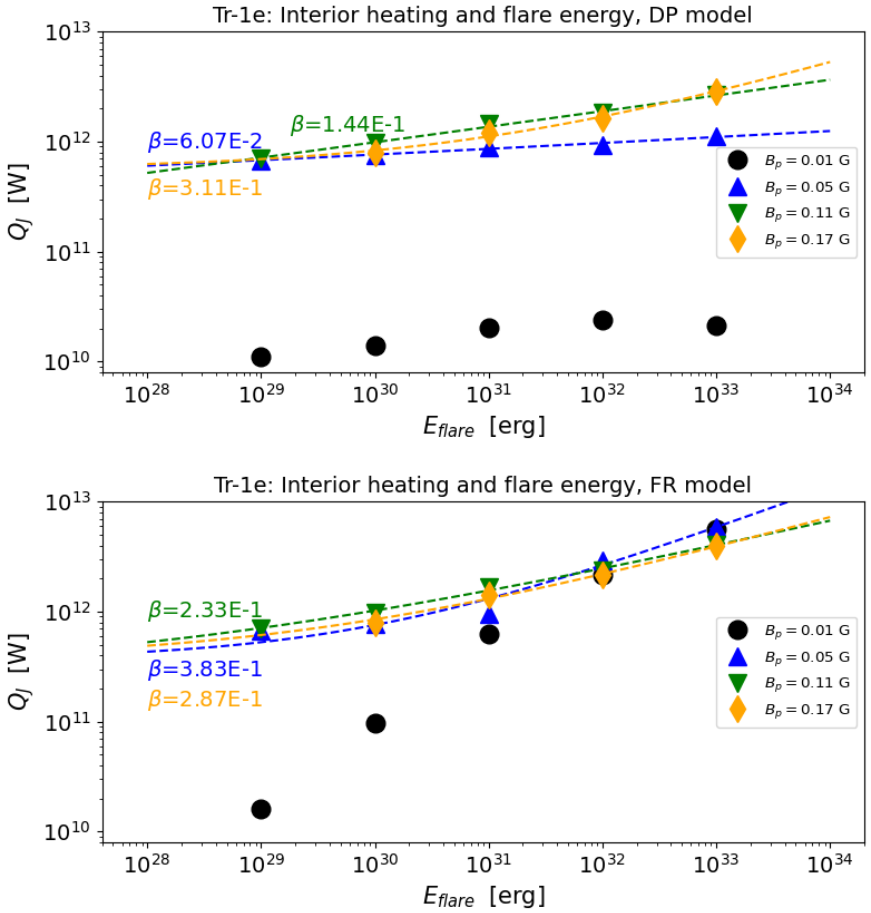

Figure 7.27.: Time–averaged interior heating rates as a function of CME–associated flare energy E_{flare} in erg. Upper and lower panel show DP and FR results. We only show heating rates for $B_p = 0.01$ G (black circles), $B_p = 0.05$ G (blue upward triangles), $B_p = 0.11$ G (green downward triangles) and $B_p = 0.17$ G (yellow diamonds).

e. For Trappist-1e we observe a reduction of efficiency for stronger planetary magnetic fields. This is caused by increased stiffness of the magnetic field due to the $\vec{j} \times \vec{B}$ force counteracting its deformation. Due to the higher energy density of CMEs near Trappist-1b this effect possibly lies outside our parameter space.

7.6. Effect of CME energy on interior Joule heating

We chose our CME model parameters according to scaling laws of flare–CME relations obtained from the Solar system. As our basic energy we considered a flare bolometric energy of 10^{31} erg. Flares of this energy occur on average once per day according to the recent flare frequency distribution of Howard et al. (2023). However, there may be less or more energetic flares. Here we address the question of how the interior heating relates

to the flare energy. For this purpose we additionally considered flare energies of 10^{29}, 10^{30}, 10^{32} and 10^{33} erg that all reside in a reasonable energy range for the Trappist-1 (Howard et al. 2023). We ran our MHD model with CMEs associated with these flare energies (see Sect. 7.2.4 for our CME models and Eqs. 7.7, 7.8 and 7.14 for flare–CME scaling laws). Unfortunately we were not able to run the same MHD model for more energetic CMEs ($E_{flare} \geq 10^{34}$ erg) due to limitations of the numerical method. However, these anyway pose extremely rare and unlikely events (Howard et al. 2023; Paudel et al. 2018). The CME duration is kept at one hour. In Fig. 7.27 we show resulting heating rates as function of flare Energy in erg. For simplicity we only consider Trappist-1e with magnetic fields of $B_p = 0.01$, 0.05, 0.11 and 0.17 G.

Heating rates in the DP CME case scale locally within our parameter space according to a power law, $Q_J \propto E_{flare}^{\beta}$, with $\beta \approx 0.06$ ($B_p = 0.05$ G), $\beta \approx 0.14$ ($B_p = 0.11$ G) and $\beta \approx 0.3$ ($B_p = 0.17$ G). The CME–planet interaction with $B_p = 0.01$ G is governed by different physics due to the magnetosphere being compressed to the surface and therefore we do not fit to these data points. In the DP case we find a tendency towards higher power law exponents with increasing magnetic field strength. This is supported by our findings in Sect. 7.4.2. Magnetic variability exerted on the magnetospheres due to mechanically dominated CMEs scales strongly with B_p since in the DP case dB/dt is generated by magnetospheric compression and nearly no intrinsic dB/dt is contained within the CME.
For $B_p = 0.05$ G the heating rates are almost constant over the considered energy range of 5 orders of magnitude and amount to $Q_J \approx 7$–8×10^{11} W. For $B_p = 0.11$ G and above Q_J rises from $Q_J \approx 7 \times 10^{11}$ ($E_{flare} = 10^{29}$ erg) to 3×10^{12} W ($E_{flare} = 10^{33}$ erg). The dependence of Q_J on B_p in the DP case enhances with increasing flare energy $E_{flare} > 10^{31}$ erg. More specifically, in the regime of power law scaling of Q_J with B_p in Fig. 7.14 ($\approx$ 0–0.07 G) the slope of $Q_J(B_p)$ increases. For the weakest considered intrinsic magnetic field of $B_p = 0.01$ G resulting heating rises from $Q_J = 10^{10}$ ($E_{flare} = 10^{29}$ erg) to $Q_J = 2 \times 10^{10}$ ($E_{flare} = 10^{32}$ erg). After that the heating rates seem to saturate or even fall again.

In the FR model case we observe a stronger scaling of heating rates with E_{flare}. For $B_p > 0.01$ G we find the same weak dependence of Q_J on the intrinsic magnetic field B_p like in Sect. 7.4.2 over the whole flare energy range. Heating rates, however, scale more strongly with E_{flare} according to a power law with exponent $\beta \approx 0.23$–0.38 for all $B_p \geq 0.05$ G. Heating rates increase by an order of magnitude from $Q_J \approx 6 \times 10^{11}$ ($E_{flare} = 10^{29}$ erg) to 4×10^{12} ($E_{flare} = 10^{33}$ erg). We again find no unifying scaling law to describe Q_J as function of B_p for $B_p < 0.05$ G due to the upstream magnetosphere being compressed to the surface. For $B_p = 0.01$ G heating rates increase from $Q_J \approx 2 \times 10^{10}$ W ($E_{flare} = 10^{29}$ erg) to 6×10^{12} W ($E_{flare} = 10^{33}$ erg). In this case heating rates thus increase by almost one order of magnitude if we increase the flare energy by an order of magnitude. Contrary to previous results in Sect. 7.4.2 the dependence of Q_J on B_p increases significantly for $E_{flare} \leq 10^{31}$ erg. We account this to the energy partition of the CME kinetic and magnetic energy. According to Eqs. 7.7–7.8

and Eqs. 7.14–7.15 the CME velocity grows slower with flare energy compared to the FR magnetic field strength. From $E_{flare} = 10^{30}$ erg to 10^{33} erg the CME velocity enhances by a factor of 1.5 while the FR magnetic field strength by 18. Therefore, by decreasing E_{flare} we quickly reach a kinetic energy dominated regime.

In summary, in the DP case, Q_J scales less strong with E_{flare} when the CME does not posses a flux rope, $Q_J^{DP} \propto E_{flare}^{0.06-0.31}$. The dependence of Q_J on B_p increases towards higher flare energies. For CMEs with a magnetic flux rope structure, however, we find a moderately strong scaling that is constant for all intrinsic magnetic fields above approximately 0.03G, $Q_J^{FR} \propto E_{flare}^{0.23-0.38}$. In the next section (Sect. 7.6.1) we discuss in detail reasons for the relatively weak scaling of interior heating rates (and thus dB/dt) with CME–associated flare energy.

7.6.1. Weak scaling of surface magnetic variability with B_p and E_{flare}

An intriguing observation made by looking at the scaling of interior Joule heating rates Q_J with flare associated CME energy (Fig. 7.27) is the relatively weak scaling of Q_J with flare energy and with the planetary magnetic field strength. In regard to DP CMEs Q_J scales according to $Q_J \propto E_{flare}^{0.06}$ ($B_p = 0.05$ G) up to $Q_J \propto E_{flare}^{0.3}$ for higher planetary magnetic fields. For FR CMEs the scaling remains fairly constant for all planetary magnetic fields with $Q_J \propto E_{flare}^{0.23-0.38}$. Although the FR magnetic field strength is indeed approximately doubled per increase of flare energy by an order of magnitude (see Table 7.2), which would fit very well into the scaling presented in Fig. 7.27 due to heating rates approximately scaling with dB/dt squared (Grayver et al. 2022), the increase in kinetic energy is not visibly reflected in these results. This is a striking result as one might expect a more pronounced scaling of compression induced magnetic field amplification within the magnetosphere with increasing CME kinetic energy. The scaling in the DP scenario is even lower than in the FR case. This leads to the conclusion that there must be some mechanism weakening the magnetosphere's inductive and thus magnetic response to CMEs while increasing the CME energy by several orders of magnitude. Potentially, there might be even an upper limit on how strong a compressed magnetic field may be amplified.

We clearly identify two different regimes that have to be studied separately, namely the mechanical regime (DP CMEs) and the combined mechanical and magnetic regime (FR CMEs). In the mechanical regime magnetic variability dB/dt is generated by mechanical perturbation of the planetary magnetosphere. In the magnetic regime flux rope dB/dt is transferred to the planetary magnetic field due to reconnection. Magnetic variability in general is governed by induction which is described by the induction equation (Eq.

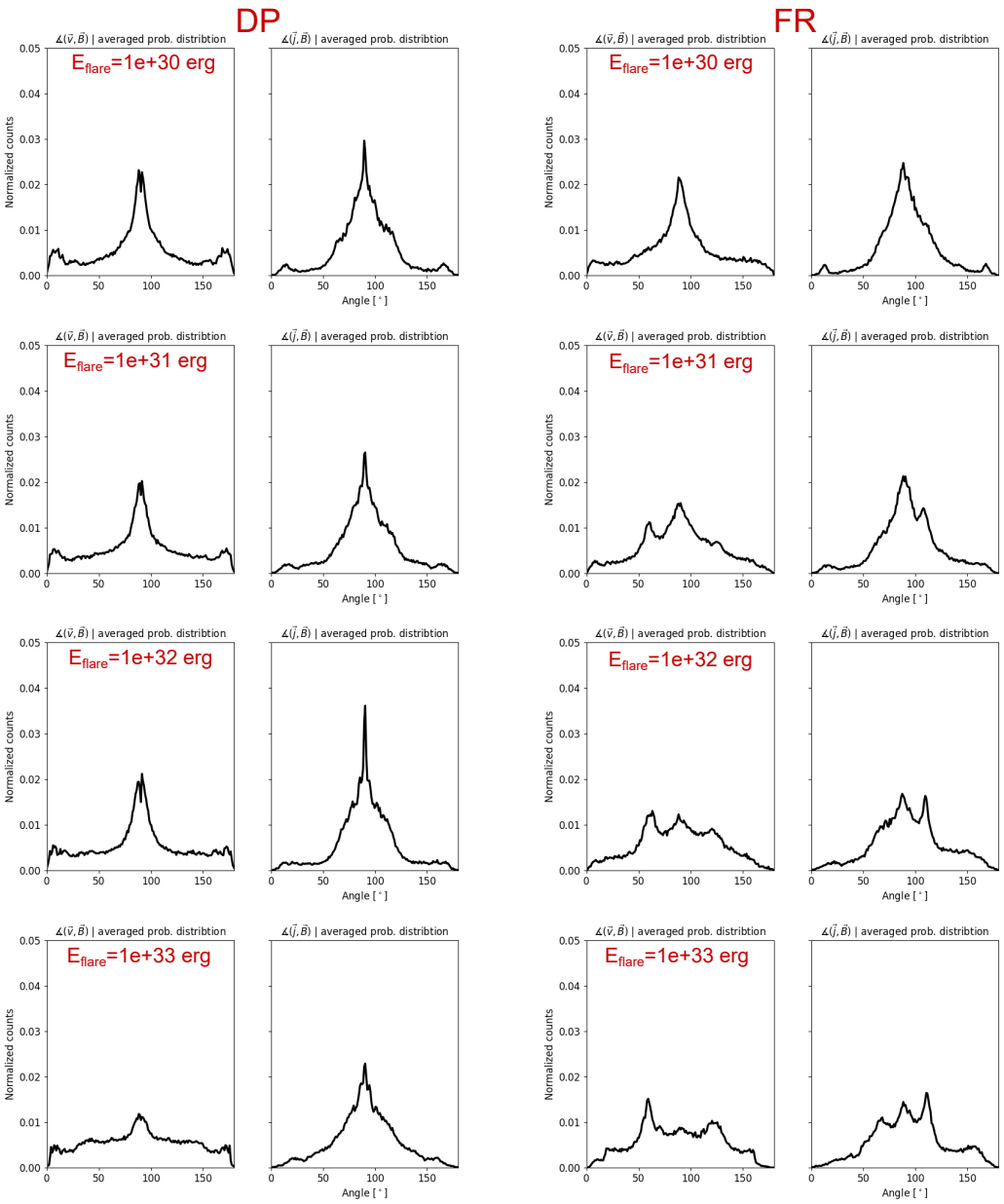

Figure 7.28.: Displayed are normalized probability distributions of the angles between velocity and magnetic field (left within one panel) and velocity and electric current (right within one panel) averaged during the CME shock, sheath and peak passing. Left panels correspond to DP and right panels to FR CME scenarios. All distributions correspond to $B = 0.17$ G simulations with CME–associated flare energy of $E_{flare} = 10^{30}$ erg (top) to $E_{flare} = 10^{33}$ erg (bottom).

5.4),

$$\frac{\partial}{\partial t}\vec{B} = \nabla \times \left(\vec{v} \times \vec{B}\right) \tag{7.35}$$

$$= - \underbrace{\vec{B}\nabla \cdot \vec{v}}_{\text{compression}} - \underbrace{(\vec{v} \cdot \nabla)\,\vec{B}}_{\text{advection}} + \underbrace{\left(\vec{B} \cdot \nabla\right)\vec{v}}_{\text{stretching}} . \tag{7.36}$$

Induction in the magnetosphere is governed by the flow across the magnetic field. The induction equation can be decomposed into several components linked to different mechanisms that cause magnetic variations.

The first term on the right hand side of Eq. 7.36 is related to the divergence of plasma motion and thus compression or rarefaction of magnetic flux. In the previous sections we have shown the dominance of magnetospheric compression in regard to magnetic variability. Magnetospheric compression is counteracted by the amplified magnetic field that enhances the magnetic pressure within the magnetosphere. Additionally, as the magnetopause is pushed nearer to the planet when exposed to higher CME dynamic pressure, the magnetic pressure rises not only with the amplified magnetic field strength ($\propto B_p^2$) but also with the lower distance r to the planet ($\propto r^{-6}$). The question is if the dynamic pressure of the CME growths fast enough with flare energy to overcome the enhanced magnetic pressure that rises due to the magnetopause being pushed nearer to the planet.
The second term in Eq. 7.36 is an advection term that describes the transport of magnetic flux with the flow. This certainly plays a significant role in magnetosphere where field lines are advected through the magnetosphere due to magnetic tension on reconnected field lines (e.g. the Dungey cycle).
The last term in Eq. 7.36 describes curvature that is enforced on magnetic field lines by velocity gradients along field lines. This consequently leads to stretching of field lines which is accompanied with an increase of magnetic field strength.

Essential for the generation of magnetic variability and thus free magnetic energy is the flow's work done against the $\vec{j} \times \vec{B}$ force, i.e. when the flow is forced in a direction perpendicular to the magnetic field by the interaction. We can identify regions in the magnetosphere where induction ($\nabla \times \vec{v} \times \vec{B}$) has the highest potential by probing the angles between plasma flow and magnetic field direction. Thus, we calculate the angle θ between velocity and magnetic field vector using their dot product,

$$\cos\theta = \frac{\vec{v} \cdot \vec{B}}{|\vec{v}||\vec{B}|} . \tag{7.37}$$

We calculate the angles in the whole magnetosphere and construct distribution functions from the corresponding data array by gathering the counts of specific angles between 0 and 180 degrees. Then we normalize the distribution with the total amount of data points. We accumulate the data for the time span between CME shock up to 10 minutes after the CME peak and average the data over this time span (see the CME profiles in

Fig. 7.5). We note that we also obtained the angle distributions for specific, stationary times during the CME event and could not find significant differences between the CME onset and later times. Therefore we restrict ourselves to the distributions averaged over the main CME phase. We repeat this process for DP and FR simulation runs with $B_p = 0.17$ G and for CME–associated flare energies from 10^{30}–10^{33} erg. We also calculate the distribution functions of angles between current density $\vec{j}$ and $\vec{B}$ to get an associated measure of the $\vec{j} \times \vec{B}$ force.

In Fig. 7.28 we show the resulting distribution functions. In the DP CME scenario (left) the distributions are all clearly unimodal with sharp maxima near 90 degrees. However, we observe that the magnetospheric flow is increasingly forced away from the direction perpendicular to the magnetic field and consequently we expect induction in the magnetosphere to potentially decline in efficiency. The angles between $\vec{j}$ and $\vec{B}$ also show increasingly deviate from 90 degrees for more energetic CMEs. Together the decline in perpendicularity between velocity, current density and magnetic field suggests that less work is done against the $\vec{j} \times \vec{B}$ force within the magnetosphere and that the magnetospheric dynamo has less potential to amplify the magnetic field within the magnetosphere which is eventually evident in a weaker increase of dB/dt on the planetary surface.

In the FR CME scenario we observe a similar trend but instead of decreasing perpendicularity the unimodal distributions transform increasingly to bimodal distributions as we increase the CME energy. The perpendicularity clearly decreases in regard to both, $\vec{v} \times \vec{B}$ and $\vec{j} \times \vec{B}$, but new peaks develop at angles around 60 and 120 degrees. These peaks are possibly forced upon the magnetospheric flow due to reconnection with the helical FR magnetic field whose peak magnetic field increases by about a factor of two per magnitude of flare energy (see Table 7.2).

In the DP scenario the distribution is increasingly flattened with increasing CME energy without a specific bimodal nature in the distribution. This leads to weaker potential in the magnetospheric dynamo and therefore to a weaker increase of dB/dt generated by the CME–planet interaction. In the Fr case new maxima develop focused around the 90 degree point, near 60 and 120 degrees, which explains the enhanced scaling of interior Joule heating rates with flare energy, as the magnetospheric dynamo loses its potential at a lower rate compared to the DP case.

Thus, we can summarize that, while increasing the kinetic energy of a mechanically dominated CME, the magnetosphere flow is increasingly forced away from a direction perpendicular to the magnetic field, which essentially decreases to efficiency of the magnetospheric dynamo. For CMEs with even higher kinetic energy ($E_{flare} \geq 10^{31}$ erg) we expect the angle distribution between $\vec{v}$ and $\vec{B}$ to flatten out, thus prohibiting any increase in magnetospheric dynamo action. For CMEs with intrinsic magnetic fields (FR CMEs) we observe no flattening of the distribution but merely the transformation to a bimodal form with the two peaks somewhat near the perpendicularity between $\vec{v}$ and $\vec{B}$. Thus we expect magnetic variability due to FR CMEs to scale further when increasing the CME energy.

Table 7.3.: Statistical flare and CME parameters †.

E_{flare} (erg)	10^{29}	10^{30}	10^{31}	10^{32}	10^{33}
Flares per day, n_E	4	4	1	10^{-2}	10^{-3}
CMEs per T, N_E ⋆	116.8	116.8	29.2	0.29	0.03

⋆ $N_E = n_E\, f\, \times T$

† Estimated number of CME events per considered timescale T and flare energy E_{flare} based on the flare frequency distribution of Howard et al. (2023) and Paudel et al. (2018). The averaging timescale is $T = 1$ year and the CME event fraction is $f = 0.084$ (Grayver et al. 2022). See the corresponding Sect. 7.7.1.

Table 7.4.: Time–averaged annual Joule heating rates⋆ in the interior of Trappist-1e due to CMEs ⋆⋆.

B_p (G)	0.01	0.05	0.11	0.17	Model
Tr-1b†					
		8.56e-1	4.66	11.33	DP
		4.94	9.1	10.1	FR
Tr-1e					
	1.34e-2	7.36e-1	9.06e-1	7.36e-1	DP
	1.23e-1	7.48e-1	9.36e-1	7.65e-1	FR

⋆ Heating rates are given in units of TW.

† Underlying $Q_J(E)$ was estimated from Tr-1e case and not obtained from simulations.

⋆⋆ Annual average heating rates are calculated using Eq. 7.38, the parameters in Table 7.3 and the single–event heating rates for different CME–associated flare energies (Sect. 7.6).

7.7. Long–term interior heating and possible effects on planets

In this section we discuss possible long term effects of CME induced interior heating on the planets Trappist-1b and e and discuss possible observational signatures of CME–planet interactions. In section 7.7.1 we discuss the annual averaged interior Joule heating rates due to frequent CME events by taking into account flare frequency distributions and the heating rates as a function of flare energy (Sect. 7.6). In Sect. 7.7.2 we assess the potential increase in surface temperature. In Sect. 7.7.3 we discuss the dynamic spectra of possible radio bursts excited by the interplanetary shock–planet interaction.

7.7.1. Flare–CME statistics and annual heating rates

With the flare frequency distributions of Trappist-1 (Howard et al. 2023; Paudel et al. 2018) and single–event average Joule heating rates for different CME–associated flare energies obtained in this study (Sect. 7.6) we are able to calculate the time–averaged heating rate over longer durations incorporating several different CME events. Given the average number of flare events per day, n_E, for each flare energy E taken from Howard et al. (2023) we can estimate the average number N_E of flares per year for each flare energy, $N_E = n_E \cdot 365$. Single event heating rates derived with our CME model are shown in Fig. 7.27. The fraction of all flare events that are associated with a CME which hits a planet is $f \approx 0.08$ according to the estimate of Grayver et al. (2022). The sum of all CME events during one year divided by the total amount of events including all energies, $N = \sum N_E$, gives us the annual averaged heating rate due to CMEs, Q_{CME},

$$Q_{CME} = \frac{f}{N} \sum_E N_E \cdot Q_E \, . \tag{7.38}$$

Resulting annual average heating rates are displayed in the lower box in Table 7.4. We also estimated the annual heating rates for Tr-1b by assuming $Q_J(E)$ having the same form as for Tr-1e (7.27). We scaled the fit function in Fig. 7.27 to match the heating rate $Q_J(E = 10^{31}$ erg) obtained from our basic model for Tr-1b (Sect. 7.4.2, Fig. 7.14). With $Q_J(E)$ obtained we applied the same calculations as for Tr-1e presented in this section. We omitted the data for $B_p = 0.01$ G due to the unlike scaling in this case (Fig. 7.27).

Annual interior heating due to CMEs are in the order of 1–10 TW for Trappist-1b and 0.1–1 TW for Trappist-1e. Comparing these results to the heating rates of Grayver et al. (2022) obtained from a homogeneous interior model we find our heating rates to lie within their σ interval but about 1–2 orders of magnitude lower compared to the mean values of Grayver et al. (2022). The comparison is certainly difficult to make, as we have not conducted a statistical study of CME events over geological time scales ourselves. But assuming the mean values of Grayver et al. (2022) to be the most accurate, we find, that, by incorporating a more realistic CME model and time–dependent MHD simulations of the CME–planet interaction, CME induced interior Joule heating gets much more insignificant. Our heating rates for Trappist-1e are also about 2 orders of magnitude lower than tidal heating rates estimated by Bolmont et al. (2020). Compared to the interior heating rates due to the planet's motion through the stellar dipole field, our obtained dissipation rates are roughly 1–2 order of magnitude lower. Thus, tidal heating can be expected to be much more important for close–in planets. This even holds for weakly eccentric orbits like probably those of the Trappist-1 planets (Grimm et al. 2018) since, for example, tidal heating rates within Io are already in the order of several 100 TW despite its low eccentricity.

7.7.2. Effects on the surface temperature

Trappist-1 and many other terrestrial exoplanets around cool stars are expected to be tidally locked to their host star, so that the same hemisphere is facing the star at all times. CME–induced interior heating is strongly localized when the planetary magnetic field exceeds a certain strength, $B_p \approx 0.05$ G in our model (see Sect. 7.4.4). Therefore we expect continuous heating of the planetary dayside if the Trappist-1 planets are magnetized and regularly hit by CMEs. If additionally the interior heat conduction and dissipation time scales are larger than the time between successive CMEs, the dissipated energy within the planet may contribute to the planetary surface heat flux due to the heat flux away from the planetary core due to the temperature gradient. When this heating power, $P_{CME} = Q_{CME}$ (Table 7.4), together with stellar radiative heating, is in equilibrium with radiative cooling of the planet's surface, P_{CME} adds to the planetary equilibrium temperature according to,

$$T_{eq} = \left(\frac{L_\star}{16\pi\sigma a^2} + \frac{P_{cme}}{4\pi\sigma R_p^2} \right)^{1/4} , \tag{7.39}$$

where $L_\star$ is the stellar luminosity and a the planet's distance to the star. The increase of planetary equilibrium temperature with the addition of CME induced interior heating is on the order of 10^{-3} K for Trappist-1b. Therefore, CME heating of the planetary interior does not affect the surface temperature of the planet but may affect the temperature gradient within the planetary mantle.

7.7.3. Emission signatures of CME–planet interactions

In this section we briefly discuss the possible observational signatures of CME–planet interactions. Interplanetary shocks and CMEs in the stellar corona can produce type II radio bursts caused by accelerated electrons at the shock (Wilson et al. 2009). The emission frequency is near the local electron plasma frequency and typically, as the CMEs emerge from the star and expand, the frequency decreases together with the electron density according to $\nu \propto \sqrt{n_e}$ (Wilson et al. 2009). The question naturally arises whether the reversed process can cause observable radio bursts. When shocks intersect a planetary obstacle the shocked plasma is compressed, heated and energized through energy released by reconnection. This process might result in a radio burst that follows an inverse dynamical spectrum compared to radio bursts from CMEs near a star. We assess this possibility by calculating the dynamic spectrum of the electron plasma frequency near the planetary shock as a function of time. We consider the time from just before the shock hitting the planetary magnetosphere until the CME peak passes the planet (≈ 12 minutes after the shock). We calculate the electron plasma frequency ν_{pe} (under the assumption of quasi neutrality, $n_e = n_i$) in all corresponding grid cells as function of time. We additionally integrate the Poynting flux through the associated grid cells. We add the Poynting fluxes associated with a certain plasma frequency at a single time together and get a spectrum where, at each frequency we have the associated integrated Poynting flux that shows us the electromagnetic energy content within

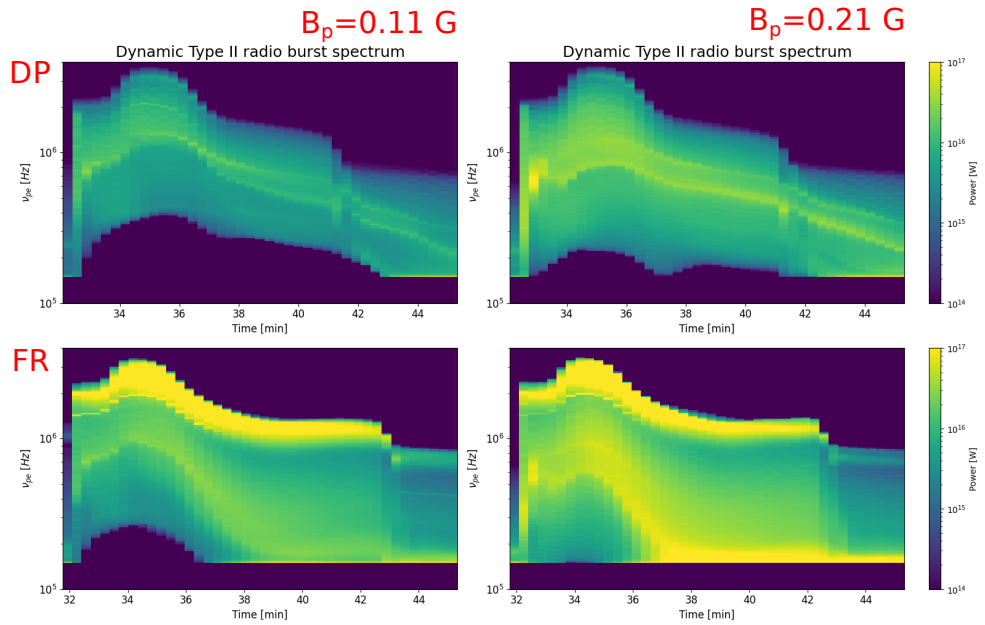

Figure 7.29.: Estimates of dynamic spectra of potential type II radio emission near the CME–planet shock interface. Color contours depict the integrated Poynting flux within a certain frequency bin (y–axis, in Hz) at a specific time (x–axis, in minutes). Upper panels depict DP CME results, lower panels FR CME results (with $E_{flare} = 10^{31}$ erg). Left and right panels correspond to a planetary magnetic field with $B_p = 0.11$ G and $B_p = 0.21$ G, respectively.

the corresponding regions as a function of frequency. By repeating this process for the mentioned time period, we eventually arrive at a dynamic spectrum, i.e. frequency as a function of time. It is evident from Figs. 7.7 and 7.8 that there is a sharp contrast in plasma densities between the magnetosheath and the magnetosphere as well as to the upstream plasma. Due to the plasma density's sharp peak within the magnetosheath we have a well constrained estimate of available electromagnetic power in the shocked plasma since the regions with low density (upstream and within the magnetosphere) are naturally separated due to the lower densities and frequencies. We integrate the spectrum within a spherical shell with minimum radius of $R_p = 1.2$ and a maximum of $R_p = 2.5$. With this choice we always include the upstream magnetospheath where density is highest.

We first consider only the CME scenario with $E_{flare} = 10^{31}$ erg. In Fig. Fig. 7.29 the dynamic spectra for Trappist-1e with $B_p = 0.11$ and 0.21 G. The electron plasma frequency in the steady state stellar wind is about 50 KHz and is slightly enhanced in the magnetospheath due to plasma compression. As soon as the CME shock intersects the magnetosphere ν_{pe} rises to approximately 20 MHz. From the shock onset the maximum plasma frequency rises to a peak near 30 MHz and then decays over the period of 4 minutes to about 10 MHz. The behavior of maximum ν_{pe} is nearly equal in the DP and FR scenario, as well as for both magnetic fields considered. The differences between the

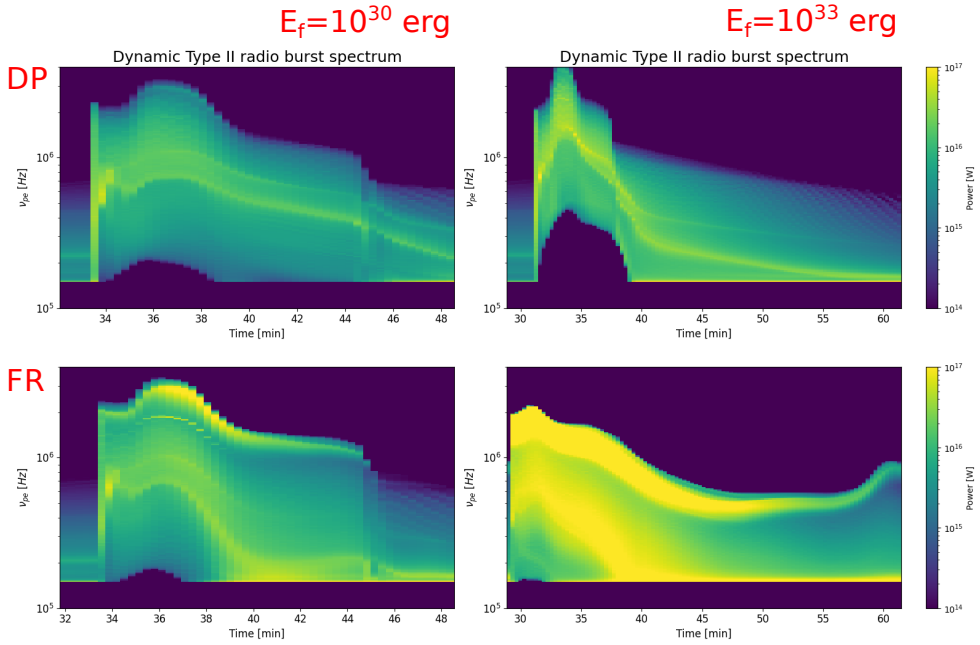

Figure 7.30.: Same caption as in Fig. 7.29 but for $E_{flare} = 10^{30}$ erg (left) and $E_{flare} = 10^{33}$ erg (right) with a planetary magnetic field strength of $B_p = 0.17$ G.

models are evident when looking at the integrated Poynting fluxes. Due to reconnection that is present between the FR and the magnetosphere, the powers corresponding to the peak frequencies are in the FR scenario on the order of 10^{17} W and last near this peak power for the whole duration of the CME sheath passing. In the DP scenario the peak powers do not follow the peak frequencies but are shifted downwards towards 1 MHz and less. Here the peak powers are on the order of $1 - -8 \times 10^{16}$ W, considerably lower than in the FR scenario. In general we can distinguish between two distinct features in the spectrum. One defines the peak frequencies and the other follows a similar trend but at strongly reduced frequencies. We interpret the upper frequency regime to correspond to the shocked CME and magnetosheath plasma while the lower distinct frequency regime corresponds to magnetospheric plasma which has a significantly lower plasma density (e.g. visible in Figs. 7.7-7.8). With the peak powers in the DP scenario originating from the planetary magnetosphere supports our results from Sect. 7.5, which show that the interaction energetics are mainly dominated by the compression of the magnetosphere. Comparing the results of $B_p = 0.11$ G and $B_p = 0.21$ G models we do not observe clear differences in the behavior of the spectrum but the powers are clearly enhanced towards the stronger magnetic field.

When considering different CME energies (10^{30} and 10^{33} erg in Fig. 7.30) and a planetary magnetic field of $B_p = 0.17$ G we see the same behavior of the spectra as in the 10^{31} erg case. The peak frequencies in the DP scenario, however, are strongly enhanced due to the higher plasma density content in the CME with $E_{flare} = 10^{33}$ erg. The peak

frequency rises up to 40 MHz while the peak frequencies in the FR scenario remain fairly the same regardless of the CME energy. The peak powers in the DP scenario are surprisingly largely unaffected by the CME energy while there is a strong correlation between CME energy and Poynting flux in the FR scenario.

Ultimately, we are interested in whether radio bursts with such dynamic spectra could also be observed on Earth. During the CME shock and sheath interacting with the magnetosphere, all peak frequencies in the FR scenario between 20 and 30 MHz exceed the ionospheric cutoff of 10 MHz. The corresponding Poynting fluxes are at 10^{17} W and higher. We use the formula for the radio flux (Eq. 6.17) and assume the same solid angle of the beam, 1.6 sr, given in Sect. 6.5.2.4. We assume radio efficiencies between $\epsilon = 10^{-4}$ and 10^{-1} and an emission bandwidth equal to the peak plasma frequency (about 20 MHz). With the distance to Trappist-1 of approximately 39 ly we find the radio flux at Earth to be in the range of $\Phi = 25 \times 10^{-3,0}\,\mu$Jy for the FR scenario. The sensitivity limit of LOFAR, for example, is roughly 50 mJy (Sect. 6.5.2). In the DP scenario the peak frequencies are hardly above the 10 MHz threshold and the powers are significantly reduced. Purely mechanical CMEs are therefore, according to our model, not capable to produce significant radio emission.

We note that ECMI driven auroral radio emission is potentially also possible. Within our parameter range, however, the maximum gyro frequency is ≈ 1 MHz when considering $B_p = 0.21$ G (with twice the field strength at the poles). Since this emission frequency lies below the terrestrial ionospheric cutoff (10 MHz) we do not expect observable radio emission to occur, even if we consider a considerably stronger up to 1 G (≈ 3 MHz).

We can therefore conclude that radio emission generated by the CME–planet interaction at Trappist-1e is probably not observable from Earth and that flux rope CMEs potentially produce stronger radio emission. The distance from the Trappist-1 system is probably the biggest problem in regard to radio observability, as the powers converted in the emission source region are even higher as those of predicted for steady state auroral regions at τ Boötis b. This makes the CME–Planet interaction at Trappist-1, or at any close–in exoplanet, an extremely energetic, potential radio emission source which exceeds the steady state converted auroral energy fluxes at τ Boötis b by 1–2 orders of magnitude. Furthermore, in contrast to stellar type 2 bursts caused by emerging CME shocks, the dynamic spectrum of a CME–planet interaction shows a distinct trend. The frequency rises abruptly and then decay at a lower rate.

7.8. Summary

In this study, we investigated the interaction between CMEs and exoplanets using MHD simulations. We chose Trappist-1b and e as an exemplary case, and studied the resulting magnetic variability on the surface of the planets. CME–generated magnetic variations at the surface of the planets induce electric currents in the planetary interior, which

dissipate energy in the form of heat. We have developed an MHD model to simulate the interaction of density pulse (DP) and flux rope (FR) CMEs with magnetized and non-magnetized planets. We considered a range of intrinsic dipolar magnetic fields from $B_p = 0$ G to a nearly Earth–like field with $B_p = 0.21$ G. We derived CME parameters from flare–CME scaling laws obtained from Solar system observations and applied them to CMEs with associated flare energies from $E_{flare} = 10^{29}$ to 10^{33} erg. Our CMEs have a duration of 1 hour. We used a planetary interior model with constant electric conductivity and calculated induction heating using the model of Grayver et al. (2022) in post–processing. For Trappist-1 we also considered an O_2 atmosphere and calculated ionospheric Joule heating during the CME event. In the following we summarize the main results of this study.

1) We find the interior Joule heating rates to significantly increase when the planet is magnetized given a CME without a magnetic flux rope. In contrast, heating rates only scale weak with B_p if the CME possesses a magnetic flux rope. The heating rates averaged within 1 hour events range from $Q_J \approx 0.1$ TW (Tr-1b) and $Q_J = 0.01$ TW (Tr-1e) to $Q_J \approx 10$ TW (Tr-1b) and $Q_J = 1$ TW (Tr-1e). This increase of interior induction heating with intrinsic magnetic field strength supports the finding of Grayver et al. (2022). Within our range of intrinsic magnetic fields heating rates for Tr-1e saturate at $B_p \approx 0.1$ G (1 TW). We attribute this to the stiffness of the magnetosphere due to counteracting $\vec{j} \times \vec{B}$–force which increases with B_p. Compression of the magnetosphere is argued to be the main driver of magnetic variability at the planetary surface. For flux rope CMEs and with weak planetary B_p the intrinsic magnetic variability of the CME can be directly transported to the planet's surface. With increasing B_p, however, the magnetic energy that can be released by mechanical perturbation exceeds the magnetic energy of the flux rope, so that from $B_p > 0.15$ G (Tr-1b) and $B_p > 0.05$ G (Tr-1e) the FR CMEs effectively resemble the DP CMEs.

2) When considering an atmosphere around Trappist-1e interior Joule heating rates are only affected for weak planetary magnetic fields $B_p < 0.1$ G. Interior heating due to CMEs with flux ropes is enhanced when an atmosphere is present due to additional tension imposed on the reconnected magnetic field lines. Ionospheric Joule heating ranges from $1–2 \times 10^4$ TW for weakly magnetized planets and drops by one order of magnitude for stronger magnetic fields. Joule heating of the upper atmosphere does not rely on electromagnetic induction but directly results from the increase of magnetospheric electric fields. With this nearly instantaneous heating during CMEs atmospheric inflation and possible erosion might be drastically enhanced.

3) We generated maps of time–averaged magnetic variability, dB/dt, above the planetary surface and took regions of highest average dB/dt as proxy for maxima in inductive heating potential. While for weak B_p average dB/dt is distributed over the whole planetary surface, the maxima of dB/dt become increasingly localized with stronger B_p and focus on areas near the upstream polar cusps within the closed field line region where the planetary magnetic field is radial. We argue that most dB/dt is generated by magnetospheric compression due to its maxima in the upstream magnetosphere. This

perturbation is then propagated via Alfvén and to a lesser extend via fast mode waves towards the polar cusps. We generated maps of inward oriented radial Poynting fluxes S_{in}^{-}, which are most likely associated with Alfvén waves, at the planetary surface and find them to correspond spatially well with the dB/dt maxima.

4) Our results suggests that, in an electromagnetic sense, planetary magnetic fields enhance the capability of planets to receive and convert the energy injected through CMEs. The generation and transfer of field–aligned Poynting fluxes towards the planet as well as inductive coupling between magnetospheric variations and the planet's interior correlates well with increasing intrinsic magnetic field strength. The dependence of this behavior is only moderately sensitive to changes in CME energy density if the planet is at least weakly magnetized. Planetary magnetic fields do not shield the planet's surface from electromagnetic energy received from CMEs and other bursty stellar wind variations.

5) We find a weak scaling of interior heating rates Q_J with CME–associated flare energy within our parameter space. For DP CMEs the scaling increases from $Q_J \propto E_{flare}^{0.06}$ for $B_p = 0.05$ G to $Q_J \propto E_{flare}^{0.3}$ for stronger magnetic fields above approximately 0.1 G where the scaling seems to saturate. Weakly magnetized planets (here $B_p \approx 0.01$ G) show no clear scaling in the DP case due to the upstream magnetosphere being compressed to the planetary surface. For FR CMEs we find Q_J to scale with E_{flare} according to $Q_J \propto E_{flare}^{0.23-0.38}$ for all $B_p > 0.01$ G. Heating rates scale strongly with E_{flare} for very weakly magnetized planets with $B_p \leq 0.01$ G.

6) From the flare frequency distribution of the Trappist-1 star we estimated the average amount of CME events given the interior heating rates as function of CME–associated flare energy. We calculated the annual average interior heating rates to be on the order of 10 TW (Tr-1b) and 1 TW (Tr-1e). These heating rates are approximately 2 orders of magnitude lower compared to the results of Grayver et al. (2022). Our heating rates are also about 1 order of magnitude lower compared to those calculated using planetary motion through a changing stellar magnetic field (Kislyakova et al. 2017). Thus, considering an MHD model of the CME–planet interaction we find the significance of CME–induced interior Joule heating to be much more insignificant compared to pure electromagnetic estimates of interior heating. Our estimated average estimates are about 2 orders of magnitude lower than estimates for tidal heating in Trappist-1b (Bolmont et al. 2020). Furthermore, the planetary equilibrium temperature is not significantly affected by CME–induced interior heating.

7) According to our Trappist-1e model, electromagnetic powers converted within the shocked plasma during the CME–planet interaction are on the order of 10^{17} W and thus exceed the converted power of the steady–state interaction of τ Boötis b with its stellar wind by 1–2 orders of magnitude. This makes CME–planet interactions at close–in exoplanets a potentially strong radio source. Radio emission originating from such CME–planet interactions exhibit dynamical spectra that are distinct from those expected from CME induced type 2 bursts emerging from stellar coronae. During the magnetospheric compression the frequencies rise and then decay at a much slower rate. At Trappist-1 we expect peak frequencies near and above 20 MHz.

8. Summary and conclusion

In this thesis we have studied the space environment of three close–in exoplanets by means of magnetohydrodynamic simulations.

Using a tentative constraint on the magnetic field strength of the Hot Jupiter τ Boötis b provided by Turner et al. (2021), who tentatively observed possible auroral radio emission from the planet, we have modeled the interaction of τ Boötis b with the surrounding steady state stellar wind. Due to the uncertainty of current stellar wind predictions we assessed the interaction energetics as a function stellar wind density and pressure as well as of planetary magnetic field orientation. Our results suggest that the interaction, albeit converting electromagnetic energy in the order of 10^{18} W, is likely not energetic enough to power the observed radio emission. The interaction is, for most of our parameter space, super–Aflvénic and thus a magnetospheric emission scenario would be most likely. However, in order to produce radio emission within the observed range of radio fluxes, radio wave generation efficiencies approximately 2 orders of magnitude higher than those observed at Jupiter are needed. The magnetic cycle of τ Boötis A on the order of hundreds of days up to one year results in periodic opening and closing of τ Boötis b's magnetosphere. A closed magnetosphere, i.e. when no planetary magnetic field line connects to the stellar wind magnetic field, results in converted electromagnetic energy fluxes one order of magnitude lower compared to the open magnetosphere scenario. We have assessed the possibility of auroral radio emission to escape the ionosphere of τ Boötis b. Our results indicate that the considered magnetic field strength of τ Boötis b is not high enough for the radio frequencies to exceed the local plasma frequencies in order to escape the planet's environment.

A striking question engaging a large amount of exoplanet researchers is why it is seemingly so difficult to observe exoplanetary magnetic fields in the radio domain. Our results suggest that, albeit the extremely high converted energy fluxes in star–planet systems in close proximity to the star is, these systems are likely not energetic enough for our current telescopes to be detectable. Furthermore we emphasize the importance of stellar wind predictions as the stellar wind energetics clearly dominate the power supply for emissions. It is certainly not enough to look for close–in giant planets in proximity to the solar system. Additionally we need sophisticated and accurate predictions of the stellar environment in order to derive expected radio fluxes from exoplanets by simulating the stellar wind–planet interactions rigorously.

In the context of Trappist-1 we studied the interaction between Trappist-1b and e with coronal mass ejections originating from the central M–dwarf star. We assessed the time–dependent energetics of the interaction and dissected the role of planetary magnetic fields in controlling the dissipation of energy in the interior of the planets. We assumed coronal mass ejections with associated flare energies between 10^{29} and 10^{33} erg.

In order to better understand the transfer of different types of energy contained in the coronal mass ejections towards the planets and their interiors, we considered purely mechanical and magnetically dominated coronal mass ejections. Our results show that the efficiency of energy conversion from purely mechanical coronal mass ejections to magnetized planets highly depends on the planetary magnetic field strength. The magnetic variability caused by the perturbation of the magnetosphere is clearly dominated by magnetospheric compression. With the increase in magnetic field strength the efficiency of magnetospheric dynamo action enhances accordingly. Therefore, when considering purely mechanical coronal mass ejections, planetary magnetic field enhance the energy intake. We additionally showed that the energy input into the magnetosphere scales with the planetary magnetic field strength cubed. When considering magnetized coronal mass ejections, planetary magnetic fields do not significantly influence the conversion of energy. Due to reconnection between flux rope and planet occurring in this scenario magnetic energy is more directly injected into the magnetosphere without the need to convert the mechanical energy of the coronal mass ejection to magnetic perturbations. For single coronal mass ejection events we found interior dissipation rates in the order of 1 to 10 TW. Above a certain planetary magnetic field, approximately 0.11 G, magnetic variability and consequently interior heating reaches its maximum. For stronger magnetic fields the dissipation rates for both coronal mass ejection models decay slowly.

Surprisingly, we found that by increasing the CME energy density by orders of magnitude the magnetic field perturbation within the magnetosphere enhances only little. The scaling is slightly enhanced for stronger planetary magnetic fields and magnetized coronal mass ejections. The magnetospheric dynamo seems to saturate at some point when the coronal mass ejection's energy content rises. With increasing incident energy the flow within the magnetosphere is forced away from a state where induction is effective, i.e. the flow is directed away from a direction perpendicular to the magnetic field. Therefore, in our model, we expect the magnetic field amplification due to magnetospheric compression to saturate for some coronal mass ejection energies above 10^{33} erg. Enhancing the planetary magnetic field strength might push the saturation limit towards higher energies.

Lastly we assessed the possibility of radio emission originating from the shocked plasma at the interface between coronal mass ejection and magnetosphere. While the energies produced in our model are not enough to cause radio emission observable at Earth due to the distance between Earth and Trappist-1, the converted powers are 1–2 orders of magnitude higher compared to the auroral powers of τ Boötis b in a steady state stellar wind. Furthermore, the dynamic spectrum of the plasma frequency during the interaction shows distinct features that could be easily distinguishable from stellar radio bursts caused by emerging coronal mass ejections.

Bibliography

Aarnio, A. N., Matt, S. P., & Stassun, K. G. 2012, ApJ, 760, 9

Aarnio, A. N., Stassun, K. G., Hughes, W. J., & McGregor, S. L. 2011, Sol. Phys., 268, 195

Adams, F. C. 2011, ApJ, 730, 27

Agol, E., Dorn, C., Grimm, S. L., et al. 2021, The Planetary Science Journal, 2, 1

Airapetian, V. S., Barnes, R., Cohen, O., et al. 2020, International Journal of Astrobiology, 19, 136

Airapetian, V. S., Danchi, W. C., Dong, C. F., et al. 2018, arXiv e-prints, arXiv:1801.07333

Airapetian, V. S., Glocer, A., Khazanov, G. V., et al. 2017, ApJ, 836, L3

Alexander, R. D., Wynn, G. A., Mohammed, H., Nichols, J. D., & Ercolano, B. 2016, MNRAS, 456, 2766

Alvarado-Gómez, J. D., Drake, J. J., Cohen, O., Moschou, S. P., & Garraffo, C. 2018, ApJ, 862, 93

Alvarado-Gómez, J. D., Hussain, G. A. J., Cohen, O., et al. 2016, A&A, 594, A95

Amari, T., Aly, J. J., Luciani, J. F., Mikic, Z., & Linker, J. 2011, ApJ, 742, L27

Anderson, B. J., Johnson, C. L., Korth, H., et al. 2014, Geophys. Res. Lett., 41, 7444

Aschwanden, M. J. 2017, ApJ, 847, 27

Aschwanden, M. J., Tarbell, T. D., Nightingale, R. W., et al. 2000, ApJ, 535, 1047

Astudillo-Defru, N., Delfosse, X., Bonfils, X., et al. 2017, A&A, 600, A13

Atreya, S. K., Mahaffy, P. R., Niemann, H. B., Wong, M. H., & Owen, T. C. 2003, Planet. Space Sci., 51, 105

Bale, S. D., Reiner, M. J., Bougeret, J. L., et al. 1999, Geophys. Res. Lett., 26, 1573

Barr, A. C., Dobos, V., & Kiss, L. L. 2018, A&A, 613, A37

Bastian, T., Cotton, B., & Hallinan, G. 2022, arXiv e-prints, arXiv:2206.14099

Baumjohann, W. & Treumann, R. A. 1996, Basic space plasma physics

Baumjohann, W. & Treumann, R. A. 2012, Basic space plasma physics (Imperial College Press)

Beard, D. B. 1960, Phys. Rev. Lett., 5, 89

Benna, M., Anderson, B. J., Baker, D. N., et al. 2010, Icarus, 209, 3

Berger, M. A. 1984, Geophysical and Astrophysical Fluid Dynamics, 30, 79

Biondo, R., Pagano, P., Reale, F., & Bemporad, A. 2021, A&A, 654, L3

Bisikalo, D. V., Kaigorodov, P. V., Ionov, D. E., & Shematovich, V. I. 2013, Astronomy Reports, 57, 715

Blackman, E. G. 2015, Space Sci. Rev., 188, 59

Bloot, S., Callingham, J. R., Vedantham, H. K., et al. 2024, A&A, 682, A170

Bochanski, J. J., Hawley, S. L., Covey, K. R., et al. 2010, AJ, 139, 2679

Bolmont, E., Breton, S. N., Tobie, G., et al. 2020, A&A, 644, A165
Bonfanti, A., Ortolani, S., & Nascimbeni, V. 2016, A&A, 585, A5
Bonfils, X., Delfosse, X., Udry, S., et al. 2013, A&A, 549, A109
Boro Saikia, S., Jin, M., Johnstone, C. P., et al. 2020, A&A, 635, A178
Bourrier, V., de Wit, J., Bolmont, E., et al. 2017a, AJ, 154, 121
Bourrier, V., Ehrenreich, D., Wheatley, P. J., et al. 2017b, A&A, 599, L3
Brogi, M., Snellen, I. A. G., de Kok, R. J., et al. 2012, Nature, 486, 502
Brown, E. L., Marsden, S. C., Mengel, M. W., et al. 2021, MNRAS, 501, 3981
Brun, A. S. & Browning, M. K. 2017, Living Reviews in Solar Physics, 14, 4
Burgasser, A. J. & Mamajek, E. E. 2017, ApJ, 845, 110
Butler, R. P., Marcy, G. W., Williams, E., Hauser, H., & Shirts, P. 1997, The Astrophysical Journal, 474, L115
Castro-González, A., Lillo-Box, J., Correia, A. C. M., et al. 2024, A&A, 684, A160
Cauley, P. W., Shkolnik, E. L., Llama, J., & Lanza, A. F. 2019, Nature Astronomy, 3, 1128
Cecconi, B., Witasse, O., Jackman, C. M., Sánchez-Cano, B., & Mays, M. L. 2022, Frontiers in Astronomy and Space Sciences, 9, 800279
Chabrier, G. & Baraffe, I. 1997, A&A, 327, 1039
Chané, E., Saur, J., Neubauer, F. M., Raeder, J., & Poedts, S. 2012, Journal of Geophysical Research (Space Physics), 117, A09217
Chané, E., van der Holst, B., Jacobs, C., Poedts, S., & Kimpe, D. 2006, A&A, 447, 727
Charbonneau, P. 2014, ARA&A, 52, 251
Chen, A. Q., Chen, P. F., & Fang, C. 2006, A&A, 456, 1153
Chen, P. F. 2011, Living Reviews in Solar Physics, 8, 1
Chen, Y.-W., Shue, J.-H., Zhong, J., & Shen, H.-W. 2023, ApJ, 957, 26
Christensen, A. B., Yee, J.-H., Bishop, R. L., et al. 2012, Journal of Geophysical Research (Space Physics), 117, A04315
Christensen, U. R., Holzwarth, V., & Reiners, A. 2009, Nature, 457, 167
Clark, R. N. 1980, Icarus, 44, 388
Cliver, E. W., Webb, D. F., & Howard, R. A. 1999, Sol. Phys., 187, 89
Cohen, O., Drake, J. J., Glocer, A., et al. 2014, The Astrophysical Journal, 790, 57 (13pp)
Cohen, O., Glocer, A., Garraffo, C., et al. 2024, ApJ, 962, 157
Cohen, O., Kashyap, V. L., Drake, J. J., et al. 2011, ApJ, 733, 67
Cohen, O., Ma, Y., Drake, J. J., et al. 2015, ApJ, 806, 41
Compagnino, A., Romano, P., & Zuccarello, F. 2017, Sol. Phys., 292, 5
Cuntz, M., Saar, S. H., & Musielak, Z. E. 2000, ApJ, 533, L151
Daley-Yates, S. & Stevens, I. R. 2018, MNRAS, 479, 1194
Dasso, S., Mandrini, C. H., Démoulin, P., & Luoni, M. L. 2006, A&A, 455, 349
Davies, A. G., Perry, J. E., Williams, D. A., & Nelson, D. M. 2024, Nature Astronomy, 8, 94
de Wit, J., Wakeford, H. R., Lewis, N. K., et al. 2018, Nature Astronomy, 2, 214
Dedner, A., Kemm, F., Kröner, D., et al. 2002, Journal of Computational Physics, 175, 645

Démoulin, P., Janvier, M., & Dasso, S. 2016, Sol. Phys., 291, 531
Desai, R. T., Freeman, M. P., Eastwood, J. P., et al. 2021, Geophys. Res. Lett., 48, e92554
Desai, R. T., Zhang, H., Davies, E. E., et al. 2020, Sol. Phys., 295, 130
Dessler, A. J. & Parker, E. N. 1959, J. Geophys. Res., 64, 2239
Dibraccio, G. A., Slavin, J. A., Boardsen, S. A., et al. 2013, Journal of Geophysical Research (Space Physics), 118, 997
Dobos, V., Barr, A. C., & Kiss, L. L. 2019, A&A, 624, A2
Donati, J. F. & Brown, S. F. 1997, A&A, 326, 1135
Donati, J. F., Moutou, C., Farès, R., et al. 2008, MNRAS, 385, 1179
Dong, C., Jin, M., Lingam, M., et al. 2018, Proceedings of the National Academy of Science, 115, 260
Dorn, C., Mosegaard, K., Grimm, S. L., & Alibert, Y. 2018, ApJ, 865, 20
Drake, J. J., Cohen, O., Yashiro, S., & Gopalswamy, N. 2013, ApJ, 764, 170
Dressing, C. D. & Charbonneau, D. 2015, ApJ, 807, 45
Duling, S., Saur, J., & Wicht, J. 2014, Journal of Geophysical Research (Space Physics), 119, 4412
Dungey, J. W. 1961, Phys. Rev. Lett., 6, 47
Eastwood, J. P., Hietala, H., Toth, G., Phan, T. D., & Fujimoto, M. 2015, Space Sci. Rev., 188, 251
Elekes, F. & Saur, J. 2023, A&A, 671, A133
Erkaev, N. V., Weber, C., Grießmeier, J. M., et al. 2022, MNRAS, 512, 4869
Eviatar, A. & Barbosa, D. D. 1984, J. Geophys. Res., 89, 7393
exoplanet.eu. 2024, Encyclopaedia of exoplanetary systems, https://exoplanet.eu/plots/ [Accessed: 26. Sep 2024]
Fares, R., Donati, J. F., Moutou, C., et al. 2009, MNRAS, 398, 1383
Fares, R., Moutou, C., Donati, J. F., et al. 2013, MNRAS, 435, 1451
Farrell, W. M., Desch, M. D., & Zarka, P. 1999, J. Geophys. Res., 104, 14025
Ferraro, V. C. A. 1952, J. Geophys. Res., 57, 15
Ferraro, V. C. A. 1960, J. Geophys. Res., 65, 3951
Forbes, T. G. 2000, J. Geophys. Res., 105, 23153
Franklin, K. L. & Burke, B. F. 1958, J. Geophys. Res., 63, 807
Galloway, D. J. & Weiss, N. O. 1981, ApJ, 243, 945
Ganushkina, N., Jaynes, A., & Liemohn, M. 2017, Space Sci. Rev., 212, 1315
García Muñoz, A. 2023, A&A, 672, A77
Garraffo, C., Drake, J. J., Cohen, O., Alvarado-Gómez, J. D., & Moschou, S. P. 2017, ApJ, 843, L33
Gérard, J. C., Bonfond, B., Grodent, D., et al. 2014, Journal of Geophysical Research (Space Physics), 119, 9072
Gillon, M., Triaud, A. H. M. J., Demory, B.-O., et al. 2017, Nature, 542, 456
Glassmeier, K.-H., Grosser, J., Auster, U., et al. 2007, Space Sci. Rev., 132, 511
Glazier, A. L., Howard, W. S., Corbett, H., et al. 2020, ApJ, 900, 27
Godolt, M., Tosi, N., Stracke, B., et al. 2019, A&A, 625, A12
Gold, T. & Hoyle, F. 1960, MNRAS, 120, 89

Gombosi, T. I. & Killeen, T. L. 1987, J. Geophys. Res., 92, 4725
Gray, R. O., Napier, M. G., & Winkler, L. I. 2001, AJ, 121, 2148
Grayver, A., Bower, D. J., Saur, J., Dorn, C., & Morris, B. M. 2022, ApJ, 941, L7
Greene, T. P., Bell, T. J., Ducrot, E., et al. 2023, Nature, 618, 39
Grießmeier, J.-M. 2015, in Astrophysics and Space Science Library, Vol. 411, Characterizing Stellar and Exoplanetary Environments, ed. H. Lammer & M. Khodachenko, 213
Griessmeier, J. M. 2017, in Planetary Radio Emissions VIII, ed. G. Fischer, G. Mann, M. Panchenko, & P. Zarka, 285–299
Grießmeier, J. M., Motschmann, U., Mann, G., & Rucker, H. O. 2005, A&A, 437, 717
Grießmeier, J. M., Preusse, S., Khodachenko, M., et al. 2007a, Planet. Space Sci., 55, 618
Grießmeier, J. M., Zarka, P., & Girard, J. N. 2011, Radio Science, 46, RS0F09
Grießmeier, J. M., Zarka, P., & Spreeuw, H. 2007b, A&A, 475, 359
Grimm, S. L., Demory, B.-O., Gillon, M., et al. 2018, A&A, 613, A68
Grodent, D. 2015, Space Sci. Rev., 187, 23
Gronoff, G., Arras, P., Baraka, S., et al. 2020, Journal of Geophysical Research (Space Physics), 125, e27639
Günther, M. N., Zhan, Z., Seager, S., et al. 2020, AJ, 159, 60
Gurumath, S. R., Hiremath, K. M., & Ramasubramanian, V. 2018, IAU Symposium, 340, 242
Hall, J. C. 2008, Living Reviews in Solar Physics, 5, 2
Hallinan, G., Antonova, A., Doyle, J. G., et al. 2008, ApJ, 684, 644
Hasegawa, H., Fujimoto, M., Phan, T. D., et al. 2004, Nature, 430, 755
Hess, S. L. G. & Zarka, P. 2011, A&A, 531, A29
Hill, T. W. 2001, J. Geophys. Res., 106, 8101
Hinson, D. P., Twicken, J. D., & Karayel, E. T. 1998, J. Geophys. Res., 103, 9505
Höning, D. & Spohn, T. 2023, Astrobiology, 23, 372
Höning, D., Tosi, N., & Spohn, T. 2019, A&A, 627, A48
Hosteaux, S., Chané, E., & Poedts, S. 2019, A&A, 632, A89
Howard, W. S., Corbett, H., Law, N. M., et al. 2019, ApJ, 881, 9
Howard, W. S., Kowalski, A. F., Flagg, L., et al. 2023, ApJ, 959, 64
Hu, R., Bello-Arufe, A., Zhang, M., et al. 2024, Nature, 630, 609
Ilin, E. & Poppenhaeger, K. 2022, MNRAS, 513, 4579
Ilin, E., Poppenhaeger, K., Schmidt, S. J., et al. 2021, MNRAS, 507, 1723
Ilin, E., Poppenhäger, K., Chebly, J., Ilić, N., & Alvarado-Gómez, J. D. 2024, MNRAS, 527, 3395
Ip, W.-H., Kopp, A., & Hu, J.-H. 2004, ApJ, 602, L53
Irwin, J., Berta, Z. K., Burke, C. J., et al. 2011, ApJ, 727, 56
Iyemori, T. 1990, Journal of Geomagnetism and Geoelectricity, 42, 1249
Jardine, M. & Collier Cameron, A. 2008, A&A, 490, 843
Jardine, M., Vidotto, A. A., & See, V. 2017, MNRAS, 465, L25
Jeffers, S. V., Mengel, M., Moutou, C., et al. 2018, MNRAS, 479, 5266

Jia, X., Slavin, J. A., Gombosi, T. I., et al. 2015, Journal of Geophysical Research (Space Physics), 120, 4763
Jian, L., Russell, C. T., Luhmann, J. G., & Skoug, R. M. 2006, Sol. Phys., 239, 393
Johnstone, C. P., Güdel, M., Lammer, H., & Kislyakova, K. G. 2018, A&A, 617, A107
Justesen, A. B. & Albrecht, S. 2019, A&A, 625, A59
Kahler, S. W. & Reames, D. V. 1991, J. Geophys. Res., 96, 9419
Karoff, C., Knudsen, M. F., De Cat, P., et al. 2016, Nature Communications, 7, 11058
Kavanagh, R. D., Vidotto, A. A., Klein, B., et al. 2021, MNRAS, 504, 1511
Kavanagh, R. D., Vidotto, A. A., Ó Fionnagáin, D., et al. 2020, in Solar and Stellar Magnetic Fields: Origins and Manifestations, ed. A. Kosovichev, S. Strassmeier, & M. Jardine, Vol. 354, 305–309
Kavanagh, R. D., Vidotto, A. A., Vedantham, H. K., et al. 2022, MNRAS, 514, 675
Kay, C., Airapetian, V. S., Lüftinger, T., & Kochukhov, O. 2019, ApJ, 886, L37
Kay, C., Opher, M., & Kornbleuth, M. 2016, ApJ, 826, 195
Keiling, A. 2009, Space Sci. Rev., 142, 73
Killen, R., Cremonese, G., Lammer, H., et al. 2007, Space Sci. Rev., 132, 433
Kilpua, E. K. J., Isavnin, A., Vourlidas, A., Koskinen, H. E. J., & Rodriguez, L. 2013, Annales Geophysicae, 31, 1251
Kilpua, E. K. J., Lugaz, N., Mays, M. L., & Temmer, M. 2019, Space Weather, 17, 498
Kislyakova, K. & Noack, L. 2020, A&A, 636, L10
Kislyakova, K. G., Fossati, L., Johnstone, C. P., et al. 2018, ApJ, 858, 105
Kislyakova, K. G., Holmström, M., Lammer, H., Odert, P., & Khodachenko, M. L. 2014, Science, 346, 981
Kislyakova, K. G., Noack, L., Johnstone, C. P., et al. 2017, Nature Astronomy, 1, 878
Kislyakova, K. G., Pilat-Lohinger, E., Funk, B., et al. 2016, MNRAS, 461, 988
Klein, B., Zicher, N., Kavanagh, R. D., et al. 2022, MNRAS, 512, 5067
Klein, L. W. & Burlaga, L. F. 1982, J. Geophys. Res., 87, 613
Kochukhov, O. 2021, A&A Rev., 29, 1
Kopp, A., Schilp, S., & Preusse, S. 2011, ApJ, 729, 116
Kopparapu, R. K., Ramirez, R., Kasting, J. F., et al. 2013, ApJ, 765, 131
Kopparapu, R. K., Ramirez, R. M., SchottelKotte, J., et al. 2014, ApJ, 787, L29
Kopparapu, R. k., Wolf, E. T., Haqq-Misra, J., et al. 2016, ApJ, 819, 84
Koskinen, T. T., Cho, J. Y. K., Achilleos, N., & Aylward, A. D. 2010, ApJ, 722, 178
Koskinen, T. T., Harris, M. J., Yelle, R. V., & Lavvas, P. 2013, Icarus, 226, 1678
Krissansen-Totton, J. 2023, The Astrophysical Journal Letters, 951, L39
Krissansen-Totton, J. & Fortney, J. J. 2022, ApJ, 933, 115
Krissansen-Totton, J., Wogan, N., Thompson, M., & Fortney, J. J. 2024, Nature Communications, 15, 8374
Lai, D., Helling, C., & van den Heuvel, E. P. J. 2010, ApJ, 721, 923
Laine, R. O. & Lin, D. N. C. 2011, The Astrophysical Journal, 745, 2
Laine, R. O., Lin, D. N. C., & Dong, S. 2008, ApJ, 685, 521
Lamers, H. J. G. L. M. & Cassinelli, J. P. 1999, Introduction to Stellar Winds
Lammer, H., Bredehöft, J. H., Coustenis, A., et al. 2009, A&A Rev., 17, 181

Laundal, K. M. & Richmond, A. D. 2016, Magnetic Coordinate Systems (Springerlink.com)
Li, W., Raeder, J., Dorelli, J., Øieroset, M., & Phan, T. D. 2005, Geophys. Res. Lett., 32, L12S08
Liemohn, M. W. 2003, Journal of Geophysical Research (Space Physics), 108, 1251
Lin, J. 2004, Sol. Phys., 219, 169
Lindsay, G. M., Luhmann, J. G., Russell, C. T., & Gosling, J. T. 1999, J. Geophys. Res., 104, 12515
Llama, J., Wood, K., Jardine, M., et al. 2011, MNRAS, 416, L41
Lockwood, A. C., Johnson, J. A., Bender, C. F., et al. 2014, ApJ, 783, L29
López-Morales, M. 2007, ApJ, 660, 732
Louis, C. K., Jackman, C. M., Hospodarsky, G., et al. 2023, Journal of Geophysical Research (Space Physics), 128, e2022JA031155
Lu, G., Baker, D. N., McPherron, R. L., et al. 1998, J. Geophys. Res., 103, 11685
Luger, R. & Barnes, R. 2015, Astrobiology, 15, 119
Luger, R., Sestovic, M., Kruse, E., et al. 2017, Nature Astronomy, 1, 0129
Maehara, H., Shibayama, T., Notsu, Y., et al. 2015, Earth, Planets and Space, 67, 59
Maggio, A., Sanz-Forcada, J., & Scelsi, L. 2011, A&A, 527, A144
Mann, G., Melnik, V. N., Rucker, H. O., Konovalenko, A. A., & Brazhenko, A. I. 2018, A&A, 609, A41
Marsden, S. C., Petit, P., Jeffers, S. V., et al. 2014, MNRAS, 444, 3517
Massetti, S., Orsini, S., Milillo, A., & Mura, A. 2007, Planet. Space Sci., 55, 1557
Matsakos, T., Uribe, A., & Königl, A. 2015, A&A, 578, A6
Mauk, B. H., Clark, G., Gladstone, G. R., et al. 2020, Journal of Geophysical Research (Space Physics), 125, e27699
Mauk, B. H., Haggerty, D. K., Paranicas, C., et al. 2017, Geophys. Res. Lett., 44, 4410
Mayor, M. & Queloz, D. 1995, Nature, 378, 355
Mengel, M. W., Fares, R., Marsden, S. C., et al. 2016, MNRAS, 459, 4325
Merka, J., Szabo, A., Narock, T. W., et al. 2003, Journal of Geophysical Research (Space Physics), 108, 1077
Mignone, A., Bodo, G., Massaglia, S., et al. 2007, in JENAM-2007, "Our Non-Stable Universe", 96–96
Mignone, A., Tzeferacos, P., & Bodo, G. 2010, Journal of Computational Physics, 229, 5896
Miller, B. P., Gallo, E., Wright, J. T., & Dupree, A. K. 2012, ApJ, 754, 137
Miller, B. P., Gallo, E., Wright, J. T., & Pearson, E. G. 2015, ApJ, 799, 163
Mittag, M., Robrade, J., Schmitt, J. H. M. M., et al. 2017, A&A, 600, A119
Mittelholz, A., Johnson, C. L., Feinberg, J. M., Langlais, B., & Phillips, R. J. 2020, Science Advances, 6, eaba0513
Moschou, S.-P., Drake, J. J., Cohen, O., Alvarado-Gomez, J. D., & Garraffo, C. 2017, ApJ, 850, 191
Moschou, S.-P., Drake, J. J., Cohen, O., et al. 2019, ApJ, 877, 105
Murray, C. D. & Dermott, S. F. 2000, Solar System Dynamics (Cambridge University Press)

Naif, S., Selway, K., Murphy, B. S., Egbert, G., & Pommier, A. 2021, Physics of the Earth and Planetary Interiors, 313, 106661
Neubauer, F. M. 1998, J. Geophys. Res., 103, 19843
Newell, P. T., Sotirelis, T., Liou, K., Meng, C. I., & Rich, F. J. 2007, Journal of Geophysical Research (Space Physics), 112, A01206
Newell, P. T., Sotirelis, T., & Wing, S. 2010, Journal of Geophysical Research (Space Physics), 115, A03216
Newton, E. R., Irwin, J., Charbonneau, D., et al. 2017, ApJ, 834, 85
Newton, E. R., Irwin, J., Charbonneau, D., et al. 2016, ApJ, 821, 93
Nichols, J. D. & Milan, S. E. 2016, MNRAS, 461, 2353
Nicholson, B. A., Vidotto, A. A., Mengel, M., et al. 2016, MNRAS, 459, 1907
Nykyri, K. & Otto, A. 2001, Geophys. Res. Lett., 28, 3565
Odstrcil, D. & Pizzo, V. J. 1999, J. Geophys. Res., 104, 28225
Pallavicini, R., Golub, L., Rosner, R., et al. 1981, ApJ, 248, 279
Palmroth, M., Laitinen, T. V., & Pulkkinen, T. I. 2006, Annales Geophysicae, 24, 3467
Palmroth, M., Pulkkinen, T. I., Janhunen, P., & Wu, C. C. 2003, Journal of Geophysical Research (Space Physics), 108, 1048
Papaloizou, J. C. B., Szuszkiewicz, E., & Terquem, C. 2018, MNRAS, 476, 5032
Park, J., Lühr, H., Knudsen, D. J., Burchill, J. K., & Kwak, Y.-S. 2017, Journal of Geophysical Research (Space Physics), 122, 2345
Parker, E. N. 1955, ApJ, 122, 293
Parker, E. N. 1958, ApJ, 128, 664
Patsourakos, S. & Georgoulis, M. K. 2017, Sol. Phys., 292, 89
Paudel, R. R., Gizis, J. E., Mullan, D. J., et al. 2018, ApJ, 858, 55
Payne, R. C. & Kaltenegger, L. 2024, Monthly Notices of the Royal Astronomical Society: Letters, 530, L13
Pineda, J. S. & Villadsen, J. 2023, Nature Astronomy, 7, 569
Pomoell, J. & Poedts, S. 2018, Journal of Space Weather and Space Climate, 8, A35
Preusse, S., Kopp, A., Büchner, J., & Motschmann, U. 2006, A&A, 460, 317
Preusse, S., Kopp, A., Büchner, J., & Motschmann, U. 2007, Planet. Space Sci., 55, 589
Priest, E. R. & Forbes, T. G. 2002, A&A Rev., 10, 313
Reindl, N., Bainbridge, M., Przybilla, N., et al. 2019, MNRAS, 482, L93
Reiners, A. 2012, Living Reviews in Solar Physics, 9, 1
Reiners, A. & Basri, G. 2010, ApJ, 710, 924
Reiners, A., Basri, G., & Browning, M. 2009, ApJ, 692, 538
Reiners, A., Schüssler, M., & Passegger, V. M. 2014, ApJ, 794, 144
Reiners, A., Shulyak, D., Anglada-Escudé, G., et al. 2013, A&A, 552, A103
Reva, A., Loboda, I., Bogachev, S., & Kirichenko, A. 2024, Sol. Phys., 299, 55
Riley, P., Caplan, R. M., Giacalone, J., Lario, D., & Liu, Y. 2016, ApJ, 819, 57
Riley, P. & Crooker, N. U. 2004, ApJ, 600, 1035
Roettenbacher, R. M. & Kane, S. R. 2017, ApJ, 851, 77
Route, M. 2019, ApJ, 872, 79
Sakata, R., Seki, K., Sakai, S., et al. 2020, Journal of Geophysical Research (Space Physics), 125, e26945

Samara, E., Patsourakos, S., & Georgoulis, M. K. 2021, The Astrophysical Journal Letters, 909, L12
Saur, J., Grambusch, T., Duling, S., Neubauer, F. M., & Simon, S. 2013, A&A, 552, A119
Saur, J., Janser, S., Schreiner, A., et al. 2018, Journal of Geophysical Research (Space Physics), 123, 9560
Saur, J., Willmes, C., Fischer, C., et al. 2021, A&A, 655, A75
Schield, M. A. 1969, J. Geophys. Res., 74, 1275
Sckopke, N. 1966, J. Geophys. Res., 71, 3125
Scolini, C., Dasso, S., Rodriguez, L., Zhukov, A. N., & Poedts, S. 2021, A&A, 649, A69
Seager, S. 2013, Science, 340, 577
See, V., Jardine, M., Fares, R., Donati, J. F., & Moutou, C. 2015, MNRAS, 450, 4323
Seli, B., Vida, K., Moór, A., Pál, A., & Oláh, K. 2021, A&A, 650, A138
Semel, M. 1989, A&A, 225, 456
Shibata, K. & Magara, T. 2011, Living Reviews in Solar Physics, 8, 6
Shkolnik, E., Bohlender, D. A., Walker, G. A. H., & Collier Cameron, A. 2008, ApJ, 676, 628
Shkolnik, E., Walker, G. A. H., & Bohlender, D. A. 2003, ApJ, 597, 1092
Shulyak, D., Reiners, A., Engeln, A., et al. 2017, Nature Astronomy, 1, 0184
Sibeck, D. G. 1990, J. Geophys. Res., 95, 3755
Siscoe, G. L., Formisano, V., & Lazarus, A. J. 1968, J. Geophys. Res., 73, 4869
Slavin, J. A., DiBraccio, G. A., Gershman, D. J., et al. 2014, Journal of Geophysical Research (Space Physics), 119, 8087
Song, H. Q., Zhang, J., Cheng, X., et al. 2020, ApJ, 901, L21
Song, P. & Russell, C. T. 1992, J. Geophys. Res., 97, 1411
Stassun, K. G., Oelkers, R. J., Paegert, M., et al. 2019, AJ, 158, 138
Stevenson, D. J., Spohn, T., & Schubert, G. 1983, Icarus, 54, 466
Storey, P. J. & Hummer, D. G. 1995, MNRAS, 272, 41
Strobel, D. F. & Atreya, S. K. 1983, in Physics of the Jovian Magnetosphere, 51–67
Strugarek, A. 2016, The Astrophysical Journal, 833, 140
Strugarek, A., Ahuir, J., Brun, A. S., et al. 2019a, in SF2A-2019: Proceedings of the Annual meeting of the French Society of Astronomy and Astrophysics, ed. P. Di Matteo, O. Creevey, A. Crida, G. Kordopatis, J. Malzac, J. B. Marquette, M. N'Diaye, & O. Venot, Di
Strugarek, A., Brun, A. S., Donati, J. F., Moutou, C., & Réville, V. 2019b, ApJ, 881, 136
Strugarek, A., Brun, A. S., Matt, S. P., & Réville, V. 2014, ApJ, 795, 86
Strugarek, A., Brun, A. S., Matt, S. P., & Réville, V. 2015, ApJ, 815, 111
Tabata, T. & Shirai, T. 2000, Atomic Data and Nuclear Data Tables, 76, 1
Telleschi, A., Güdel, M., Briggs, K. R., Audard, M., & Palla, F. 2007, A&A, 468, 425
Tilley, M. A., Segura, A., Meadows, V., Hawley, S., & Davenport, J. 2019, Astrobiology, 19, 64
Tosi, N., Godolt, M., Stracke, B., et al. 2017, A&A, 605, A71

Tóth, G., Sokolov, I. V., Gombosi, T. I., et al. 2005, Journal of Geophysical Research (Space Physics), 110, A12226
Trávníček, P., Hellinger, P., & Schriver, D. 2007, Geophys. Res. Lett., 34, L05104
Tremblin, P. & Chiang, E. 2013, MNRAS, 428, 2565
Treumann, R. A. 2006, A&A Rev., 13, 229
Trigilio, C., Biswas, A., Leto, P., et al. 2023, arXiv e-prints, arXiv:2305.00809
Turbet, M., Bolmont, E., Ehrenreich, D., et al. 2020, A&A, 638, A41
Turbet, M., Bolmont, E., Leconte, J., et al. 2018, A&A, 612, A86
Turner, J. D., Christie, D., Arras, P., Johnson, R. E., & Schmidt, C. 2016, MNRAS, 458, 3880
Turner, J. D., Grießmeier, J.-M., Zarka, P., & Vasylieva, I. 2019, A&A, 624, A40
Turner, J. D., Grießmeier, J.-M., Zarka, P., Zhang, X., & Mauduit, E. 2024, A&A, 688, A66
Turner, J. D., Zarka, P., & Grießmeier, J.-M. 2022, in Bulletin of the American Astronomical Society, Vol. 54, 404.02
Turner, J. D., Zarka, P., Grießmeier, J.-M., et al. 2021, A&A, 645, A59
Turner, J. D., Zarka, P., Griessmeier, J.-M., et al. 2023, arXiv e-prints, arXiv:2310.05363
Turnpenney, S., Nichols, J. D., Wynn, G. A., & Burleigh, M. R. 2018, ApJ, 854, 72
Turnpenney, S., Nichols, J. D., Wynn, G. A., & Jia, X. 2020, MNRAS, 494, 5044
Tyler, R. H., Henning, W. G., & Hamilton, C. W. 2015, The Astrophysical Journal Supplement Series, 218, 22
Tziotziou, K., Georgoulis, M. K., & Raouafi, N.-E. 2012, ApJ, 759, L4
Unglaub, K. 2008, A&A, 486, 923
Unterborn, C. T., Foley, B. J., Desch, S. J., et al. 2022, ApJ, 930, L6
Vaiana, G. S., Cassinelli, J. P., Fabbiano, G., et al. 1981, ApJ, 245, 163
Van Doorsselaere, T., Wardle, N., Del Zanna, G., et al. 2011, ApJ, 727, L32
Van Grootel, V., Fernandes, C. S., Gillon, M., et al. 2018, ApJ, 853, 30
Van Looveren, G., Güdel, M., Boro Saikia, S., & Kislyakova, K. 2024, A&A, 683, A153
Varela, J., Brun, A. S., Strugarek, A., et al. 2022, A&A, 659, A10
Varela, J., Reville, V., Brun, A. S., Pantellini, F., & Zarka, P. 2016, A&A, 595, A69
Varela, J., Réville, V., Brun, A. S., Zarka, P., & Pantellini, F. 2018, Astronomy & Astrophysics, 616, A182
Vasyliūnas, V. M. & Song, P. 2005, Journal of Geophysical Research (Space Physics), 110, A02301
Vedantham, H. K., Callingham, J. R., Shimwell, T. W., et al. 2020, Nature Astronomy, 4, 577
Vida, K., Kővári, Z., Pál, A., Oláh, K., & Kriskovics, L. 2017, ApJ, 841, 124
Vida, K., Kriskovics, L., Oláh, K., et al. 2016, A&A, 590, A11
Vida, K., Leitzinger, M., Kriskovics, L., et al. 2019, A&A, 623, A49
Vidal-Madjar, A., Lecavelier des Etangs, A., Désert, J. M., et al. 2003a, Nature, 422, 143
Vidal-Madjar, A., Lecavelier des Etangs, A., Désert, J.-M., et al. 2003b, Nature, 422, 143
Vidotto, A. A. 2021, Living Reviews in Solar Physics, 18, 3

Vidotto, A. A. & Donati, J. F. 2017, A&A, 602, A39
Vidotto, A. A., Fares, R., Jardine, M., et al. 2012, MNRAS, 423, 3285
Vidotto, A. A., Fares, R., Jardine, M., Moutou, C., & Donati, J. F. 2015, MNRAS, 449, 4117
Vidotto, A. A., Jardine, M., & Helling, C. 2010, ApJ, 722, L168
Vidotto, A. A., Jardine, M., & Helling, C. 2011, MNRAS, 411, L46
Villadsen, J. & Hallinan, G. 2019, ApJ, 871, 214
Vourlidas, A., Lynch, B. J., Howard, R. A., & Li, Y. 2013, Sol. Phys., 284, 179
Walls, F. L. & Dunn, G. H. 1974, J. Geophys. Res., 79, 1911
Wang, J. & Ford, E. B. 2011, MNRAS, 418, 1822
Wang, Y., Zhuang, B., Hu, Q., et al. 2016, Journal of Geophysical Research (Space Physics), 121, 9316
Weber, C., Erkaev, N. V., Ivanov, V. A., et al. 2018, MNRAS, 480, 3680
Weber, C., Lammer, H., Shaikhislamov, I. F., et al. 2017, MNRAS, 469, 3505
Weber, E. J. & Davis, Leverett, J. 1967, ApJ, 148, 217
Weimer, D. R., Bowman, B. R., Sutton, E. K., & Tobiska, W. K. 2011, Journal of Geophysical Research (Space Physics), 116, A01312
Wheatley, P. J., Louden, T., Bourrier, V., Ehrenreich, D., & Gillon, M. 2017, MNRAS, 465, L74
Wilson, O. C. 1978, ApJ, 226, 379
Wilson, T. L., Rohlfs, K., & Hüttemeister, S. 2009, Tools of Radio Astronomy
Winslow, R. M., Lugaz, N., Philpott, L., et al. 2020, ApJ, 889, 184
Winslow, R. M., Philpott, L., Paty, C. S., et al. 2017, Journal of Geophysical Research (Space Physics), 122, 4960
Winters, J. G., Henry, T. J., Jao, W.-C., et al. 2019, AJ, 157, 216
Wood, B. E., Müller, H.-R., Redfield, S., et al. 2021, ApJ, 915, 37
Wright, J. T. & Gaudi, B. S. 2013, in Planets, Stars and Stellar Systems. Volume 3: Solar and Stellar Planetary Systems, ed. T. D. Oswalt, L. M. French, & P. Kalas, 489
Wright, N. J. & Drake, J. J. 2016, Nature, 535, 526
Wright, N. J., Newton, E. R., Williams, P. K. G., Drake, J. J., & Yadav, R. K. 2018, MNRAS, 479, 2351
Yang, J., Boué, G., Fabrycky, D. C., & Abbot, D. S. 2014, ApJ, 787, L2
Yang, Z., Zhang, L., Meng, G., et al. 2023, A&A, 669, A15
Yashiro, S. & Gopalswamy, N. 2009, in IAU Symposium, Vol. 257, Universal Heliophysical Processes, ed. N. Gopalswamy & D. F. Webb, 233–243
Youssef, M. 2012, NRIAG Journal of Astronomy and Geophysics, 1, 172
Zarka, P. 1998, J. Geophys. Res., 103, 20159
Zarka, P. 2007, Planet. Space Sci., 55, 598
Zarka, P., Cecconi, B., & Kurth, W. S. 2004, Journal of Geophysical Research: Space Physics, 109
Zarka, P., Magalhães, F. P., Marques, M. S., et al. 2021, Journal of Geophysical Research (Space Physics), 126, e29780
Zarka, P., Marques, M. S., Louis, C., et al. 2018, A&A, 618, A84
Zarka, P., Treumann, R. A., Ryabov, B. P., & Ryabov, V. B. 2001, Ap&SS, 277, 293

Zhilkin, A. G. & Bisikalo, D. V. 2019, Astronomy Reports, 63, 550
Zhilkin, A. G. & Bisikalo, D. V. 2020, Astronomy Reports, 64, 563
Zieba, S., Kreidberg, L., Ducrot, E., et al. 2023, Nature, 620, 746

Appendices

A. General calculations, derivations and technical aspects

A.1. Calculation of Gauss coefficients of a tilted magnetic dipole

In order to describe a magnetic dipole with an arbitrary inclined magnetic axis (angle θ_B with respect to the z–axis) the three first order Gauss coefficients are needed. Starting with the well known relation between all the first order Gauss coefficients (Laundal & Richmond 2016)

$$\tan(\theta_B) = \sqrt{\left(\frac{g_1^1}{g_1^0}\right)^2 + \left(\frac{h_1^1}{g_1^0}\right)^2} \,, \tag{A.1}$$

we can solve for g_1^0 as a function of g_1^1 and h_1^1. Hence,

$$(g_1^0)^2 = \frac{(g_1^1)^2 + (h_1^1)^2}{\tan^2(\theta_B)} \,. \tag{A.2}$$

Inserting Eq. A.2 into the relation $B_{eq}^2 = (g_1^0)^2 + (g_1^1)^2 + (h_1^1)^2$ (Laundal & Richmond 2016) we arrive at

$$B_{eq}^2 = \frac{(g_1^1)^2 + (h_1^1)^2}{\tan^2(\theta)} + \frac{\left[(g_1^1)^2 + (h_1^1)^2\right]\,\tan^2(\theta_B)}{\tan^2(\theta_B)} \tag{A.3}$$

$$= \frac{(g_1^1)^2\left[1 + \tan^2(\theta_B)\right] + (h_1^1)^2\left[1 + \tan^2(\theta_B)\right]}{\tan^2(\theta_B)} \,. \tag{A.4}$$

For $(g_1^1)^2$ it follows

$$(g_1^1)^2 \frac{1 + \tan^2(\theta_B)}{\tan^2(\theta_B)} = B_{eq}^2 - (h_1^1)^2 \frac{1 + \tan^2(\theta_B)}{\tan^2(\theta_B)} \,, \tag{A.5}$$

and consequently

$$(g_1^1)^2 = B_{eq}^2 \frac{\tan^2(\theta_B)}{1 + \tan^2(\theta_B)} - (h_1^1)^2 \,. \tag{A.6}$$

The well known relationship between h_1^1, g_1^1 and the longitude of the magnetic north pole, λ_{np} (Laundal & Richmond (2016)),

$$\lambda_{np} = 360^\circ - \arctan\left(\frac{h_1^1}{g_1^1}\right) \Leftrightarrow \frac{h_1^1}{g_1^1} = \tan(360^\circ - \lambda_{np}) \,, \tag{A.7}$$

can be solved for the h_1^1. Taking the square root then yields

$$(h_1^1)^2 = \tan^2(360° - \lambda_{np})(g_1^1)^2 \,. \tag{A.8}$$

Using the above in Eq. A.6 and after solving for $(g_1^1)^2$ we arrive at

$$(g_1^1)^2 = B_{eq}^2 \frac{\tan^2(\theta_B)}{1+\tan^2(\theta_B)} - \tan^2(360° - \lambda_{np})(g_1^1)^2 \tag{A.9}$$

$$(g_1^1)^2 \left[1 + \tan^2(360° - \lambda_{np})\right] = B_{eq}^2 \frac{\tan^2(\theta_B)}{1+\tan^2(\theta_B)} \tag{A.10}$$

$$(g_1^1)^2 = B_{eq}^2 \frac{\tan^2(\theta_B)}{1+\tan^2(\theta_B)} \frac{1}{1+\tan^2(360° - \lambda_{np})} \,. \tag{A.11}$$

Putting all coefficients together we arrive at the formulas for the three dipole Gauss coefficients:

$$g_1^1 = B_{eq} \frac{\tan(\theta_B)}{\sqrt{1+\tan^2(\theta_B)}} \frac{1}{\sqrt{1+\tan^2(360° - \lambda_{np})}} \tag{A.12}$$

$$h_1^1 = \tan(360° - \lambda_{np})\, g_1^1 \tag{A.13}$$

$$g_1^0 = \frac{\sqrt{(g_1^1)^2 + (h_1^1)^2}}{\tan(\theta_B)} \,. \tag{A.14}$$

B. Tau Boötis b

B.1. Poynting fluxes as function of radial distance from the planet

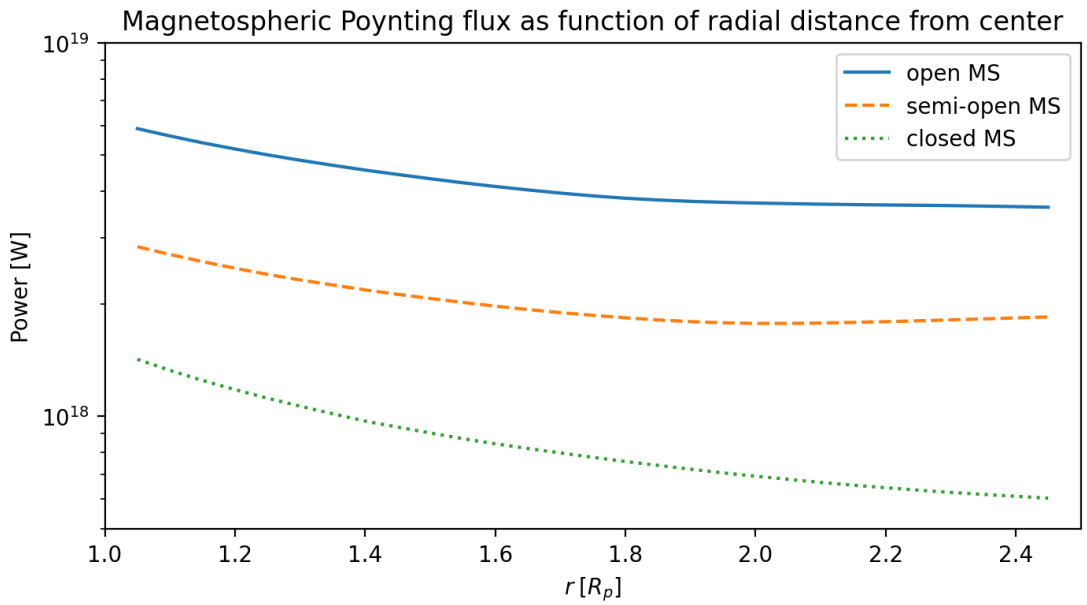

Figure B.1.: Magnetospheric Poynting flux as function of radial distance from the planet's center calculated from Eq. 6.5 for the open (blue), semi–open (orange) and closed (green) magnetosphere model.

Here we study the dependence of magnetospheric Poynting fluxes as a function of radial distance from the planet. The particular choice of integrating Poynting fluxes over a spherical shell with radius $r = 2R_p$ is based on the fact that radio emission around Jupiter and most solar system planets with intrinsic magnetic fields originates from altitudes of about 1 R_p or higher above the planets (see e.g. Zarka 1998) rather than from within the ionosphere or even further below. We do not have evidence if this translates to extrasolar planets but simply assume so. For the ECMI mechanism to work efficiently the ratio between electron gyro frequency and plasma frequency, $\nu_{g,e}/\nu_{p,e}$, must be significantly larger than 1 which turns the magnetospheric region at high altitudes to favored radio source regions where plasma densities are strongly reduced compared to other regions of the magnetosphere. (Zarka 1998; Treumann 2006; Weber

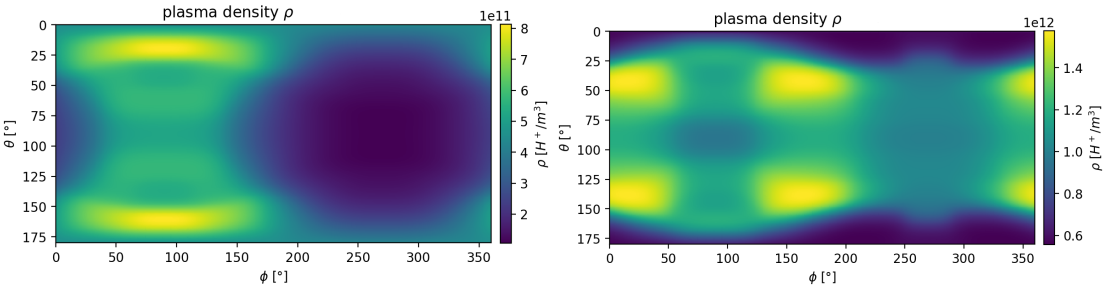

Figure B.2.: Plasma density maps over a sphere with $r = 2\ R_p$ for the open (left panel) and closed (right panel) MS case.

et al. 2017). Considering the plasma and neutral particle density within the modeled magnetosphere we also chose a location (i.e. the radius) where ion–neutral collisions are significantly reduced (e.g. above the ionosphere). The favored radius according to this constraint lies between 1.3 and 3 R_p (see Sect. B.2 and Fig. B.3).
In order to show that the choice of $r = 2\ R_p$ or any other radial distance within the magnetosphere does not influence the results and the derived conclusions significantly (despite controlling the emission frequency since stronger magnetic fields cause higher gyro frequencies) we integrated the Poynting flux (Eq. 6.5) for shells with radii between 1 and 2.5 R_p above the planet. The results are displayed in Fig. B.1 for the open (blue), semi-open (orange) and closed (green) magnetosphere model. We note that the Poynting flux is not a conserved quantity in this system since several possibilities for conversion from or to electromagnetic energy exist within the magnetosphere (e.g. deceleration due to magnetic stresses, ion–neutral collisions, conversion between electromagnetic and thermal energy). As it can be seen in Fig. B.1 the Poynting flux variation as function of r amounts to a factor of ∼1.5–2 for the open MS, ∼ 1 – 1.5 for the semi–open MS and ∼2 for the closed MS. Given the uncertainties with which our study is anyway afflicted (such as the uncertainty of the stellar wind density, magnetic field strength, etc.), the uncertainty by the choice of the shell radius upon the Poynting fluxes is negligible. The choice of magnetic field strength, for instance, has much larger influence on the Poynting fluxes due to its B^2 dependence.

B.2. On the neutral atmosphere model assumptions and its interaction with the plasma

In this section we discuss some properties and assumptions on our neutral atmosphere model presented in Sect. 6.2.1 as well as how the atmosphere affects the plasma focusing on our basic model (Table 6.1).
The aim of this work is not a detailed description of the ionosphere of the planet, but its magnetosphere and larger space environment. Our simplistic atmosphere model only acts through collisions with the plasma and affects the photo–ionization rate (i.e. plasma production) which both directly scale with the neutral particle density (Eqs. 5.5,

??). Due to the exponential decrease of neutral particle density (Eq. 5.5) with radial distance from the planet the atmosphere's effect on the plasma population drastically decreases with increasing altitude. The denser the neutral atmosphere the more the magnetospheric plasma is decelerated which leads to plasma pile up around the planet mimicking an ionosphere. Figure B.3 shows plasma density profiles within the magnetosphere as function of radial distance from the center. The black dotted line represents the plasma density along the polar axes. Red and magenta lines represent equatorial upstream and downstream profiles respectively. The orange solid line denotes the neutral particle density according to Eq. 5.5, the green dotted line shows the corresponding ion–neutral collision frequency. As visible in Fig. B.3 the effect of ion–neutral collisions and thus the amount of plasma pile up is drastically reduced above an altitude near 1.3 R_p. There the neutral particle density is $n(r = 1.3R_p) \approx 5 \times 10^{10}$ m^{-3}. The ion–neutral collision frequency is ~ 0.5 s^{-1} at the surface and drastically decreases with altitude. In our studies we focus on the region $1R_p$ above the planets surface and thus above the ionospheric shell. At $r = 2$ R_p the collisions are negligible because the collision frequency has decreased to about $\sim 10^{-7}$ s^{-1}.

The large scale height of 4373 km increases the extent of the atmosphere but is needed in order to sufficiently resolve the atmosphere in our model. However, the atmospheres of Hot Jupiter exoplanets are expected to be strongly inflated due to intense stellar irradiation (e.g. Vidal-Madjar et al. 2003b) which is partially mimicked by the large scale height. The surface neutral particle density n_0 corresponds to an atmosphere pressure near 10^{-3} nbar assuming a temperature between 1000 and 2000 K. Here the mixing ratio of plasma (hydrogen ions) and neutral particles is roughly 50 %. The neutral atmosphere consists of molecular hydrogen which is the most abundant molecule in all solar system gas giants.

In order to demonstrate the minor role of the neutral atmosphere at $r = 2$ R_p we show plasma density maps over a shell at this altitude in Fig. B.2. The left and right panels display the density map of the open and closed MS case, respectively. There the neutral particle density is $n(r = 2\ R_p) \approx 4.6 \times 10^5$ m^{-3} according to Eq. 5.5 and Fig. B.3 leading to a neutral–plasma mixing ratio of about 10^{-6}. Regions of high plasma density (i.e. at the day side) indicate regions where the interaction between the neutral atmosphere and plasma is strongest (at $r = 2$ R_p) in terms of ion–neutral collisions and recombination. However, the effect of the neutral atmosphere on the plasma is an order of magnitude lower than in regions within the ionosphere below ~ 1.3 R_p.

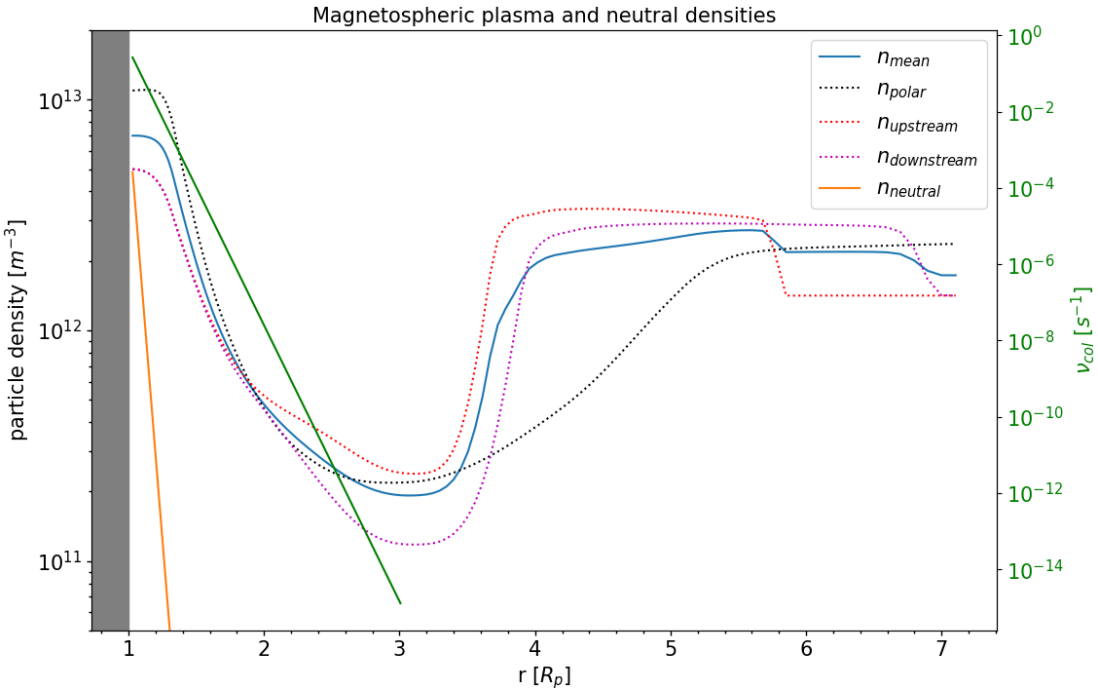

Figure B.3.: Plasma density profiles along the polar axis (black dotted line), upstream (red) and downstream x–axis (magenta). The blue solid line denotes the mean plasma density profile. The orange solid line shows the neutral particle density according to our atmosphere model (Eq. 5.5). The green solid line (right y–axis) denotes ion–neutral collision frequencies.

C. Trappist-1

C.1. Derivation of the photo–ionization rate with given mass loss rate

In Sect. 7.2.2 we described our model for the atmosphere of Trappist-1e. In the literature estimates for the mass loss rate of O_2 are given (Bourrier et al. 2017a) and we included it by choosing a photo–ionization rate that would result in the given mass loss rate. From Eq. 7.2,

$$\dot{M}_{\mathrm{O}_2} = m_{\mathrm{O}_2}\, \nu_{ion} \int_V n_{\mathrm{O}_2}(r)\, d\mathrm{V} \ , \tag{C.1}$$

we start by expanding the volume integral and by factoring out constants. We integrate over the whole radially symmetric atmosphere from the surface at R_p up to an arbitrary height z. The θ and ϕ integrals can be carried out immediately:

$$\dot{M}_{\mathrm{O}_2} = m_{\mathrm{O}_2}\, \nu_{ion}\, n_{\mathrm{O}_2,0} \int_0^{2\pi} \int_0^{\pi} \int_{R_p}^{R_p+z} r^2 \sin\theta \exp\left(\frac{R_p - r}{H}\right) dr d\theta d\phi \tag{C.2}$$

$$= m_{\mathrm{O}_2}\, n_{\mathrm{O}_2,0}\, \nu_{ion} 2\pi \int_0^{\pi} \sin\theta d\theta \int_{R_p}^{R_p+z} r^2 \exp\left(\frac{R_p - r}{H}\right) dr \tag{C.3}$$

$$= \underbrace{m_{\mathrm{O}_2}\, n_{\mathrm{O}_2,0}\, \nu_{ion} 2\pi \left[-\cos\theta\right]_0^{\pi}}_{C} \int_{R_p}^{R_p+z} r^2 \exp\left(\frac{R_p - r}{H}\right) dr \ . \tag{C.4}$$

With the substitution $u = R_p/H - r/H$ we continue,

$$\dot{M}_{\mathrm{O}_2} = -HC \int_{u(R_p)}^{u(R_p+z)} H^2 e^u \left(\frac{R_p}{H} - u\right)^2 du = -HC \int_{u(R_p)}^{u(R_p+z)} e^u \left(R_p^2 - 2R_p u H + u^2 H^2\right) du \tag{C.5}$$

$$= -H^3 C \left[\underbrace{\int_{u(R_p)}^{u(R_p+z)} \frac{R_p^2 e^u}{H^2} du}_{\frac{R_p^2}{H^2}\left[e^{-z/H}-1\right]} - \int_{u(R_p)}^{u(R_p+z)} \frac{2R_p e^u u}{H} du + \int_{u(R_p)}^{u(R_p+z)} e^u u^2 du \right] \tag{C.6}$$

$$= -H^3 C \left[\frac{R_p^2}{H^2}\left(e^{-z/H} - 1\right) - \int_{u(R_p)}^{u(R_p+z)} \frac{2R_p e^u u}{H} du + \underbrace{\int_{u(R_p)}^{u(R_p+z)} e^u u^2 du}_{\star} \right] . \tag{C.7}$$

The $\star$ term on the right side can be solved using integration by parts, which leads to

$$(\star) = \left[u^2 e^u\right]_{u(R_p)}^{R_p+z} - \underbrace{\int 2ue^u du}_{(\star\star)} . \tag{C.8}$$

Again integrating by parts the $(\star\star)$ term, we arrive at

$$(\star\star) \left[\left(\frac{R_p - r}{H}\right)^2 e^{(R_p-r)/H} \right]_{u(R_p)}^{R_p+z} - \left[\left[2ue^u\right]_{u(R_p)}^{R_p+z} - \int 2e^u du \right] \tag{C.9}$$

$$\Leftrightarrow \left(\frac{-z}{H}\right)^2 e^{-z/H} - \left[2\frac{R_p - r}{H} e^{(R_p-z)/H} \right]_{R_p}^{R_p+z} + 2\left[e^{(R_p-r)/H}\right]_{u(R_p)}^{R_p+z} \tag{C.10}$$

$$\Leftrightarrow \frac{z^2}{H^2} e^{-z/H} + 2\frac{z}{H} e^{-z/H} + 2\left(e^{-z/H} - 1\right) . \tag{C.11}$$

Plugging the combined solution of the $(\star)$ term into Eq. C.7 we arrive at

$$\dot{M} = -H^3 C \left[\frac{R_p^2}{H^2}\left(e^{-z/H} - 1\right) \underbrace{\int \frac{2R_p e^u u}{H} du}_{(\star\star\star)} + \frac{z^2}{H^2} e^{-z/H} + 2\frac{z}{H} e^{-z/H} + 2\left(e^{-z/H} - 1\right) \right] . \tag{C.12}$$

We solve $(\star\star\star)$ using integration by parts, i.e. $\hat{u} = u$ and $\hat{v}' = e^u$, which results in

$$(\star\star\star) = \left[\frac{2R_p}{H} u e^u\right]_{u(R_p)}^{R_p+z} - \int \frac{2R_p}{H} e^u du \tag{C.13}$$

$$= \frac{2R_p}{H}\frac{-z}{H} e^{-z/H} - \frac{2R_p}{H}\left[e^{-z/H} - 1\right] . \tag{C.14}$$

Inserting Eq. C.14 into Eq. C.12 and simplifying the result gives

$$\dot{M} = -H^3 C \left[\frac{R_p^2}{H^2}\left(e^{-z/H} - 1\right) + \frac{2R_p}{H}\left(z e^{-z/H} + H\left(e^{-z/H} - 1\right)\right) + \frac{z^2}{H^2} e^{-z/H} + \frac{2z}{H} e^{-z/H} + 2e^{-z/H} - 2\right] \tag{C.15}$$

$$= -C\left[H e^{-z/H}\left(R_p^2 + 2R_p z + 2R_p H + z^2 + 2zH + 2H^2\right) - H R_p^2 - 2R_p H^2 - 2H^3\right] . \tag{C.16}$$

Inserting the constant C defined in Eq. C.4 into Eq. C.16 finally results in the formula given in 7.3. Parts of this derivation were done with the help of Wolfram Alpha.

Acknowledgments

I would like to express my special thanks to Joachim Saur, who has been my supervisor and mentor over the years. The countless and instructive discussions have helped a lot to steer the projects in the right direction and, above all, they have contributed significantly to my development, for which I am endlessly grateful. I am also very grateful for the ambitious support I received in my search for a position to gain a foothold in science.

I would also like to express my deepest thanks to Alexander Grayver. The Trappist project would only have been half as exciting and instructive without him. Thank you for the discussions and especially for providing the induction model, which contributed significantly to the results of this work.

Thanks also go to Stefan Duling, who provided many basic implementations for Pluto and for any discussion. Thanks also to the whole working group, especially Stephan Schlegel, Jason Winkenstern and David Strack for their support and the occasional chat in between.

Finally, I would like to express a special thanks to Katharina Lohmann, my faithful companion and the best distraction from work one could wish for. I thank my family for always standing by my side, no matter what and when. In the most difficult times, there is nothing better than hearing your parents' voice.

With regard to the provision of resources, we would also like to express our gratitude:

This project has received funding from the European Research Council (ERC) under the European Union's Horizon 2020 research and innovation programme (grant agreement No. 884711).

The authors gratefully acknowledge the Gauss Centre for Supercomputing e.V. (www.gauss-centre.eu) for funding this project by providing computing time through the John von Neumann Institute for Computing (NIC) on the GCS Supercomputer JUWELS at Jülich Supercomputing Centre (JSC).

This work used resources of the Deutsches Klimarechenzentrum (DKRZ) granted by its Scientific Steering Committee (WLA) under project ID 1350.

We furthermore thank the Regional Computing Center of the University of Cologne (RRZK) for providing computing time on the DFG-funded (Funding number: INST 216/512/1FUGG) High Performance Computing (HPC) system CHEOPS as well as support.

We would also like to thank the Pluto team for developing, providing and maintaining the Pluto code.

Statement on Data Availability

All processed output data and results in form of visualizations, diagrams and text–based data files are archived on the server `neptun.geo.uni-koeln.de` at

`/raid0/archivierung/absolventen_archivierung/`

`/2025_PhD_FElekes_StellarWindPlanetInteractions_Exoplanets`

which can be reached via the university network.

Due to the large storage space needed to archive all the raw data, especially the time–depended simulation results, we only provide the necessary data to reproduce the simulations. Thus, the modified Pluto code we used and input scripts are provided.
A readme-file is attached to the simulation input data with instructions on reproducing the data.
Raw simulation output is archived privately and will be made available on request.

Eidesstattliche Erklärung

Hiermit versichere ich an Eides statt, dass ich die vorliegende Dissertation selbstständig und ohne die Benutzung anderer als der angegebenen Hilfsmittel und Literatur angefertigt habe. Alle Stellen, die wörtlich oder sinngemäß aus veröffentlichten und nicht veröffentlichten Werken dem Wortlaut oder dem Sinn nach entnommen wurden, sind als solche kenntlich gemacht. Ich versichere an Eides statt, dass diese Dissertation noch keiner anderen Fakultät oder Universität zur Prüfung vorgelegen hat; dass sie - abgesehen von unten angegebenen Teilpublikationen und eingebundenen Artikeln und Manuskripten - noch nicht veröffentlicht worden ist sowie, dass ich eine Veröffentlichung der Dissertation vor Abschluss der Promotion nicht ohne Genehmigung des Promotionsausschusses vornehmen werde. Die Bestimmungen dieser Ordnung sind mir bekannt. Darüber hinaus erkläre ich hiermit, dass ich die Ordnung zur Sicherung guter wissenschaftlicher Praxis und zum Umgang mit wissenschaftlichem Fehlverhalten der Universität zu Köln gelesen und sie bei der Durchführung der Dissertation zugrundeliegenden Arbeiten und der schriftlich verfassten Dissertation beachtet habe und verpflichte mich hiermit, die dort genannten Vorgaben bei allen wissenschaftlichen Tätigkeiten zu beachten und umzusetzen. Ich versichere, dass die eingereichte elektronische Fassung der eingereichten Druckfassung vollständig entspricht.

Teilpublikationen

- Elekes, F. Saur J. 2023, *Space environment and magnetospheric Poynting fluxes of the exoplanet τ Boötis b*, AA, 671, A133, doi:10.1051/0004-6361/202244947.

Bonn, 02.12.2024 Filip Elekes